MONASH University

Molecular investigation of physiochemistry of liquid phase and MOF-derived nanomaterials

Swarit Dwivedi

(M.Tech. in Chemical Engineering)

A thesis submitted for the degree of Doctor of Philosophy at

Department of Chemical Engineering

Monash University, Clayton, 3800

Australia

May, 2021

Copyright notice

Abstract

With the potentially catastrophic consequences of climate change in observance, researchers are exploring innovative strategies to combat the rising levels of CO_2 into the atmosphere. Although renewable energy resources can cater to the global energy demand in future, carbon capture and utilisation technologies (CCUS) are the need of the hour. Researchers reported numerous heterogeneous catalysis reactions for CO_2 hydrogenation into value-added C1 platform chemicals. However, the cost of hydrogen produced from renewable sources limits the application of most reaction schemes. Despite this, optimising the kinetics (high activity) and the thermodynamics (high yield and selectivity) of CO_2 hydrogenation remain a challenge. Our group reported metal organic framework (MOF)-derived advanced catalytic materials with a controlled reaction environment (liquid media) for enhanced activity and increased yield of CO/CO_2 hydrogenation. However, the physiochemistry of liquid media and the MOF-derived catalysts are not well understood at molecule length scale. In this work, we study the dynamics of liquid media (formaldehyde-methanol-water), the morphology of MOF-derived nanomaterial (thermally decomposed Zr-MOFs) using computational methods that are presently capable of simulating a large number of atoms (> 10000). We also report a reactive molecular dynamics forcefield parameter set (ReaxFF) trained for simulating Ru/C/H/O chemistry for CO_2 hydrogenation on ruthenium nanoparticles. Understanding of these advanced materials and the liquid phase at molecular length scale.

Our group earlier reported that in the presence of methanol and methanol-water mixtures, CO hydrogenation yields formaldehyde. The yield is affected by the micro-phase structure of formaldehyde-methanol-water mixtures. In this work, we report the solvation shell dynamics and hydrogen bond network in formaldehyde-methanol-water mixtures by classical molecular dynamics simulations. At low methanol concentrations, methanol clusters hydrophobically around methoxymethanol, whereas at high concentrations, methanol forms linear chains and solvated methoxymethanol within a chain/ring structure. However, water is mostly present at hydrophilic sites at near equimolar concentrations, which breaks the linear methanol chains. The observed microphase structure supports the previously reported hypothesis, which reasoned methanol solvation fort high yield of formaldehyde in methanol. This work also extends the same hypothesis across the whole concentration range of methanol-water mixture.

Experimentally, probing the micro-phase structure of low molecular weight polar solvent, co-solvent, and solute mixtures such as formaldehyde-methanol-water mixtures is challenging for contemporary experimental techniques. Methanol-water mixtures were previously reported for their hydrogen-bonding network by sophisticated resonant inelastic X-ray scattering spectroscopic measurements only. We present Small-Angle Neutron Scattering experiments on formaldehyde-methanol-water mixtures of varying concentrations to validate our observations via classical molecular dynamics simulations. We report an experimental methodology for probing hydrophobic clusters in formaldehyde-methanol-water and mixtures of similar nature. We identified hydrophobic methanol clustered around methoxymethanol at low methanol mol-fractions (x_m = 0.1, 0.3). The clusters composed of 6-10 molecules and have a radius of ~ 3 Å (x_m = 0.1) and ~ 5 Å (x_m = 0.3). We first demonstrate the capability of SANS as an experimental technique to measure such mixtures.

Metal Organic Frameworks (MOFs) are known for losing their structural characteristics at high temperatures and pressures, limiting their ability to act as catalysts for many heterogeneous reaction systems. However, recently a carbonaceous metal embedded nanomaterial derived from thermal decomposition of MOFs is reported for exceptional catalytic properties. High activity and stability are common observations in their application for various catalytic reactions. Our group reported Ru encapsulated thermally decomposed modified MIL-140C CO_2 hydrogenation to methanol with fast kinetics and high yield. The MOF-derived catalyst is experimentally reported as Zr and Ru finely dispersed in carbonaceous ribbons. We report the atomistic mechanisms that govern the structural transformation during thermal decomposition and the control parameters for this structural transformation. We first develop a reactive molecular dynamics forcefield parameter set for Zr-MOF chemistry by training previous Zr/C/H/O/N ReaxFF parameters to ZrO cluster BDC linker binding energy data (quantum mechanics, DFT). After that, we report the mechanism of structure collapse along with the negative thermal expansion coefficient of MIL-140C, UiO-66, and UiO-67. We identify CO, CO_2, H2, and C_2H_2 as the main gaseous products during the degradation of organic linkers. We report ZrO_x nanoparticles similar to the tetragonal phase of ZrO_2 and size of the order of ~1 nm, embedded in a disrupted organic linker phase.

We report the effect of cluster arrangement, pore size, linker chemistry, and reaction environment on morphology of the thermally decomposed MOF by comparing thermal decomposition of MIL-140C, m-MIL-140C (BPyDC linker), UiO-66, and Uio-67 under vacuum, CO_2, and H_2 environment. We observe a smaller size well dispersed of ZrO_x

nanoparticles under the H_2 atmosphere than CO_2. MOF with a larger pore size (UiO-67 and MIL-140C) also result in smaller nanoparticles in compared UiO-66. MIL-140C and UiO-67 undergo different mechanisms for cluster agglomeration. However, they result in similar size particles when the MOFs are subject to a sufficient heating regime.

Traditional Quantum Mechanics (QM)-based method become extremely expensive for large system sizes. Therefore, prediction simulating the effect of MOF-derived materials or liquid phase on the CO_2 hydrogenation chemistry on Ru surface becomes challenging. One feasible is reactive molecular dynamics simulation. However, the ReaxFF Ru/C/H/O parameters initially developed do not accurately reproduce the CO_2 hydrogenation chemistry. Therefore, we train Ru/C/H/O ReaxFF force-field parameters to reproduce the binding energy data of key reaction intermediated. We report the trained force-field parameters and test the force-field to simulate Ru-water interface and CO activation on Ru nanoparticles of different sizes.

Declaration

This thesis is an original work of my research and contains no material which has been accepted for the award of any other degree or diploma at any university or equivalent institution and that, to the best of my knowledge and belief, this thesis contains no material previously published or written by another person, except where due reference is made in the text of the thesis.

Print Name: Swarit Dwivedi

Publications

During enrolment (included in thesis)

- Dwivedi, S., Mata, J., Mushrif, S. H., Chaffee, A. L., & Tanksale, A. (2020). Molecular Clustering in Formaldehyde–Methanol–Water Mixtures Revealed by High-Intensity, High-q Small-Angle Neutron Scattering. *The Journal of Physical Chemistry Letters*, *12*, 480-486.
- Dwivedi, S., Kowalik, M., Rosenbach, N., Alqarni, D. S., Shin, Y. K., Yang, Y., ... & van Duin, A. C. (2020). Atomistic Mechanisms of Thermal Transformation in a Zr-Metal Organic Framework, MIL-140C. *The Journal of Physical Chemistry Letters*, *12*, 177-184.
- Dwivedi, S., Mushrif, S. H., Chaffee, A. L., & Tanksale, A. (2020). Solvation behaviour and micro-phase structure of formaldehyde-methanol-water mixtures. *Journal of Molecular Liquids*, *301*, 112444.

In Preparation (included in thesis)

- Dwivedi, S., Kowalik, M., Pakkiam, V., Mullins, J., Sarmiento, S., van Duin, A. C., Tanksale, A., Chaffee, A. L. (2021). Understanding the effect of framework topology, linker chemistry, and chemical environment on the thermally decomposed MOFs. *In preparation*

- Dwivedi, S., Mohan, O., Kowalik, M., Chaffee, A. L., Mushrif, S. H., van Duin, A. C., Tanksale, A. (2021). Development of a ReaxFF reactive force field for CO_2 hydrogenation on ruthenium, *In preparation*

Other collaborative works (not included in thesis)

- Gupta, P., Dwivedi, S., van Duin, A.C., Seethamraju, S. and Tanksale, A., Coke resistant catalyst for hydrogen production in a versatile, multi-fuel, reformer. *Under review*
- Amini, N., Dwivedi, S., Haritos, V S., Tanksale, A., Polar solvents enhance the efficiency of microwave pre-treatment of woody biomass, *In preparation*

Thesis including published works declaration

I hereby declare that this thesis contains no material which has been accepted for the award of any other degree or diploma at any university or equivalent institution and that, to the best of my knowledge and belief, this thesis contains no material previously published or written by another person, except where due reference is made in the text of the thesis.

This thesis includes three original papers published in peer reviewed journals and two manuscripts in preparation. The core theme of the thesis is understanding the physiochemistry of liquid phase and MOF-derived nanomaterials in context of CO/CO_2 hydrogenation. The ideas, development and writing up of all the papers in the thesis were the principal responsibility of myself, the student, working within the department of chemical engineering under the supervision of Associate Professor Akshat Tanksale, Professor Alan L. Chafee, and Associate Professor Samir H. Mushrif (University of Alberta).

The inclusion of co-authors reflects the fact that the work came from active collaboration between researchers and acknowledges input into team-based research.

In the case of chapter 3, my contribution to the work involved the following:

Thesis Chapter	Publication Title	Status	Nature and % of student contribution
3	Solvation behaviour and micro-phase structure of formaldehyde-methanol-water mixtures	Published	80%. Conception, designing experiments, collection and analysis of experimental data, and writing first draft

Co-author names	Nature of contribution	Monash student?
Samir H. Mushrif	7% discussion, suggestions, funding acquisition, Supervisor	No
Alan L. Chaffee	5% discussion, suggestions, funding acquisition, Supervisor	No
Akshat Tanksale	8% discussion, suggestions, funding acquisition, Supervisor	No

In the case of chapter 4, my contribution to the work involved the following:

Thesis Chapter	Publication Title	Status	Nature and % of student contribution
4	Molecular Clustering in Formaldehyde–Methanol–Water Mixtures Revealed by High-Intensity, High-q Small-Angle Neutron Scattering	Published	80%. Conception, designing experiments, collection and analysis of data, and writing first draft

Co-author names	Nature of contribution	Monash student?
Jitendra Mata	6% method development, discussion, suggestions, funding acquisition, Collaborator (Scientist at ANSTO)	No
Samir H. Mushrif	3% discussion, suggestions, funding acquisition, Supervisor	No
Alan L. Chaffee	3% discussion, suggestions, funding acquisition, Supervisor	No
Akshat Tanksale	8% experiments, data analysis, discussion, suggestions, funding acquisition, Supervisor	No

In the case of chapter 5, my contribution to the work involved the following:

Thesis Chapter	Publication Title	Status	Nature and % of student contribution
5	Atomistic Mechanisms of Thermal Transformation in a Zr-Metal Organic Framework, MIL-140C	Published	70%. Conception, designing experiments, collection and analysis of data, and writing first draft

Co-author names	Nature of contribution	Monash student?
Malgorzata Kowalik	5% discussion, suggestions, writing, Postdoc (Collaborator, Pennsylvania State University)	No
Nilton Rosenbach	4% method development, Assistant Professor	No
Dalal S. Alqarni	1% discussion, Ph.D. Student (School of Chemistry)	Yes
Yun Kyung Shin	2% method development, Postdoc (Collaborator, Pennsylvania State University)	No

Yongjian Yang	2% discussion, Postdoc (Collaborator, Pennsylvania State University)	No
John C Mauro	3% suggestions, Professor (Collaborator, Pennsylvania State University)	No
Akshat Tanksale	3% suggestions, Supervisor	No
Alan L Chaffee	5% suggestions, Supervisor	No
Adri CT van Duin	5% suggestions, Professor (Collaborator, Pennsylvania State University)	No

I have renumbered sections of submitted or published papers in order to generate a consistent presentation within the thesis.

Student name: Swarit Dwivedi **Date**: 19/05/2021

I hereby certify that the above declaration correctly reflects the nature and extent of the student's and co-authors' contributions to this work. In instances where I am not the responsible author, I have consulted with the responsible author to agree on the respective contributions of the authors.

Main Supervisor name: Akshat Tanksale **Date:** 19/05/2021

Acknowledgements

My sincerest thanks to my supervisors, Associate Professor Akshat Tanksale (Supervisor), Professor Alan L. Chaffe (co-supervisor), Associate Professor Samir H. Mushrif (co-supervisor), for their continuous academic and moral support. I feel fortunate that they selected me to be their student. Their constant guidance and support has shaped my research ethics, critical thinking, and rational approach (if any). I humbly the Australian Research Council for providing financial support for this research project (DP170104017). I thank the Faculty of Engineering and the Department of Chemical Engineering, Monash University, for supporting this research project. My special thanks to Lilyanne Price, Tracy Groves, Dr. Kim Phu and Professor Mark Benezak Hall. I am extremely thankful to my candidature panel chairs and examiners, especially Professor Nikhil Medhekar, to provide helpful suggestions and advice during the milestone seminars.

I would like to sincerely thank the Monash e-Research platform team and the NCI-Gadi team for providing computational resources throughout my candidature. I especially thank Philip Chan from the Monash e-Research platform for help and technical support while using the supercomputing facilities. I thank Australian Synchrotron and Australian Nuclear Science and Technological Organisation for providing the beamline grant. I thank my collaborator, Dr. Jitendra Mata, for the guidance and support during the Neutron Scattering work.

During my Ph.D., I was fortunate to visit Nanyang Technological University and Pennsylvania State University for collaborative research. I extend my sincere thanks to Professor Adri van Duin and Professor John C. Mauro from Pennsylvania State University for hosting me and collaborating in this research work. I thank Assistant Professor Jithin John Varghese, Dr. Ojus Mohan, Dr. Yun K. Shin, Dr. Yongjian Yang, and Dr. Vallabh Vasudevan for valuable discussions on molecular simulations. I thank the PennState-Monash collaboration for funding my research visit.

I want to thank Dr. Vikram Singh Raghuwanshi (Monash University) and Dr. Malgorzata Kowalik (Pennsylvania State University) for the constant support, help, and guidance. The Ph.D. journey would have much difficult without their guidance.

The support from my family was vital during the most formidable challenges I faced. I thank my father, Anil Dwivedi, my mother, Poonam Dwivedi, my brother Divyansh Dwivedi, and my girlfriend Sireesha for all their love and support throughout my Ph.D. journey.

Table of Contents

Chapter - 1

1 Introduction

1.1 Background

In the last 200 years, the amount of CO_2 released into the atmosphere has disturbed the natural carbon cycle, and a dramatic rise in atmospheric CO_2 concentrations is evident[1]. This increase in CO_2 concentration is causing a shift in the average global temperature, resulting in uncontrollable chains of reactions, catastrophic to the environmental eco-system. The sustainable and renewable energy alternatives (solar, wind, hydro, nuclear, etc.) still require technological advancements for their conversion efficiency. Moreover, an effective energy storage strategy is to be developed to cater to the global energy demands. The transition from conventional energy sources to renewable alternatives is likely to be gradual, spanning over decades[2]. Besides, replacing or discontinuing the industrial processes producing CO_2 is not practical. An alternative approach to combat alarmingly high CO_2 concentrations must be explored.

The Carbon Capture, Utilization, and Storage (CCUS) technologies present a viable option to achieve net zero-emission and utilize the excess CO_2 from the atmosphere[3]. The CCUS technologies aim to capture CO_2 at the onset of its emission and from the atmosphere to store it to convert it into value-added chemicals. Although there are significant challenges in all the three dimensions of CCUS technologies, the developing technologies show potential for converting CO_2 from a waste to a by-product within industrial space. Multiple industrial-scale plants have already demonstrated the viability of CCUS technologies with the capacity of utilising ~ 1 gigatons CO_2 per year[4].

Carbon dioxide (CO_2) and Carbon monoxide (CO) are highly stable molecules and require a catalytic reaction system for an energy-efficient conversion to value-added chemicals. Over the years, researchers have explored a wide variety of catalytic systems to facilitate this[5]. We focus on catalytic reaction systems that lead to the hydrogenation of CO and CO_2 into various building blocks of C1 chemistry, such as methane, methanol, formaldehyde, and formic acid.

These C1 building blocks could be further utilised a raw material for producing a vast majority of organic chemicals of industrial importance.

For CO or CO_2 hydrogenation to various C1 platform chemicals, transition metals are widely used and explored for their suitable catalytic properties. The relative binding energy of the reactants and products are relatively similar and are of intermediate strength. Moreover, the abundance of fermi band electrons in d-block elements inherently allows multiple oxidation states, making them a good catalyst. Iron, Ruthenium, Nickel, Copper, Rhodium, and Palladium have been reported for hydrogenation of CO_2 into C1 building blocks[6]. Ruthenium (Ru) is widely studied for CO_2 reforming and Fischer-Tropsch (producing Olefins > C2) synthesis by CO_2 hydrogenation[7,8]. In Liquid media, Ru has also been reported to produce formaldehyde[9,10]. However, the molecular understanding of the reaction environment, temperature, pressure, and catalyst phase needs to be explored in greater detail to better design the reaction system to lower down conversion cost.

1.2 Research Scope and Objectives

To achieve energy-efficient CO_2 utilisation, the thermodynamics and kinetics of the catalytic reaction system need to optimise. In the last decade, liquid-phase catalytic reaction schemes and advanced catalytic materials have reported significant advances in kinetics and the thermodynamics of heterogeneous catalytic reaction systems. Compared to the traditional catalysts, the advanced catalytic materials have features like large surface area, tuneable pore size with desired product selectivity, tuneable acidity, and a variety of binding sites for the activation of CO/CO_2[11–13].

On the other hand, the reaction environment (e.g., liquid media) has been reported for the catalytic reaction system in many different ways affecting the thermodynamics and the kinetics[10,14–16]. For instance, it may give acidic sites on the surface[16–18], mediate a proton transfer[19–21], stabilise the reaction intermediates and transition states[22,23], and stabilise reactant and product differently in the bulk phase changing their adsorption capacity[10,24,25].

In recent years, our group has developed novel methods for producing formaldehyde and methane from CO and CO_2 using Ru-based catalysts[9,10,14,26]. These methods report faster kinetics and better yield, thus, show potential for industrial-scale productions. This thesis aims to use computational chemistry tools to understand so far not well-understood effects of liquid

phase dynamics, the morphology of MOF-derived catalysts and formulate a hypothesis to explain the observed yield and kinetics and guide future experiments.
We have hereby further elaborated our goals for both liquid phase and MOF-derived catalysts in the subsequent subsections.

1.2.1 Liquid Phase Heterogeneous Catalysis

A solvent's role in a heterogeneous chemical reaction system is subjective and depends on reactants, products, reaction pathways, and catalysts. Mixtures of water and a polar co-solvent are widely popular for saving operational cost, energy, tuning selectivity, and yield. Due to the recent international green chemical laws, tuning solvents is a key component of designing a heterogenous catalytic reaction system[27,28]. Understanding the liquid phase and the solvation dynamics of the multi-component mixtures is a widely investigated chemical physics domain. However, the effect of liquid media on a catalytic reaction is principally studied for their impact on either stabilizing reaction intermediates/transition state or their role as a co-catalyst[29]. In recent years our group reported a novel process for the production of formaldehyde directly from syn-gas[9,10]. The catalyst used was Ni-Ru supported on Alumina while various solvents (such as water, methanol, DMSO, ethanol, etc.) were used. Among these solvents, methanol resulted in the best yield. The *ab inito* MD simulations confirmed that in methanol, methoxymethanol (solvated formaldehyde) is stabilized by a ring/chain structure of methanol[10]. Therefore, the stability of the product in the solvent phase is high, and desorption is likely to be a favourable process.
In the gas phase, Ni and Ru are known for converting syn gas to methane and methanol[30–32]. However, in the liquid phase (polar) presence, the reaction pathway to formaldehyde production becomes more feasible than the methane production one. As a wide range of polar solvents show formaldehyde pathway to be best suited, polar solvents likely stabilize the polar reaction intermediates but not the non-polar CH and CH_2 which are required for methane formation. As formaldehyde's high yield, possibly due to its stabilization in methanol, further prompted us to study a mixture of methanol-water mixtures motivated by using green solvents and simplify the reaction design. Interestingly, the results of methanol-water mixtures showed an unexpected behaviour[10]. A good understanding of the micro-phase structure of formaldehyde-methanol-water mixtures was necessary to understand the formaldehyde's yield in varying methanol-water composition. We aim to,

a) study the micro-phase structure of formaldehyde-methanol-water mixtures and formulate a hypothesis for the non-linear yield of formaldehyde on varying methanol-water mixture composition.
b) investigate the micro-phase structures experimentally. Low molecular weight liquid-phase structures are difficult to achieve experimentally and have remained a challenge to contemporary experimental techniques.

1.2.2 MOF-derived advanced catalytic materials

Recently, the thermally decomposed Zr-MOFs (MIL-140C and UiO-67) with Ru were reported for high yield and faster kinetics for CO_2 hydrogenation to methane[26,33,34]. However, the morphology and control parameters for further optimizing the structure of the decomposed MOF remain unclear. The available *ab-initio* based methods become impractical when dealing with large system size (> few hundred atoms) and timescales (> few ps), which is required for acceptable framework collapse mechanism and experimentally comparable cluster size. On the other hand, classical molecular dynamics are incapable of simulating the chemical changes during thermal decomposition. Therefore, we first aim to develop a reactive Zr/C/H/O forcefield to simulate the Zr-MOF chemistry and then understand the control parameters for tunning the thermally decomposed MOF. We aim to,

a) train ReaxFF forcefield parameters to simulate Zr/C/H/O chemistry for Zr-MOFs
b) understand the effect of cluster topology, linker chemistry, temperature, and the chemical environment on the mechanism of framework collapse and the morphology and the chemical structure of the decomposed MOF.

1.2.3 Reactive molecular dynamics forcefield for Ru/C/H/O chemistry

The computational cost increases with the increase in system size, which makes the Quantum Mechanics (QM) based methods impractical and inefficient for simulating the combined effect of multiple controlling factors (catalyst phase, liquid media, thermodynamic state, etc.). However, classical molecular dynamics (MD) simulation is incapable of simulating reactions. Therefore, we aim to develop a reactive molecular dynamics forcefield, ReaxFF[35], which is capable of simulating reactions in a large system size (in the order of 10,000 atoms) with practical computational cost (with 1 computing core, 1 ns of molecular dynamics of ~1,000 atoms with 0.25 fs timestep can be simulated in ~ 1 day).

ReaxFF is a bond order based reactive MD forcefield which is trained on the QM data. A ReaxFF forcefield was recently reported to simulation Ru/N/H chemistry and reported the

effect of the particle size on the activity and selectivity of reaction pathway of ammonia synthesis[36]. To the best of our understanding, no ReaxFF forcefield has been trained for CO/CO_2 hydrogenation on Ruthenium surface. Therefore, our aim is to train a reactive forcefield the reproduces the binding energy (reported by density functional theory (DFT) simulations[37,38]) of key reaction intermediates of CO_2 hydrogenation.

1.3 Thesis outline and structure

In addition to the introduction, this thesis includes following chapters,

Chapter – 2 Literature Review

This chapter provides a brief overview of Heterogeneous catalysis for conversion of CO/CO_2 into value-added chemicals. After this we present a thorough background of the effect of a liquid phase play in heterogeneous catalytic reactions. Based on the previous studies, we presented our argument for investigating the solvation dynamics of formaldehyde-methanol-water for liquid phase catalytic reaction with Ru-catalyst and formaldehyde as the main reaction product. After the liquid media, we thoroughly discuss MOF-derived catalytic materials for their morphology and application in heterogeneous analysis. Our discussion is focused but not limited to the activity, surface area, thermal stability, and future of MOF-derived materials as an ideal catalyst.

Chapter – 3 Solvation behaviour and the Micro-Phase structure of Formaldehyde-methanol-water mixtures

In this chapter, we investigate the dynamics of formaldehyde-methanol-water mixtures. We presented a set of OPLS-AA forcefield parameters for molecular dynamic simulation of methoxymethanol (a metastable form of formaldehyde in methanol) and methanediol (a metastable form of formaldehyde in water). We investigate the solvation structure of methoxymethanol and methanediol in varying methanol-water concentrations. The solvation structure of these mixtures was presented for the first time in our study which was published in *The Journal of Molecular Liquids (Elsevier)* in 2020[39].

Chapter – 4 Molecular cluster in formaldehyde-methanol-water mixtures revealed by High-intensity, High-q Small-Angle Neutron Scattering

In chapter 3, our molecular dynamic simulations suggested the presence of hydrophobically clustered methoxymethanol and methanol molecules at low methanol concentrations ($x_m \leq 0.3$). In this chapter, we investigate formaldehyde-methanol-water mixtures by Small-Angle

Neutron Scattering measurement. We formulated a rigorous background subtraction methodology which was guided by our molecular dynamics understanding of these mixtures. Our results confirm the presence of hydrophobic clusters of methanol and methoxymethanol in low methanol ($x_m \leq 0.3$), low formaldehyde ($x_{Fa} \leq 0.02$), formaldehyde-methanol-water mixtures. Our study is the first demonstration of using SANS as a measurement technique to understand these small organic hydrophobic ternary mixtures. The results of this chapter were published in *The Journal of Physical Chemistry Letters (American Chemical Society)* in 2021[40].

Chapter – 5 Atomistic Mechanism of thermal transformation in a Zr-Metal Organic Framework, MIL-140C

In this chapter, we investigate the thermal decomposition of MIL-140C (a Zr-based MOF) to understand the mechanism of the framework collapse and the morphology of the decomposed structure. Simulating thermal decomposition where reactions are involved, experimental time-scale is in order of minutes to hours, and the number of atoms in a simulation box is in the order of 10,000 is extremely difficult, and the most suitable method is reactive MD forcefield. Therefore, we present a ReaxFF forcefield, trained to simulate Zr/C/H/O chemistry in Zr-MOFs. We presented the mechanism of thermal decomposition, chemical pathways for linker decomposition, and the morphology of ZrO_x clusters in the thermally degraded MOF. The results of this chapter were published in *The Journal of Physical Chemistry Letters (American Chemical Society)* in 2021[41].

Chapter – 6 Understanding the effect of framework topology, linker chemistry, and chemical environment on the thermally decomposed MOFs

In this chapter, we investigate the effect of MOF's metal cluster topology and linker on the morphology of the decomposed MOF. We study the MIL series and the UiO series for elucidating the effect of the topology, whereas within UiO series, we simulated the thermal decomposition of UiO-66 and UiO-67 to understand the effect of the linker. We also decomposed a modified MIL-140C where some/all of the linkers were replaced by bi-pyridine di-carboxylates to understand the effect of functional linkers. We finally simulated MIL-140C under H_2 and CO_2 environments to find out the impact of the chemical environment on the decomposed MOF.

Chapter – 7 Development of ReaxFF forcefield parameters to simulate Ru/C/H/O chemistry for CO_2 hydrogenation on Ru hcp(001) surface

In this chapter, we train the previously reported Ru/C/H/O ReaxFF forcefield parameters[42] to reproduce the DFT binding energy data for CO_2 hydrogenation on Ru hcp 001 surface. The trained forcefield reproduces the DFT binding energies of the reaction intermediates and their minimum energy configuration and it reproduces the dynamics of the adsorbed water layer as reported by previous *ab initio* MD study[43]. We also test the force-field to reproduce previously studied Ru-water interface and C-O activation on Ru nanoparticles. The forcefield reported in this chapter can be used for simulating CO_2 hydrogenation with further training if needed.

Chapter – 8 Conclusions and future Recommendations

We present our key findings of the liquid phase solvation, MOF-derived nanomaterials, and trained Ru/C/H/O force-field parameters in context of CO_2 hydrogenation. We also provide recommendations for computations and experiments to further investigate the effect of liquid phase and MOF-derived materials in context of heterogeneous CO_2 hydrogenation.

1.4 References:

(1) Core Writing Team eds. Contribution of Working Groups I, II and III to the Fourth Assessment Report of the Intergovernmental Panel on Climate Change. *IPCC 2007 Clim. Change 2007 Synth. Rep.* **2007**, *104*.

(2) *Transition to Renewable Energy Systems: STOLTEN:ENERGY PROCESS O-BK*; Stolten, D., Scherer, V., Eds.; Wiley-VCH Verlag GmbH & Co. KGaA: Weinheim, Germany, 2013. https://doi.org/10.1002/9783527673872.

(3) Singh, U.; Colosi, L. M. The Case for Estimating Carbon Return on Investment (CROI) for CCUS Platforms. *Appl. Energy* **2021**, *285*, 116394. https://doi.org/10.1016/j.apenergy.2020.116394.

(4) Majumdar, A.; Deutch, J. Research Opportunities for CO_2 Utilization and Negative Emissions at the Gigatonne Scale. *Joule* **2018**, *2* (5), 805–809. https://doi.org/10.1016/j.joule.2018.04.018.

(5) Norhasyima, R. S.; Mahlia, T. M. I. Advances in CO_2 Utilization Technology: A Patent Landscape Review. *J. CO_2 Util.* **2018**, *26*, 323–335. https://doi.org/10.1016/j.jcou.2018.05.022.

(6) Zhou, W.; Cheng, K.; Kang, J.; Zhou, C.; Subramanian, V.; Zhang, Q.; Wang, Y. New Horizon in C1 Chemistry: Breaking the Selectivity Limitation in Transformation of Syngas

and Hydrogenation of CO_2 into Hydrocarbon Chemicals and Fuels. *Chem. Soc. Rev.* **2019**, *48* (12), 3193–3228. https://doi.org/10.1039/C8CS00502H.

(7) Li, W.-Z.; Liu, J.-X.; Gu, J.; Zhou, W.; Yao, S.-Y.; Si, R.; Guo, Y.; Su, H.-Y.; Yan, C.-H.; Li, W.-X.; Zhang, Y.-W.; Ma, D. Chemical Insights into the Design and Development of Face-Centered Cubic Ruthenium Catalysts for Fischer–Tropsch Synthesis. *J. Am. Chem. Soc.* **2017**, *139* (6), 2267–2276. https://doi.org/10.1021/jacs.6b10375.

(8) Gual, A.; Godard, C.; Castillón, S.; Curulla-Ferré, D.; Claver, C. Colloidal Ru, Co and Fe-Nanoparticles. Synthesis and Application as Nanocatalysts in the Fischer–Tropsch Process. *Catal. Today* **2012**, *183* (1), 154–171. https://doi.org/10.1016/j.cattod.2011.11.025.

(9) Bahmanpour, A. M.; Hoadley, A.; Tanksale, A. Formaldehyde Production via Hydrogenation of Carbon Monoxide in the Aqueous Phase. *Green Chem.* **2015**, *17* (6), 3500–3507. https://doi.org/10.1039/C5GC00599J.

(10) Bahmanpour, A. M.; Hoadley, A.; Mushrif, S. H.; Tanksale, A. Hydrogenation of Carbon Monoxide into Formaldehyde in Liquid Media. *ACS Sustain. Chem. Eng.* **2016**, *4* (7), 3970–3977. https://doi.org/10.1021/acssuschemeng.6b00837.

(11) Chaffee, A. CO_2 Conversion to Hydrocarbons with MOF-Derived Materials as Catalysts. In *ABSTRACTS OF PAPERS OF THE AMERICAN CHEMICAL SOCIETY*; AMER CHEMICAL SOC 1155 16TH ST, NW, WASHINGTON, DC 20036 USA, 2019; Vol. 257.

(12) i Xamena, F. X. L.; Abad, A.; Corma, A.; Garcia, H. MOFs as Catalysts: Activity, Reusability and Shape-Selectivity of a Pd-Containing MOF. *J. Catal.* **2007**, *250* (2), 294–298.

(13) Jahangiri, H.; Bennett, J.; Mahjoubi, P.; Wilson, K.; Gu, S. A Review of Advanced Catalyst Development for Fischer–Tropsch Synthesis of Hydrocarbons from Biomass Derived Syn-Gas. *Catal Sci Technol* **2014**, *4* (8), 2210–2229. https://doi.org/10.1039/C4CY00327F.

(14) Chan, F. L.; Altinkaya, G.; Fung, N.; Tanksale, A. Low Temperature Hydrogenation of Carbon Dioxide into Formaldehyde in Liquid Media. *Catal. Today* **2018**, *309*, 242–247. https://doi.org/10.1016/j.cattod.2017.06.012.

(15) van Santen, R. A.; Neurock, M. *Molecular Heterogeneous Catalysis*; Wiley-VCH Verlag GmbH & Co. KGaA: Weinheim, Germany, 2006. https://doi.org/10.1002/9783527610846.

(16) Adams, J. S.; Chemburkar, A.; Priyadarshini, P.; Ricciardulli, T.; Lu, Y.; Maliekkal, V.; Sampath, A.; Winikoff, S.; Karim, A. M.; Neurock, M.; Flaherty, D. W. Solvent Molecules Form Surface Redox Mediators in Situ and Cocatalyze O_2 Reduction on Pd. *Science* **2021**, *371* (6529), 626–632. https://doi.org/10.1126/science.abc1339.

(17) Mellmer, M. A.; Sanpitakseree, C.; Demir, B.; Bai, P.; Ma, K.; Neurock, M.; Dumesic, J. A. Solvent-Enabled Control of Reactivity for Liquid-Phase Reactions of Biomass-Derived Compounds. *Nat. Catal.* **2018**, *1* (3), 199–207. https://doi.org/10.1038/s41929-018-0027-3.
(18) Choudhary, V.; Mushrif, S. H.; Ho, C.; Anderko, A.; Nikolakis, V.; Marinkovic, N. S.; Frenkel, A. I.; Sandler, S. I.; Vlachos, D. G. Insights into the Interplay of Lewis and Brønsted Acid Catalysts in Glucose and Fructose Conversion to 5-(Hydroxymethyl)Furfural and Levulinic Acid in Aqueous Media. *J. Am. Chem. Soc.* **2013**, *135* (10), 3997–4006. https://doi.org/10.1021/ja3122763.
(19) Li, G.; Wang, B.; Resasco, D. E. Water-Mediated Heterogeneously Catalyzed Reactions. *ACS Catal.* **2020**, *10* (2), 1294–1309. https://doi.org/10.1021/acscatal.9b04637.
(20) Farnesi Camellone, M.; Negreiros Ribeiro, F.; Szabová, L.; Tateyama, Y.; Fabris, S. Catalytic Proton Dynamics at the Water/Solid Interface of Ceria-Supported Pt Clusters. *J. Am. Chem. Soc.* **2016**, *138* (36), 11560–11567. https://doi.org/10.1021/jacs.6b03446.
(21) Wang, H.-F.; Liu, Z.-P. Formic Acid Oxidation at Pt/H $_2$ O Interface from Periodic DFT Calculations Integrated with a Continuum Solvation Model. *J. Phys. Chem. C* **2009**, *113* (40), 17502–17508. https://doi.org/10.1021/jp9059888.
(22) Wan, H.; Vitter, A.; Chaudhari, R. V.; Subramaniam, B. Kinetic Investigations of Unusual Solvent Effects during Ru/C Catalyzed Hydrogenation of Model Oxygenates. *J. Catal.* **2014**, *309*, 174–184. https://doi.org/10.1016/j.jcat.2013.09.020.
(23) Michel, C.; Auneau, F.; Delbecq, F.; Sautet, P. C–H versus O–H Bond Dissociation for Alcohols on a Rh(111) Surface: A Strong Assistance from Hydrogen Bonded Neighbors. *ACS Catal.* **2011**, *1* (10), 1430–1440. https://doi.org/10.1021/cs200370g.
(24) Mellmer, M. A.; Sener, C.; Gallo, J. M. R.; Luterbacher, J. S.; Alonso, D. M.; Dumesic, J. A. Solvent Effects in Acid-Catalyzed Biomass Conversion Reactions. *Angew. Chem. Int. Ed.* **2014**, *53* (44), 11872–11875. https://doi.org/10.1002/anie.201408359.
(25) Bertero, N. M.; Trasarti, A. F.; Apesteguía, C. R.; Marchi, A. J. Solvent Effect in the Liquid-Phase Hydrogenation of Acetophenone over Ni/SiO2: A Comprehensive Study of the Phenomenon. *Appl. Catal. Gen.* **2011**, *394* (1–2), 228–238. https://doi.org/10.1016/j.apcata.2011.01.003.
(26) Alqarni, D. S.; Lee, C. W.; Knowles, G. P.; Vogt, C.; Marshall, M.; Gengenbach, T. R.; Chaffee, A. L. Ru-Zirconia Catalyst Derived from MIL140C for Carbon Dioxide Conversion to Methane. *Catal. Today* **2020**, S0920586120305563. https://doi.org/10.1016/j.cattod.2020.07.080.

(27) Capello, C.; Fischer, U.; Hungerbühler, K. What Is a Green Solvent? A Comprehensive Framework for the Environmental Assessment of Solvents. *Green Chem.* **2007**, *9* (9), 927. https://doi.org/10.1039/b617536h.

(28) Jessop, P. G. Searching for Green Solvents. *Green Chem.* **2011**, *13* (6), 1391. https://doi.org/10.1039/c0gc00797h.

(29) Varghese, J. J.; Mushrif, S. H. Origins of Complex Solvent Effects on Chemical Reactivity and Computational Tools to Investigate Them: A Review. *React. Chem. Eng.* **2019**, *4* (2), 165–206. https://doi.org/10.1039/C8RE00226F.

(30) Venvik, H. J.; Yang, J. Catalysis in Microstructured Reactors: Short Review on Small-Scale Syngas Production and Further Conversion into Methanol, DME and Fischer-Tropsch Products. *Catal. Today* **2017**, *285*, 135–146. https://doi.org/10.1016/j.cattod.2017.02.014.

(31) Mutschler, R.; Moioli, E.; Züttel, A. Modelling the CO_2 Hydrogenation Reaction over Co, Ni and Ru/Al_2O_3. *J. Catal.* **2019**, *375*, 193–201. https://doi.org/10.1016/j.jcat.2019.05.023.

(32) Wang, W.-H.; Himeda, Y.; Muckerman, J. T.; Manbeck, G. F.; Fujita, E. CO_2 Hydrogenation to Formate and Methanol as an Alternative to Photo- and Electrochemical CO_2 Reduction. *Chem. Rev.* **2015**, *115* (23), 12936–12973. https://doi.org/10.1021/acs.chemrev.5b00197.

(33) Lippi, R.; D'Angelo, A. M.; Li, C.; Howard, S. C.; Madsen, I. C.; Wilson, K.; Lee, A. F.; Sumby, C. J.; Doonan, C. J.; Patel, J.; Kennedy, D. F. Unveiling the Structural Transitions during Activation of a CO_2 Methanation Catalyst Ru0/ZrO_2 Synthesised from a MOF Precursor. *Catal. Today* **2021**, *368*, 66–77. https://doi.org/10.1016/j.cattod.2020.04.043.

(34) Lippi, R.; Howard, S. C.; Barron, H.; Easton, C. D.; Madsen, I. C.; Waddington, L. J.; Vogt, C.; Hill, M. R.; Sumby, C. J.; Doonan, C. J.; Kennedy, D. F. Highly Active Catalyst for CO_2 Methanation Derived from a Metal Organic Framework Template. *J. Mater. Chem. A* **2017**, *5* (25), 12990–12997. https://doi.org/10.1039/C7TA00958E.

(35) Senftle, T. P.; Hong, S.; Islam, M. M.; Kylasa, S. B.; Zheng, Y.; Shin, Y. K.; Junkermeier, C.; Engel-Herbert, R.; Janik, M. J.; Aktulga, H. M.; Verstraelen, T.; Grama, A.; van Duin, A. C. T. The ReaxFF Reactive Force-Field: Development, Applications and Future Directions. *Npj Comput. Mater.* **2016**, *2* (1), 15011. https://doi.org/10.1038/npjcompumats.2015.11.

(36) Kim, S.-Y.; Lee, H. W.; Pai, S. J.; Han, S. S. Activity, Selectivity, and Durability of Ruthenium Nanoparticle Catalysts for Ammonia Synthesis by Reactive Molecular Dynamics Simulation: The Size Effect. *ACS Appl. Mater. Interfaces* **2018**, *10* (31), 26188–26194. https://doi.org/10.1021/acsami.8b05070.

(37) Mohan, O.; Shambhawi, S.; Xu, R.; Lapkin, A. A.; Mushrif, S. H. Investigating CO_2 Methanation on Ni and Ru: DFT Assisted Microkinetic Analysis. *ChemCatChem* **2021**, cctc.202100073. https://doi.org/10.1002/cctc.202100073.

(38) Mohan, O.; Trinh, Q. T.; Banerjee, A.; Mushrif, S. H. Predicting CO_2 Adsorption and Reactivity on Transition Metal Surfaces Using Popular Density Functional Theory Methods. *Mol. Simul.* **2019**, *45* (14–15), 1163–1172. https://doi.org/10.1080/08927022.2019.1632448.

(39) Dwivedi, S.; Mushrif, S. H.; Chaffee, A. L.; Tanksale, A. Solvation Behaviour and Micro-Phase Structure of Formaldehyde-Methanol-Water Mixtures. *J. Mol. Liq.* **2020**, *301*, 112444. https://doi.org/10.1016/j.molliq.2020.112444.

(40) Dwivedi, S.; Mata, J.; Mushrif, S. H.; Chaffee, A. L.; Tanksale, A. Molecular Clustering in Formaldehyde–Methanol–Water Mixtures Revealed by High-Intensity, High-q Small-Angle Neutron Scattering. *J. Phys. Chem. Lett.* **2021**, *12* (1), 480–486. https://doi.org/10.1021/acs.jpclett.0c03515.

(41) Dwivedi, S.; Kowalik, M.; Rosenbach, N.; Alqarni, D. S.; Shin, Y. K.; Yang, Y.; Mauro, J. C.; Tanksale, A.; Chaffee, A. L.; van Duin, A. C. T. Atomistic Mechanisms of Thermal Transformation in a Zr-Metal Organic Framework, MIL-140C. *J. Phys. Chem. Lett.* **2021**, *12* (1), 177–184. https://doi.org/10.1021/acs.jpclett.0c02930.

(42) van Duin, A. C. T.; Dasgupta, S.; Lorant, F.; Goddard, W. A. ReaxFF: A Reactive Force Field for Hydrocarbons. *J. Phys. Chem. A* **2001**, *105* (41), 9396–9409. https://doi.org/10.1021/jp004368u.

(43) Michaelides, A.; Alavi, A.; King, D. A. Different Surface Chemistries of Water on Ru{0001}: From Monomer Adsorption to Partially Dissociated Bilayers. *J. Am. Chem. Soc.* **2003**, *125* (9), 2746–2755. https://doi.org/10.1021/ja028855u.

Chapter - 2

2 Literature Review

2.1 Heterogenous catalytic hydrogenation of CO_2

A heterogeneous catalytic reaction system can generally be described in terms of different components in the reaction scheme. The schematic in Fig. 2.1 shows these components, namely, the reactants, products, reaction environment, and the catalyst phase. The traditional heterogeneous catalyst generally consists of a metal supported on a porous solid. However, numerous examples of advanced catalytic materials have a different physical and chemical characteristic to a traditional catalyst[1–3]. The metal oxide support in a traditional catalyst is mostly used to provide a fine dispersion of metal nanoparticles for better kinetics. To enhance the activity of the catalyst, a promoter may be used in the reaction system. A combination of catalyst material, support, and promoter can greatly affect the reaction pathway keeping the reactant and reaction environment fixed[4].

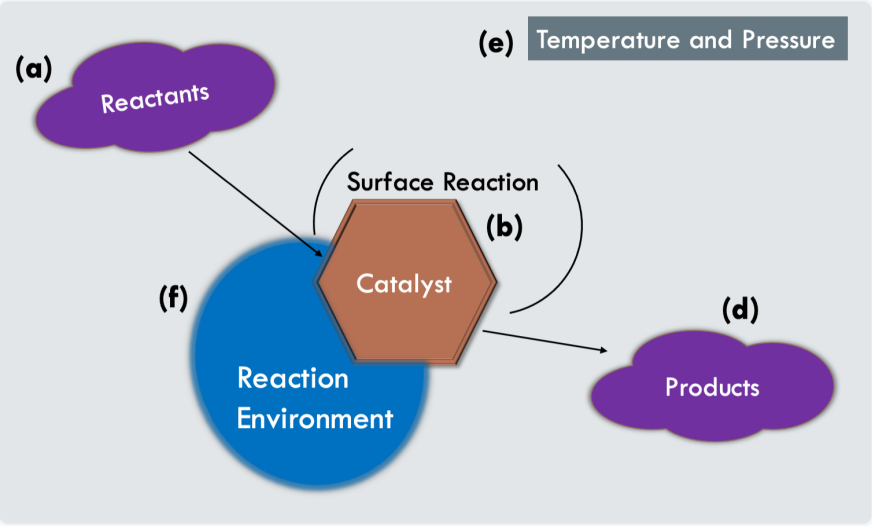

Figure 2.1: Schematic shows the heterogeneous catalytic system and the control parameters.

Figure 2.2 shows the CO_2 hydrogenation to a few key value-added products, along with the catalysts suitable for the conversion. One metal can lead to different products depending upon

reaction conditions. Ru as a catalyst is shown for hydrogenating CO_2 into CH_4 in a gas phase reaction under moderately low temperatures (250 – 500 K) and moderately high pressures (1 bar – 30 bar)[5]. However, Ru has also been reported for CO_2 conversion into CH_2O in the presence of a liquid media[6,7]. Moreover, a series of Olefins (Fischer-Tropsch synthesis) were reported at a high $CO:H_2$ stoichiometric ratio at high temperatures and pressures[8,9]. The influencing factors such as the liquid media[6], relative concentration of reactants[10], size, and shape of the catalyst[11,12], support[5], promotor, etc., affect the reaction pathway, stability of the reaction intermediates, and the activation barrier. Therefore, a good understanding of these parameters at a molecular length scale is required for developing a catalytic reaction system with high yield and fast kinetics. In the subsequent subsections, we present a brief overview of heterogeneous catalytic reactions for CO_2 hydrogenation to methane, methanol, formaldehyde, and formic acid.

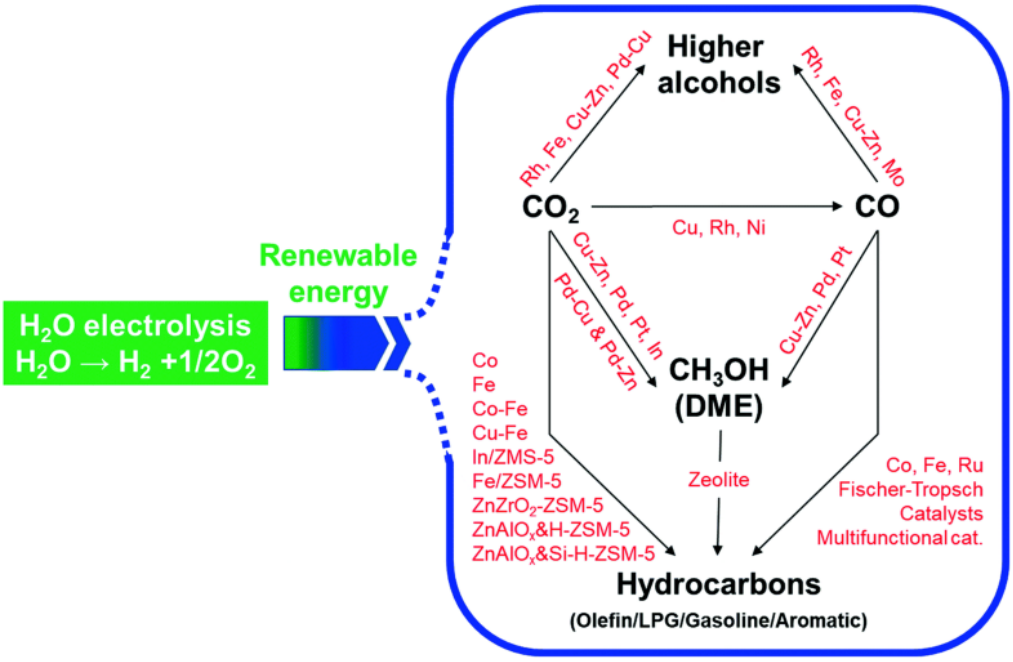

Figure 2.2: CO_2 hydrogenation to key value-added chemicals with the active catalysts reported in literature for the conversion. Re-printed with permission[13].

2.1.1 Conversion to Methane

CO_2 hydrogenation into methane in gas-phase (Sabatier Reaction) is exothermic. Therefore, lower temperatures favour the forward reaction, and a 100% conversion is feasible at low temperatures. If a cheap renewable source of hydrogen is available, the kinetics of this conversion limits the feasibility of the process for production at industrial scales.

$$CO_{2_{(g)}} + 4H_{2_{(g)}} \rightarrow CH_{4_{(g)}} + 2H_2O_{(g)} \ (\Delta H = -165kJ\ mol^{-1}) \qquad \text{(Eq. 1)}$$

To achieve faster kinetics, adjusting the reaction temperatures and pressures are higher temperatures and pressures may be explored with a trade-off of energy cost. Figure 2.3(a) shows the percentage conversion of CO_2 hydrogenation to methane with a temperature range of 0 ºC to 1000 ºC under two different pressures of 1 bar and 30 bar[14]. The equilibrium conversion to methane is high and above 95% till ~ 250 ºC for 1 bar and ~ 400 ºC for 30 bars. However, for 1 bar, the percentage conversion of CO_2 and H_2 drops, and the selectivity shift from CH_4 towards the formation of CO. On increasing pressure to 30 bars, the conversion and selectivity are retained till ~ 400 ºC as methane formation reduces the number of overall gaseous molecules. Still, after 400 ºC, the effect of temperature dominates. The formation of CO from CO_2 may be a consequence of Reverse Water Gas Shift (RWGS), CO_2 reforming with methane, and the reverse Boudouard reaction, all of which are endothermic in nature and their selectivity increases with temperature. Therefore, increasing temperatures and pressures only help up to a specific range and for enhancing the kinetics of CO_2 hydrogenation further, advanced catalytic engineering is needed.

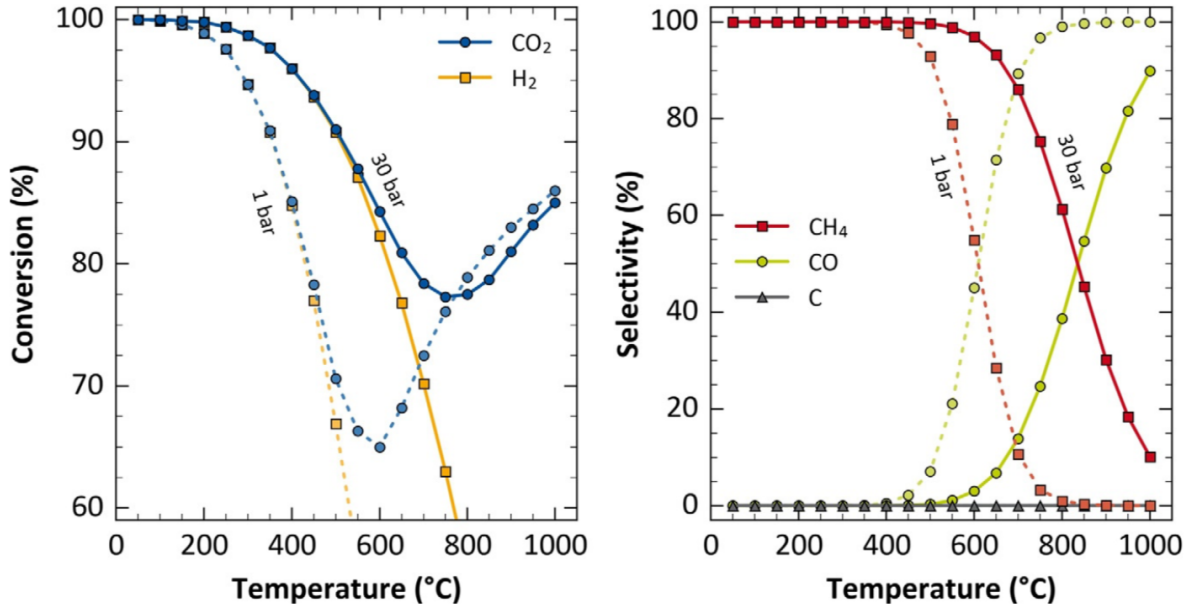

Figure 2.3: (a) Shows CO_2 and H_2 conversion at equilibrium based on the gas-phase free energy. (b) Shows the selectivity between CH_4, CO, and C as per the equilibrium calculated from the theoretical free energy. The figure is reprinted with permission from recently published review[14] where the thermodynamic data was obtained from NASA database[15].

The reaction mechanism of CO_2 methanation has been widely studied over different transition metals also with different levels of theory (computationally). Figure 2.4 shows a recent study that presents the novel results and compares the previously reported DFT energies[16]. The most probable pathway for CO_2 methanation was determined. For Ni, the fcc 111 surface was found active for CO_2 methanation, whereas, for Ru, the hcp 001 surface was determined as the active phase. On Ru and Ni both, CO_2* goes through dissociation. The CO* hydrogenation to form HCO* whereas, on Ru, COH* intermediate is preferred before the fission of C-O bond. After the C-O bond activation, C is successively hydrogenated to form CH_4*.

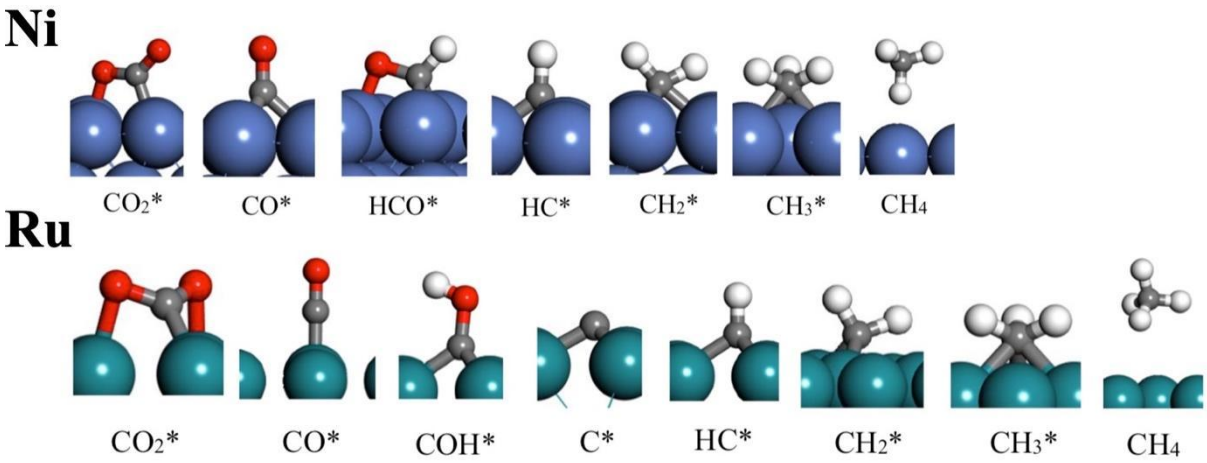

Figure 2.4 Reaction intermediates of the most probable pathway for CO_2 methanation on Ni fcc (111) and Ru hcp (001). Adapted from[16].

2.1.2 Conversion to Methanol

The concept of methanol economy uses the idea of capturing CO_2 and converting it to methanol and subsequently methanol to the various value-added chemicals for catering to the global energy requirements[17]. Therefore, CO_2 conversion into methanol has been widely studied. Thermodynamically, CO_2 conversion into methanol is exothermic, feasible at STP (eq. 2), and is favoured by high pressures and low temperatures. The increased yield of methanol at high pressures conditions with elevated reaction temperatures is also attributed to the condensation of methanol[18]. At the thermodynamic state of ~240 ºC and 200 bar pressure, methanol exists as the liquid phase, which favours the equilibrium entropically.

$$CO_{2(g)} + 3H_{2(g)} \rightarrow CH_3OH_{(l)} + H_2O_{(l)} \ (\Delta G° = -9.5\ kJ/mol) \qquad \text{(Eq. 2)}$$

A majority of CO_2 conversion to methanol reports use Cu-based catalysts where ZnO_2 as promotor and Al_2O_3 as support increases the activity and stability of the catalyst

significantly[19,20]. The ZnO_2 or ZrO_2 helps in the fine dispersion of Cu metal particles by acting as a spacer and the alumina support provides thermal and mechanical stability to these nanoparticles[21–23]. The hydrophilic nature of Al_2O_3 creates a problem for methanol formation and could be avoided by replacing it with ZrO_2 support[22]. In addition, several Pd-based and bimetallic catalysts of Au-Ag, Pd-Cu, Ni-Ga, etc., have also been reported for efficient conversion[19,24–26].

The reaction mechanism on the widely studied and used Cu/ZrO_2 catalyst. Figure 2.5 shows the DFT optimised energies and the Gibbs free energies at 473 K[27]. Adsorption of CO_2 at the interface is required for activation followed by CO_2 hydrogenation into formate intermediate. The adsorbed hydrogen mediates the hydrogenation of CO_2 on the Cu particle. After that, the formate intermediate dissociates to methoxy intermediate, which further hydrogenates to methanol. The dissociated oxygen of CO_2 hydrogenates and form a water molecule.

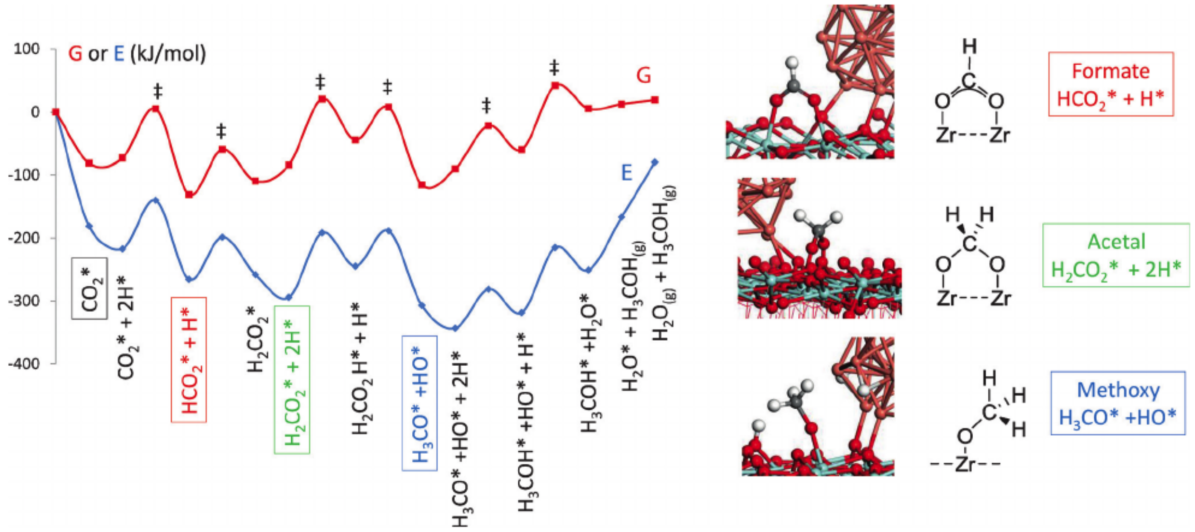

Figure 2.5: Shows the Gibbs free energy (red) and the energy pathway for CO_2 hydrogenation on Cu/ZrO_2 interface. On the right, the minimum energy configuration of key reaction intermediates at the Cu/ZrO_2 interface are shown. Re-printed with permission[27].

2.1.3 Conversion to Formaldehyde

CO_2 hydrogenation into formaldehyde is challenging, and only a limited number of studies report the heterogeneous catalytic reactions for the conversion of CO_2 into formaldehyde. The main reason for the difficulty is the thermodynamics, i.e., the reaction is endothermic (ΔH^o = 39.8 kJ/mol) and an entropically not favourable (ΔS^o = - 67 $JK^{-1}mol^{-1}$), which equates to the positive Gibbs free energy (ΔG^o = 59.8 kJ/mol) in the gas-phase reaction. Formaldehyde was

reported as a kinetic product in low concentrations (< 1 % conversion) by a Pt-Cu nanoparticle supported on SiO_2 and Ni-Co bimetallic nanoparticle catalysts.

$$CO_{2_{(g)}} + H_{2_{(g)}} \rightarrow CH_2O_{(g)} + H_2O_{(g)} \ (\Delta G° = 59.8\ kJ/mol) \quad \text{(Eq. 3)}$$

$$CO_{(g)} + H_{2_{(g)}} \rightarrow CH_2O_{(g)} \ (\Delta G° = 34.6\ kJ/mol) \quad \text{(Eq. 4)}$$

$$CO_{(aq)} + H_{2_{(aq)}} \rightarrow CH_2O_{(aq)} \ (\Delta G° = -7.1\ kJ/mol) \quad \text{(Eq. 5)}$$

Although not feasible in the gas phase, CO hydrogenation into formaldehyde has negative free energy in aqueous media). Bahmanpour et. al.[6,7] reported a Ni-Ru catalyst system with formaldehyde as a stable product in the presence of methanol and other solvents, but the best yield of formaldehyde was observed in pure methanol. The same group also reported the CO high yield of formaldehyde at a low temperature suitable for energy-efficient conversion[28]. Although CO and CO_2 conversion into formaldehyde are challenging, formaldehyde is a key reaction intermediate during the formation of methanol, methane, dimethyl-ether (DME), and oxyethylene ethers (OME). It is noteworthy to mention that it is unclear whether the reaction pathways go through formaldehyde intermediate or formate intermediate[29,30].

2.1.4 Conversion to Formic acid

CO_2 can theoretically be converted into formic acid via hydrogenation (eq. 7). The overall reaction is endothermic, and the Gibbs free energy of the reaction is 32 kJ/mol due to the phase change during the reaction. Formic acid exists as a liquid, and hence the free energy is positive due to the higher entropy of the reaction. Generally, such reactions are feasible in a liquid phase and the free energy of formation of formic acid within a liquid media is -4 kJ/mol[31]. To further improve the selectivity of formic acid, a secondary reaction may be involved in the reaction system that consumes formic acid after its formation, which leads to a shift in equilibrium. For CO_2 hydrogenation to formic acid, the commonly used secondary reaction systems are its esterification or its neutralisation with a weak base.

$$CO_{2_{(g)}} + H_{2_{(g)}} \rightarrow HCOOH_{(l)} \ (\Delta G° = 32.9\ kJ/mol\ ) \quad \text{(Eq. 7)}$$

$$CO_{2_{(aq)}} + H_{2_{(aq)}} \rightarrow HCOOH_{(aq)} \ (\Delta G° = -4\ kJ/mol\ ) \quad \text{(Eq. 8)}$$

Several heterogeneous catalysis systems were reported for CO_2 hydrogenation into formic acid. Pd[32], Au[33], Pd-Ni bimetallic[34], and gamma-Al_2O_3 supported Ru[35] were reported suitable for conversion to formic acid. These reaction systems were also tested with the secondary reaction schemes to increase the yield and shift the equilibrium.

Understanding the reaction mechanism of CO_2 hydrogenation to formic acid, the common agreement is the binding of CO_2 and H_2 to the metal surface followed by a nucleophilic attack

of adsorbed hydrogen to the C of bonded CO_2, which forms formate intermediate on the surface. After that, the formate can dissociate from the surface and is solubilised in the solvent as an ion or after getting protonated depending on the pH and the type of solvent[36]. The formation of the H-COO bond can be tuned by the metal support and the designed bimetallic catalysts. For example, a Pd-Ni catalyst has been reported, where the H binds to the Pd atoms and attacks the CO_2 molecule adsorbed to Ni atom[34].

2.2 Molecular modelling of heterogenous CO_2 hydrogenation

In the last two decades, molecular modelling and advanced spectroscopic techniques have elucidated a number of details about the elementary steps of catalytic reaction mechanisms. Experimentally, elucidating the reaction mechanism is a complex and challenging task. However, with the recent advancement in experimental techniques such as surface-enhanced Raman spectroscopy, an attempt is made to understand the surface reaction intermediates in real-time. Regardless, due to the limitations at length and time scale, the sensitivity of the measurements, and the particle difficulty of conducting a controlled experiment - the computational tools are most robust and viable for understanding the reaction mechanisms. Various *ab initio*, DFT, Reactive MD, path-integral MD simulation techniques have been used for investigating the catalytic reaction systems over the years. On the other hand, classical molecular dynamics and GCMC simulations have been used to indirectly probe the different aspects of the reaction system to gain a molecular understanding and further guide the experiments to optimise the reaction scheme.

Quantum mechanics-based simulation methods have been used to explore CO and CO_2 hydrogenation the reaction pathways on many metal surfaces[37]. In such methods, the binding energies of possible reaction intermediates are calculated at different surface sites. After which, the transition state is explored for each possible elementary reaction. This calculation is initial performed at 0 K, and a temperature correction factor is applied to account for the additional energy at the desired temperature[38,39]. After this, the most feasible reaction pathway is predicted via micro-kinetic modelling[40,41]. With the advancements in computational chemistry and numerical modelling techniques, these calculations have become straightforward, and the major challenge lies in the choice of pseudopotentials or accuracy of the applied method[42,43]. A recent review of computational studies of the surface reaction mechanisms may be referred to for a better overview[37].

Figure 2.6 shows three possible reaction pathways for CO_2 hydrogenation to methane on a Ni (111) surface[44]. In this study, the calculation suggests path 2 to be the most feasible pathway for CO_2 conversion to methane where CO_2 dissociates to CO, and CO further dissociates to C. After that, C hydrogenates to CH_4 and desorbs. The elementary step for the reaction path-2 is the fission of the CO* bond to form C* and O* on the surface. Further studies report that the CO diffusion mostly occurs on the step edge, which suggests that particle size is a key factor that facilitates the CO* bond fission.

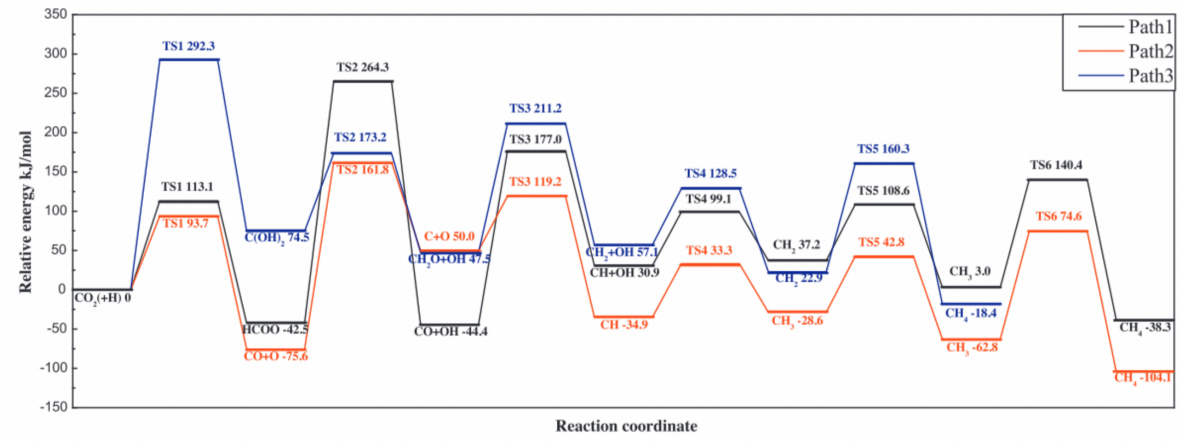

Fig. 7. Potential energy diagram of three mechanisms of CO_2 methanation.

Figure 2.6: Three Possible reaction pathways from CO_2 + H_2 to CH_4 on Ni (111) with relative energies calculated by DFT geometry optimisation. Re-printed with permission[44].

Ruthenium has been reported for Fischer-Tropsch synthesis producing Olefins[45]. It was reported that a larger particle size (~ 8 nm) is desired to facilitate the C-C coupling chain growth[46]. Recently, carefully thought and designed DFT and *ab initio* MD tools were used to investigate the CO activation for Fischer-Tropsch synthesis[8,9,47,48]. Among contradicting views, the common understanding is that the CO* fission occurs on the stepped edge site of Ru hcp 001 surface either as CO* or after hydrogenation of oxygen as COH*[47]. Higher pressure at a stoichiometric ratio of CO:H_2 is required for forming adlayers of CO* on the stepped site, which helps in the activation of CO* bond[11,45]. The support (mainly Al_2O_3 and TiO_2) plays an important role in the size and the shape of the Ru particles and providing additional sites for CO* dissociation at the interface of Ru and the support increases the activity of the catalyst further[48,49]. Understanding the role of support is even a greater challenge for the computational tools to address.

Like the above-mentioned examples, the control parameters in the catalytic systems can be fine-tuned for high yield and the selectivity of the product. However, as the control parameters become complex, elucidating their effect on the reaction energies and barriers becomes a challenge. Liquid phase heterogeneous catalysis is one such example. In the presence of a liquid solvent, CO_2 hydrogenation on Pd-Ni has been shown to produce formic acid[34]. In this case, it is rational to hypothesise that the polar transition states and reaction intermediates are likely to be stabilised by the presence of a polar solvent. Moreover, the entropy of phase change may no longer be associated with formic acid in a liquid phase environment. However, atomistic simulations of the relative surface coverage, the activation barriers, and micro-kinetic modelling of liquid phase reactions are computationally costly due to the large system size. Therefore, specific aspects of the reaction system are generally explored for deriving conclusions or forming a more robust hypothesis.

Recent advancements in organometallic chemistry, mainly MOFs and other carbonaceous nanomaterials with embedded metal particles, opened a possibility to explore and tune a suitable catalytic material for the desired application. Metal Organic Frameworks (MOFs) are known for large surface area, pore volume, and a wide variety of structures and compositions. However, MOFs are metastable, and the framework collapses at high temperatures and pressures[50–52]. Moreover, many MOFs are not stable in polar solvents. This limits the ability of MOFs to function as a catalyst. The thermal pyrolysis of MOF is reported to results in a carbonaceous material with embedded metal nanoparticles[53]. These MOF-derived carbonaceous materials have been reported for CO_2 utilisation[54]. The carbonaceous materials have a network of disrupted organic linkers, and the metal nanoparticles are finely dispersed within this network. The thermal decomposition and the dynamics of framework collapse are not well understood, which is important for the further development of these materials.

This thesis develops an understanding of the liquid phase and MOF-derived carbonaceous materials in catalytic reaction systems. Moreover, we develop reactive MD forcefield parameters that can be used to simulate the catalytic systems with Ru metal at a nanometre length scale. In the next two sections, we provide a critical review of background literature in the liquid phase and MOF-derived nanomaterials.

2.3 Effect of liquid media on a catalytic reaction system

In heterogeneous catalytic reactions, solvents can play many different roles depending upon the reaction system. Water is one of the most used solvents. It has been investigated and reported for stabilising reactants and products differently, stabilising reaction intermediates and transition states for selectivity, improving the reaction kinetics by lowering the activation energy barriers[55,56], acting as a co-catalyst by mediating proton transfer[57–59], and acting as a source of Lewis and Bronsted acidity[60–62]. Solvents other than water were also reported for their effect in liquid phase heterogeneous catalytic reaction systems[6,61], but the molecular scale understanding of their role in the reaction mechanism is limited. Methanol, Ethanol, DMSO, and THF are some commonly used solvents in liquid-phase catalytic reactions. It is noteworthy to mention that the solvent used are generally polar solvents. One of the purposes is to stabilise the transition state and the reaction intermediate and lower the activation energy barrier to activate the reaction pathways that are otherwise not feasible in gas-phase conditions.

The role of a solvent is very dependent on the metal-solvent interaction. To illustrate this, we present a few case studies from the literature. Once the catalytic metal is solvated in water, it forms a relatively static layer on the surface. The thickness and dynamic nature of this layer depend upon the metal-water interaction. Water molecules on a Ru (hcp-001) surface form a hexagonal shape where three water molecules are adsorbed on the surface. The remaining three molecules are part of a secondary layer, hydrogen-bonded to the first layer of water molecules[63,64]. This type of adsorption behaviour is commonly seen in most of the closed pack (hcp) surfaces[4]. After this first solvation layer, the dynamics of the subsequent layer depend upon the interaction strength of metal with water and subsequently affects the transport of reactants and products between the bulk and the surface. Moreover, reactants and products now compete with water for the active sites, affecting the reaction kinetics. However, in principle, the equilibrium should not be affected by the competition for a catalytic site.

Water on a metal surface can also undergo either homolytic or heterolytic fission of H-OH bond. Heterolytic fission forms reactive H+, which is stabilised by the water in the solvation layer and has the potential of playing an important role in the reaction mechanism by increasing the acidity of the surface[4,57,58,58,65,66]. The OH- is stabilised on the surface by the transfer of an additional electron to the metal and OH is simply adsorbed as HO*. Therefore, the heterolytic fission of H-OH depends upon metal's work function and is only seen when the energy for additional is not observed for every metal. Kizhakevariam et al.[67] reported the work function

of various transition metal element and their work function and concluded that for heterogeneous fission of H-OH bond the work function of the metal should be more than 4.88 eV. Since Ru's (hcp001) work function is below 4.88 eV, heterolytic fission of water is unlikely. However, in case of a bimetallic catalyst, it depends upon the composition of the two metals and their affinity for the electron. For example, Pt has the tendency of heterolytic fission of H-OH bond and Ru of homolytic fission. However, in a 1/3 or 2/3 composition of Pt-Ru bimetallic catalyst, water undergoes heterolytic fission. Wang et al.[59] reported a Pt-Ru catalyst for HCOOH conversion to CO_2 in liquid phase where water was observed to show heterolytic bond fission.

In recent years, our lab group has reported a liquid phase catalytic reaction scheme for direct conversion of CO into formaldehyde in the presence of a liquid media[6]. The liquid media affected the yield of formaldehyde significantly. Methanol as the solvent phase resulted in the best yield of formaldehyde among water, methanol-water mixtures, methanol, DMSO and ethanol. Formaldehyde in presence of methanol is stabilised as its metastable form methoxymethanol. This secondary reaction scheme in liquid media could be the reason for higher yield of methanol. However, when a mixture of methanol-water was used instead of pure methanol, a non-linear trend in formaldehyde yield was observed. The yield reaches a minimum around equimolar compositions and rises on increasing methanol concentration further. This trend in the yield directly indicates an effect of the liquid phase on the reaction equilibrium. Methoxymethanol in pure methanol is solvated by a ring/chain structure of 8-10 methanol molecules, which is determined to create an additional entropic barrier and result in a high yield of methanol. However, the increase in the yield on decreasing methanol after equimolar composition is not understood.

To develop a green reaction scheme for CO/CO_2 conversion using water as a solvent with small amount of methanol is desirable. However, the trend observed on changing methanol concentration remains unexplained. Understanding the effect of liquid media on the yield of formaldehyde is crucial for developing and optimising this reaction scheme. Moreover, this will also contribute to the understanding of other liquid phase heterogeneous catalysis reaction schemes.

2.4 MOF derived Carbonaceous Materials

Controlled thermal decomposition of MOF results in MOF-derived carbonaceous material with the metal or metal oxide of the MOF embedded in its disrupted organic linkers. The mass loss during the decomposition is associated with small organic molecules produced from the linker. For example, Li and co-workers reported a Co nanoparticle embedded C-N containing support derived from ZIF-67 for the esterification of alcohols[68]. This catalyst showed remarkably high activity and the ability to withstand higher temperatures than the parent MOF. The same group also reported other Co containing MOF-derived catalysts for oxidative amidation of aldehydes with formamides[69], hydrogenation of nitriles into primary amines or imines[70]. They have also reported the thermally decomposed ZIF-8 with $Ru_3(CO_2)_{12}$) molecules inside cages[71]. This MOF-derived catalyst showed high activity with 100% conversion for 2-aminobenzyl alcohol conversion to 2-aminobenzaldehyde. The MOFs with encapsulated metal nanoparticles are generally designed to provide a fine dispersion of encapsulated metal/metal oxide nanoparticles. The metal/metal oxide cluster of the MOF in such assemblies mostly only acts as a support.

As Ruthenium is active metal for CO_2 hydrogenation, recently, Ru encapsulated MOF-derived nanomaterials have been reported for CO_2 conversion into methane[72]. The catalyst was prepared in-situ from Ru encapsulated UiO-66 and provided excellent activity. It was reported to be stable for 160 h under the experimental condition, which is desirable in an industrial catalyst. Another similar Ru/ZrO_2 catalyst, prepared from Ru encapsulated MIL-140C, was reported for CO_2 hydrogenation[73]. The MIL-140C catalyst was modified by replacing 10% of the BPDC (bi-phenyl di-carboxylate) linkers by BPyDC (bi-pyridine di-carboxylate) linker to support the Ru nanoparticles within the pores of the MOF. Figure 2.7 shows the schematic for experimental observations made in during the thermally decomposed Ru-MIL-140C. The Ru-MIL-140C was active for CO_2 hydrogenation, but the kinetics showed slow kinetics. However, after the thermal decomposition, the catalyst was highly active and achieved a better yield in hours.

In addition to the fine dispersion of metal/metal oxide nanoparticles and their ability to retain the structure at high temperatures/pressures, the MOF-derived catalyst has additional features that are desired in an ideal catalyst. The metal nanoparticles are less prone to sinter as they are embedded in a fibrous organic layer. The carbonaceous phase being hydrophobic and the metal nanoparticles hydrophilic could be advantageous for catalytic reaction systems. The organic

phase could also be fine-tuned for its connectivity, and the strength of the material could be improved for an industrial application.

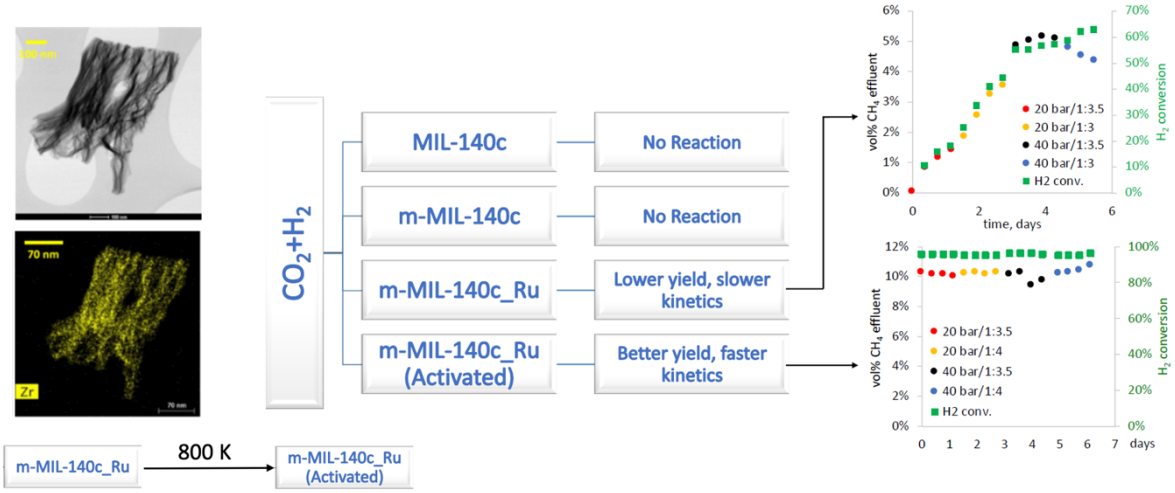

Figure 2.7: Shows CO_2 conversion to methane on a thermally decomposed modified MIL-140C catalyst reported by Dalal et al.[73]*. The TEM images on the left show the thermally decomposed m-MIL-140C with a fine dispersion of Zr shown by EDX mapping.*

A wide variety of MOFs are available, and new MOFs and Covalent Organic Frameworks (COFs) are being rapidly discovered. Therefore, various thermally decomposed MOF-derived catalyst could be prepared and optimised for their application in catalytic reaction systems. The effect of the linker, metal oxide, reaction environment, temperature, etc., on the morphology of the MOF-derived catalyst is yet not known. Therefore, in the present thesis, we aim to understand the morphology of thermally decomposed Zr-MOFs. We also aim to understand the effect of the linker, reaction environment, and metal clusters on the decomposed MOF.

2.5 Literature gaps and Thesis aims

Based on the literature review, we identify that,

a) although high yield of CO hydrogenation to formaldehyde is attributed to its solvation in methanol, its yield in methanol-water mixtures remains unexplained.
b) morphology of thermally decomposed MIL-140C need further investigation. Moreover, computationally thermal decomposition of Zr-MOFs is not yet studied.
c) control parameters for tuning morphology of thermally decomposed MOFs have not been explored.

The scope of the present thesis is to,

a) understand the micro-phase structure of methanol-water mixtures to formulate a hypothesis for the effect of liquid media on the yield of formaldehyde by CO hydrogenation,
b) understand the morphology of MOF-derived carbonaceous materials that enhance the kinetics of CO_2 conversion into methane.
c) develop a reactive molecular dynamics forcefield parameter set for simulating Ru/C/H/O chemistry for CO_2 hydrogenation.

2.1. References

(1) Centi, G.; Perathoner, S. Creating and Mastering Nano-Objects to Design Advanced Catalytic Materials. *Coordination Chemistry Reviews* **2011**, *255* (13–14), 1480–1498. https://doi.org/10.1016/j.ccr.2011.01.021.

(2) Oar-Arteta, L.; Wezendonk, T.; Sun, X.; Kapteijn, F.; Gascon, J. Metal Organic Frameworks as Precursors for the Manufacture of Advanced Catalytic Materials. *Materials Chemistry Frontiers* **2017**, *1* (9), 1709–1745.

(3) Ampelli, C.; Perathoner, S.; Centi, G. Carbon-Based Catalysts: Opening New Scenario to Develop next-Generation Nano-Engineered Catalytic Materials. *Chinese Journal of Catalysis* **2014**, *35* (6), 783–791. https://doi.org/10.1016/S1872-2067(14)60139-X.

(4) van Santen, R. A.; Neurock, M. *Molecular Heterogeneous Catalysis*; Wiley-VCH Verlag GmbH & Co. KGaA: Weinheim, Germany, 2006. https://doi.org/10.1002/9783527610846.

(5) Frontera, P.; Macario, A.; Ferraro, M.; Antonucci, P. Supported Catalysts for CO_2 Methanation: A Review. *Catalysts* **2017**, *7* (12), 59. https://doi.org/10.3390/catal7020059.

(6) Bahmanpour, A. M.; Hoadley, A.; Mushrif, S. H.; Tanksale, A. Hydrogenation of Carbon Monoxide into Formaldehyde in Liquid Media. *ACS Sustainable Chem. Eng.* **2016**, *4* (7), 3970–3977. https://doi.org/10.1021/acssuschemeng.6b00837.

(7) Bahmanpour, A. M.; Hoadley, A.; Tanksale, A. Formaldehyde Production via Hydrogenation of Carbon Monoxide in the Aqueous Phase. *Green Chem.* **2015**, *17* (6), 3500–3507. https://doi.org/10.1039/C5GC00599J.

(8) Gual, A.; Godard, C.; Castillón, S.; Curulla-Ferré, D.; Claver, C. Colloidal Ru, Co and Fe-Nanoparticles. Synthesis and Application as Nanocatalysts in the Fischer–Tropsch Process. *Catalysis Today* **2012**, *183* (1), 154–171. https://doi.org/10.1016/j.cattod.2011.11.025.

(9) Yang, J.; Ma, W.; Chen, D.; Holmen, A.; Davis, B. H. Fischer–Tropsch Synthesis: A Review of the Effect of CO Conversion on Methane Selectivity. *Applied Catalysis A: General* **2014**, *470*, 250–260. https://doi.org/10.1016/j.apcata.2013.10.061.

(10) Stangeland, K.; Kalai, D.; Li, H.; Yu, Z. CO_2 Methanation: The Effect of Catalysts and Reaction Conditions. *Energy Procedia* **2017**, *105*, 2022–2027. https://doi.org/10.1016/j.egypro.2017.03.577.

(11) Ciobica, I. M.; van Santen, R. A. Carbon Monoxide Dissociation on Planar and Stepped Ru(0001) Surfaces. *J. Phys. Chem. B* **2003**, *107* (16), 3808–3812. https://doi.org/10.1021/jp030010x.

(12) Van Santen, R. A. Complementary Structure Sensitive and Insensitive Catalytic Relationships. *Acc. Chem. Res.* **2009**, *42* (1), 57–66. https://doi.org/10.1021/ar800022m.

(13) Xiao, J.; Guo, X.; Song, C. Use of CO_2 as Source of Carbon for Energy-Rich Cn Products. In *An Economy Based on Carbon Dioxide and Water*; Aresta, M., Karimi, I., Kawi, S., Eds.; Springer International Publishing: Cham, 2019; pp 211–238. https://doi.org/10.1007/978-3-030-15868-2_6.

(14) Mebrahtu, C.; Krebs, F.; Abate, S.; Perathoner, S.; Centi, G.; Palkovits, R. CO_2 Methanation: Principles and Challenges. In *Studies in Surface Science and Catalysis*; Elsevier, 2019; Vol. 178, pp 85–103. https://doi.org/10.1016/B978-0-444-64127-4.00005-7.

(15) McBride, B. J. Coefficients for Calculating Thermodynamic and Transport Properties of Individual Species; NASA Langley Research Center, 1993; Vol. 4513.

(16) Mohan, O.; Shambhawi, S.; Xu, R.; Lapkin, A. A.; Mushrif, S. H. Investigating CO_2 Methanation on Ni and Ru: DFT Assisted Microkinetic Analysis. *ChemCatChem* **2021**, cctc.202100073. https://doi.org/10.1002/cctc.202100073.

(17) Olah, G. A. Beyond Oil and Gas: The Methanol Economy. *Angew. Chem. Int. Ed.* **2005**, *44* (18), 2636–2639. https://doi.org/10.1002/anie.200462121.

(18) Stangeland, K.; Li, H.; Yu, Z. Thermodynamic Analysis of Chemical and Phase Equilibria in CO_2 Hydrogenation to Methanol, Dimethyl Ether, and Higher Alcohols. *Ind. Eng. Chem. Res.* **2018**, *57* (11), 4081–4094. https://doi.org/10.1021/acs.iecr.7b04866.

(19) Jadhav, S. G.; Vaidya, P. D.; Bhanage, B. M.; Joshi, J. B. Catalytic Carbon Dioxide Hydrogenation to Methanol: A Review of Recent Studies. *Chemical Engineering Research and Design* **2014**, *92* (11), 2557–2567. https://doi.org/10.1016/j.cherd.2014.03.005.

(20) Kattel, S.; Ramírez, P. J.; Chen, J. G.; Rodriguez, J. A.; Liu, P. Active Sites for CO_2 Hydrogenation to Methanol on Cu/ZnO Catalysts. *Science* **2017**, *355* (6331), 1296–1299. https://doi.org/10.1126/science.aal3573.

(21) Twigg, M. V.; Spencer, M. S. Deactivation of Supported Copper Metal Catalysts for Hydrogenation Reactions. *Applied Catalysis A: General* **2001**, *212* (1–2), 161–174. https://doi.org/10.1016/S0926-860X(00)00854-1.

(22) Witoon, T.; Chalorngtham, J.; Dumrongbunditkul, P.; Chareonpanich, M.; Limtrakul, J. CO 2 Hydrogenation to Methanol over Cu/ZrO_2 Catalysts: Effects of Zirconia Phases. *Chemical Engineering Journal* **2016**, *293*, 327–336. https://doi.org/10.1016/j.cej.2016.02.069.

(23) Wang, J.; Li, G.; Li, Z.; Tang, C.; Feng, Z.; An, H.; Liu, H.; Liu, T.; Li, C. A Highly Selective and Stable ZnO-ZrO_2 Solid Solution Catalyst for CO $_2$ Hydrogenation to Methanol. *Sci. Adv.* **2017**, *3* (10), e1701290. https://doi.org/10.1126/sciadv.1701290.

(24) Jiang, X.; Koizumi, N.; Guo, X.; Song, C. Bimetallic Pd–Cu Catalysts for Selective CO_2 Hydrogenation to Methanol. *Applied Catalysis B: Environmental* **2015**, *170–171*, 173–185. https://doi.org/10.1016/j.apcatb.2015.01.010.

(25) Bahruji, H.; Bowker, M.; Hutchings, G.; Dimitratos, N.; Wells, P.; Gibson, E.; Jones, W.; Brookes, C.; Morgan, D.; Lalev, G. Pd/ZnO Catalysts for Direct CO_2 Hydrogenation to Methanol. *Journal of Catalysis* **2016**, *343*, 133–146. https://doi.org/10.1016/j.jcat.2016.03.017.

(26) Bansode, A.; Urakawa, A. Towards Full One-Pass Conversion of Carbon Dioxide to Methanol and Methanol-Derived Products. *Journal of Catalysis* **2014**, *309*, 66–70. https://doi.org/10.1016/j.jcat.2013.09.005.

(27) Larmier, K.; Liao, W.-C.; Tada, S.; Lam, E.; Verel, R.; Bansode, A.; Urakawa, A.; Comas-Vives, A.; Copéret, C. CO_2 -to-Methanol Hydrogenation on Zirconia-Supported Copper Nanoparticles: Reaction Intermediates and the Role of the Metal-Support Interface. *Angew. Chem. Int. Ed.* **2017**, *56* (9), 2318–2323. https://doi.org/10.1002/anie.201610166.

(28) Chan, F. L.; Altinkaya, G.; Fung, N.; Tanksale, A. Low Temperature Hydrogenation of Carbon Dioxide into Formaldehyde in Liquid Media. *Catalysis Today* **2018**, *309*, 242–247. https://doi.org/10.1016/j.cattod.2017.06.012.

(29) Ahmad, W.; Chan, F. L.; Hoadley, A.; Wang, H.; Tanksale, A. Synthesis of Oxymethylene Dimethyl Ethers (OME_n) via Methanol Mediated CO_x Hydrogenation over Ru/BEA Catalysts. *Applied Catalysis B: Environmental* **2020**, *269*, 118765. https://doi.org/10.1016/j.apcatb.2020.118765.

(30) Ahmad, W.; Chan, F. L.; Chaffee, A. L.; Wang, H.; Hoadley, A.; Tanksale, A. Dimethoxymethane Production via Catalytic Hydrogenation of Carbon Monoxide in Methanol Media. *ACS Sustainable Chem. Eng.* **2020**, *8* (4), 2081–2092. https://doi.org/10.1021/acssuschemeng.9b06913.

(31) Reymond, H.; Corral-Pérez, J. J.; Urakawa, A.; Rudolf von Rohr, P. Towards a Continuous Formic Acid Synthesis: A Two-Step Carbon Dioxide Hydrogenation in Flow. *React. Chem. Eng.* **2018**, *3* (6), 912–919. https://doi.org/10.1039/C8RE00142A.

(32) Su, J.; Yang, L.; Lu, M.; Lin, H. Highly Efficient Hydrogen Storage System Based on Ammonium Bicarbonate/Formate Redox Equilibrium over Palladium Nanocatalysts. *ChemSusChem* **2015**, *8* (5), 813–816. https://doi.org/10.1002/cssc.201403251.

(33) Preti, D.; Resta, C.; Squarcialupi, S.; Fachinetti, G. Carbon Dioxide Hydrogenation to Formic Acid by Using a Heterogeneous Gold Catalyst. *Angew. Chem.* **2011**, *123* (52), 12759–12762. https://doi.org/10.1002/ange.201105481.

(34) Nguyen, L. T. M.; Park, H.; Banu, M.; Kim, J. Y.; Youn, D. H.; Magesh, G.; Kim, W. Y.; Lee, J. S. Catalytic CO_2 Hydrogenation to Formic Acid over Carbon Nanotube-Graphene Supported PdNi Alloy Catalysts. *RSC Adv.* **2015**, *5* (128), 105560–105566. https://doi.org/10.1039/C5RA21017H.

(35) Hao, C.; Wang, S.; Li, M.; Kang, L.; Ma, X. Hydrogenation of CO_2 to Formic Acid on Supported Ruthenium Catalysts. *Catalysis Today* **2011**, *160* (1), 184–190. https://doi.org/10.1016/j.cattod.2010.05.034.

(36) Wang, W.-H.; Himeda, Y.; Muckerman, J. T.; Manbeck, G. F.; Fujita, E. CO_2 Hydrogenation to Formate and Methanol as an Alternative to Photo- and Electrochemical CO_2 Reduction. *Chem. Rev.* **2015**, *115* (23), 12936–12973. https://doi.org/10.1021/acs.chemrev.5b00197.

(37) Podrojková, N.; Sans, V.; Oriňak, A.; Oriňaková, R. Recent Developments in the Modelling of Heterogeneous Catalysts for CO_2 Conversion to Chemicals. *ChemCatChem* **2020**, *12* (7), 1802–1825. https://doi.org/10.1002/cctc.201901879.

(38) Sutton, J. E.; Vlachos, D. G. A Theoretical and Computational Analysis of Linear Free Energy Relations for the Estimation of Activation Energies. *ACS Catal.* **2012**, *2* (8), 1624–1634. https://doi.org/10.1021/cs3003269.

(39) Weijing, D.; Weihong, Z.; Xiaodong, Z.; Baofeng, Z.; Lei, C.; Laizhi, S.; Shuangxia, Y.; Haibin, G.; Guanyi, C.; Liang, Z.; Ge, S. The Application of DFT in Catalysis and Adsorption

Reaction System. *Energy Procedia* **2018**, *152*, 997–1002. https://doi.org/10.1016/j.egypro.2018.09.106.

(40) Mao, Y.; Wang, H.; Hu, P. Theory and Applications of Surface Micro-kinetics in the Rational Design of Catalysts Using Density Functional Theory Calculations. *WIREs Comput Mol Sci* **2017**, *7* (6). https://doi.org/10.1002/wcms.1321.

(41) Stamatakis, M. Kinetic Modelling of Heterogeneous Catalytic Systems. *J. Phys.: Condens. Matter* **2015**, *27* (1), 013001. https://doi.org/10.1088/0953-8984/27/1/013001.

(42) Mohan, O.; Trinh, Q. T.; Banerjee, A.; Mushrif, S. H. Predicting CO_2 Adsorption and Reactivity on Transition Metal Surfaces Using Popular Density Functional Theory Methods. *Molecular Simulation* **2019**, *45* (14–15), 1163–1172. https://doi.org/10.1080/08927022.2019.1632448.

(43) Mallikarjun Sharada, S.; Karlsson, R. K. B.; Maimaiti, Y.; Voss, J.; Bligaard, T. Adsorption on Transition Metal Surfaces: Transferability and Accuracy of DFT Using the ADS41 Dataset. *Phys. Rev. B* **2019**, *100* (3), 035439. https://doi.org/10.1103/PhysRevB.100.035439.

(44) Ren, J.; Guo, H.; Yang, J.; Qin, Z.; Lin, J.; Li, Z. Insights into the Mechanisms of CO_2 Methanation on Ni(111) Surfaces by Density Functional Theory. *Applied Surface Science* **2015**, *351*, 504–516. https://doi.org/10.1016/j.apsusc.2015.05.173.

(45) Loveless, B. T.; Buda, C.; Neurock, M.; Iglesia, E. CO Chemisorption and Dissociation at High Coverages during CO Hydrogenation on Ru Catalysts. *J. Am. Chem. Soc.* **2013**, *135* (16), 6107–6121. https://doi.org/10.1021/ja311848e.

(46) Kang, J.; Deng, W.; Zhang, Q.; Wang, Y. Ru Particle Size Effect in Ru/CNT-Catalyzed Fischer-Tropsch Synthesis. *Journal of Energy Chemistry* **2013**, *22* (2), 321–328. https://doi.org/10.1016/S2095-4956(13)60039-X.

(47) Foppa, L.; Iannuzzi, M.; Copéret, C.; Comas-Vives, A. Adlayer Dynamics Drives CO Activation in Ru-Catalyzed Fischer–Tropsch Synthesis. *ACS Catal.* **2018**, *8* (8), 6983–6992. https://doi.org/10.1021/acscatal.8b01232.

(48) Zhang, Y.; Yang, X.; Yang, X.; Duan, H.; Qi, H.; Su, Y.; Liang, B.; Tao, H.; Liu, B.; Chen, D.; Su, X.; Huang, Y.; Zhang, T. Tuning Reactivity of Fischer–Tropsch Synthesis by Regulating TiO_x Overlayer over Ru/TiO2 Nanocatalysts. *Nat Commun* **2020**, *11* (1), 3185. https://doi.org/10.1038/s41467-020-17044-4.

(49) Mutschler, R.; Moioli, E.; Züttel, A. Modelling the CO_2 Hydrogenation Reaction over Co, Ni and Ru/Al_2O_3. *Journal of Catalysis* **2019**, *375*, 193–201. https://doi.org/10.1016/j.jcat.2019.05.023.

(50) Kandiah, M.; Nilsen, M. H.; Usseglio, S.; Jakobsen, S.; Olsbye, U.; Tilset, M.; Larabi, C.; Quadrelli, E. A.; Bonino, F.; Lillerud, K. P. Synthesis and Stability of Tagged UiO-66 Zr-MOFs. *Chem. Mater.* **2010**, *22* (24), 6632–6640. https://doi.org/10.1021/cm102601v.

(51) Mohamed, S. A.; Chong, S.; Kim, J. Thermal Stability of Methyl-Functionalized MOF-5. *J. Phys. Chem. C* **2019**, *123* (49), 29686–29692. https://doi.org/10.1021/acs.jpcc.9b08060.

(52) Healy, C.; Patil, K. M.; Wilson, B. H.; Hermanspahn, L.; Harvey-Reid, N. C.; Howard, B. I.; Kleinjan, C.; Kolien, J.; Payet, F.; Telfer, S. G.; Kruger, P. E.; Bennett, T. D. The Thermal Stability of Metal-Organic Frameworks. *Coordination Chemistry Reviews* **2020**, *419*, 213388. https://doi.org/10.1016/j.ccr.2020.213388.

(53) Shen, K.; Chen, X.; Chen, J.; Li, Y. Development of MOF-Derived Carbon-Based Nanomaterials for Efficient Catalysis. *ACS Catal.* **2016**, *6* (9), 5887–5903. https://doi.org/10.1021/acscatal.6b01222.

(54) Chaffee, A. CO_2 Conversion to Hydrocarbons with MOF-Derived Materials as Catalysts. In *ABSTRACTS OF PAPERS OF THE AMERICAN CHEMICAL SOCIETY*; AMER CHEMICAL SOC 1155 16TH ST, NW, WASHINGTON, DC 20036 USA, 2019; Vol. 257.

(55) Wan, H.; Vitter, A.; Chaudhari, R. V.; Subramaniam, B. Kinetic Investigations of Unusual Solvent Effects during Ru/C Catalyzed Hydrogenation of Model Oxygenates. *Journal of Catalysis* **2014**, *309*, 174–184. https://doi.org/10.1016/j.jcat.2013.09.020.

(56) Michel, C.; Auneau, F.; Delbecq, F.; Sautet, P. C–H versus O–H Bond Dissociation for Alcohols on a Rh(111) Surface: A Strong Assistance from Hydrogen Bonded Neighbors. *ACS Catal.* **2011**, *1* (10), 1430–1440. https://doi.org/10.1021/cs200370g.

(57) Li, G.; Wang, B.; Resasco, D. E. Water-Mediated Heterogeneously Catalyzed Reactions. *ACS Catal.* **2020**, *10* (2), 1294–1309. https://doi.org/10.1021/acscatal.9b04637.

(58) Farnesi Camellone, M.; Negreiros Ribeiro, F.; Szabová, L.; Tateyama, Y.; Fabris, S. Catalytic Proton Dynamics at the Water/Solid Interface of Ceria-Supported Pt Clusters. *J. Am. Chem. Soc.* **2016**, *138* (36), 11560–11567. https://doi.org/10.1021/jacs.6b03446.

(59) Wang, H.-F.; Liu, Z.-P. Formic Acid Oxidation at Pt/H_2O Interface from Periodic DFT Calculations Integrated with a Continuum Solvation Model. *J. Phys. Chem. C* **2009**, *113* (40), 17502–17508. https://doi.org/10.1021/jp9059888.

(60) Adams, J. S.; Chemburkar, A.; Priyadarshini, P.; Ricciardulli, T.; Lu, Y.; Maliekkal, V.; Sampath, A.; Winikoff, S.; Karim, A. M.; Neurock, M.; Flaherty, D. W. Solvent Molecules Form Surface Redox Mediators in Situ and Cocatalyze O_2 Reduction on Pd. *Science* **2021**, *371* (6529), 626–632. https://doi.org/10.1126/science.abc1339.

(61) Mellmer, M. A.; Sanpitakseree, C.; Demir, B.; Bai, P.; Ma, K.; Neurock, M.; Dumesic, J. A. Solvent-Enabled Control of Reactivity for Liquid-Phase Reactions of Biomass-Derived Compounds. *Nat Catal* **2018**, *1* (3), 199–207. https://doi.org/10.1038/s41929-018-0027-3.

(62) Choudhary, V.; Mushrif, S. H.; Ho, C.; Anderko, A.; Nikolakis, V.; Marinkovic, N. S.; Frenkel, A. I.; Sandler, S. I.; Vlachos, D. G. Insights into the Interplay of Lewis and Brønsted Acid Catalysts in Glucose and Fructose Conversion to 5-(Hydroxymethyl)Furfural and Levulinic Acid in Aqueous Media. *J. Am. Chem. Soc.* **2013**, *135* (10), 3997–4006. https://doi.org/10.1021/ja3122763.

(63) Held, G.; Menzel, D. The Structure of the p($\sqrt{3} \times \sqrt{3}$)R30° Bilayer of D_2O on Ru(001). *Surface Science* **1994**, *316* (1–2), 92–102. https://doi.org/10.1016/0039-6028(94)91131-2.

(64) Michaelides, A.; Alavi, A.; King, D. A. Different Surface Chemistries of Water on Ru{0001}: From Monomer Adsorption to Partially Dissociated Bilayers. *J. Am. Chem. Soc.* **2003**, *125* (9), 2746–2755. https://doi.org/10.1021/ja028855u.

(65) Andersson, K.; Nikitin, A.; Pettersson, L. G. M.; Nilsson, A.; Ogasawara, H. Water Dissociation on Ru(001): An Activated Process. *Phys. Rev. Lett.* **2004**, *93* (19), 196101. https://doi.org/10.1103/PhysRevLett.93.196101.

(66) Desai, S. K.; Neurock, M. First-Principles Study of the Role of Solvent in the Dissociation of Water over a Pt-Ru Alloy. *Phys. Rev. B* **2003**, *68* (7), 075420. https://doi.org/10.1103/PhysRevB.68.075420.

(67) Kizhakevariam, N.; Stuve, E. M. Coadsorption of Water and Hydrogen on Pt(100): Formation of Adsorbed Hydronium Ions. *Surface Science* **1992**, *275* (3), 223–236. https://doi.org/10.1016/0039-6028(92)90796-9.

(68) Zhong, W.; Liu, H.; Bai, C.; Liao, S.; Li, Y. Base-Free Oxidation of Alcohols to Esters at Room Temperature and Atmospheric Conditions Using Nanoscale Co-Based Catalysts. *ACS Catal.* **2015**, *5* (3), 1850–1856. https://doi.org/10.1021/cs502101c.

(69) Bai, C.; Yao, X.; Li, Y. Easy Access to Amides through Aldehydic C–H Bond Functionalization Catalyzed by Heterogeneous Co-Based Catalysts. *ACS Catal.* **2015**, *5* (2), 884–891. https://doi.org/10.1021/cs501822r.

(70) Long, J.; Shen, K.; Li, Y. Bifunctional N-Doped Co@C Catalysts for Base-Free Transfer Hydrogenations of Nitriles: Controllable Selectivity to Primary Amines vs Imines. *ACS Catal.* **2017**, *7* (1), 275–284. https://doi.org/10.1021/acscatal.6b02327.

(71) Ji, S.; Chen, Y.; Fu, Q.; Chen, Y.; Dong, J.; Chen, W.; Li, Z.; Wang, Y.; Gu, L.; He, W.; Chen, C.; Peng, Q.; Huang, Y.; Duan, X.; Wang, D.; Draxl, C.; Li, Y. Confined Pyrolysis within Metal–Organic Frameworks To Form Uniform Ru_3 Clusters for Efficient Oxidation of Alcohols. *J. Am. Chem. Soc.* **2017**, *139* (29), 9795–9798. https://doi.org/10.1021/jacs.7b05018.

(72) Lippi, R.; Howard, S. C.; Barron, H.; Easton, C. D.; Madsen, I. C.; Waddington, L. J.; Vogt, C.; Hill, M. R.; Sumby, C. J.; Doonan, C. J. Highly Active Catalyst for CO 2 Methanation Derived from a Metal Organic Framework Template. *Journal of Materials Chemistry A* **2017**, *5* (25), 12990–12997.

(73) Alqarni, D. S.; Lee, C. W.; Knowles, G. P.; Vogt, C.; Marshall, M.; Gengenbach, T.; Chaffee, A. L. Ru-Zirconia Catalyst Derived from MIL140C for Carbon Dioxide Conversion to Methane. *Catalysis Today* **2020**, S0920586120305563. https://doi.org/10.1016/j.cattod.2020.07.080.

Chapter 3

3 Solvation behaviour and the Micro-Phase structure of Formaldehyde-methanol-water mixtures

3.1 Overview

In recent years, our group has developed a novel method for the synthesis of formaldehyde (HCHO) via hydrogenation of CO and CO_2.[1,2] The process involves a heterogeneous catalytic reaction where CO and H_2 react on a solid catalyst surface (Ni-Ru) suspended in a liquid phase. The liquid phase has the ability to tailor the reaction pathway, making formaldehyde synthesis feasible, which is not otherwise possible in the gas phase. The solvent plays an important role in shifting the reaction equilibrium, and we hypothesise that it may play a role in kinetics. Formaldehyde is solvated in water as methanediol and in methanol as methoxymethanol (Eq. 1 and 2, respectively).

Hydration of HCHO to methanediol

$$HCHO + H_2O \leftrightharpoons HOCH_2OH \quad \dots (1)$$

Acetylation of HCHO to methoxymethanol

$$HCHO + CH_3OH \leftrightharpoons HOCH_2OCH_3 \quad \dots (2)$$

The formaldehyde yield first decreased with the increasing concentration of methanol in water, but the yield increased again at >0.7 mole-fraction of methanol (Fig. 1a).[2] Ab initio molecular dynamics simulation of a binary mixture of methanol and methoxymethanol showed that the eight-member ring/chain of methanol surrounds one molecule of methoxymethanol (Fig. 1b).[2] Our hypothesis suggests that the entropy barrier of methanol-water hydrogen bonding affects the stabilisation of formaldehyde, resulting in a lower yield. However, there is no good theoretical model or experimental data to understand the hydrogen bonding network in these ternary mixtures. Therefore, to understand the increased yield for formaldehyde in a low methanol concentration range, we study the solvation of formaldehyde in methanol-water mixtures.

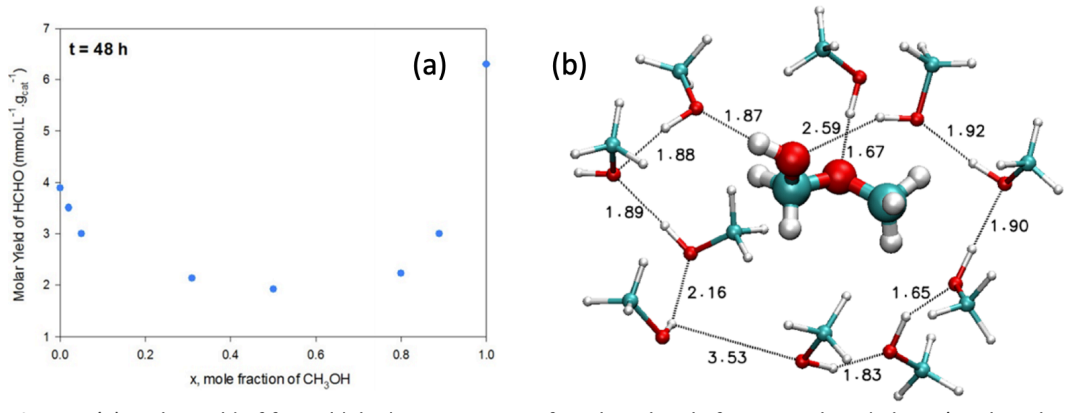

Fig. 3.1: (a) Molar yield of formaldehyde on variation of methanol mole fraction in liquid phase (methanol –water mixture). (b) One molecule of methoxymethanol in methanol as solvent where interaction length shown in the figure that supports hydrogen bonding. Adopted From[2]

References:

(1) Bahmanpour, A. M.; Hoadley, A.; Tanksale, A. Formaldehyde Production via Hydrogenation of Carbon Monoxide in the Aqueous Phase. *Green Chem.* **2015**, *17* (6), 3500–3507. https://doi.org/10.1039/C5GC00599J.

(2) Bahmanpour, A. M.; Hoadley, A.; Mushrif, S. H.; Tanksale, A. Hydrogenation of Carbon Monoxide into Formaldehyde in Liquid Media. *ACS Sustain. Chem. Eng.* **2016**, *4* (7), 3970–3977. https://doi.org/10.1021/acssuschemeng.6b00837.

3.2 Included Publication

This work has been published in Journal of Molecular Liquids (Elsevier) in January 2020:

Dwivedi, S., Mushrif, S. H., Chaffee, A. L., & Tanksale, A. (2020). Solvation behaviour and micro-phase structure of formaldehyde-methanol-water mixtures. *Journal of Molecular Liquids*, *301*, 112444.

The article and the supplementary information are provided herewith with the permission of Elsevier.

Journal of Molecular Liquids 301 (2020) 112444

Contents lists available at ScienceDirect

Journal of Molecular Liquids

journal homepage: www.elsevier.com/locate/molliq

Solvation behaviour and micro-phase structure of formaldehyde-methanol-water mixtures

Swarit Dwivedi[a], Samir H. Mushrif[b], Alan L. Chaffee[c], Akshat Tanksale[a,*]

[a]Department of Chemical Engineering, Monash University, Clayton 3800, Victoria, Australia
[b]Department of Chemical and Materials Engineering, University of Alberta, 9211-116 St., Edmonton, Alberta T6G 1H9, Canada
[c]School of Chemistry, Monash University, Clayton 3800, Victoria, Australia

ARTICLE INFO

Article history:
Received 16 September 2019
Received in revised form 9 December 2019
Accepted 1 January 2020
Available online 8 January 2020

Keywords:
Solvation dynamics
Formaldehyde
Formalin solution

ABSTRACT

Solvation of formaldehyde as methanediol and/or methoxymethanol in methanol-water mixtures of varying concentration was studied using classical molecular dynamics simulations. Varying strength of hydrophobic and hydrophilic interactions affect the arrangement of solvent within the solvation shell. Ether oxygen of methoxymethanol was observed to be hydrophobic in nature with hydrophilic interactions weaker than bulk due to the steric hindrance by the methyl group. At equimolar methanol-water compositions, water is more likely to occupy the hydrophilic sites. The total number of hydrogen bonds formed between solute and solvent decreased non-linearly, which was attributed to formaldehyde forming a distribution of different metastable complexes and micro-phase ordering. This non-linearity may influence the energetics of these solutions. The lifetime of hydrogen bonding was studied to build an understanding of the strength of hydrophilic interactions. The arrangement of methanol and water around solvated formaldehyde was visualised using spatial distribution function.

1. Introduction

Formaldehyde is a valuable chemical used as a raw material for the production of several commodities ranging from commercial to household products [1]. Formaldehyde consumption rate exceeds 30 million tonnes per year with a predicted annual growth of 4% [1]. It is used for the preparation of formaldehyde based resins (with urea, phenol, melamine, etc.), nano-porous organics gels, adhesives, plastics, foam, polyurethane paints, disinfectant, and in biomedical fixation. Commercially available formaldehyde solution, better known as formalin, is an aqueous solution of formaldehyde (37 wt%), where some methanol (10–15 wt%) is added to prevent precipitation of high molecular weight oligomers. This solution is then diluted or concentrated according to the requirements of the application. Formaldehyde in methanol-water mixtures has been a subject of study for almost a century across various disciplines of science and technology. However, the complex physical and chemical behaviour of this ternary mixture is still not very well understood. The complexities arise due to the oligomerisation of hydrated (methanediol) and alkoxylated (methoxymethanol) forms of formaldehyde. In the presence of water and methanol, formaldehyde rapidly converts into methanediol Eq. (1) and methoxymethanol Eq. (2), respectively. Methanediol and methoxymethanol are metastable and they undergo dehydration and de-alkoxylation when being isolated, respectively [2-5].

$$\underset{\text{Formaldehyde}}{HCHO} + \underset{\text{Water}}{H_2O} \rightleftharpoons \underset{\text{Methanediol}}{CH_2(OH)_2} \quad (1)$$

$$\underset{\text{Formaldehyde}}{HCHO} + \underset{\text{Methanol}}{CH_3OH} \rightleftharpoons \underset{\text{Methoxymethanol}}{HOCH_2OCH_3} \quad (2)$$

The hydration of formaldehyde and the formation of its oligomers has been studied in much more detail [6-10] in comparison to the alkoxylation of formaldehyde and their oligomerisation [11,12]. Over the years researchers have tried to determine the equilibrium constants of these reactions using NMR spectroscopy [6,5,12,13] and other experimental techniques, such as chemically enhanced absorption rate of solvation of formaldehyde gas coupled with high resolution densimetry [13] and vapour–liquid equilibrium modelling [14]. Even after many attempts, an accurate quantitative estimation of the chemical composition of the liquid phase of formaldehyde–methanol–water mixtures across broad temperature and concentration range is not yet established. This is mainly because of the number of different reactions involved (hydration, alkoxylation and

* Corresponding author.
E-mail address: Akshat.Tanksale@monash.edu (A. Tanksale).

https://doi.org/10.1016/j.molliq.2020.112444
0167-7322/

oligomerisation) and their high sensitivity towards concentration of solute, solvent composition, temperature, pressure, presence of salt, and pH of the system. These complexities and the difficulties in the identification of formaldehyde's different metastable complexes through various spectroscopic methods are why formaldehyde has also been referred to as an elusive molecule [15]. However, when formaldehyde is in low concentration (<2.5 wt%), nearly all of the dissolved formaldehyde is in the form of monomers [4,6,13]. To understand the basic solvation behaviour, we have considered low concentration formaldehyde solutions where oligomerisation is negligible.

Computationally, aqueous formaldehyde was initially studied at infinite dilution without hydration reaction [16,17]. It was found that a cage-like solvation structure around the molecule hinders its translation and rotation. Later, the reaction mechanism of hydration/dehydration [18-20] and molecular structure of aqueous solutions was reported [21-23]. The $n_0 \rightarrow \pi*$ electronic transition of formaldehyde in water has been studies using *ab initio* methods [24-26]. These studies are consistent with the theoretical predictions of carbonyl addition reaction mechanism [27-29]. Raman and infrared spectroscopic studies reported measured vibration frequencies in the aqueous formaldehyde solutions, but are subject to many contradictions as the assignments do not agree [30-32]. Structural and spectroscopic properties for methanediol conformers in water were reported using *ab initio* calculations [21]. Recently, vibration frequency data have been reported for a wide concentration range of formaldehyde-methanol-water solutions [33].

An improved understanding of low concentration formaldehyde-methanol-water mixtures has developed in recent years. The chemical distribution of formaldehyde across its metastable complexes was reported using NMR and other spectroscopic studies [5,6,33]. Now, there is a need to understand the liquid phase dynamics of these solutions. Liquid phase dynamics of the binary mixture of methanol-water has been a subject of many scientific investigations [34-41]. When methanol is mixed with water, it is homogeneous. However, microscopic ordering is observed in these mixtures because of molecular cluster formation [39,42,43]. A negative excess entropy is observed when methanol and water are mixed [44,45]. However, the overall exothermic nature makes the process of mixing spontaneous [44-46].

Recently, an alternative pathway for the formation of formaldehyde and poly (oxymethylene) dimethyl ethers are being explored by catalytic reduction of CO and CO_2 in a liquid phase [47-52]. Our group has reported a liquid phase catalytic processes for single step conversion of CO and H_2 into formaldehyde [48,49]. Methanol-water mixtures were used as a liquid phase where methanol concentration significantly affected the yield of formaldehyde. In pure methanol, an 8–10 membered ring/chain structure of methanol stabilises methoxymethanol [48]. However, the effect of methanol-water mixtures on the solvation of formaldehyde is yet to be understood. We focused the present study on understanding the strength of the interactions and distribution of methanol and water around methoxymethanol and methanediol. We aimed to identify any features of the local environment of solvated formaldehyde that can potentially affect the energetics of these mixtures. The present force-field based molecular dynamics study provides a good approximation of equilibrium micro-phase structure which could be further investigated by ab-initio calculations for these complex solutions with diverse applications.

2. Computational methodology

To understand the solvation dynamics and micro-phase of formaldehyde-methanol-water mixtures, classical molecular dynamics simulations were performed using GROMACS [53]. VMD (Visual Molecular Dynamics) [54] was used for visualisation of the trajectory data. OPLS–AA [55] force field parameters were used for methanediol, methoxymethanol, and methanol molecules whereas extended simple point charge (SPC/E) model was used for water. Particle Mesh Ewald (PME) method was used for the calculation of electrostatic and van der Walls interactions. A cut off radius of 1.2 nm was used for both electrostatic and van der Walls forces to optimise the computational effort. A distribution of solute and solvent molecules was randomly placed in a cubic computational box with periodic boundary condition and energy was minimised using the steepest descent method. Thereafter, temperature was generated using velocity rescale thermostat equilibrating the system for 100 ps. Density was optimised by an NPT run for 500 ps with Berendsen thermostat and barostat [56]. Finally, the system was allowed to reach dynamic equilibrium using the NVT ensemble with Nose-Hoover Chain thermostat [57]. The initial 2.5 ns of the molecular dynamics trajectory was used to ensure the equilibrium and the 7.5 ns after that was used for the visualisation. All the simulations had a time-step of 1 fs where velocities and coordinates were sampled after every 50 time-steps. Methanediol and methoxymethanol structure and their partial charges were taken from the online topology bank [58] where partial charges and structure are optimised by DFT [59] at B3LYP/6-31G* level of theory [58]. For simplicity, solutes are abbreviated as methanediol (md) and methoxymethanol (mm), and solvents as methanol (m), and water (w) where needed.

2.1. Composition

Methanol-water systems with formaldehyde as solute were simulated at 7 different compositions where the mole-fraction of methanol (x_m) varies from 0 to 1 with the number of molecules as shown in Table 1. The simulation box mimics the physical system of total 100 formaldehyde molecules dissolved in 5000 solvent molecules (different combination of methanol and water). As we know from Eqs. (1) & (2), methanediol or methoxymethanol was taken as formaldehyde by consuming one molecule of methanol or water, respectively. The number of methoxymethanol and methanediol molecules per 100 molecules of formaldehyde were calculated using the equilibrium constant ($K_{eq} = 40$) for an assumed reaction Eq. (3) as reported in a previous NMR study [6]. For every molecule of methanediol / methoxymethanol, one molecule of water / methanol was decreased from the solvent phase Eqs. (1) and (2), respectively). Table 1 shows list of all solute and solvent molecules for each system simulated. The density (ρ (g/cm^3)) and cubic box edge length (a (nm)) is reported in Table 1 after averaging over the last 200 ps of a 500 ps long NPT run. It is noted that x_m represents the mole-fraction of methanol in the methanol-water mixtures before formaldehyde solvation.

$$CH_2(OH)_2 + CH_3OH \rightleftharpoons (CH_3O)CH_2(OH) + H_2O$$
Methanediol Methanol Methoxymethanol Water (3)

2.2. Computational parameters and validation

Computational parameters for methanediol and methoxymethanol molecules used in the simulation are described

Table 1
Distribution of molecules in different simulation boxes along with density and cell size. 'a' is the cell dimension, whereas ρ is the density.

x_m	md	mm	m	w	ρ (g/cm^3)	a (nm)
0	100	0	0	4900	1.043	5.29
0.1	21	79	421	4479	1.014	5.47
0.3	6	94	1406	3494	0.955	5.83
0.5	3	97	2403	2497	0.901	6.18
0.7	1	99	3401	1499	0.854	6.52
0.9	0	100	4400	500	0.808	6.86
1	0	100	4900	0	0.790	7.00

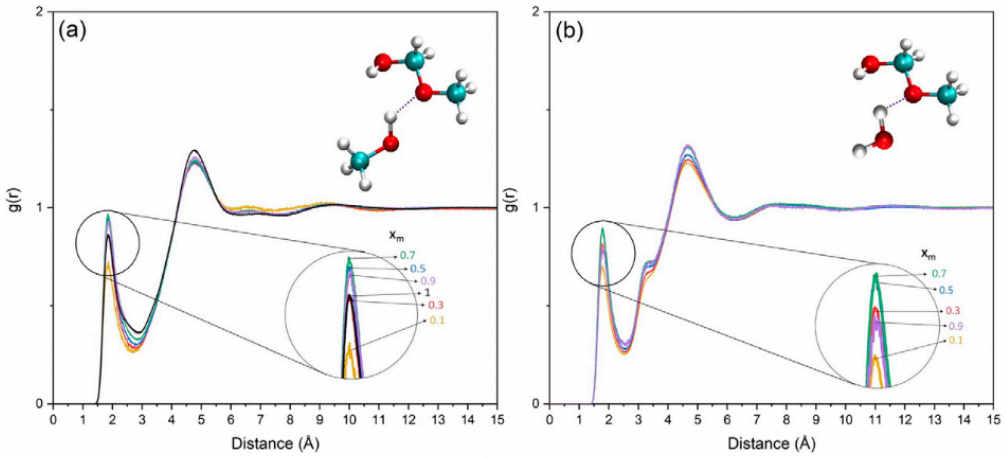

Fig. 2. Radial pair distribution function of ether oxygen of methoxymethanol and H of solvent. (a) $g(r)_{OC_{mm}-H_m}$ and (b) $g(r)_{OC_{mm}-H_w}$.

(a) methanol and (b) water. With increasing x_m, interaction between OC_{mm} and hydrogen of solvent increases till $x_m = 0.7$ and decreases afterwards. The g(r) within the first solvation shell is notably < 1 which suggests weak interactions. The g(r) and potential of mean force $W(r)$ are related as $(g(r) = \exp \frac{-W(r)}{K_B T})$ where $W(r)$ is work done to bring two particles from infinite separation to distance r. This suggests that the interaction is weaker than the bulk interaction. This can be explained by the presence of the methyl group that prevents the formation of a hydrogen bond with ether oxygen due to steric hindrance. Therefore, the ether oxygen behaves hydrophobic within the first solvation shell.

The hydroxyl group of mm can form 4 different types of hydrogen bonds, namely $O_{mm} - H_m$, $H_{mm} - O_m$, $O_{mm} - H_w$, and $H_{mm} - O_w$. There is also the possibility that while counting interaction between the oxygen of mm and hydrogen of water we count the hydrogen of another water molecule which is present nearby because the oxygen of the same molecule is interacting with the hydrogen of mm. Therefore, to avoid this, we plot the radial distribution function between the oxygen of solute and oxygen of the solvent (Fig. 3). A detailed discussion on radial pair distribution function between $O_{mm} - H_m$, $H_{mm} - O_m$, $O_{mm} - H_w$, and $H_{mm} - O_w$ pairs can be found in Appendix A.

Fig. 3 shows that increasing methanol mole-fraction in the solvent phase increases the strength of interaction in the first solvation shell with both methanol and water. However, strength in the second solvation shell remains nearly the same. After, $x_m = 0.7$, the strength of second solvation shell decreases and a finer first minimum is observed which implies a relatively more stable first solvation shell. Therefore, the addition of methanol favours the hydrophilic interactions.

3.2. Hydrogen bond

Theoretically, the maximum number of hydrogen bonds that can be formed between methoxymethanol and solvent is 5. Two bonds by each hydroxyl and ether oxygen and one bond by hydroxyl hydrogen. Similarly, the maximum number of hydrogen bonds that can be formed between methanediol and solvent is 6 - 3 bonds by each of the two hydroxyl groups. In Fig. 4, number of hydrogen bonds

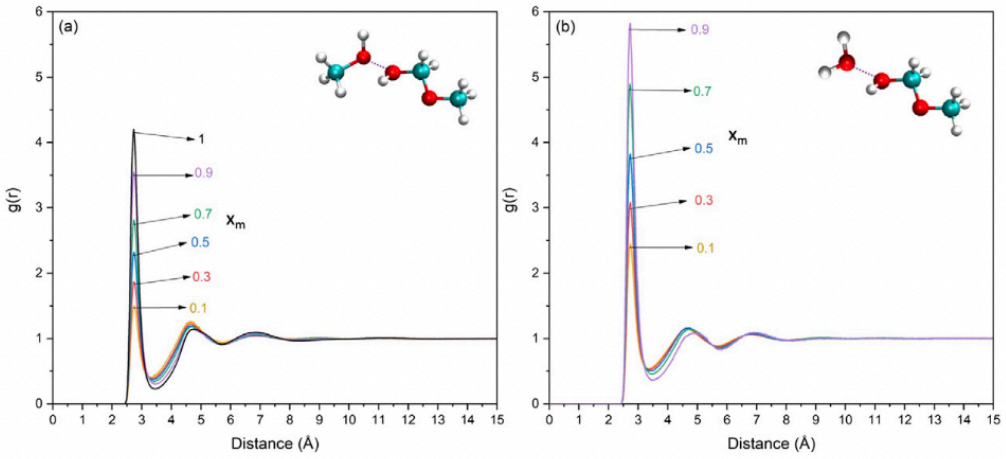

Fig. 3. Radial pair distribution function between the hydroxyl oxygen of methoxymethanol and oxygen of solvent (a) methanol and (b) water.

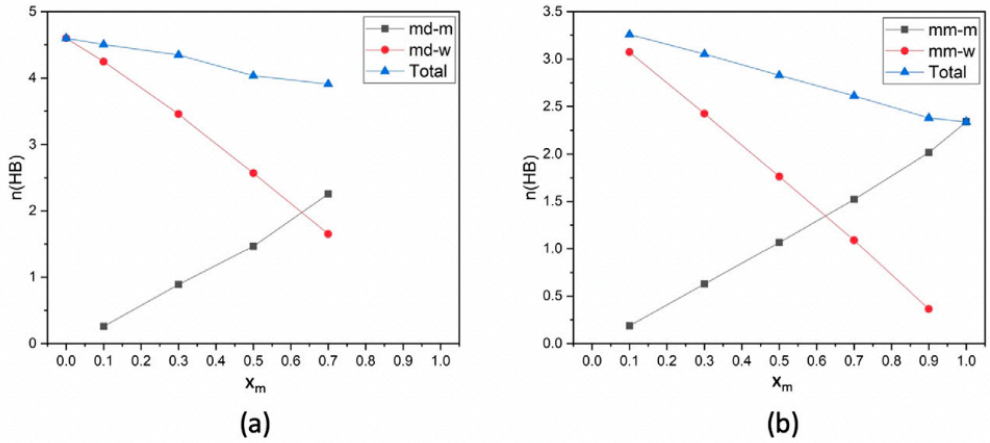

Fig. 4. Number of hydrogen bonds per molecule between solute and solvent with respect to increasing methanol concentration.

per molecule of solute ((a) md and (b) mm), averaged over the trajectory is plotted against x_m. It can be seen that, with increasing methanol concentration in the solvent phase, the number of hydrogen bonds with methanol increases. The total number of hydrogen bonds between solute and solvent decreases by increasing x_m.

The frequency of the formation of hydrogen bonds and their lifetime has a significant effect on the structure of the solvation shell. Although the size of the solvation shell is important as it affects the mobility and stability of the solute, the strength of hydrogen bonding is equally important since it affects the local electronic behaviour, which in turn, may affect the affinity of the solute towards a potential electrophile/nucleophile. Fig. 5 shows the lifetime of hydrogen bonds formed between solute and solvent.

Increasing methanol mole-fraction increases the lifetime of hydrogen bonds. This phenomenon is expected when a polar co-solvent is present with water as described below.

Methanol and water stabilise each other through their polar interactions while one being hydrogen bonded to the solute. We can also see that the lifetime of hydrogen bonds for mm ($x_m = 0.1$) with water is lower than what is observed for md in pure water.

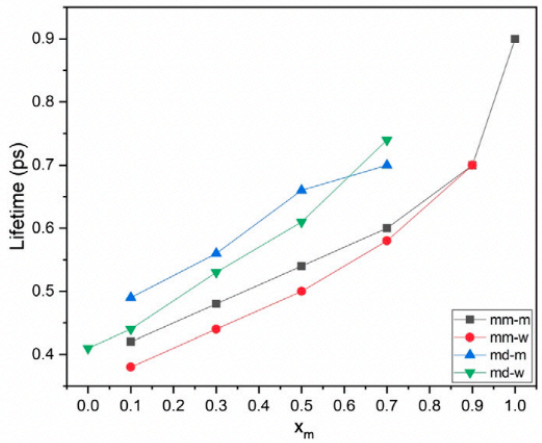

Fig. 5. Lifetime in ps of hydrogen bonding of solute with solvent.

This shows that the strength of hydrogen bonding between mm and water in $x_m = 0.1$ methanol-water mixture is less than that of md and pure water. Thereafter, the lifetime increases linearly with increasing x_m till $x_m = 0.7$. Interestingly, there is a sudden jump in mm-methanol lifetime from $x_m = 0.9$ to pure methanol. Our earlier CPMD study suggested that there is a 8–10 member ring/chain structure of methanol surrounding mm in pure methanol [48] and this structure should provide more stability and support to the hydrogen bonded molecules. Moreover, pure methanol exists in the form of hydrogen bonded chains of 3–10 molecules [37,39,61], and on the addition of even a small amount of water can significantly break these chains. Similar behaviour was observed in a recent X-ray absorption spectroscopy experiments by Lam et al. [43]. With the addition of a small amount of water, a significant change in hydrogen bonding behaviour of methanol was observed in their experiments. From Fig. 4, we observed that on increasing x_m, the total number of hydrogen bonds decreases between solute and solvent. However, from Fig. 5, we see that the lifetime of each hydrogen bond increases, which complements the observed increase in g(r) on increasing x_m. This increase in the lifetime of hydrogen bonding is a result of increased activation energy to break the hydrogen bond [45]. Table 3 shows the activation energy (KJ/mol) to break the hydrogen bond between solute and solvent, and this explains the stronger hydrophilic interactions on increasing the amount of co-solvent.

The average number of hydrogen bonds formed between solute and solvent for each of the mixtures has been calculated by taking the weighted average (Avg_{HB}) of all hydrogen bonds formed per molecule by both methanediol and methoxymethanol Eq. (4). As seen in Fig. 6a, average number of hydrogen bonds per solute molecule decreases from 4.6 (pure water) to 2.34 (pure methanol) in

Table 3
Activation energy (KJ/mol) for formation of hydrogen bond between solute and solvent.

x_m	md-m	md-w	mm-m	mm-w
0		9.534		
0.1	10.043	10.303	9.742	10.11
0.3	11.040	11.351	10.913	11.148
0.5	11.742	12.246	11.567	11.936
0.7	12.117	12.901	12.158	12.537
0.9			12.814	13.24
1			13.581	

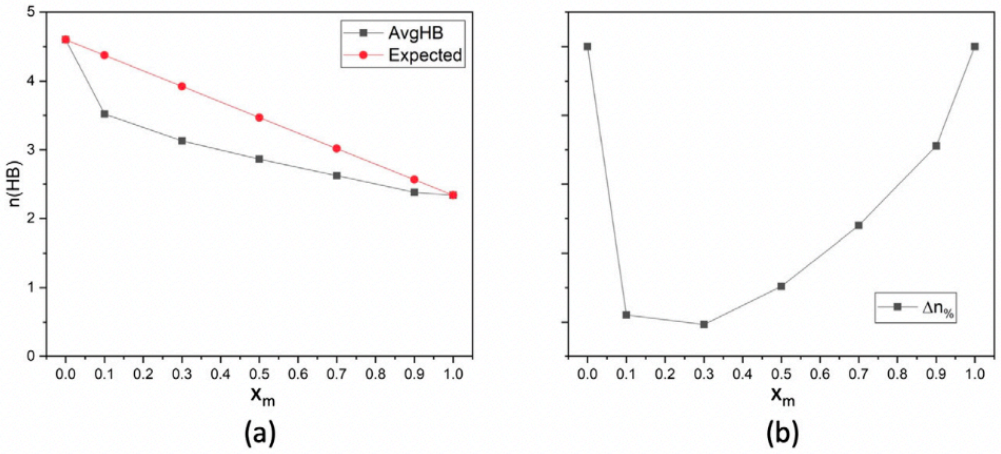

Fig. 6. Deviation observed in hydrogen bonding behaviour. (a) Average number of hydrogen bonds and (b) percentage deviation ($\Delta n\%$).

the solvent phase. A non-linear decrement indicates the presence of non-homogeneity and is also seen in methanol-water mixtures elsewhere [35,60]. However, we see that Avg_{HB} drops from the expected value in methanol-water mixtures. The percentage drop from the expected value ($\Delta n_{\%}$, Eq. (5)) has been plotted against x_m in Fig. 6b.

$$Avg_{HB} = \frac{n(md)}{n(md)+n(mm)} \times n(HB)_{md} + \frac{n(mm)}{n(md)+n(mm)} \times n(HB)_{mm} \quad (4)$$

$$\Delta n_{\%} = \frac{n(HB)_{Avg} - n(HB)_{Expected}}{n(HB)_{Expected}} \times 100 \quad (5)$$

3.3. Hydrophobic interaction

Amphiphile -like molecules have hydrophilic and hydrophobic sites within them. As a result, they can orient themselves within the aqueous phase to maximise hydrophilic interactions in order to minimise energy. In our system, we have methanediol, methoxymethanol, and methanol that can display amphiphile-like behaviour. The CH_2 group in methanediol, the CH_3 in methanol and the CH_3 and CH_2 groups in methoxymethanol may act as hydrophobic regions for the solute. Fig. 7 a & b show g(r) C1 of methoxymethanol with C of methanol and O of water, respectively (refer to Table 2 for the atom names). We can see that on increasing methanol mole-fraction the interaction of $C1_{mm}$ increases with both methanol and water.

On increasing x_m, despite the fact that the amount of water in the system decreases, the strength of interaction of the solute with water increases significantly in comparison to methanol, where only a small change is observed. Therefore, at low x_m better hydrophobic clustering is probable. Fig. 8 a & b shows the g(r) of $C2_{mm}$ with C of methanol and O of water, respectively. Contrary to what was observed in the case of $C1_{mm}$, here the strength remains nearly the same for both cases of water and methanol when considering the first solvation shell. Therefore, the hydrophilic effect where methanol is more attracted to the methylene carbon of

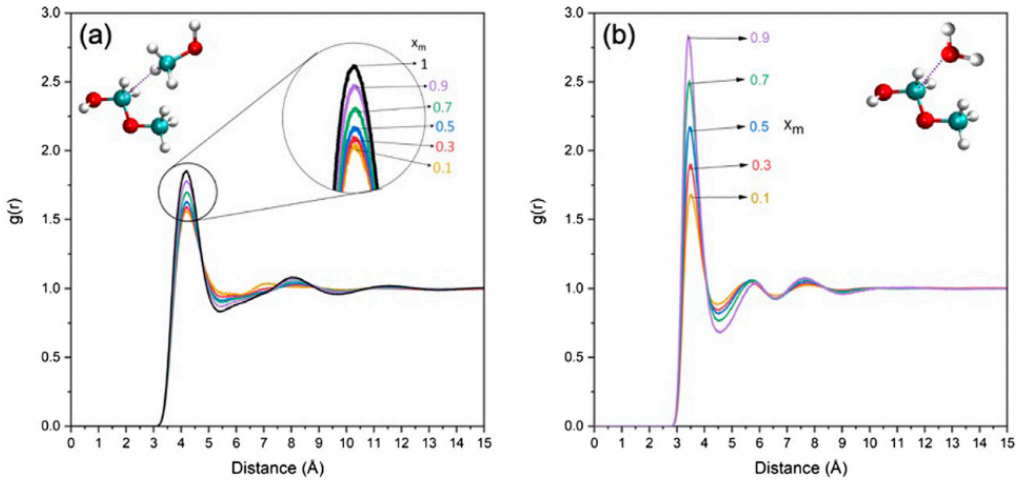

Fig. 7. Radial pair distribution function between $C1_{mm}$ with (a) C of methanol and (b) O of water.

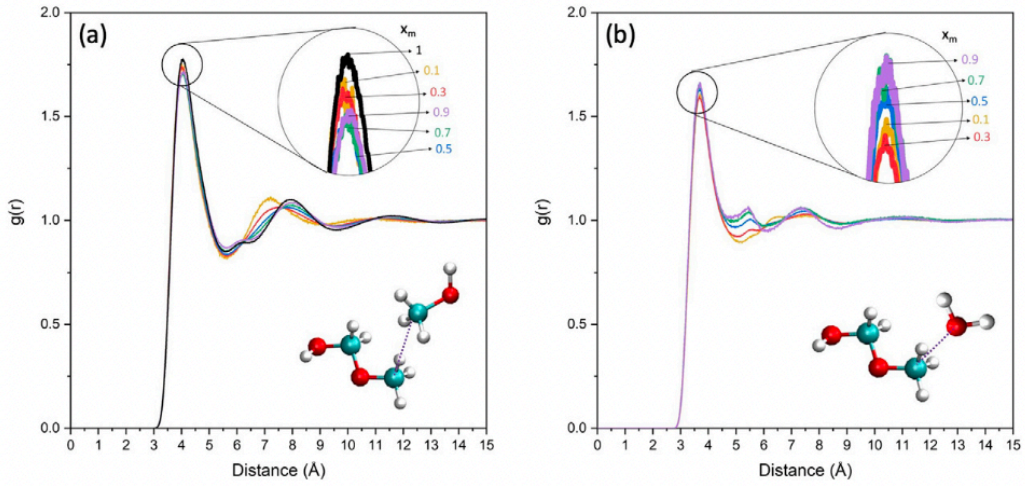

Fig. 8. Radial pair distribution function between $C2_{mm}$ with (a) C of methanol and (b) O of water.

methoxymethanol is effective at low mole-fractions of methanol. It is noteworthy to mention that a hydrophobic clustering around the ether oxygen is likely due to interactions that are weaker than bulk interactions, analogous to the explanation with respect to the hydrophilic behaviour (Section 3.1).

Fig. 9 a & b show g(r) of methoxymethanol with methanol and water, respectively. Interaction with methanol at low $x_m(= 0.1, 0.3)$ is higher and thereafter, remains more or less the same upon increasing x_m. However, the interaction with water increases significantly upon increasing x_m (Fig. 9a).

Therefore, more extensive hydrophobic interactions are observed at low x_m and the strength of hydrophilic interaction with water increases on increasing x_m (Fig. 9 b). The coordination number methanol and water around mm can be found by integrating these radial distribution functions within the first solvation shell and multiplying by the total number of pairs available in the system. The total number of methanol and water molecules within the first solvation shell (on integrating center of mass g(r)) of methoxymethanol are given in Table 4.

3.4. Spatial distribution and micro-phase ordering

The spatial distribution functions were calculated for the density determination of methanol and water around methoxymethanol. These functions represent the probability distribution of methanol and water within a specific distance from methoxymethanol (Fig. 10). In the case of $x_m = 0.1$ (Fig. 10a), due to the strong hydrophobic interactions a considerable amount of methanol is present within the solvation shell surrounding the hydrophobic group of the solute. On increasing methanol ($x_m = 0.3$, Fig. 10b), we see that ether group is surrounded by methanol and the methylene group is also surrounded by methanol as the strength of interaction increases on increasing methanol concentration. This clearly represents a case of hydrophobic clustering of methanol around formaldehyde in low methanol mole-fraction systems. This hydrophobic clustering is probably a manifestation of entropic effects which helps to stabilise the solute at low mole-fraction compositions. Thereafter, a transition from mostly water to mostly methanol in first solvation shell takes place. In the case of equimolar composition (Fig. 10c),

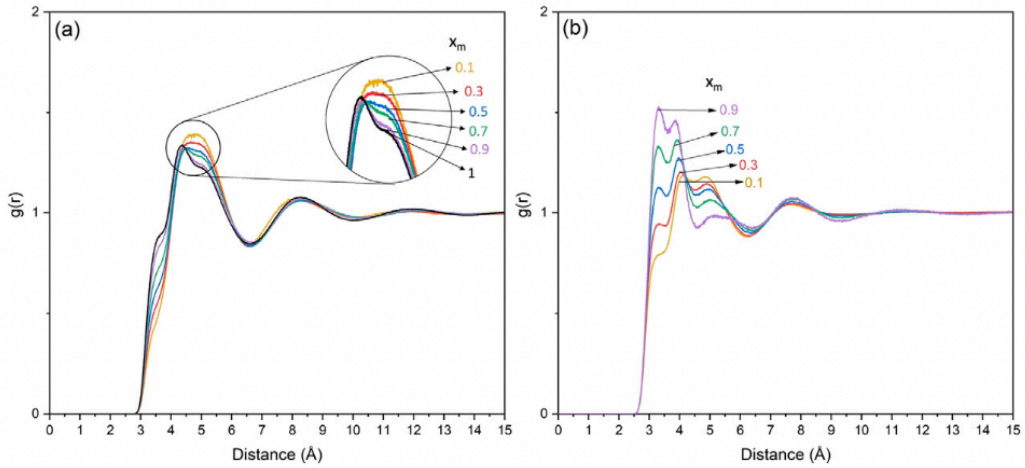

Fig. 9. Center of mass radial distribution function between methoxymethanol and (a) methanol and (b) water.

Table 4
Number of molecules of methanol and water within the first solvation shell around methoxymethanol, calculated by integrating the center of mass radial distribution functions in Fig. 9 a & b.

x_m	m	w	Total
0.1	2.66	24.79	27.45
0.3	7.60	16.30	23.90
0.5	11.27	10.48	21.75
0.7	13.79	5.74	19.53
0.9	15.99	1.65	17.63
1	16.85		16.85

water is present only in the hydrophilic sites, whereas the first solvation shell is filled with methanol. At $x_m = 0.7$ (Fig. 10d) we can see a small red area representing water around the hydroxyl group which is due to strong hydrophilic interactions at the increased co-solvent concentration, despite it possessing a low mole-fraction of water. At $x_m \geq 0.9$ nearly all the space of the first solvation shell is occupied by methanol (not shown).

The free energy of solvation was calculated using the alchemical free energy methods by simulating a series of physically unrealisable intermediate states. The abstract intermediate states are non-observable and were defined using a decoupling parameter, λ. The free energy was found to vary between -25 KJ/mol to -30 KJ/mol within the composition range of $x_m = 0.3$ to $x_m = 0.9$. The enthalpy of solvation (ΔH_{sol}) was found to be around -55 KJ/mol which is due to the hydrogen bonding between the solute and the solvent. However, the entropic contribution ($-T\Delta s$, around 27 KJ/mol) is due to the clustering of methanol and water around methoxymethanol.

4. Conclusion

A computational model for classical molecular dynamics study of low concentration formaldehyde-methanol-water mixtures is presented. Formaldehyde in methanol-water mixtures was simulated as methanediol and/or methoxymethanol depending upon the methanol-water mixture composition. The radial distribution function g(r) of previously published data was validated. For the hydroxyl group, the strength of hydrophilic interaction with solvent increases on increasing x_m. However, weaker than bulk interactions were observed within the first solvation shell of the ether oxygen. These weak interactions of ether oxygen result from steric hindrance by the methyl groups of methoxymethanol. The extent of hydrogen bonding with solvated formaldehyde and methanol-water mixtures is less than expected. This behaviour is expected to influence the bulk hydrogen bonding network and can potentially affect the energetics of these solutions. The lifetime of hydrogen bonding increases on the addition of methanol and is attributed to the increased activation energy for breaking the hydrogen bond. However, for $x_m = 0.1$, the lifetime of hydrogen bonding between mm and w is less than that between md and w in pure water. The lifetime decreases unexpectedly from that in case of pure methanol on the addition of a small quantity of water (at $x_m = 0.9$). This might

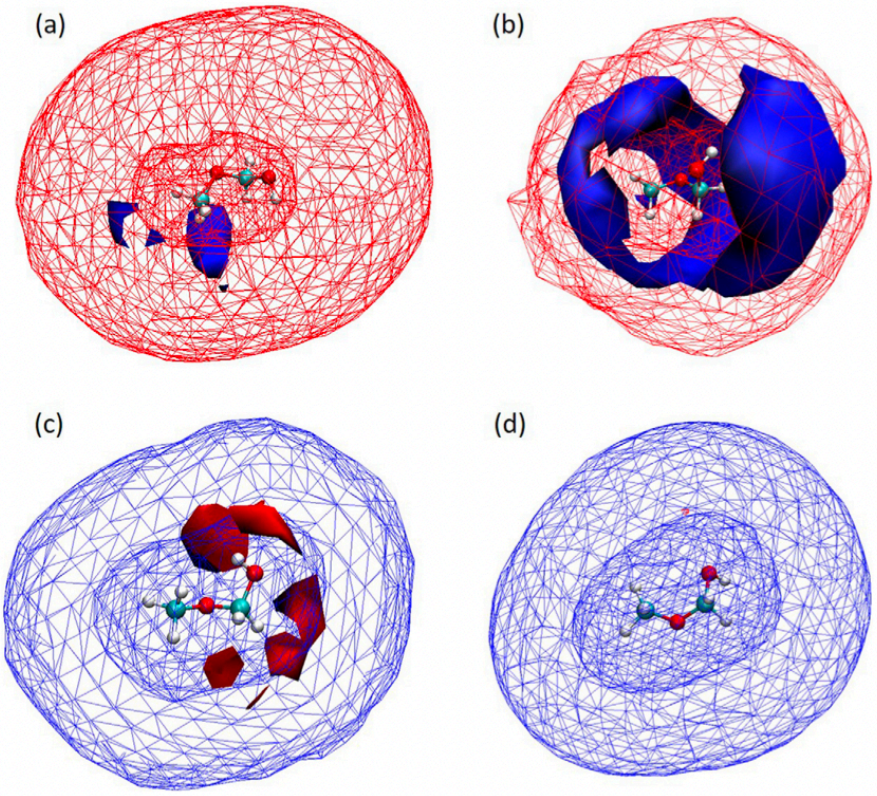

Fig. 10. Spatial distribution function of methanol and water around methoxymethanol where methanol is blue and water is red iso-surface and/or wireframe. x_m = (a) 0.1 (iso-value = 0.02), (b) 0.3 (iso-value = 0.035), (c) 0.5 (iso-value = 0.045), and (d) 0.7 (iso-value = 0.045).

be a consequence of destabilisation of methanol ring/chain structure that is observed around methoxymethanol in pure methanol. Due to a strong hydrophobic effect, methanol clusters around the hydrophobic end of methoxymethanol at low methanol mole-fractions. At equimolar mixture composition, water is more likely to occupy the hydrophilic sites. As formaldehyde in methanol-water mixtures is used for various chemical and biological reactions, this varying clustering behaviour might have a significant effect on the reactivity of the solvated formaldehyde. This model may provide a base for detailed *ab initio* study of the molecular structure of these mixtures.

CRediT authorship contribution statement

Swarit Dwivedi: Data Curation, Validation, Visualisation, Methodology, Formal analysis, Writing - original draft. **Samir H. Mushrif:** Conceptualization, Methodology, Formal analysis, Funding acquisition, Writing - review & editing. **Alan L. Chaffee:** Formal analysis, Funding acquisition, Writing - review & editing. **Akshat Tanksale:** Conceptualization, Formal analysis, Funding acquisition, Writing - review & editing.

Declaration of competing interest

The authors declare that they have no known competing financial interests or personal relationships that could have appeared to influence the work reported in this paper.

Acknowledgments

This research was funded by the Australian Government through the Australian Research Council's Discovery Projects funding scheme (project DP170104017). The authors gratefully acknowledge a generous allocation of computer resources through the Monash eResearch Centre.

Appendix A. Hydrophilic interactions

Fig. A.11 shows the radial distribution functions between hydroxyl group of mm and solvent. Hydroxyl H of solute and O of methanol and water are shown in Fig. A.11 (a) and (b), respectively, whereas, the O of solute and H of water and methanol are shown in Fig. A.11 (c) and (d), respectively. Strong interactions between hydroxyl groups are observed and increase with the increase in x_m. A notably bigger second solvation shell is observed with water and a similar trend is also observed in case of md (Fig. A.12). Methanol H and O has g(r) close to 1 in second solvation shell with hydroxyl O and H of methoxymethanol.

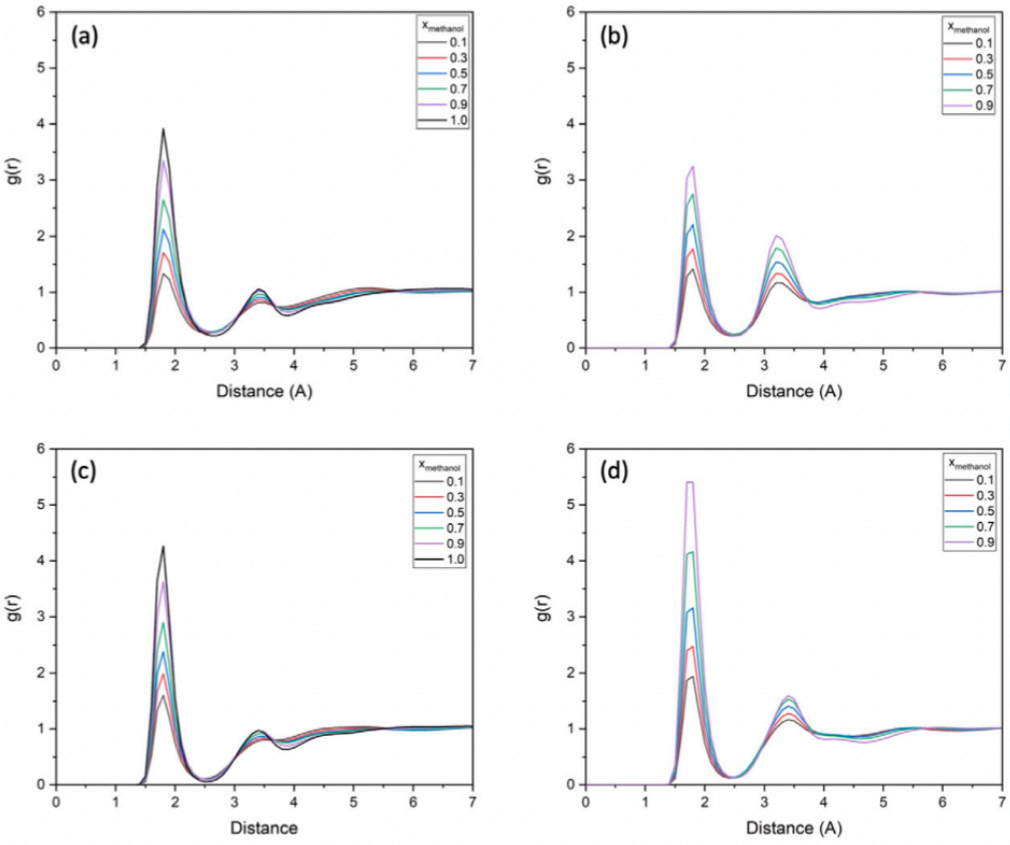

Fig. A.11. Radial pair distribution function of hydroxyl group of methoxymethanol and hydroxyl group of solvent. (a) $g(r)_{OH_{mm}-O_m}$, (b) $g(r)_{OH_{mm}-H_w}$, (c) $g(r)_{HO_{mm}-O_m}$, and $g(r)_{HO_{mm}-O_w}$.

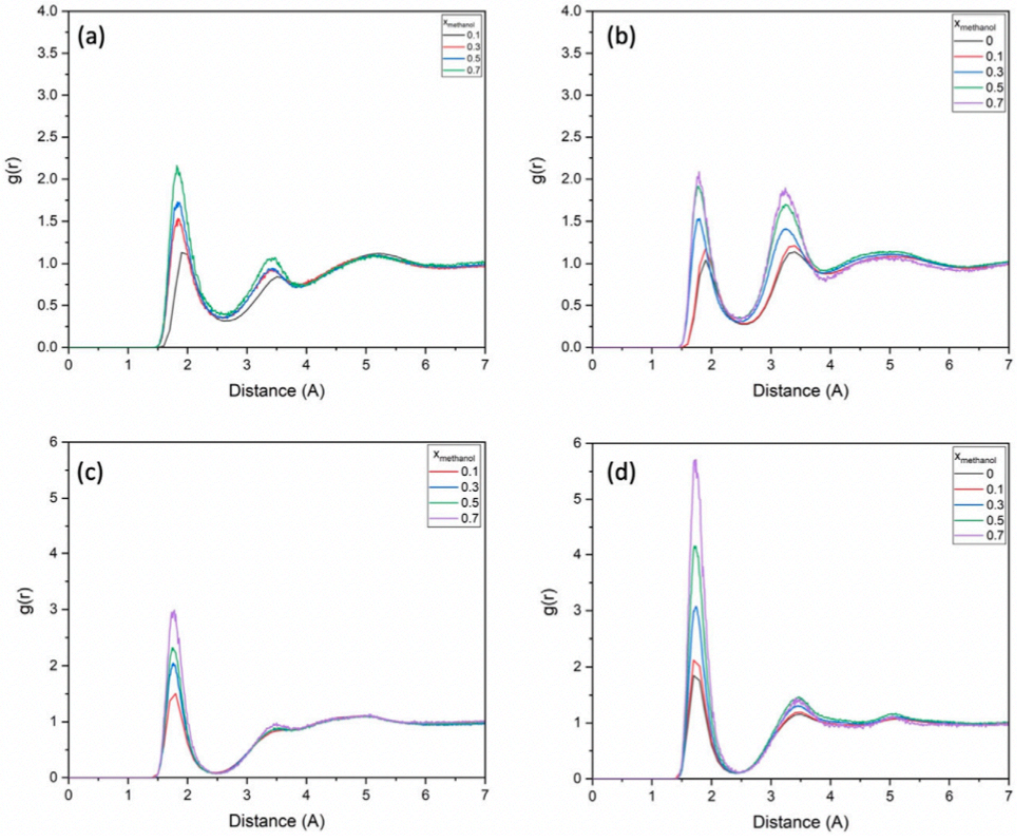

Fig. A.12. Radial pair distribution function of hydroxyl group of methanediol and hydroxyl group of solvent. (a) $g(r)_{OH_{md}-O_m}$, (b) $g(r)_{OH_{md}-H_w}$, (c) $g(r)_{HO_{md}-O_m}$, and $g(r)_{HO_{md}-O_w}$.

On the other hand, interaction with water in the second solvation shell increases on the addition of methanol. Therefore, a more strongly attached water layer is observed on the addition of water at the same time as the amount of water in the second solvation shell decreases.

The minimum after the first solvation shell is similar for all composition which means a similar distinction between first and second solvation shell. However, for the second solvation shell, a lower minima is observed for higher x_m. This signifies a finer second solvation shell for higher methanol mole-fraction, notably, in case of $x_m = 0.9\&1$. The solvation shell of hydroxyl groups is separated more precisely than seen in ether oxygen.

References

[1] A.M. Bahmanpour, A. Hoadley, A. Tanksale, Critical review and exergy analysis of formaldehyde production processes, Rev. Chem. Eng. 30 (6) (2014) 583–604.
[2] J. Winkelman, M. Ottens, A. Beenackers, The kinetics of the dehydration of methylene glycol, Chem. Eng. Sci. 55 (11) (2000) 2065–2071.
[3] J. Winkelman, O. Voorwinde, M. Ottens, A. Beenackers, L. Janssen, Kinetics and chemical equilibrium of the hydration of formaldehyde, Chem. Eng. Sci. 57 (19) (2002) 4067–4076.
[4] F. Walker, The state of formaldehyde in aqueous solutions, J. Phys. Chem. 35 (4) (1931) 1104–1113.
[5] M. Rivlin, U. Eliav, G. Navon, NMR studies of the equilibria and reaction rates in aqueous solutions of formaldehyde, J. Phys. Chem. B 119 (12) (2015) 4479–4487.
[6] K.Z. Gaca, J.A. Parkinson, L. Lue, J. Sefcik, Equilibrium speciation in moderately concentrated formaldehyde-methanol-water solutions investigated using 13C and 1H nuclear magnetic resonance spectroscopy, Ind. Eng. Chem. Res. 53 (22) (2014) 9262–9271.
[7] A.A. Zavitsas, M. Coffiner, T. Wiseman, L.R. Zavitsas, Reversible hydration of formaldehyde. Thermodynamic parameters, J. Phys. Chem. 74 (14) (1970) 2746–2750.
[8] H. Sutton, T. Downes, Rate of hydration of formaldehyde in aqueous solution, J. Chem. Soc. Chem. Commun. (1) (1972) 1–2.
[9] G.M. Maggiora, I.H. Williams, Intermolecular interaction energies from minimal-basis SCF calculations. Interactions pertinent to formaldehyde hydration, J. Mol. Struct. THEOCHEM 88 (1-2) (1982) 23–35.
[10] D.R. Kent, IV, S.L. Widicus, G.A. Blake, W.A. Goddard, III, A theoretical study of the conversion of gas phase methanediol to formaldehyde, J. Chem. Phys. 119 (10) (2003) 5117–5120.
[11] H.-G. Schecker, G. Schulz, Untersuchungen zur Hydratationskinetik von Formaldehyd in wäßriger Lösung, Z. Phys. Chem. 65 (1_4) (1969) 221–224.
[12] I. Hahnenstein, H. Hasse, C.G. Kreiter, G. Maurer, 1H-and 13C-NMR-spectroscopic study of chemical equilibria in solutions of formaldehyde in water, deuterium oxide, and methanol, Ind. Eng. Chem. Res. 33 (4) (1994) 1022–1029.
[13] I. Hahnenstein, M. Albert, H. Hasse, C.G. Kreiter, G. Maurer, NMR spectroscopic and densimetric study of reaction kinetics of formaldehyde polymer formation in water, deuterium oxide, and methanol, Ind. Eng. Chem. Res. 34 (2) (1995) 440–450.
[14] M. Albert, I. Hahnenstein, H. Hasse, G. Maurer, Vapor-liquid equilibrium of formaldehyde mixtures: new data and model revision, AICHE J. 42 (6) (1996) 1741–1752.

[15] C. Barrientos, P. Redondo, H. Martínez, A. Largo, Computational prediction of the spectroscopic parameters of methanediol, an elusive molecule for interstellar detection, Astron. J. 784 (2) (2014) 132.
[16] S. Tolosa, J. Sansón, Molecular dynamics study of infinitely dilute aqueous solutions of small biological molecules. Calculation of the static and dynamic properties of formaldehyde, Chem. Phys. 213 (1-3) (1996) 203–210.
[17] S. Tolosa, J. Sansón, MD study of an infinitely dilute aqueous solution of formaldehyde using different ab initio potentials, Chem. Phys. 223 (2-3) (1997) 251–257.
[18] N. Matubayasi, S. Morooka, M. Nakahara, H. Takahashi, Chemical equilibrium of formaldehyde and methanediol in hot water: free-energy analysis of the solvent effect, J. Mol. Liq. 134 (1-3) (2007) 58–63.
[19] S. Böhm, D. Antipova, J. Kuthan, Methanediol decomposition mechanisms: a study considering various ab initio approaches, Int. J. Quantum Chem. 58 (1) (1996) 47–55.
[20] M. Mugnai, G. Cardini, V. Schettino, C.J. Nielsen, Ab initio molecular dynamics study of aqueous formaldehyde and methanediol, Mol. Phys. 105 (17-18) (2007) 2203–2210.
[21] P. Delcroix, M. Pagliai, G. Cardini, D. Bgu, B. Hanoune, Structural and spectroscopic properties of methanediol in aqueous solutions from quantum chemistry calculations and ab initio molecular dynamics simulations, Chem. A Eur. J. 119 (2) (2015) 290–298.
[22] V.K. Yadav, Hydrogen bond dynamics and vibrational spectral diffusion in aqueous solution of formaldehyde: a first principles molecular dynamics study, Theor. Chem. Accounts 137 (10) (2018) 129.
[23] M. Rodler, Ab initio studies of the structures and energies of methanediol and 1, 1-ethenediol, Chem. Phys. 105 (3) (1986) 345–353.
[24] H. Fukunaga, K. Morokuma, Cluster and solution simulation of formaldehyde-water complexes and solvent effect on formaldehyde 1 (n,. pi.*) transition, J. Phys. Chem. 97 (1) (1993) 59–69.
[25] Z. Xu, S. Matsika, Combined multireference configuration interaction/molecular dynamics approach for calculating solvatochromic shifts: application to the n $\rightarrow \pi^*$ electronic transition of formaldehyde, Chem. A Eur. J. 110 (43) (2006) 12035–12043.
[26] A. Öhrn, G. Karlström, A theoretical study of the solvent shift to the transition in formaldehyde with an effective discrete quantum chemical solvent model including non-electrostatic perturbation, Mol. Phys. 104 (19) (2006) 3087–3099.
[27] I.H. Williams, G.M. Maggiora, R.L. Schowen, Theoretical models for mechanism and catalysis in carbonyl addition, J. Am. Chem. Soc. 102 (27) (1980) 7831–7839.
[28] I.H. Williams, D. Spangler, D.A. Femec, G.M. Maggiora, R.L. Schowen, Theoretical models for transition-state structure and catalysis in carbonyl addition, J. Am. Chem. Soc. 102 (21) (1980) 6619–6621.
[29] I.H. Williams, Theoretical modelling of specific solvation effects upon carbonyl addition, J. Am. Chem. Soc. 109 (21) (1987) 6299–6307.
[30] G. Möhlmann, Raman spectra of aqueous solutions of formaldehyde and its oligomers, J. Raman Spectrosc. 18 (3) (1987) 199–203.
[31] N. Lebrun, P. Dhamelincourt, C. Focsa, B. Chazallon, J. Destombes, D. Prevost, Raman analysis of formaldehyde aqueous solutions as a function of concentration, J. Raman Spectrosc. 34 (6) (2003) 459–464.
[32] B. Hanoune, L. Paccou, P. Delcroix, Y. Guinet, Raman identification of H2CO in aqueous solutions, J. Raman Spectrosc. 42 (5) (2011) 1202–1204.
[33] K.Z. Gaca-Zajac, B.R. Smith, A. Nordon, A.J. Fletcher, K. Johnston, J. Sefcik, Investigation of IR and Raman spectra of species present in formaldehyde-water-methanol systems, Vib. Spectrosc. 97 (2018) 44–54.
[34] L. Dougan, S. Bates, R. Hargreaves, J. Fox, J. Crain, J. Finney, V. Reat, A. Soper, Methanol-water solutions: a bi-percolating liquid mixture, J. Chem. Phys. 121 (13) (2004) 6456–6462.
[35] J. Pang, H. Yang, J. Ma, R. Cheng, Solvation behaviors of N-isopropylacrylamide in water/methanol mixtures revealed by molecular dynamics simulations, J. Phys. Chem. B 114 (26) (2010) 8652–8658.
[36] N.F. van der Vegt, D. Nayar, The hydrophobic effect and the role of cosolvents, J. Phys. Chem. B 121 (43) (2017) 9986–9998.
[37] S. Dixit, A. Soper, J.L. Finney, J. Crain, Water structure and solute association in dilute aqueous methanol, Europhys. Lett. 59 (3) (2002) 377.
[38] T. Sato, A. Chiba, R. Nozaki, Hydrophobic hydration and molecular association in methanol-water mixtures studied by microwave dielectric analysis, J. Chem. Phys. 112 (6) (2000) 2924–2932.
[39] J.-H. Guo, Y. Luo, A. Augustsson, S. Kashtanov, J.-E. Rubensson, D.K. Shuh, H. Ågren, J. Nordgren, Molecular structure of alcohol-water mixtures, Phys. Rev. Lett. 91 (15) (2003) 157401.
[40] M. Nagasaka, K. Mochizuki, V. Leloup, N. Kosugi, Local structures of methanol-water binary solutions studied by soft X-ray absorption spectroscopy, J. Phys. Chem. B 118 (16) (2014) 4388–4396.
[41] K. Yoshida, S. Ishida, T. Yamaguchi, Hydrogen bonding and clusters in supercritical methanol-water mixture by neutron diffraction with H/D substitution combined with empirical potential structure refinement modelling, Mol. Phys. (2019) 1–14.
[42] S. Dixit, J. Crain, W. Poon, J. Finney, A. Soper, Molecular segregation observed in a concentrated alcohol-water solution, Nature 416 (6883) (2002) 829.
[43] R.K. Lam, J.W. Smith, R.J. Saykally, Communication: Hydrogen Bonding Interactions in Water-Alcohol Mixtures from X-ray Absorption Spectroscopy, 2016.
[44] R.M. Levy, E. Gallicchio, Computer simulations with explicit solvent: recent progress in the thermodynamic decomposition of free energies and in modeling electrostatic effects, Annu. Rev. Phys. Chem. 49 (1) (1998) 531–567.
[45] D. van der Spoel, P.J. van Maaren, P. Larsson, N. Tîmneanu, Thermodynamics of hydrogen bonding in hydrophilic and hydrophobic media, J. Phys. Chem. B 110 (9) (2006) 4393–4398.
[46] H. Renon, J.M. Prausnitz, Local compositions in thermodynamic excess functions for liquid mixtures, AICHE J. 14 (1) (1968) 135–144.
[47] L.E. Heim, H. Konnerth, M.H. Prechtl, Future perspectives for formaldehyde: pathways for reductive synthesis and energy storage, Green Chem. 19 (10) (2017) 2347–2355.
[48] A.M. Bahmanpour, A. Hoadley, S.H. Mushrif, A. Tanksale, Hydrogenation of carbon monoxide into formaldehyde in liquid media, ACS Sustain. Chem. Eng. 4 (7) (2016) 3970–3977.
[49] A.M. Bahmanpour, A. Hoadley, A. Tanksale, Formaldehyde production via hydrogenation of carbon monoxide in the aqueous phase, Green Chem. 17 (6) (2015) 3500–3507.
[50] F.L. Chan, G. Altinkaya, N. Fung, A. Tanksale, Low temperature hydrogenation of carbon dioxide into formaldehyde in liquid media, Catal. Today 309 (2018) 242–247.
[51] M. Li, Y. Long, Z. Deng, H. Zhang, X. Yang, G. Wang, Ruthenium trichloride as a new catalyst for selective production of dimethoxymethane from liquid methanol with molecular oxygen as sole oxidant, Catal. Commun. 68 (2015) 46–48.
[52] N. Schmitz, E. Ströfer, J. Burger, H. Hasse, Conceptual design of a novel process for the production of poly (oxymethylene) dimethyl ethers from formaldehyde and methanol, Ind. Eng. Chem. Res. 56 (40) (2017) 11519–11530.
[53] D. Van Der Spoel, E. Lindahl, B. Hess, G. Groenhof, A.E. Mark, H.J. Berendsen, GROMACS: fast, flexible, and free, J. Comput. Chem. 26 (16) (2005) 1701–1718.
[54] W. Humphrey, A. Dalke, K. Schulten, VMD: visual molecular dynamics, J. Mol. Graph. 14 (1) (1996) 33–38.
[55] D. Kony, W. Damm, S. Stoll, W.F. Van Gunsteren, An improved OPLS-AA force field for carbohydrates, J. Comput. Chem. 23 (15) (2002) 1416–1429.
[56] H.J. Berendsen, J. v. Postma, W.F. van Gunsteren, A. DiNola, J. Haak, Molecular dynamics with coupling to an external bath, J. Chem. Phys. 81 (8) (1984) 3684–3690.
[57] G.J. Martyna, M.L. Klein, M. Tuckerman, Nosé-Hoover chains: the canonical ensemble via continuous dynamics, J. Chem. Phys. 97 (4) (1992) 2635–2643.
[58] A.K. Malde, L. Zuo, M. Breeze, M. Stroet, D. Poger, P.C. Nair, C. Oostenbrink, A.E. Mark, An automated force field topology builder (ATB) and repository: version 1.0, J. Chem. Theory Comput. 7 (12) (2011) 4026–4037.
[59] M.C.H. Wolfram Koch, A Chemist's Guide to Density Functional Theory, 2nd Edition, Wiley. 2001.
[60] A. Luzar, D. Chandler, Hydrogen-bond kinetics in liquid water, Nature 379 (6560) (1996) 55.
[61] L. Pauling, The Nature of the Chemical Bond., 260. Cornell university press Ithaca, NY, 1960.

Chapter 4

4 Molecular cluster in formaldehyde-methanol-water mixtures revealed by High-intensity, High-q Small-Angle Neutron Scattering

4.1 Overview

In chapter 3, we studied the micro-phase structure of formaldehyde-methanol-water mixtures. Based on the solvation shell of methoxymethanol across varying methanol-water compositions, we extend the previously reported hypothesis across a range of methanol-water concentrations. We report that methanol clusters hydrophobically around methoxymethanol at low methanol compositions (Fig. 1). A better yield than equimolar mixtures is also observed at low methanol compositions. Our previously published *ab intio* molecular dynamics study showed an 8-10 membered ring/chain structure surrounds methoxymethanol, stabilising methoxymethanol. However, water is more likely to occupy hydrophilic sites at equimolar and compositions (Figure 1) and hence prevents the formation of the ring/chain structure. Thus, the lower stability of the products around the equimolar composition may influence the equilibrium of the catalytic reaction. However, there is no experimental evidence of such hydrophobic molecular clusters. Understanding the structure of formaldehyde–methanol-water mixtures at molecular length scales is a challenge to the contemporary experimental techniques due to their dynamical and chemical nature. The liquid-phase molecular structure of methanol-water mixtures has been studied mainly by X-ray emission, X-ray absorption, and neutron diffraction spectroscopic methods complemented by molecular simulations. However, the changing hydrophobic and hydrophilic interactions upon changing the mixture composition are not fully understood. We use molecular dynamics simulations and the Small Angle Neutron Scattering (SANS) measurements to predict the molecular clustering in these mixtures.

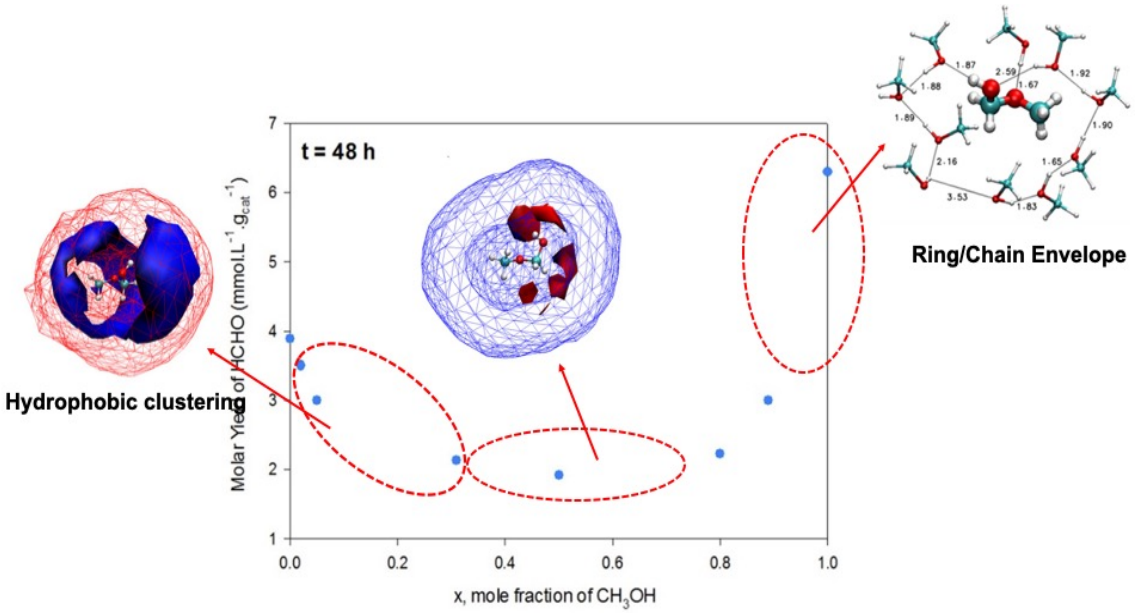

Figure 1. *Molar yield of formaldehyde on varying methanol mole-fraction in methanol-water mixture which is the solvent phase. Spatial distribution function shows methanol (blue) and water (red) arrange around methoxymethanol with hydrophobic clustering at low x_m, water at hydrophilic sites at equimolar compositions. Molecular arrangement of methanol molecules around methoxymethanol in ring structure in pure methanol as elucidated by ab initio molecular dynamics study.*

4.2 Included Publication

This work has been published in The Journal of Physical Chemistry Letters (American Chemical Society) in December 2020:

Dwivedi, S., Mata, J., Mushrif, S. H., Chaffee, A. L., & Tanksale, A. (2020). Molecular Clustering in Formaldehyde–Methanol–Water Mixtures Revealed by High-Intensity, High-q Small-Angle Neutron Scattering. *The Journal of Physical Chemistry Letters*, *12*, 480-486.

THE JOURNAL OF PHYSICAL CHEMISTRY LETTERS
A JOURNAL OF THE AMERICAN CHEMICAL SOCIETY

pubs.acs.org/JPCL Letter

Molecular Clustering in Formaldehyde–Methanol–Water Mixtures Revealed by High-Intensity, High-q Small-Angle Neutron Scattering

Swarit Dwivedi, Jitendra Mata, Samir H. Mushrif, Alan L. Chaffee, and Akshat Tanksale*

Cite This: J. Phys. Chem. Lett. 2021, 12, 480–486 Read Online

ACCESS | Metrics & More | Article Recommendations | Supporting Information

ABSTRACT: Methanol–Water (mw) mixtures, with or without a solute, display a nonideal thermodynamic behavior, typically attributed to the structure of the microphase. However, experimental observation of the microphase structures at the molecular length scale has been a challenge. We report the presence of molecular clusters in mw and formaldehyde–methanol–water (fmw) mixtures using small-angle neutron scattering (SANS) experiments and molecular dynamics (MD) simulations. Hydrophobic clusters of methanol in mw and formaldehyde–methanol in fmw mixtures were observed at low methanol compositions ($x_m \leq 0.3$). A three-dimensional hydrogen-bonded network of water with the solute is observed at $x_m = 0.5$. Linear chains of methanol surrounding the formaldehyde and water molecules were observed at high methanol compositions ($x_m \geq 0.7$). The calculated size of the molecular clusters ($r \approx 0.5$ nm, spherical) from the SANS data and their volume fraction closely matched the MD simulation results.

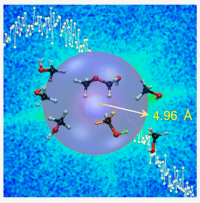

The composition of methanol–water (mw) mixtures affect the mixture's thermodynamic properties, including the enthalpy of mixing, free energy of solvation, and the excess molar volume, which do not vary linearly. This anomalous thermodynamic behavior is attributed to the dynamic structures at a molecular length scale, referred to as the "microphase".[1−4] The formation of microphase structures is due to trade-offs between the enthalpic gains and the entropic penalties, which eventually stabilize the system. In the midst of ongoing contradicting views,[5−8] the common understanding is that methanol forms hydrophobic clusters at low methanol compositions,[2,9] a bipercolating mixture near equimolar compositions,[9] and linear chains of methanol at high methanol compositions, in which the water molecule is either caged or exists in a free form within the mixture.[5,10] To understand the structure of the microphase, researchers explored experimental techniques such as neutron diffraction,[9−12] X-ray techniques,[5,13−15] and Raman spectroscopy.[16] Ab initio[5,17] and classical molecular dynamics simulations[2,10,18] were also used to simulate the microphase structure and complement the experimental observations. However, a quantitative analysis of the presence of microphase structures as a function of solvent composition is yet to be established.

Recently, we showed that syngas and CO_2 can be hydrogenated into formaldehyde in methanol–water mixtures and that the concentration of methanol has a significant impact on the product yield.[19] It is known that, when a small organic compound[20] is solvated in mw mixtures, the chemical and the physical behaviors of the solute are distinct at different mixture compositions. For example, the equilibrium of heterogeneous catalysis reactions[19] are greatly affected by the mw mixture composition. The solvation structure plays a central role in explaining most of these phenomena.

Formaldehyde hydrates in the presence of water and exists in its metastable form, methanediol (md).[21,22] At higher formaldehyde concentrations (>3 wt %), dimers and trimers of formaldehyde start forming, and as formaldehyde concentrations increase further, a precipitate of paraformaldehyde (pFa) is obtained.[22,23] Addition of methanol prevents the oligomerization of formaldehyde, and such formaldehyde–methanol–water (fmw) mixtures are commonly known as formalin solutions. In the presence of methanol, formaldehyde mostly remains in its metastable monomeric form, methoxymethanol (mm).[24] The ability of the metastable monomers (md and mm) to react or adsorb/desorb on to the catalytic surface is likely to be affected by their solvation environment. For example, Mugnai et al.[25] reported a cagelike solvation structure around formaldehyde in water, which hindered the translation and rotation of the formaldehyde and thus affected its hydration.[25−27] Moreover, mm is solvated by a ring/chain structure of 8−10 methanol molecules, which is reported to be the reason for the high catalytic yield of formaldehyde in the presence of methanol.[19] However, the stability and the solvation environment of mm in the mw mixtures remains poorly understood.[24,28] Our recent molecular dynamics (MD) work predicted the presence of methanol around the hydrophobic sites of mm and methanol at low methanol concentrations.[29] To the best of our knowledge, no

Received: November 26, 2020
Accepted: December 16, 2020
Published: December 29, 2020

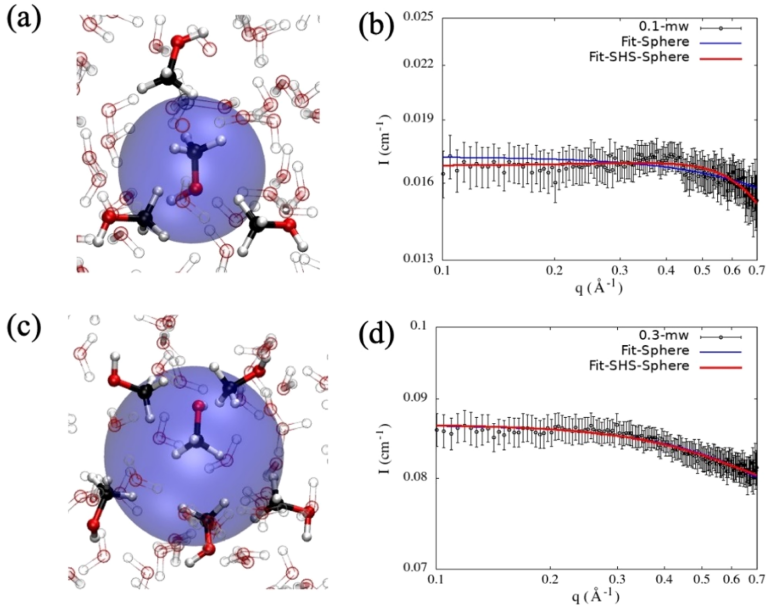

Figure 1. MD snapshot and scattering curves for mw mixtures where (a) MD snapshot for 0.1-mw, (b) scattering curve and model fit for 0.1-mw, (c) MD snapshot for 0.3-mw, and (d) scattering curve and model fit for 0.3-mw.

experimental study reports the solvation structure of formaldehyde in mw mixtures.

Hitherto, small-angle neutron scattering (SANS) has not been explored to resolve the microphase structure of liquid mixtures such as fmw. In the present work, we demonstrate molecular dynamics simulations to guide the background subtraction and formulate a method to identify the molecular clusters at a high-q range. Recent advancements in the experimental infrastructure,[30] specifically the improved performance of the detector, facilitate the meaningful collection of scattering data at a high-q range for such liquid mixtures. The neutron scattering data at a high-q range, when fitted with the cluster models such as Guinier, Sphere, and Ellipsoid, resolves any cluster formed at a molecular length scale. Understanding these molecular clusters may pave a path to optimize the liquid-phase catalytic reaction mechanisms to produce formaldehyde. Moreover, we believe that this work can be extended to investigate the topology of other liquid mixtures of a similar nature, which is not possible otherwise.

We observed small (<1 nm) molecular clusters in liquid mixtures using a SANS experiment, which could only be possible because of (a) enhanced contrast between hydrogenated clusters and deuterated solvent and (b) the measurement of high-q, high-intensity SANS, which was enabled by a significantly higher count rate detector installed at the Australian Nuclear Science and Technology Organisation (ANSTO) in 2019.

The detailed experimental methods are provided in the Supporting Information, but briefly, the methods are described below.

Classical Molecular Dynamics Simulations. Classical MD simulations were performed using the GROMACS simulation package, and the Visual Molecular Dynamics (VMD) software package[31] was used for visualization. The all-atom optimized potentials for liquid simulations (OPLS-AA) force field[29,32] was used to define the interaction parameters of methanol, mm, and md, while the SPC/E[33] model was used for water.

Preparation of Liquid Mixtures for SANS Experiments. We prepared three sets of mixtures with formaldehyde (fa) mole fractions x_{fa} of 0, 0.01, and 0.02. Each set was comprised of seven methanol (m)-water (w) compositions (x_m = 0, 0.1, 0.3, 0.5, 0.7, 0.9, and 1). Formaldehyde−methanol−water mixtures are denoted as x_m-(mole%fa)fmw; for example, 0.1−1fmw means 1 mol % formaldehyde in mw mixture with x_m = 0.1, and 0.3-mw means mw mixture with x_m = 0.3, without any formaldehyde. To achieve a contrast between the molecular clusters and the free solvent, fmw mixtures were prepared such that normal methanol (m) and deuterated-water (d-w) were used when the volume fraction of methanol (Vf_m) was less than or equal to 0.5 (i.e., x_m = 0,0.1, and 0.3), and deuterated-methanol (d-m) and normal water (w) was used when $Vf_m \geq 0.5$ (i.e., $x_m \geq 0.5$). All the mixture compositions and their Vf values are given in the Supporting Information (Table S2). The molecular clusters in the present study are defined as the solvent molecules within the first solvation shell of the solute, including the solute. For example, at a low x_m of an fmw mixture, mm and methanol molecules within the first solvation shell of mm are considered as a cluster.

SANS Experiments and Data Fitting. The prepared liquid mixtures were subjected to high-intensity, high-q (scattering vector) SANS experiments at the Quokka beamline of the

https://dx.doi.org/10.1021/acs.jpclett.0c03515
J. Phys. Chem. Lett. 2021, 12, 480−486

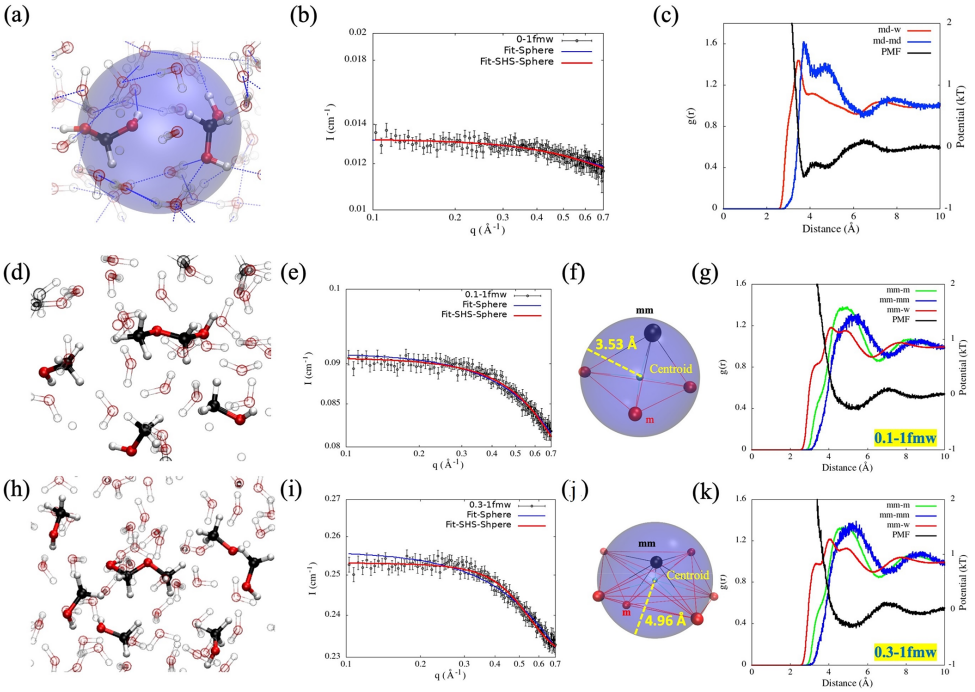

Figure 2. (a) MD snapshot, (b) SANS data with Sphere and SHS-Sphere fitting curves and (c) g(r)-com of md-md and md-w, and the potential of mean force (PMF) for md-md interaction in 0.0−1fmw sample, showing md clustered in water. MD snapshot; SANS data with Sphere and SHS-Sphere fitting curves; centroids of molecules in the cluster, superimposed by a sphere of radius predicted by the SHS-sphere fits on SANS data; and g(r)-com of md-md and md-w, and the potential of mean force (PMF) for md-md interaction in (d−g) 0.1−1fmw mixture and (h−k) 0.3−1fmw mixture.

ANSTO. The liquid mixtures, prepared in a Hellma cell of 1 or 2 mm thickness, were kept at 4 °C during measurements. We used the data modeling program SASview to fit the SANS data. The data were fitted with sphere, ellipsoid, and sticky-hard-sphere (SHS) models. The first two models did not account for the interparticle interactions that arise from the hydrophilic and the hydrophobic interactions between the solute molecules. Therefore, a structure factor was introduced via the SHS model. More details about the SHS model are provided in the Supporting Information, Section 1e.

The background-subtracted scattering intensity $I(q)$ was fitted with various models to reveal the presence of clusters in mixtures with $x_m \leq 0.5$. No meaningful clustering was observed for mixtures with $x_m \geq 0.5$ (Supporting Information, Section 2). In the subsequent sections, we discuss our observations for mw mixtures and compare our results to the previously reported analysis of these mixtures. Thereafter, we discuss the fmw mixtures at low, equimolar, and high methanol concentrations. The Vf of the clusters obtained by fitting the scattering data shows similar trends to the Vf calculated from MD simulations, as discussed in the Supporting Information, Section 2.

Molecular Clustering in a Methanol−Water Mixture. It is well-established, via soft X-ray absorption spectroscopy, that, at low methanol concentrations ($x_m \approx 0.05$), the three-dimensional (3-D) hydrogen-bonding network of water is not affected and that methanol is hydrated by a shell of water.[9,13] At $x_m \approx 0.27$, hydrophobic clusters of methanol were reported.[9] However, it is unclear if the tendency of forming these hydrophobic clusters gradually increases on increasing the methanol concentration and if the formation of a hydrophobic cluster within the hydration shell of water is possible at low methanol concentrations ($0 < x_m < 0.27$). Figure 1a shows a snapshot of a cluster of four methanol molecules from the MD trajectory of the 0.1-mw mixture. The hydrophobic tails of methanol orientate toward each other. The coordination number of methanol-methanol molecules is 2.2, as calculated by the center of the mass radial pair distribution function (g(r)-com$_{m-m}$). Figure 1b shows the SANS curve for a 0.1-mw mixture, with Sphere and SHS-Sphere model fits. A sphere with a radius of 2.67 Å, as predicted by the SHS-Sphere model, was drawn from the centroid of the molecules (centroid of the centroids of molecules forming the cluster), visualized in Figure 1a. When the methanol concentration was increased to $x_m = 0.3$, the number of molecules in the first coordination shell increased. Figure 1c shows a snapshot from the MD trajectory of this mixture, where six molecules of methanol formed a hydrophobic cluster surrounded by water. The

https://dx.doi.org/10.1021/acs.jpclett.0c03515
J. Phys. Chem. Lett. 2021, 12, 480−486

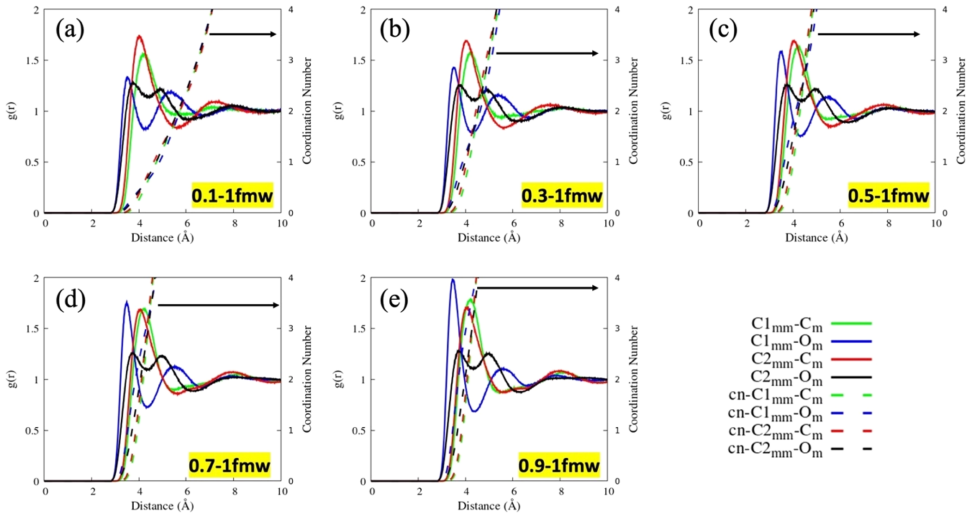

Figure 3. Radial pair distribution function between the carbon of methoxymethanol and the carbon or oxygen of methanol is analyzed in order to elucidate the probable orientation of methanol. (a−e) Radial pair distribution function and the coordination number for pairs C1 mm-Cm, C1 mm-Om, C2 mm-Cm, and C2 mm-Om.

formation of a hydrophobic cluster was gradual at dilute methanol concentrations, thus increasing the possibility of an interaction of the hydration spheres of methanol molecules. This observation concurs with the previously reported MD study, which showed that hydrophobic clustering increases at low concentration ranges and at higher temperatures, where it is easier to break the hydrogen-bonding network of water.[34]

Solvation Shell Structure of Formaldehyde−Methanol−Water at Low Methanol Concentrations. The metastable form of formaldehyde in water is md, which has a CH_2- group attached to two −OH groups. Therefore, the molecule tends to form hydrophobic clusters. Simultaneously, it has a large surface available for hydrophilic interactions due to the presence of two −OH groups on one carbon. Figure 2a shows a snapshot from the MD trajectory of the 0.0−1fmw mixture, where two md molecules are in proximity of each other. The sphere drawn in Figure 2a is centered at the centroid of the cluster with a radius of 3.27 Å, which was obtained by fitting the SHS-Sphere model on the 0.0−1fmw SANS curve (Figure 2b). This cluster's formation is likely due to the inherent tendency of water to preserve its 3-D hydrogen-bonding network, like in the low-concentration mw mixtures. Moreover, the g(r)-$com_{md\text{-}md}$ (Figure 2c) shows two peaks in the 3−5 Å range, which is due to the hydrophilic (at ∼4 Å) and hydrophobic (at ∼5 Å) interaction within the hydration sphere. Assuming no more than two molecules form a cluster, the coordination number of ∼0.5 between md-md from the g(r)-$com_{md\text{-}md}$ (Figure 2c) suggests that ∼67% of the md molecules in the liquid mixture are clustered, whereas the remaining are free md molecules.

The dominant metastable form of formaldehyde in all fmw mixtures, with $x_m \geq 0.1$, is mm,[24,29] whose details are described in the Supporting Information, Section 1a. The mm molecule has a CH_3- and a CH_2- group. Therefore, the formation of hydrophobic clusters with methanol is expected. Figure 2d shows the MD simulation snapshot for a 0.1−1fmw mixture, where the hydrophobic tails of three methanol molecules are oriented toward the mm molecule's hydrophobic sites. The coordination number of methanol around mm in the first solvation shell (g(r)-$com_{mm\text{-}m}$) is 3.12 (Figure 2g). The Sphere model fit on the scattering data predicted a radius of 2.74 Å, whereas the SHS-Sphere model predicted a radius of 3.53 Å (Figure 2e). Figure 2f shows a sphere with a radius of 3.53 Å as predicted by the SHS-Sphere model, centered at the centroid of the MD snapshot cluster shown in Figure 2d. The sphere in Figure 2f encapsulates all molecular centroids of the cluster, which shows excellent agreement between the simulation and the experiment. Figure 2g shows the center of the mass radial pair distribution function (g(r)-com) between mm-m, mm-w, and mm-mm molecules. The g(r)-$com_{mm\text{-}mm}$ shows a single broad peak in the range of 4−6 Å, contrary to the 0.0−1fmw mixture (Figure 2c). Moreover, the lower peak height signifies that only the hydrophobic interaction is dominant between the mm molecules, and the strength of the interaction between two mm molecules is less than that of two md molecules. This observation also supports that, upon addition of methanol, the formation of dimers and trimers of formaldehyde is reduced.

When the methanol concentration is increased to $x_m = 0.3$ (0.3−1fmw), the number of methanol molecules inside the solvation shell of mm increases. Figure 2h shows a snapshot from the MD trajectory, where six methanol molecules are present around one molecule of mm. The g(r)-$com_{mm\text{-}m}$ (Figure 2k) integrates to a coordination number of 7.9 until the first minimum. Similar to the 0.1−1fmw mixture, the hydrophobic tails of methanol molecules are oriented toward the hydrophobic sites of mm. Figure 2i shows the Sphere and the SHS-Sphere model fit. The former model fit results in a sphere with a radius of 2.29 Å, whereas the latter gives a radius

https://dx.doi.org/10.1021/acs.jpclett.0c03515
J. Phys. Chem. Lett. 2021, 12, 480−486

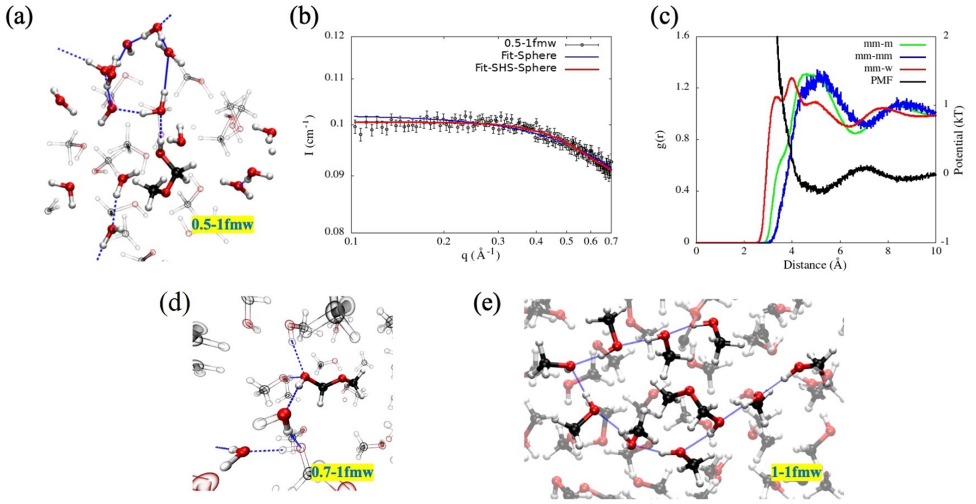

Figure 4. (a) MD snapshot of the solvation environment, (b) the background-subtracted scattering curve, and (c) the g(r) for the 0.5−1fmw mixture. The MD snapshot of the solvation environment is shown for the (d) 0.7−1fmw and (e) 1−1fmw mixtures (radius = 4.96 Å).

of 4.96 Å. Figure 2j shows a sphere of radius 4.96 Å, drawn from the centroid of the cluster and it encapsulates all the molecular centroids. Because of the specific orientation of the methanol molecules around mm, the shape is closer to an ellipsoid. When the scattering curve was fitted with the SHS-Ellipsoid model (see Supporting Information, Table S6), an equatorial radius of 6.18 Å is observed when the polar radius is fixed at 3 Å. Figure 2k shows the g(r)-com between mm-mm, mm-m, and mm-w molecules. The relative strength of the interaction between mm-mm and mm-m increases compared to the 0.1−1fmw mixture, an effect of which is also manifested in the scattering curve. Because of the increased interparticle (mm-mm) interactions, introducing a structure factor for the 0.3−1fmw mixture is necessary and is apparent in the scattering curve (Figure 2i). This result also supports the argument that, in dilute concentrations, the formation of a hydrophobic cluster is likely and that the 3-D network of water is fragmented.[13,35]

To confirm that the methanol molecules are hydrophobically oriented around methanol at low methanol concentrations, we compared the g(r) between $C1_{mm}$-C_m and $C1_{mm}$-O_m and between $C2_{mm}$-C_m and $C2_{mm}$-O_m (Figure 3). The $C1_{mm}$ originates from the formaldehyde carbon and $C2_{mm}$ from the methanol's carbon, which makes up the methoxymethanol molecule. For a hydrophilic interaction between mm and methanol, we would expect the g(r) to show the O_m-C_{mm} distance to be shorter than that of C_m-C_{mm}. Conversely, for a hydrophobic interaction, we would expect the g(r) to show the C_m-C_{mm} distance to be shorter than that of O_m-C_{mm}. The first peak in the g(r) between C(1 or 2)$_{mm}$-O_m is due to the methanol molecules present around methoxymethanol, a result of the hydrophilic interactions. However, most of the methanol molecules contributing to the second peak are due to hydrophobic interactions. In contrast, the first peak of C(1 or 2)$_{mm}$-C_m is due to hydrophobic interactions between methanol and mm. For x_m = 0.1 and 0.3, the height of the first peak of the C(1 or 2)$_{mm}$-C_m g(r) is higher than the first peak of C(1 or 2)$_{mm}$-O_m g(r), which shows that the strength of interaction is more significant for the hydrophobic interactions. Figure 3a shows that the coordination number is low (<0.2), until the first minimum of the C(1 or 2)$_{mm}$-O_m, and increases to ∼1 for the first minima of C(1 or 2)$_{mm}$-C_m, indicating that more methanol molecules are hydrophobically oriented and their oxygen is counted in the second peak of C_{mm}-O_m g(r). The difference between the first peak of C(1 or 2)$_{mm}$-C_m and the second peak of C(1 or 2)$_{mm}$-O_m is ∼1.5 Å, which supports our observation that the molecules contributing to the first peak of C(1 or 2)$_{mm}$-C_m g(r) and the second peak of C(1 or 2)$_{mm}$-O_m g(r) are largely the same. Therefore, the g(r) in Figure 3a,b reveals that methanol molecules are hydrophobically oriented toward the hydrophobic ends of the mm molecule at low methanol concentrations. However, this is not the case for $x_m \geq 0.5$ mixtures (Figure 3c−e); the strength of hydrophilic interactions between $C1_{mm}$-O_m increases and is more prominent for higher methanol concentration mixtures. This orientation changes on further increasing the x_m. The coordination number for the first peak of C(1 or 2)$_{mm}$-O_m indicates more hydrophilic interactions between methanol and mm. This is also due to a greater number of methanol molecules in the mixture. However, the greater increase in the coordination of C(1 or 2)$_{mm}$-O_m than C(1 or 2)$_{mm}$-C_m at lower distances shows that fewer molecules of methanol are hydrophobically interacting with mm. This gap in coordination number fades after the first minima of C(1 or 2)$_{mm}$-O_m.

Solvation Structure of Formaldehyde−Methanol−Water at High Methanol Concentrations. In the 0.5−1fmw mixture, the volume fraction of methanol was 0.68, and d-m and water were used as the solvent. It implies that any observed cluster in the scattering data will be formed by mm and water. Figure 4a shows the solvation environment for the 0.5−1fmw mixture via

https://dx.doi.org/10.1021/acs.jpclett.0c03515
J. Phys. Chem. Lett. 2021, 12, 480−486

an MD snapshot. A fragmented network of water molecules hydrogen-bonded to each other was observed at the mm molecule's hydrophilic site. The scattering curve with SHS-Sphere fit (Figure 4b) resulted in a cluster with a radius of 4.32 Å, which is smaller than that of the cluster observed for 0.3−1fmw. This is confirmed by the g(r)-com of mm-w shown in Figure 4c. The smaller size of the cluster is due to the small size of water molecules forming this cluster and because of the strong hydrogen bonds between the water molecules and mm (i.e., shorter bond lengths). At higher x_m (i.e., ≥0.7), the mm was mostly surrounded by methanol molecules. Water is present at the mm molecules' hydrophilic sites; however, a network of hydrogen-bonded water was not observed. In such cases, no meaningful scattering data could be resolved after the background subtraction. This can be attributed to the fact that methanol forms linear chains and mostly surrounds the mm molecule. For 0.7−1fmw, Figure 4d shows three molecules of water present around one molecule of mm, and hence cluster formation is unlikely. In 1−1fmw, mm is surrounded by a linear chain structure of methanol molecules, as shown in Figure 4e. The mm molecule in pure methanol surrounded by a ring structure of 8−10 methanol molecules was reported in our earlier ab initio MD study.[19] Guo et. al[5] also showed that water is expected to exist in free form or trapped in methanol chains at high x_m methanol−water mixtures.

In summary, the solvation environment of methanol in water and formaldehyde in methanol−water mixtures was studied via small-angle neutron scattering at a high-intensity and high-q range, and MD simulations guided the background subtraction. Sphere, Ellipsoid, SHS-Sphere, and SHS-Ellipsoid models were fitted against the scattering data to analyze the size and shape of the molecular clusters. The SHS-Sphere and SHS-Ellipsoid models provided the best fit as the SHS model captures the interparticle interactions between molecular clusters. The cluster size and Vf calculated by experiments matched the simulation results. At low methanol concentration (x_m = 0.1 and 0.3), a hydrophobic cluster of methanol was observed. The size of the cluster increased from 3.53 to 4.96 Å for x_m = 0.1 and 0.3, respectively. In a formaldehyde−water (x_m = 0.0) mixture, formaldehyde clusters formed in a hydration shell. When methanol was added (x_m = 0.1 and x_m = 0.3), the tendency of formaldehyde to form clusters becoame weaker, and methanol oriented itself hydrophobically around methoxymethanol. At an equimolar mixture composition, a fragmented network of hydrogen-bonded water molecules was observed around the hydrophilic site of formaldehyde. No meaningful clustering could be resolved at compositions $x_m \geq$ 0.7 due to methanol forming a linear chain structure and solvating the methoxymethanol and water.

■ ASSOCIATED CONTENT

Supporting Information

The Supporting Information is available free of charge at https://pubs.acs.org/doi/10.1021/acs.jpclett.0c03515.

A detailed description of computational and experimental methodology, background-subtracted scattering data, and volume fraction results (PDF)

■ AUTHOR INFORMATION

Corresponding Author

Akshat Tanksale − *Department of Chemical Engineering, Monash University, Clayton, Victoria 3800, Australia;* orcid.org/0000-0002-7087-0912; Email: Akshat.Tanksale@monash.edu

Authors

Swarit Dwivedi − *Department of Chemical Engineering, Monash University, Clayton, Victoria 3800, Australia;* orcid.org/0000-0002-4639-5576

Jitendra Mata − *Australian Centre for Neutron Scattering, Australian Nuclear Science and Technology Organisation, Lucas Heights, NSW 2234, Australia;* orcid.org/0000-0001-9225-7900

Samir H. Mushrif − *Department of Chemical and Materials Engineering, University of Alberta, Edmonton, Alberta T6G 1H9, Canada;* orcid.org/0000-0002-0002-9634

Alan L. Chaffee − *School of Chemistry, Monash University, Clayton, Victoria 3800, Australia;* orcid.org/0000-0001-5100-6910

Complete contact information is available at: https://pubs.acs.org/10.1021/acs.jpclett.0c03515

Author Contributions

The manuscript was written through contributions of all authors. All authors have given approval to the final version of the manuscript.

Funding

Australian Research Council, Discovery Project, DP170104017. Australian Nuclear Science and Technology Organisation, Quokka beamline (Proposal No. 7415).

Notes

The authors declare no competing financial interest.

■ ACKNOWLEDGMENTS

This research was funded by the Australian Government through the Australian Research Council's Discovery Projects funding scheme (Project DP170104017). The authors appreciate the financial support of the Australian Centre for Neutron Scattering (ACNS), Australian Nuclear Science and Technology Organisation (ANSTO), for providing beamtime on the Quokka (Proposal No. 7415). The authors gratefully acknowledge a generous allocation of computer resources through the Monash eResearch Centre at the Monash Advanced Research Computing Hybrid (MonARCH) HPC/HTC Cluster. This work benefited from the use of the SasView application, originally developed under NSF Award No. DMR-0520547. SasView contains code developed with funding from the European Union's Horizon 2020 research and innovation programme under the SINE2020 project, Grant No. 654000.

■ ABBREVIATIONS

mm, methoxymethanol; md, methanoldiol; m, methanol; w, water; g(r)-com, center of mass radial pair distribution function; fmw, formaldehyde−methanol−water mixture; mw, methanol−water mixture

■ REFERENCES

(1) Tanaka, H.; Gubbins, K. E. Structure and Thermodynamic Properties of Water-Methanol Mixtures: Role of the Water-Water Interaction. *J. Chem. Phys.* **1992**, *97* (4), 2626−2634.

(2) Allison, S. K.; Fox, J. P.; Hargreaves, R.; Bates, S. P. Clustering and Microimmiscibility in Alcohol-Water Mixtures: Evidence from Molecular-Dynamics Simulations. *Phys. Rev. B: Condens. Matter Mater. Phys.* **2005**, *71* (2), 024201.

(3) Koh, C. A.; Tanaka, H.; Walsh, J. M.; Gubbins, K. E.; Zollweg, J. A. Thermodynamic and Structural Properties of Methanol-Water Mixtures: Experiment, Theory, and Molecular Simulation. *Fluid Phase Equilib.* **1993**, *83*, 51−58.
(4) Galicia-Andrés, E.; Dominguez, H.; Pusztai, L.; Pizio, O. Composition Dependence of Thermodynamic, Dynamic and Dielectric Properties of Water-Methanol Model Mixtures. Molecular Dynamics Simulation Results with the OPLS-AA Model for Methanol. *J. Mol. Liq.* **2015**, *212*, 70−78.
(5) Guo, J.-H.; Luo, Y.; Augustsson, A.; Kashtanov, S.; Rubensson, J.-E.; Shuh, D. K.; Ågren, H.; Nordgren, J. Molecular Structure of Alcohol-Water Mixtures. *Phys. Rev. Lett.* **2003**, *91* (15), 157401.
(6) Dixit, S.; Soper, A. K.; Finney, J. L.; Crain, J. Water Structure and Solute Association in Dilute Aqueous Methanol. *Europhys. Lett.* **2002**, *59* (3), 377−383.
(7) Franks, F.; Ives, D. J. G. The Structural Properties of Alcohol-Water Mixtures. *Q. Rev., Chem. Soc.* **1966**, *20* (1), 1−44.
(8) Soper, A. K.; Finney, J. L. Hydration of Methanol in Aqueous Solution. *Phys. Rev. Lett.* **1993**, *71* (26), 4346−4349.
(9) Dougan, L.; Bates, S. P.; Hargreaves, R.; Fox, J. P.; Crain, J.; Finney, J. L.; Réat, V.; Soper, A. K. Methanol-Water Solutions: A Bi-Percolating Liquid Mixture. *J. Chem. Phys.* **2004**, *121* (13), 6456−6462.
(10) Dixit, S.; Crain, J.; Poon, W. C. K.; Finney, J. L.; Soper, A. K. Molecular Segregation Observed in a Concentrated Alcohol-Water Solution. *Nature* **2002**, *416* (6883), 829−832.
(11) Soper, A. K.; Finney, J. L. Hydration of Methanol in Aqueous Solution. *Phys. Rev. Lett.* **1993**, *71* (26), 4346−4349.
(12) Yoshida, K.; Ishida, S.; Yamaguchi, T. Hydrogen Bonding and Clusters in Supercritical Methanol-Water Mixture by Neutron Diffraction with H/D Substitution Combined with Empirical Potential Structure Refinement Modelling. *Mol. Phys.* **2019**, *117* (22), 3297−3310.
(13) Nagasaka, M.; Mochizuki, K.; Leloup, V.; Kosugi, N. Local Structures of Methanol-Water Binary Solutions Studied by Soft X-Ray Absorption Spectroscopy. *J. Phys. Chem. B* **2014**, *118* (16), 4388−4396.
(14) Takamuku, T.; Saisho, K.; Nozawa, S.; Yamaguchi, T. X-Ray Diffraction Studies on Methanol-Water, Ethanol-Water, and 2-Propanol-Water Mixtures at Low Temperatures. *J. Mol. Liq.* **2005**, *119* (1−3), 133−146.
(15) Takamuku, T.; Yamaguchia, T.; Asato, M.; Matsumoto, M.; Nishi, N. Structure of Clusters in Methanol-Water Binary Solutions Studied by Mass Spectrometry and X-Ray Diffraction. *Z. Naturforsch., A: Phys. Sci.* **2000**, *55* (5), 513.
(16) Yu, Y.; Fan, W.; Wang, Y.; Zhou, X.; Sun, J.; Liu, S. C-H···O Interaction in Methanol-Water Solution Revealed from Raman Spectroscopy and Theoretical Calculations. *J. Phys. Chem. B* **2017**, *121* (34), 8179−8187.
(17) Jorgensen, W. L.; Madura, J. D. Quantum and Statistical Mechanical Studies of Liquids. 25. Solvation and Conformation of Methanol in Water. *J. Am. Chem. Soc.* **1983**, *105* (6), 1407−1413.
(18) Skaf, M. S.; Ladanyi, B. M. Molecular Dynamics Simulation of Solvation Dynamics in Methanol-Water Mixtures. *J. Phys. Chem.* **1996**, *100* (46), 18258−18268.
(19) Bahmanpour, A. M.; Hoadley, A.; Mushrif, S. H.; Tanksale, A. Hydrogenation of Carbon Monoxide into Formaldehyde in Liquid Media. *ACS Sustainable Chem. Eng.* **2016**, *4* (7), 3970−3977.
(20) Vishnyakov, A.; Neimark, A. V. Molecular Dynamics Simulation of Nafion Oligomer Solvation in Equimolar Methanol-Water Mixture. *J. Phys. Chem. B* **2001**, *105* (32), 7830−7834.
(21) Hahnenstein, I.; Albert, M.; Hasse, H.; Kreiter, C. G.; Maurer, G. NMR Spectroscopic and Densimetric Study of Reaction Kinetics of Formaldehyde Polymer Formation in Water, Deuterium Oxide, and Methanol. *Ind. Eng. Chem. Res.* **1995**, *34* (2), 440−450.
(22) Rivlin, M.; Eliav, U.; Navon, G. NMR Studies of the Equilibria and Reaction Rates in Aqueous Solutions of Formaldehyde. *J. Phys. Chem. B* **2015**, *119* (12), 4479−4487.
(23) Walker, F. The State of Formaldehyde in Aqueous Solutions. *J. Phys. Chem.* **1931**, *35* (4), 1104−1113.
(24) Gaca, K. Z.; Parkinson, J. A.; Lue, L.; Sefcik, J. Equilibrium Speciation in Moderately Concentrated Formaldehyde-Methanol-Water Solutions Investigated Using ^{13}C and ^{1}H Nuclear Magnetic Resonance Spectroscopy. *Ind. Eng. Chem. Res.* **2014**, *53* (22), 9262−9271.
(25) Mugnai, M.; Cardini, G.; Schettino, V.; Nielsen, C. J. *Ab Initio* Molecular Dynamics Study of Aqueous Formaldehyde and Methanediol. *Mol. Phys.* **2007**, *105* (17−18), 2203−2210.
(26) Delcroix, P.; Pagliai, M.; Cardini, G.; Bégué, D.; Hanoune, B. Structural and Spectroscopic Properties of Methanediol in Aqueous Solutions from Quantum Chemistry Calculations and Ab Initio Molecular Dynamics Simulations. *J. Phys. Chem. A* **2015**, *119* (2), 290−298.
(27) Thompson, M. A. QM/MMpol: A Consistent Model for Solute/Solvent Polarization. Application to the Aqueous Solvation and Spectroscopy of Formaldehyde, Acetaldehyde, and Acetone. *J. Phys. Chem.* **1996**, *100* (34), 14492−14507.
(28) Hahnenstein, I.; Hasse, H.; Kreiter, C. G.; Maurer, G. 1H- and 13C-NMR-Spectroscopic Study of Chemical Equilibria in Solutions of Formaldehyde in Water, Deuterium Oxide, and Methanol. *Ind. Eng. Chem. Res.* **1994**, *33* (4), 1022−1029.
(29) Dwivedi, S.; Mushrif, S. H.; Chaffee, A. L.; Tanksale, A. Solvation Behaviour and Micro-Phase Structure of Formaldehyde-Methanol-Water Mixtures. *J. Mol. Liq.* **2020**, *301*, 112444.
(30) Wood, K.; Mata, J. P.; Garvey, C. J.; Wu, C.-M.; Hamilton, W. A.; Abbeywick, P.; Bartlett, D.; Bartsch, F.; Baxter, P.; Booth, N.; et al. QUOKKA, the Pinhole Small-Angle Neutron Scattering Instrument at the OPAL Research Reactor, Australia: Design, Performance, Operation and Scientific Highlights. *J. Appl. Crystallogr.* **2018**, *51* (2), 294−314.
(31) Humphrey, W.; Dalke, A.; Schulten, K. VMD: Visual Molecular Dynamics. *J. Mol. Graphics* **1996**, *14* (1), 33−38.
(32) Kony, D.; Damm, W.; Stoll, S.; Van Gunsteren, W. F. An Improved OPLS-AA Force Field for Carbohydrates. *J. Comput. Chem.* **2002**, *23* (15), 1416−1429.
(33) Mark, P.; Nilsson, L. Structure and Dynamics of the TIP3P, SPC, and SPC/E Water Models at 298 K. *J. Phys. Chem. A* **2001**, *105* (43), 9954−9960.
(34) Mallamace, F.; Corsaro, C.; Mallamace, D.; Vasi, C.; Vasi, S.; Stanley, H. E. Dynamical Properties of Water-Methanol Solutions. *J. Chem. Phys.* **2016**, *144* (6), 064506.
(35) Li, F.; Wang, Y.; Men, Z.; Sun, C. Exploring the Hydrogen Bond Kinetics of Methanol-Water Solutions Using Raman Scattering. *Phys. Chem. Chem. Phys.* **2020**, *22* (44), 26000−26004.

https://dx.doi.org/10.1021/acs.jpclett.0c03515
J. Phys. Chem. Lett. 2021, 12, 480−486

Molecular Clustering in Formaldehyde-Methanol-Water Mixtures Revealed by High Intensity, High-q Small Angle Neutron Scattering

*Swarit Dwivedi[1], Jitendra Mata[2], Samir H. Mushrif[3], Alan L. Chaffee[4], Akshat Tanksale[1]**

1. *Department of Chemical Engineering, Monash University, Clayton 3800, Victoria, Australia*
2. *Australian Centre for Neutron Scattering, Australian Nuclear Science and Technology Organisation, Lucas Heights, NSW, 2234, Australia*
3. *Department of Chemical and Materials Engineering, University of Alberta, 9211-116 St., Edmonton, Alberta T6G 1H9, Canada*
4. *School of Chemistry, Monash University, Clayton 3800, Victoria, Australia*

* *Corresponding Author, Email: Akshat.Tanksale@monash.edu*

Electronic Supplementary Information

1. Experiments and Methods

1a. Classical molecular dynamics simulations

Classical molecular dynamics (MD) simulations were performed using the GROMACS simulation package, where the OPLS-AA forcefield[1,2] was used to define the interaction parameters of methanol, methoxymethanol (mm) and methanediol (md), while the SPC/E[3] model was used for water. The interaction parameters used for methanediol and methoxymethanol were previously published and tested against the radial pair distribution function *g(r)* obtained from a QM/MM study[4]. The Visual Molecular Dynamics (VMD) software package[5] was used for visualisation and analysis of the molecular trajectory. Number of molecules of md, mm, methanol, and water mimicking the mixture compositions were randomly packed in a cubical box (Table S1). The system's potential energy was minimised using the conjugate gradient method with a tolerance of 10 KJ/mol. The velocity was generated randomly corresponding to a temperature of 298 K using the V-rescale[6] thermostat and equilibrated for 100 ps. Thereafter, the system was subjected to an NPT ensemble for 150 ps to optimise density. The Parrinello-Rahman[7] barostat and the Berendsen[8] thermostat were used, with the time constant of 0.1 ps applied for both.

Table S1: Composition, size, density for each MD simulation box.

Name	n_{md}	n_{mm}	n_{m}	n_{w}	Box length (nm)	Density (gm/cm^3)
0.1-mw	0	0	500	4500	5.55	0.945
0.3-mw	0	0	1500	3500	5.91	0.895
0.5-mw	0	0	2500	2500	6.24	0.854
0.7-mw	0	0	3500	1500	6.55	0.821
0.9-mw	0	0	4500	500	6.86	0.788
0-1fmw	100	0	0	5000	5.36	0.983
0.1-1fmw	0	100	500	4500	5.60	0.948
0.3-1fmw	0	100	1500	3500	6.02	0.871
0.5-1fmw	0	100	2500	2500	6.28	0.859
0.7-1fmw	0	100	3500	1500	6.59	0.825
0.9-1fmw	0	100	4500	500	6.89	0.792
1-1fmw	0	100	5000	0	7.04	0.776
0-2fmw	200	0	0	5000	5.42	0.989
0.1-2fmw	0	200	500	4500	5.65	0.952
0.3-2fmw	0	200	1500	3500	6.00	0.904
0.5-2fmw	0	200	2500	2500	6.32	0.863
0.7-2fmw	0	200	3500	1500	6.63	0.828
0.9-2fmw	0	200	4500	500	6.93	0.796
1-2fmw	0	200	5000	0	7.07	0.781

For the production run, the system was subjected to an NVT ensemble for 10 ns. The molecular coordinates were saved every 0.1 ps and only the last 7.5 ns of the trajectory data were used for analysis to ensure that the system was equilibrated. The temperature was kept at 298 K using a Nose-Hoover chains[9] thermostat with a time constant of 0.2 ps. The electrostatic and van der Walls forces were defined with the Particle Mesh Ewald algorithm[10] with the cut-off distance of 1.2 nm.

Varying the methanol concentration, changes the molecular form of formaldehyde. When methanol concentration (x_m) is 0, formaldehyde is in the form of methanediol, however, with the addition of methanol in the *fmw* mixture, most of the methanediol is converted into methoxymethanol (reaction R1) as the equilibrium constant is 40[11].

$CH_2(OH)_2 + CH_3OH \rightarrow CH_3OCH_2OH + H_2O$ ... (R1)
md *m* *mm* *w*

At x_m = 0.1, nearly 80% of the formaldehyde is in form of methoxymethanol, while at x_m = 0.3 it increases to ~96%. Therefore, at all methanol concentrations $x_m \geq 0.1$, formaldehyde present in the liquid mixture was simulated as methoxymethanol.

1b. Preparation of liquid mixtures

We prepared three sets of mixtures with a formaldehyde (fa) mole-fraction, x_{fa} = 0, 0.01, and 0.02. Each set was comprised of seven methanol (m)-water (w) compositions (x_m = 0, 0.1, 0.3, 0.5, 0.7, 0.9, 1). In the present work, formaldehyde-methanol-water mixtures are denoted as x_m-(mole%$_{fa}$)fmw, for example, 0.1-1fmw means 1 mole% formaldehyde in *mw* mixture with x_m = 0.1, and 0.3-mw means *mw* mixture with x_m = 0.3, without any formaldehyde. To achieve a contrast between the molecular clusters and the free solvent, *fmw* mixtures were prepared such that normal methanol (m) and deuterated-water (d-w) were used when the volume fraction of methanol (Vf_m) ≤ 0.5 (i.e. $x_m = 0, 0.1,$ and 0.3), and deuterated-methanol (d-m) and normal water (w) was used when $Vf_m \geq 0.5$ (i.e. $x_m \geq 0.5$). All the mixture compositions and their *Vf* are given in Table S2. The volume fractions are calculated as per Eq. 1.

$$Vf_m = \frac{V_m}{V_m + V_{Fa} + V_w} = \frac{x_m M_m/\rho_m}{\frac{x_m M_m}{\rho_m} + \frac{x_{Fa} M_{Fa}}{\rho_{Fa}} + \frac{x_w M_w}{\rho_w}} \quad \text{(Eq. 1)}$$

Table S2: Composition and volume fraction of samples used

Name	x_{Fa}	x_m	x_{d-m}	x_w	x_{d-w}	Vf_{Fa}	Vf_m **or** Vf_{d-m}	Vf_w **or** Vf_{d-w}
0.1-mw	0	0.1	-	-	0.9	0.000	0.199	0.801
0.3-mw	0	0.3	-	-	0.7	0.000	0.490	0.510
0.5-mw	0	-	0.5	0.5	-	0.000	0.692	0.308
0.7-mw	0	-	0.3	0.7	-	0.000	0.840	0.160
0.9-mw	0	-	0.1	0.9	-	0.000	0.953	0.047
0.0-1fmw	0.01	0.000			0.990	0.017	0.000	0.983
0.1-1fmw	0.01	0.099	-	-	0.891	0.015	0.197	0.789
0.3-1fmw	0.01	0.297	-	-	0.693	0.012	0.484	0.504
0.5-1fmw	0.01	-	0.495	0.495	-	0.010	0.685	0.305
0.7-1fmw	0.01	-	0.693	0.297	-	0.009	0.832	0.159
0.9-1fmw	0.01	-	0.891	0.099	-	0.008	0.945	0.047
1-1fmw	0.01		0.990	0.000		0.007	0.993	0.000
0.0-2fmw	0.02	0.000			0.980	0.033	0.000	0.967

0.1-2fmw	0.02	0.098	-	-	0.882	0.029	0.194	0.777
0.3-2fmw	0.02	0.294	-	-	0.686	0.024	0.478	0.498
0.5-2fmw	0.02	-	0.49	0.49	-	0.02	0.678	0.302
0.7-2fmw	0.02	-	0.686	0.294	-	0.018	0.825	0.157
0.9-2fmw	0.02	-	0.882	0.098	-	0.016	0.938	0.046
1-2fmw	0.02		0.980	0.000	-	0.015	0.985	0.000

Methanol-water mixtures were prepared by mixing m and d-w, or d-m and w in appropriate relative amounts. To prepare *fmw* mixtures, we first prepared fa-m, fa-(d-m), fa-w, and fa-(d-w) mixtures by dissolving paraformaldehyde (pFa) in m, d-m, w, and d-w, respectively in a microwave reactor. The mixture was heated to 80 ºC for 2 hours to ensure complete depolymerisation of pFa oligomers into its metastable monomeric forms (mm, md, and their deuterated isomers). Thereafter, they were mixed in the appropriate ratio (Table S3) to make the fa-(d-m)-w and fa-m-(d-w) mixtures.

Table S3: Weight of mixture components in gm to prepare the formaldehyde-methanol-water mixtures

Mixture	**Mole-fraction**				**Weight (g)**				
	x_w	x_m	x_{fa}	x_w/x_m	**w (w)**	**w (d-w)**	**w (m)**	**w (d-m)**	**w (pFa)**
0.0-mw	1	0	0			2	0		0
0.1-mw	0.9	0.1	0	9.00		1.8	0.32		0
0.3-mw	0.7	0.3	0	2.33		1.4	0.96		0
0.5-mw	0.5	0.5	0	1.00	0.9			1.8	0
0.7-mw	0.3	0.7	0	0.43	0.54			2.52	0
0.9-mw	0.1	0.9	0	0.11	0.18			3.24	0
1.0-mw	0	1	0	0.00	0			3.6	0
0.0-1fmw	0.99	0	0.01			1.98	0		0.03
0.1-1fmw	0.891	0.099	0.01	9.00		1.782	0.317		0.03
0.3-1fmw	0.693	0.297	0.01	2.33		1.386	0.950		0.03
0.5-1fmw	0.495	0.495	0.01	1.00	0.891			1.782	0.03
0.7-1fmw	0.297	0.693	0.01	0.43	0.535			2.495	0.03
0.9-1fmw	0.099	0.891	0.01	0.11	0.178			3.208	0.03
1.0-1fmw	0	0.99	0.01	0.00	0			3.564	0.03
0.0-2fmw	0.98		0.02			1.96	0		0.06
0.1-2fmw	0.882	0.098	0.02	9.00		1.764	0.314		0.06
0.3-2fmw	0.686	0.294	0.02	2.33		1.372	0.941		0.06
0.5-2fmw	0.49	0.49	0.02	1.00	0.882			1.764	0.06
0.7-2fmw	0.294	0.686	0.02	0.43	0.529			2.467	0.06
0.9-2fmw	0.098	0.882	0.02	0.11	0.176			3.175	0.06
1.0-2fmw	0	0.98	0.02	0.00	0			3.528	0.06

.

1c. SANS experiments and data fitting protocols

The prepared liquid mixtures were subjected to high intensity, high-q (scattering vector, Eq. 2) SANS experiments at the Quokka beamline of the ANSTO. The liquid mixtures, prepared in a Hellma® cell of 1 mm or 2 mm thickness, were kept at 4 ºC during measurements.

The scattering data are presented as a function of the scattering vector, q

$$q = \frac{4\pi}{\lambda}\sin\left(\frac{\theta}{2}\right) \qquad \text{(Eq. 2)}$$

where λ is the incident neutron wavelength and θ is the scattering angle. The sample-detector distance of 1.3 m was used in offset mode with an incident wavelength of λ = 5 Å, providing an effective q-range of 0.04 - 0.8 $Å^{-1}$. The new BNL detector at ANSTO has a high threshold, allowing us to obtain a 4 m collimation with 1.3 m detector distance without any attenuation. This infrastructure enabled us to use the high intensity neutron scattering measurements of our samples. The data were reduced from raw counts on the 2D detector to a radially averaged 1D scattering pattern, with the assumption of radially isotropic scattering. The sensitivity of each detector pixel was calibrated by comparing its response to a flat scatterer, and then the scattering from an empty Hellma® cell was subtracted. Further background subtraction is discussed in section 1.d. The absolute intensity scale was provided by normalising each sample for its thickness (1 or 2 mm), and then comparing the scattering from an empty beam measurement.

We used the data modelling program SASview to fit the SANS data. This program uses standard iterative least-squares fitting, in which selected parameters of the chosen cluster model (e.g. spherical and ellipsoid) can be refined to optimise the fit. Parameters were refined from several starting points to ensure that a global, rather than a local, minimum was found. For each mixture, the scattering curve (I_{sample}) had its respective background subtracted to provide the resulting curve (I) for further analysis (Eq. 3). For *mw* mixtures, the background was calculated as the volume fraction (Vf) weighted sum of

the m and d-w, or d-m and w scattering curves. However, for *fmw* mixtures, the background calculation was guided by molecular dynamics simulation, as explained in section 1.d. The Guinier model, sphere model, and the ellipsoid model were initially used to estimate the size of the molecular clusters. The scales for the sphere and the ellipsoid model were defined as the *Vf* of the hydrogenated (i.e., not deuterated) molecules in *mw* mixtures and the hydrogenated molecules present within the first solvation shell for *fmw* mixtures.

$$I = I_{sample} - I_{background} \quad \text{(Eq. 3)}$$

There is also a probability of two solvated formaldehyde molecules interacting within the mixture giving rise to a variation in the scattering curve. The initial fitting using the sphere and the ellipsoid model do not account for the interparticle interactions that arises from the hydrophilic and the hydrophobic interactions between the solute molecules. Therefore, a structure factor was introduced via the sticky-hard-sphere (SHS) model. More details about the SHS model are provided in section

1d. Background subtraction guided by MD simulations

From the MD simulations, the solvation environment can be elucidated, i.e. the number of molecules present within a certain distance of the solute, the number of hydrogen bonds, and the spatial distribution of the molecules within the solvation shell. From the g(r)-com, the number of solvent molecules within the first solvation shell (until the first minimum) were identified and are summarised in Table S4. We considered the first solvation shell around methanol (in *mw*) or mm and md (in *fmw*) as the molecular cluster in the present study.

In order to subtract the scattering caused by the hydrogenated solvent molecules not forming any cluster, a factor χ was introduced (Eq. 4) to calculate the background. χ is the fraction of hydrogenated solvent molecules present within the cluster, which was calculated from the MD simulation data (Table S4). Using χ, the background scattering curves for $x_m \leq 0.3$ were calculated by combining the scattering curves for m and d-w (Eq. 5), whereas for $x_m \geq 0.5$, the curves were calculated by combining d-m and w (Eq. 6).

$$\chi_m = \frac{n_{\text{m - cluster}}}{n_{\text{m - total}}} \quad \text{(Eq. 4)}$$

$$I_{background} = (1 - \chi_m) V f_m \times I_m + (V f_{\text{d - w}}) I_{\text{d - w}} \quad \text{(Eq. 5)}$$

$$I_{background} = V f_{\text{d - m}} \times I_{\text{d - m}} + (1 - \chi_w) V f_w \times I_w \quad \text{(Eq. 6)}$$

An empirical composition of the cluster was derived using the coordination number of the first solvation shell (*g(r)-com*), which was then used to calculate the solute SLD (Table S5). The SLD of the solvent was taken as the bulk *Vf* weighted sum of the solvent SLDs (Table S5). The SLD of the cluster was calculated by the scattering length contribution of each atom forming the cluster (mm and m for $x_m \leq 0.3$, and mm and w for $x_m \geq 0.5$).

Table S4: Total number of solvent molecules that are present within the first solvation shell of solvated formaldehyde molecules and the total number of solvent molecules simulated

x_m	$n_{\text{m - cluster}}$ #	$n_{\text{w - cluster}}$ *	$n_{\text{m - total}}$ $	$n_{\text{w - total}}$ &
0.1-1fmw	156	1189	500	4500
0.3-1fmw	395	1406	1500	3500
0.5-1fmw	561	480	2500	2500
0.7-1fmw	684	255	3500	1500
0.9-1fmw	780	71	4500	500
0.1-2fmw	307	2319	500	4500
0.3-2fmw	764	1525	1500	3500
0.5-2fmw	949	1065	2500	2500
0.7-2fmw	1320	604	3500	1500
0.9-2fmw	1602	175	4500	500

#Total number of methanol within the first solvation shell around all the formaldehyde molecules in the simulation box.
*Total number of water molecules within the first solvation shell around all the formaldehyde molecules in the simulation box.
$Total number of methanol molecules in the simulation box.
&Total number of water molecules in the simulation box.

Table S5: Physical and chemical characteristics of the molecular cluster and the calculated SLDs used for curve fitting.

Mixture	Empirical Composition	Density	Solute SLD ($\times 10^6$)	Solvent SLD ($\times 10^6$)
0.1/0.3-mw	COH_4	0.792	-0.377	6.335
0.5/0.7/0.9-mw	H_2O	0.996	-0.559	5.805
0.0-1fmw	$CO_2D_2H_2$	1.000	2.9025	6.3351
0.1-1fmw	$C_{5.12}O_{5.12}H_{18.48}$	0.842	-0.1681	5.0180
0.3-1fmw	$C_{9.9}O_{9.9}H_{37.6}$	0.815	-0.2704	3.0968
0.5-1fmw	$C_2O_{11.61}H_2D_{23.22}$	0.996	0.7022	3.8775
0.7-1fmw	$C_2O_{7.11}H_2D_{14.22}$	0.997	1.3497	4.7991
0.9-1fmw	$C_2O_{3.43}H_2D_{6.86}$	0.998	2.7300	5.5071

1-1fmw	$C_2O_2H_2D_4$	1.000	4.0202	5.8048
0.0-2fmw	$CO_2D_2H_2$	1.000	2.9025	6.3351
0.1-2fmw	$C_{5.07}O_{5.07}H_{18.28}$	0.843	0.6107	5.0406
0.3-2fmw	$C_{9.64}O_{9.64}H_{36.56}$	0.816	-0.2677	3.1427
0.5-2fmw	$C_2O_{12.65}H_2D_{25.3}$	0.996	0.6107	3.9172
0.7-2fmw	$C_2O_{7.04}H_2D_{14.08}$	0.997	1.3651	4.8175
0.9-2fmw	C2O3.75H5.5D4	0.997	2.5332	5.5165
1-2fmw	$C_2O_2H_2D_4$	1.000	4.0202	5.8048

1e. Introduction of structure factor via sticky-hard-sphere (SHS) model

The SHS model describes a structure factor for the interaction of non-ionic cluster particles which, consequently, is suitable for the present study. A potential well is defined by the particle diameter (σ), the depth (U_0), and the thickness (Δ) of the well (Fig. 1). However, in SHS model, the depth and the thickness are modelled as more two more physically realisable parameters, namely, the perturbation $\left(\tau = \frac{\Delta}{\Delta + \sigma}\right)$ and the stickiness $\left(\epsilon = \frac{1}{12\tau} exp\left(\frac{U_0}{kT}\right)\right)$. The τ was set to 0.1 for all the mixtures, which corresponds to a 1 Å thick potential well for a 9 Å radius cluster. The ϵ derived by using $\frac{U_0}{kt}$ as the potential of mean force (PMF) at the first peak of the radial pair distribution function between two metastable monomers of formaldehyde. The PMF between two species is defined as the work done needed to bring them from infinite separation in the bulk environment to distance r from each other and is mathematically given as, $PMF = -\ln(g(r)) + \ln(g(\infty))$. The r was considered at the distance of maximum interaction, i.e. the distance of the first peak in the radial pair distribution function *g(r)*.

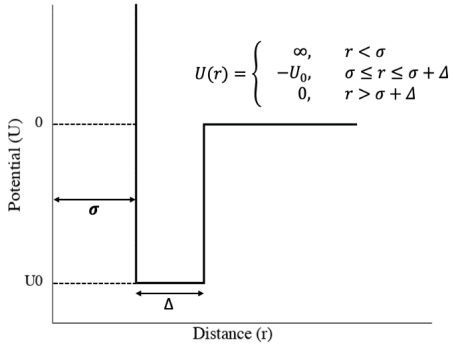

Figure S1. Square-well potential used in the sticky-hard-sphere model.

2. RESULTS

2a. Overview of all the SANS fitting curves

Figure S2 shows all the background subtracted scattering curve for the mixtures subjected to SANS measurements. It is evident that for scattering curves with $x_m \geq 0.5$ show low intensity after background subtraction and also does not results in a meaningful clustering when subjected to cluster models.

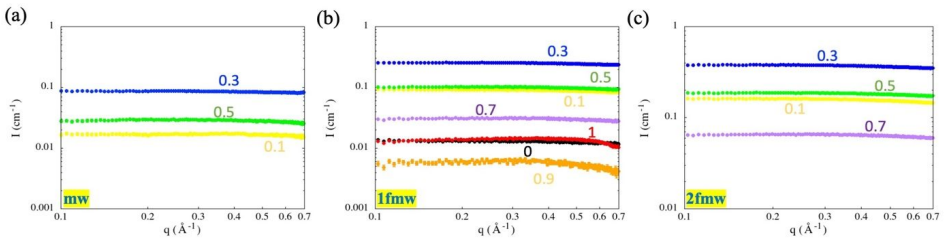

Figure S2: Scattering curves after background subtraction for (a) mw, (b) 1fmw, (c) 2fmw mixtures. The methanol mole-fractions (x_m) in the mixture is shown on each curve.

Table S6: The cluster size (Å) and scale or Vf obtained from fitting the SANS curve using Guinier, Sphere, Ellipsoidal, SHS-Sphere, and SHS-Ellipsoidal models

Sample	Guinier		Sphere		Ellipsoidal		SHS-Sphere		SHS-Ellipsoidal	
	Rg	Scale	R	Scale	R	Scale	R	Vf	R	Vf
0.1-mw	1.28	0.01	1.33	0.2	1.02	0.2	2.67	0.077	2.77	0.086
0.3-mw	2.48	0.01	1.51	0.49	1.28	0.49	3.01	0.111	3.02	0.111
0.5-mw	1.62	0.01	1.50	0.31	1.27	0.31	2.87	0.062	2.81	0.062
0.0-1fmw	1.02	0.01	3.12	0.017	3.32	0.017	3.27	0.019	3.50	0.015
0.1-1fmw	1.17	0.05	2.74	0.076	2.64	0.076	3.53	0.053	3.76	0.055
0.3-1fmw	2.00	0.05	3.59	0.139	3.94	0.139	4.96	0.075	6.18	0.100
0.5-1fmw	1.23	0.05	3.58	0.069	3.93	0.069	4.32	0.065	4.97	0.067
0.1-2fmw	1.64	0.05	2.70	0.148	2.56	0.148	3.72	0.076	4.06	0.084
0.3-2fmw	2.63	0.05	3.34	0.267	3.54	0.267	5.03	0.108	6.68	0.138
0.5-2fmw	1.56	0.05	3.26	0.149	3.39	0.149	4.76	0.076	5.17	0.116

2b. Volume fraction of molecular clusters

Fig. S3 shows the comparison of *Vf* obtained from the SHS-Sphere and SHS-Ellipsoid fits, the MD simulations, and the total hydrogenated molecules in the experimental mixture. The cluster *Vf* of all the 2fmw mixtures are higher than the corresponding 1fmw mixtures due to the increase in the number of clusters as the formaldehyde concentration is increased. Moreover, for both 1fmw and 2fmw

mixtures we observe same trends, in which the *Vf* of the clusters increased from x_m = 0.1 to 0.3 and then decreased for x_m = 0.5. This trend is consistent with the size of the clusters, which increased from 3.53 Å to 4.96 Å and then decreased to 4.32 Å, respectively.

For the SHS-Sphere and SHS-Ellipsoid models, the *Vf* estimation was using as a fitting parameter to achieve the desired fit whereas in the Sphere model the *Vf* was kept fixed as the *Vf* predicted by MD simulations. From the MD simulation the *Vf* was calculated as the shown in Eq. 8. For all the 1fmw mixtures (Fig. S3(a)), the *Vf* obtained from SANS fits closely matched with the MD *Vf*. However, for all the 2fmw mixtures (Fig. S3(b)), MD overestimates the *Vf* of the clusters compared to the SANS fits *Vf*.

$$MD\ Vf = \begin{cases} \chi_m \times Vf_m + Vf_{fa} & x_m < 0.5 \\ \chi_w \times Vf_w + Vf_{fa} & x_m \geq 0.5 \end{cases} \qquad \text{(Eq. 8)}$$

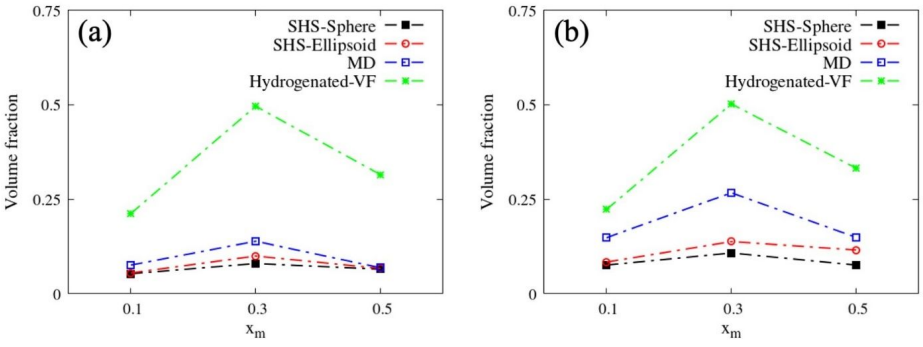

Figure S3: Comparison of Vf of the molecular clusters obtained from SANS data fits, MD simulations, and the hydrogenated molecules' bulk Vf. (a) 1fmw mixtures and (b) 2fmw mixtures.

The overestimation of MD *Vf* can be explained by the increased inter-cluster interaction. For example, the *g(r)-com*$_{\text{mm-mm}}$ showed that the mm-mm coordination number for the 0.1-1fmw mixture was 0.39 and for 0.1-2fmw it was 0.74. This increased coordination between mm molecules overestimates the χ_m (Eq. 4), as some methanol molecules are counted in the solvation shell of more than one interacting mm molecule.

Acknowledgement:

This research was funded by the Australian Government through the Australian Research Council's Discovery Projects funding scheme (project DP170104017). The authors appreciate the financial support of the Australian Centre for Neutron Scattering (ACNS), Australian Nuclear Science and Technology Organisation (ANSTO), for providing beamtime on the Quokka (Proposal No 7415). The authors gratefully acknowledge a generous allocation of computer resources through the Monash eResearch Centre at the Monash Advanced Research Computing Hybrid (MonARCH) HPC/HTC Cluster. This work benefited from the use of the SasView application, originally developed under NSF award DMR-0520547. SasView contains code developed with funding from the European Union's Horizon 2020 research and innovation programme under the SINE2020 project, grant agreement No 654000.

Reference:

(1) Dwivedi, S., S. H. Mushrif, A. L. Chaffee, and A. Tanksale Solvation Behaviour and Micro-Phase Structure of Formaldehyde-Methanol-Water Mixtures. *Journal of Molecular Liquids* **2020**, *301*, 112444.

(2) Kony, D., W. Damm, S. Stoll, and W. F. Van Gunsteren An Improved OPLS-AA Force Field for Carbohydrates. *J. Comput. Chem.* **2002**, *23* (15), 1416–1429.

(3) Mark, P. and L. Nilsson Structure and Dynamics of the TIP3P, SPC, and SPC/E Water Models at 298 K. *J. Phys. Chem. A* **2001**, *105* (43), 9954–9960.

(4) Delcroix, P., M. Pagliai, G. Cardini, D. Bégué, and B. Hanoune Structural and Spectroscopic Properties of Methanediol in Aqueous Solutions from Quantum Chemistry Calculations and Ab Initio Molecular Dynamics Simulations. *J. Phys. Chem. A* **2015**, *119* (2), 290–298.

(5) Humphrey, W., A. Dalke, and K. Schulten VMD: Visual Molecular Dynamics. *Journal of Molecular Graphics* **1996**, *14* (1), 33–38.

(6) Bussi, G., D. Donadio, and M. Parrinello Canonical Sampling through Velocity Rescaling. *The Journal of Chemical Physics* **2007**, *126* (1), 014101.

(7) Parrinello, M. and A. Rahman Crystal Structure and Pair Potentials: A Molecular-Dynamics Study. *Phys. Rev. Lett.* **1980**, *45* (14), 1196–1199.

(8) Berendsen, H. J. C., J. P. M. Postma, W. F. van Gunsteren, A. DiNola, and J. R. Haak Molecular Dynamics with Coupling to an External Bath. *The Journal of Chemical Physics* **1984**, *81* (8), 3684–3690.

(9) Martyna, G. J., M. L. Klein, and M. Tuckerman Nosé–Hoover Chains: The Canonical Ensemble via Continuous Dynamics. *The Journal of Chemical Physics* **1992**, *97* (4), 2635–2643.

(10) Darden, T., D. York, and L. Pedersen Particle Mesh Ewald: An $N \cdot \log(N)$ Method for Ewald Sums in Large Systems. *The Journal of Chemical Physics* **1993**, *98* (12), 10089–10092.

(11) Gaca, K. Z., J. A. Parkinson, L. Lue, and J. Sefcik Equilibrium Speciation in Moderately Concentrated Formaldehyde–Methanol–Water Solutions Investigated Using ^{13}C and ^{1}H Nuclear Magnetic Resonance Spectroscopy. *Ind. Eng. Chem. Res.* **2014**, *53* (22), 9262–9271.

Chapter 5

5 Atomistic Mechanism of thermal transformation in a Zr-Metal Organic Framework, MIL-140C

5.1 Overview

Our group recently reported a thermally decomposed Ru encapsulated Zr-MOF for excellent kinetics and high yield of CO_2 hydrogenation to methane. Experimentally the morphology of the final structure is determined as ZrO_x, similar to the tetragonal phase of ZrO_2. In this chapter, we first develop and after that simulate the thermal decomposition of MIL-140C. We first report the mechanisms governing the structure collapse under high temperatures. We also report the morphology of the thermally decomposed MOF. Understanding the atomistic mechanism will enable us to design these MOF-derived nanomaterials better.

5.2 Included Publication

This work has been published in The Journal of Physical Chemistry Letters (American Chemical Society) in December 2020:

Dwivedi, S., Kowalik, M., Rosenbach, N., Alqarni, D. S., Shin, Y. K., Yang, Y., ... & van Duin, A. C. (2020). Atomistic Mechanisms of Thermal Transformation in a Zr-Metal Organic Framework, MIL-140C. *The Journal of Physical Chemistry Letters*, *12*, 177-184.

THE JOURNAL OF PHYSICAL CHEMISTRY Letters

pubs.acs.org/JPCL Letter

Atomistic Mechanisms of Thermal Transformation in a Zr-Metal Organic Framework, MIL-140C

Swarit Dwivedi, Malgorzata Kowalik, Nilton Rosenbach, Dalal S. Alqarni, Yun Kyung Shin, Yongjian Yang, John C. Mauro, Akshat Tanksale, Alan L. Chaffee,* and Adri C.T. van Duin*

Cite This: J. Phys. Chem. Lett. 2021, 12, 177−184 Read Online

ACCESS | Metrics & More | Article Recommendations | Supporting Information

ABSTRACT: To understand the mechanisms responsible for thermal decomposition of a Zr-MOF (MIL-140C), we perform atomistic-scale molecular dynamics (MD) simulations and discuss the simulation data in comparison with the TEM images obtained for the decomposed Zr-MOF. First, we introduce the ReaxFF parameters suitable for the Zr/C/H/O chemistry and then apply them to investigate the thermal stability and morphological changes in the MIL-140C during heating. Based on the performed simulations we propose an atomic mechanism for the collapse of the MIL-140C and the molecular pathways for carbon monoxide formation, the main product of the MIL-140C thermal degradation. We also determine that the oxidation state of the ZrO_x clusters, evolved due to the thermal degradation, approximates the tetragonal phase of ZrO_2. Both simulations and experiments show a distribution of very small ZrO_x clusters embedded in the disrupted organic sheet that could contribute to the unusual high catalytic activity of the decomposed MIL-140C.

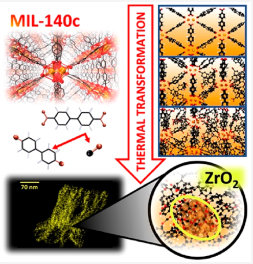

Metal organic frameworks (MOFs) consist of an ordered array of metal clusters connected via organic molecules defined as the linkers. There is an extraordinary variety of novel structures, both known and conceivable.[1] Researchers have explored MOFs as potential heterogeneous catalysts due to their high porosity, active site dispersion, and large surface area.[2−7] There are many examples of their successful use as a catalyst in solvent systems at relatively mild temperatures,[8−11] whereas there are not quite as many examples for gas-phase catalytic reactions, since high temperatures and pressures can lead to decomposition of the MOF structures.[3,5,12] For many MOFs, poor stability in water also limits their application for aqueous phase catalytic reactions.[13,14] Over the years, researchers have tried to overcome these limitations by choosing a combination of metal cluster and linkers that provide improved binding strength[15,16] and by functionalizing the organic linkers for improved hydrophobicity, adsorption capacity, framework flexibility,[17,18] etc.

Zr-MOFs, where the metal cluster is a zirconium oxide-based coordinated complex, are inherently more stable at elevated temperatures (e.g., 700−800 K) and in water.[12,17,19,20] Nevertheless, when subjected to temperatures higher than 800 K, Zr-MOFs start losing mass due to the decomposition of the organic linkers and result in the evolution of organic gaseous molecules[21,22] and the characteristics of the residual solid change. The chemistry associated with the thermal decomposition of these MOFs is still not well studied.[12,23−25] Yet, in select circumstances, decomposed MOF structures, incorporating active metal atoms, have demonstrated exceptional activity for gas-phase catalytic reactions.[26,27] MIL-140C is a Zr-MOF with ZrO_7 metal oxide-based clusters with BPDC (biphenyl dicarboxylic acid) linkers. MIL-140C is a good candidate for separating biomolecules from aqueous solutions of amino acids and is also being explored as a potential heterogeneous catalyst.[14,19] Recently, a thermally decomposed MIL-140C with Ru and a small proportion of modified linkers was reported as a stable catalyst for CO_2 conversion into methane.[27] It was suggested that after the decomposition, the metal clusters are finely dispersed within the disrupted or even carbonized organic linkers, which is responsible for the exceptional catalytic properties of the thermally decomposed MOFs.[28,29] Understanding thermal decomposition of MIL-140C is crucial for the development of a controlled pyrolysis route to candidate catalytic materials at temperatures and pressures appropriate to gas-phase reactions.[30]

Here, we combine ReaxFF molecular dynamics and experiments to understand the thermal decomposition of MIL-140C. The ReaxFF force field has been successfully applied to the understanding of the thermal stability,[24,25] the water stability,[23,31] and the glass-forming ability[32−34] of a number of different MOFs. First, a ReaxFF parameter set suitable for the Zr/C/H/O chemistry simulations is introduced. Then, the proposed ReaxFF force field is used to

Received: September 24, 2020
Accepted: November 30, 2020
Published: December 15, 2020

investigate the thermal stability and the morphological changes during thermal decomposition of MIL-140C. We determine a sequence of the organic linker detachment and further degradation. Specifically, the detachment of the linkers with no additional $\pi-\pi$ stacking interactions (named cross-linkers) is followed by the detachment of the ones with an extra $\pi-\pi$ stacking interactions between them (named vertical linkers). Finally, we propose reaction pathways for carbon monoxide production and analyze a structure of the evolved metal clusters within disrupted organic linkers and compare with the TEM images obtained for the decomposed Zr-MOF.

Development of the ReaxFF Parameter Set. A ReaxFF force field describing Zr-MOF is developed by combining previously tested Zr/O/H parameters for yttria-stabilized zirconia (YSZ) solid oxide fuel cell membranes[35] and the C/H/O parameters derived for glycine.[36] The original Zr/O/H force field parameters have been trained against extensive density functional theory (DFT) data on a range of systems that include Mulliken charge populations, equations of state for several phases of ZrO_2, and surfaces energies for the orthorhombic ZrO_2 phase. The C/H/O parameters have also been extensively optimized to reproduce the DFT-derived energies and used to investigate the glycine tautomerization process in the gas phase and in water. The original Zr/C/H/O parameters are further optimized against the DFT data for the description of the Zr-MOF materials. The training data set includes atomic charges, bond lengths, valence and dihedral angles, and heats of formation of Zr-MOF nodes, modeled as clusters with different degrees of coordination, whereby selected linkers are truncated as formate/benzoate groups. All DFT data are calculated with the Gaussian 09 package[37] using the M06-2X functional[38] and the 6-31g(d,p) all-electron basis set[39] to describe O, C, and H atoms, whereas Zr atoms are described with the LANL2DZ effective core potential.[40] These DFT data were obtained for the finite cluster models comprising the $Zr_6O_4(OH)_4$ node with degrees of coordination ranging from 8 to 12 formate/benzene-1,4-dicarboxylates (BDC) (eq 1).

$$Zr_6O_4(OH)_4L_{12} \underset{+HL}{\overset{-HL}{\rightleftharpoons}} Zr_6O_5(OH)_3L_{11} \underset{+HL}{\overset{-HL}{\rightleftharpoons}} Zr_6O_6(OH)_2L_{10} \underset{+HL}{\overset{-HL}{\rightleftharpoons}} Zr_6O_7OHL_9 \underset{+HL}{\overset{-HL}{\rightleftharpoons}} Zr_6O_8L_9 \quad (1)$$

The training set included energies for the formation of such finite models from $(ZrO_2)_n$ and formic or terephthalic acid with n ranging from 1 to 6. We also include energies for the removal of formate/benzene-1,4-dicarboxylates linkers, calculated based on the following reactions in which the labile $\mu-$OH proton is also removed to maintain neutrality. ReaxFF and DFT energies for these reactions are tabulated in a table given in the Supporting Information.

The force field optimization was performed with the ReaxFF standalone program, using a successive one-parameter parabolic extrapolations algorithm. In such procedure, each parameter is allowed to modify within a suitable range to ensure physically realistic final values. We performed a parameter search by looping optimization multiple times and picking the force field with the lowest total error given by the sum of the least-squares of the deviations between the ReaxFF calculation and the corresponding DFT value running over all training set points.

In order improve the description of Zr-MOF, valence and dihedral angle parameters to describe double-well angular terms (O−Zr−O), rotation (Zr−O−C−C), and tilting (Zr−O−C−O) out of the plane of the organic linkers,[41] not available in the original force fields, were also included in the new force field. We use typical values, taken from the ReaxFF parameters database for similar systems, or the mean values of the allowed interval as initial guess for these parameters. Although Zr/C bond interactions were not considered during parameters optimization, since formation of such bonds is not expected in the oxygen-rich environment of the simulations, as suggested elsewhere,[25] we include off-diagonal terms to describe nonbonded interactions for such a pair also using the mean values of the allowed interval as an initial guess for the parameters.

Reactive Molecular Dynamics Simulation Methodology. All atomistic simulations are performed with the proposed ReaxFF parameter set implemented in the ADF Modeling Suite.[42] The initial structure of MIL-140C is the DFT optimized geometry reported elsewhere.[43] We use the Berendsen thermostat[44] with a damping constant of 100 fs and the Berendsen barostat[44] with a damping constant of 1500 fs for all presented simulations. We chose a 0.25 fs time step and the periodic boundary conditions in all three dimensions.

To test the proposed ReaxFF parameter set against the physical properties of MIL-140C, a constant pressure simulation (NPT) at a temperature (T = 300 K) and atmospheric pressure (P = 1 atm) is initially performed. An average density obtained from this NPT simulations is 1.097 g/cm^3 (seen in Figure 1(a)), whereas the experimental density[43] is ∼1.23 g/cm^3, indicating ∼10% discrepancy. This density remains stable over the longer simulation time that is shown in Figure S2 in the Supporting Information. The cell angle (β = 85.02°) after 150 ps NPT simulation remains similar to the starting DFT structure (β = 84.51°). A detailed comparison of cell parameters with previously reported MIL-140C structures (experiments and simulations) is included in the Supporting Information. To emulate thermal degradation of this system, we applied the following simulation scenario. The equilibrated system (150 ps at 300 K) is first heated to 2000 K at a rate of 2 K/ps and is followed by a short (50 ps) constant temperature simulation at 2000 K. Then, the system is cooled to 300 K at a rate of 4 K/ps. This decomposed MOF is kept at constant temperature (T = 300 K) for an extra 50 ps, so the structural changes of the Zr−O clusters can be assessed. To ensure the consistency of the simulation, we extracted the two statistically different initial configurations (after 100 and 110 ps equilibration at 300 K) and subjected these initial structures to the same heating and cooling regime. Both configurations resulted in a similar decomposition behavior to the structure after the 150 ps equilibration discussed in this work (see Supporting Information, section 2). Additionally, the structures of MIL-140C at 600 K and 800 K are extracted from the simulation trajectory during the heating stage and subjected to 100 ps constant temperature simulations. While the MIL-140C framework remains stable at 600 K, some of the organic linkers were observed to dissociate from the zirconia nodes at 800 K. This observation agrees with the experimentally observed degradation temperature to be around 700 to 800 K.[19,43] Nevertheless, thermal degradation of the MOF measured in minutes/hours is not accessible for MD simulation times (measured in nanoseconds), so all simulations reported here are performed at relatively higher

https://dx.doi.org/10.1021/acs.jpclett.0c02930
J. Phys. Chem. Lett. 2021, 12, 177−184

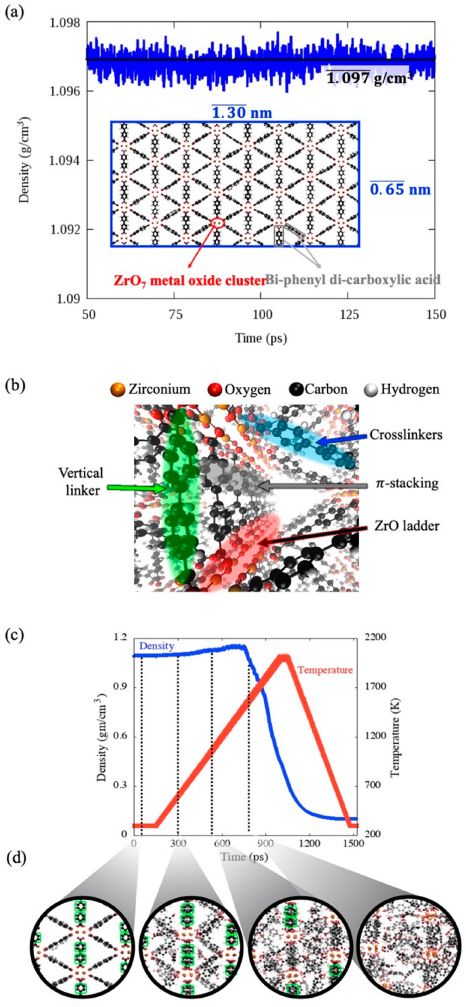

Figure 1. (a) The density fluctuation for MIL-140c and its molecular structure. The average value of the equilibrated density of MIL-140c as a function of time, after the initial 150 ps of NPT simulations at constant temperature T = 300 K and pressure P = 1 atm, is 1.097 g/cm^3. The molecular structure of MIL-140C is given in an inset blue box. The average values for width and height of the fluctuating simulations box are 1.30 and 0.65 nm, respectively, where the depth (not shown) is 0.26 nm. (b) The structural features of MIL-140C structure. (c) The density and temperature of the system versus the time. (d) The progression of the structural change versus the temperature during heating at 300, 800, 1220, and 1630 K, from left to right. Thermally stable vertical linkers in (c) are highlighted in green for better visualization.

temperatures that enable us to observe more reactions in a shorter time.

Experimental Methodology. For the catalytic applications of MIL-140C, generally, some of the organic linkers are replaced with a similar linker with the capability of binding a noble metal. Our recent work demonstrated one such modified MIL-140C (m-MIL-140C) against which we compare the simulation results. Here, 10% of 4,4′-biphenyldicarboxylic acid linkers were replaced with 2,2-bipyridine-5,5-dicarboxylic acid linkers. The modified MIL-140C with mixed linkers was synthesized by adapting the synthesis procedure for MIL-140C previously reported by Liang et al.[45] The thermal decomposition of m-MIL-140C was achieved in a vertical quartz u-tube reactor in a ceramic oven for 4 h at 500 °C under CO_2 + H_2 environment.[27] Transmission electron microscopy (TEM) for the thermally transformed m-MIL-140C was performed using the FEI Tecnai G2 T20 transmission electron microscope. More details on the experimental methodology can be found elsewhere.[27] Since only 10% of the linkers were modified and the TGA curve of the m-MIL-140C is similar to that of MIL-140C, we do not expect a significant difference in the morphology of the decomposed structures.

Mechanism of Framework Collapse. In Figure 1(b), the structural elements of MIL-140C at 300 K are indicated, i.e., an array of zirconium oxide (ZrO ladder) and two types of the organic linkers. The cross-linkers connect these ladders diagonally, and vertical linkers connect the ladders vertically with additional $\pi-\pi$ stacking interactions between them. Figure 1 (c) shows the thermal history of MIL-140C and its density as a function of time. The density profile shows that the structure remains stable for the first 150 ps at 300 K. After this first 150 ps, the density increases linearly from 1.097 g/cm^3 to 1.108 g/cm^3 with temperature increasing from 300 K (150 ps) to 750 K (375 ps) and then nonlinearly increasing up to 1500 K (750 ps). The linear increase in the density is typically attributed to the negative thermal expansion coefficient of MIL-140C (Supporting Information) and other similar Zr-MOFs are already reported for negative thermal expansion coefficient.[46,47] However, the nonlinear increase in density is due to the detachment of the linkers from the metal clusters, first observed when the system reaches the temperature of 750 K. The structures observed in the simulations at temperatures 300, 800, 1220, and 1630 K are presented in Figure 1 (d).

The initial detachment of the cross-linkers from the metal ladders observed in our simulation agrees well with the experimentally reported decomposition temperature of MIL-140C (~750 K).[19] The vertical linkers are relatively more stable than the cross-linkers due to the additional stability provided by the π stacking (Figure 1(b)). Moreover, in the DFT optimized structure,[43] the Zr−O−(C) bond length for the vertical linker is 2.197 Å. In contrast, for cross-linkers, it is 2.215 Å, which indicates the additional stability of vertical linker in the DFT optimized structure. At 1220 K (610 ps), the vertical linkers are relatively stable and the cross-linkers break but remain in the pore space. The cross-linkers then reconfigure themselves within the pores, facilitating the contraction and a nonlinear increase in the density. From approximately 1500 K, the vertical linkers start to detach, and the density rapidly falls as a consequence. For the vertical linker degradation, this temperature clearly overestimates the experimental one[43] but, as mentioned previously, allows for the thermal degradation to be simulated in a much shorter time.

Chemical Behavior of Structural Decomposition. Figure 2(a) shows the time evolution of the potential energy (E_p) per atom

https://dx.doi.org/10.1021/acs.jpclett.0c02930
J. Phys. Chem. Lett. 2021, 12, 177−184

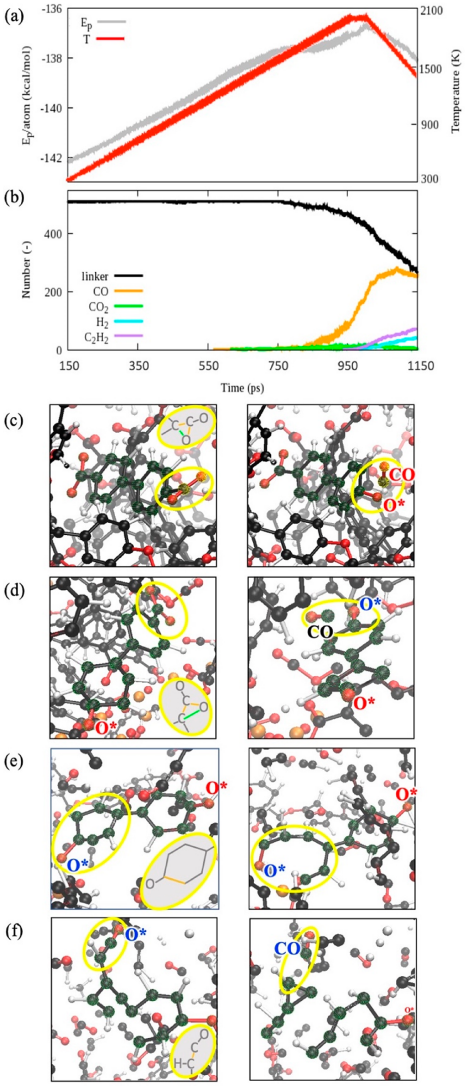

Figure 2. Decomposition of the organic linker and the evolution of gaseous molecules, where (a) shows the potential energy per atom with time, (b) shows the number of organic linkers and other gaseous molecules evolved, and (c–f) show the reaction pathway (left to right) of CO production from the broken linker.

and the thermal history of the system. A linear increase in potential energy is observed until around 700 ps, closely correlated to the constant heating rate. However, after 700 ps, even though the system's temperature continues to increase at the same rate, the potential energy starts to increase at a slower rate due to the gasification (decomposition) of the linkers. Further, after 850 ps, the clustering of the gasified fragments along with the expanding simulation box (to maintain constant pressure) results in further fluctuations in E_p. The E_p decreases after 900 ps as a result of cooling. Figure 2(b) shows how the number of biphenyldicarboxylate linkers and small molecules evolve during the simulation. Although the linkers' detachment starts at around 400 ps (800 K), their decomposition into smaller molecules occurs from about 700 ps (1500 K).

Carbon monoxide is a major product of BPDC linker degradation, and a relatively limited production of acetylene and hydrogen at higher temperature is also observed. These are products of phenyl ring degradation. Figures 2(c) and (d) show the formation of two CO molecules that follows the same molecular pathway. The schematic for this carbon monoxide production is presented in the insets highlighted in gray (the breaking bonds are shown in orange and forming ones in green). As can be seen, the broken bonds allow for a release of one carbon monoxide molecule at each end of the linker, leaving connected phenyl rings with the reactive oxygen atoms. Figure 2(e) and (f) show the phenyl ring's opening that eventually releases another CO molecule. However, some of these reactive rings reorganize themselves into a heteroatom 7-membered ring, as seen in Figure 3(a), and can become a source of hydrogen or acetylene molecules. The molecular pathways for these limited H_2 or C_2H_2 productions resulting in a release of yet another CO molecule, characteristic for higher temperatures, are presented in Figure 3(b).

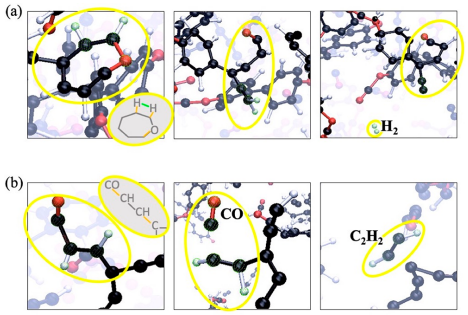

Figure 3. Reaction of the decomposition leading to the production of a (a) H_2 molecule and (b) C_2H_2 molecule. The red bonds in the schematic structure are broken and the green bond is formed during the reaction (left to right). A molecule of CO also forms during the formation of C_2H_2.

Morphology of the Decomposed Structure. The size of the evolved Zr-nanoclusters, as well as the oxidation state of zirconium, can be estimated based on the radial pair distribution function ($g(r)$) of the zirconium atoms for the final structure of the decomposed MOF based on the further short NPT simulation at 300 K. In Figure 4(a), a part of the decomposed MIL-140C structure at 300 K is presented. The Zr atoms are indicated as a surface for a better representation of the nanoclusters (the oxygen atoms that belong to a given cluster are not visible in this representation). This final morphology shows the ZrO_x nanoclusters embedded in a sheet of disrupted organic liners where pores are evident. The TEM images for the thermally decomposed m-MIL-140C are presented in Figure 4(b) for

https://dx.doi.org/10.1021/acs.jpclett.0c02930
J. Phys. Chem. Lett. 2021, 12, 177−184

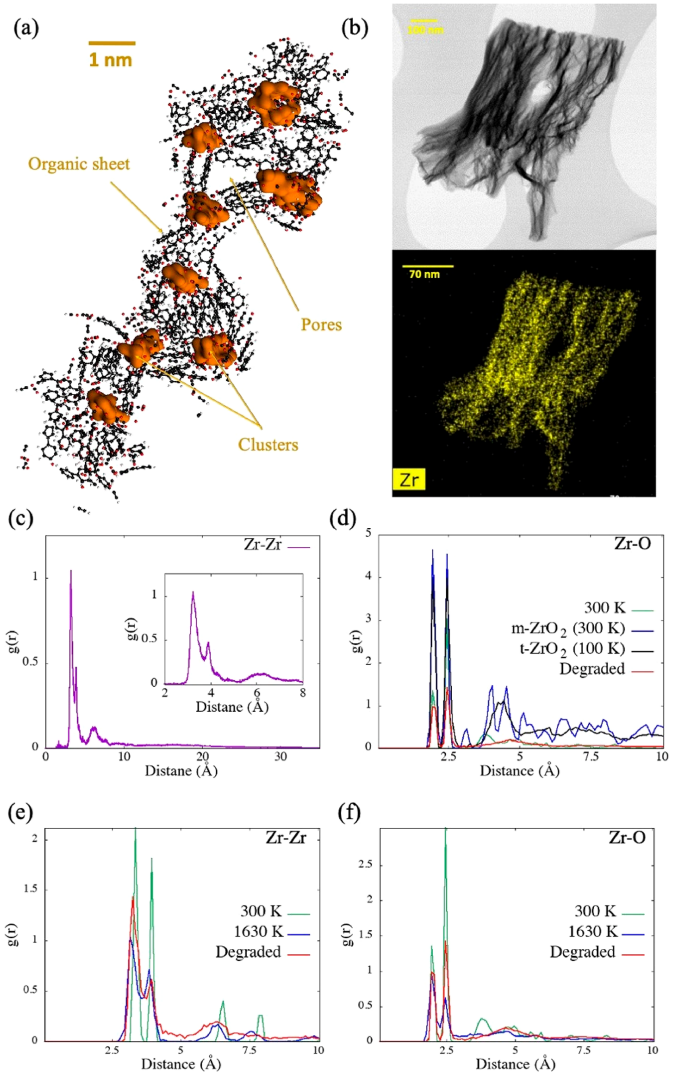

Figure 4. Morphology of the thermally decomposed MIL-140c where (a) is the structure at 300 K after heating to 2000 K, (b) the TEM of the decomposed modified-MIL-140c in CO_2 + H_2 environment and the elemental analysis with Zr distribution.[27] Radial pair distribution functions, g(r), are also illustrated, where (c) shows Zr - Zr in the decomposed structure and (d) shows Zr - O in the final degraded structure as compared to m-ZrO_2 (300 K), t-ZrO_2 (100 K), MIL-140c (300 K). Plots (e) & (f) show g(r) between Zr−Zr and Zr−O, respectively, during the decomposition.

comparison. These images show a characteristic fine distribution of the Zr-nanoclusters that corresponds well to the Zr-nanoclusters observed in our simulations. As we can see in Figure 4 (c), the $g(r)$ fades to 0 between 10 Å and 20 Å, indicating that pairs of Zr atoms are not ordered after 20 Å. As one can notice, the calculated $g(r)$ for zirconium atom pairs is not approaching 1, which indicates its solid-state character for the considered distances (smaller than 20 Å). The size of the nanoclusters is qualitatively estimated to be on the order of ∼1 nm as shown by the scale bar in Figure 4 (a). The cluster size is likely to depend upon the temperature regime as seen in our earlier experiments with m-MIL-140C.[27] TEM and PXRD data

https://dx.doi.org/10.1021/acs.jpclett.0c02930
J. Phys. Chem. Lett. 2021, 12, 177−184

were used to measure the size of ZrO_x nanoclusters, and the cluster size increased from 2 to 3 to 5 nm when we increased the decomposition temperature from 500 to 850 °C. The temperature regime presented in this work does not necessarily correspond to the experimental temperatures of either 500 or 800 °C; however, the sizes of the nanoclusters are of similar order. Therefore, there is scope of studying different temperature regimes to identify the correlation between the computational temperature regime and the experimental decomposition temperature.

In Figure 4 (d), the $g(r)$ value for Zr−O atom pairs for the decomposed structure is compared to the Zr−O $g(r)$ value for MIL-140C at 300 K, m-ZrO_2 (monoclinic) simulated at 300 K, and t-ZrO_2 (tetragonal) at 100 K. As the structure decomposes, the Zr−O(Zr) bond (the first peak) remains nearly the same, but the second peak, which corresponds to the Zr−O(C) bond, decreases in intensity. The simulation of a crystalline ZrO_2 with the monoclinic structure shows the third peak near 3 Å, which is absent in the degraded structure (compare the black and red line in Figure 4(d)). Nonetheless, the $g(r)$ peaks' observed position can indicate that the morphology of the degraded metal cluster is similar to that of the tetragonal ZrO_2 structure. Again, the calculated radial distribution functions are not approaching 1, indicating their solid-state character for the considered distances (<10 Å).

During the decomposition, the long-range order (third and fourth peak) is partially maintained for the Zr−Zr (Figure 4(e)) at 1630 K and is eventually lost in the final structure at 300 K. However, for Zr−O (Figure 4(f)), the long-range order is lost at 1630 K due to the detachment of linkers. It is also evident from the Zr−O peaks (Figure 4(f)) that the second peak intensity significantly decreases due to the reduced number of Zr−O(C) bonds, indicating the formation of the ZrO_x cluster. While only one set of heating/cooling conditions is applied in the current study, the thermal treatment and atmosphere could play an essential role in controlling the final morphology of these clusters. Therefore, future research is needed to investigate the possible variations of the evolution of these metal clusters.

In summary, a ReaxFF parameter set suitable for Zr-MOFs simulations are presented and used to investigate the thermal decomposition of MIL-140C. For temperatures lower than 750 K, we observe a linear increase in the system density, which can be attributed to the negative thermal expansion coefficient. The nonlinear rise in density above 800 K is due to the organic linkers' detachment from the metal clusters. Further, the decomposition of the linkers due to heating of the system results in formation of gaseous molecules, mainly carbon monoxide. The thermally degraded MIL-140C consists of the ZrO_x metal nanoclusters embedded in disrupted organic linkers. The size of these metal clusters is estimated to be on the order of 1 nm, whereas the Zr-coordination state changed from a Zr with seven O neighbors in (MIL-140C) to a coordination state relevant to condensed-phase monoclinic or tetragonal ZrO_2.

■ ASSOCIATED CONTENT

Supporting Information

The Supporting Information is available free of charge at https://pubs.acs.org/doi/10.1021/acs.jpclett.0c02930.

Supporting information file with additional details of the development and consistency of the ReaxFF force field (PDF)

ReaxFF force field parameters for Zr-MOFs (TXT)

■ AUTHOR INFORMATION

Corresponding Authors

Alan L. Chaffee − *School of Chemistry, Monash University, Clayton 3800, Victoria, Australia;* orcid.org/0000-0001-5100-6910; Email: alan.chaffee@monash.edu

Adri C.T. van Duin − *Department of Mechanical Engineering, The Pennsylvania State University, University Park, Pennsylvania 16802, United States;* orcid.org/0000-0002-3478-4945; Email: acv13@psu.edu

Authors

Swarit Dwivedi − *Department of Chemical Engineering, Monash University, Clayton 3800, Victoria, Australia;* orcid.org/0000-0002-4639-5576

Malgorzata Kowalik − *Department of Mechanical Engineering, The Pennsylvania State University, University Park, Pennsylvania 16802, United States*

Nilton Rosenbach − *Centro Universitário Estadual da Zona Oeste, 23070-200 Campo Grande, Rio de Janeiro, Brazil*

Dalal S. Alqarni − *School of Chemistry, Monash University, Clayton 3800, Victoria, Australia*

Yun Kyung Shin − *Department of Mechanical Engineering, The Pennsylvania State University, University Park, Pennsylvania 16802, United States;* orcid.org/0000-0001-8198-001X

Yongjian Yang − *Department of Materials Science and Engineering, The Pennsylvania State University, University Park, Pennsylvania 16802, United States*

John C. Mauro − *Department of Materials Science and Engineering, The Pennsylvania State University, University Park, Pennsylvania 16802, United States;* orcid.org/0000-0002-4319-3530

Akshat Tanksale − *Department of Chemical Engineering, Monash University, Clayton 3800, Victoria, Australia;* orcid.org/0000-0002-7087-0912

Complete contact information is available at: https://pubs.acs.org/10.1021/acs.jpclett.0c02930

Notes

The authors declare no competing financial interest.

■ ACKNOWLEDGMENTS

S.D., M.K., Y.K.S., A.C., and A.C.T.vD. acknowledge funding from the Penn State/Monash 2018 Collaboration Development funds. This project is also partially funded by the U.S. Department of Energy grant no. DE-EE0008195. The authors gratefully acknowledge a generous allocation of computer resources through the Monash eResearch Centre. Simulations in this work were also conducted, in part, with Advanced Cyberinfrastructure computational resources provided by the Institute for Cyber Science at The Pennsylvania State University (https://ics.psu.edu/).

■ REFERENCES

(1) Batten, S. R.; Neville, S. M.; Turner, D. R. *Coordination Polymers: Design, Analysis, and Application*; The Royal Society of Chemistry: 2009.

(2) Farrusseng, D.; Aguado, S.; Pinel, C. Metal−Organic Frameworks: Opportunities for Catalysis. *Angew. Chem., Int. Ed.* **2009**, *48* (41), 7502−7513.
(3) Wu, C.-D.; Zhao, M. Incorporation of Molecular Catalysts in Metal−Organic Frameworks for Highly Efficient Heterogeneous Catalysis. *Adv. Mater.* **2017**, *29* (14), 1605446.
(4) Llabrés i Xamena, F. X.; Abad, A.; Corma, A.; Garcia, H. MOFs as Catalysts: Activity, Reusability and Shape-Selectivity of a Pd-Containing MOF. *J. Catal.* **2007**, *250* (2), 294−298.
(5) Lee, J.; Farha, O. K.; Roberts, J.; Scheidt, K. A.; Nguyen, S. T.; Hupp, J. T. Metal−Organic Framework Materials as Catalysts. *Chem. Soc. Rev.* **2009**, *38* (5), 1450−1459.
(6) Gascon, J.; Corma, A.; Kapteijn, F.; Llabres i Xamena, F. X. Metal Organic Framework Catalysis: Quo Vadis? *ACS Catal.* **2014**, *4* (2), 361−378.
(7) Furukawa, H.; Cordova, K. E.; O'Keeffe, M.; Yaghi, O. M. The Chemistry and Applications of Metal-Organic Frameworks. *Science* **2013**, *341* (6149), 1230444−1230444.
(8) Liu, J.; Chen, L.; Cui, H.; Zhang, J.; Zhang, L.; Su, C.-Y. Applications of Metal−Organic Frameworks in Heterogeneous Supramolecular Catalysis. *Chem. Soc. Rev.* **2014**, *43* (16), 6011−6061.
(9) Doonan, C. J.; Sumby, C. J. Metal−Organic Framework Catalysis. *CrystEngComm* **2017**, *19* (29), 4044−4048.
(10) Oar-Arteta, L.; Wezendonk, T.; Sun, X.; Kapteijn, F.; Gascon, J. Metal Organic Frameworks as Precursors for the Manufacture of Advanced Catalytic Materials. *Mater. Chem. Front.* **2017**, *1* (9), 1709−1745.
(11) Trickett, C. A.; Helal, A.; Al-Maythalony, B. A.; Yamani, Z. H.; Cordova, K. E.; Yaghi, O. M. The Chemistry of Metal−Organic Frameworks for CO 2 Capture, Regeneration and Conversion. *Nat. Rev. Mater.* **2017**, *2* (8), 1−16.
(12) Howarth, A. J.; Liu, Y.; Li, P.; Li, Z.; Wang, T. C.; Hupp, J. T.; Farha, O. K. Chemical, Thermal and Mechanical Stabilities of Metal−Organic Frameworks. *Nat. Rev. Mater.* **2016**, *1* (3), 15018.
(13) Burtch, N. C.; Jasuja, H.; Walton, K. S. Water Stability and Adsorption in Metal−Organic Frameworks. *Chem. Rev.* **2014**, *114* (20), 10575−10612.
(14) Wang, C.; Liu, X.; Keser Demir, N.; Chen, J. P.; Li, K. Applications of Water Stable Metal−Organic Frameworks. *Chem. Soc. Rev.* **2016**, *45* (18), 5107−5134.
(15) Cavka, J. H.; Jakobsen, S.; Olsbye, U.; Guillou, N.; Lamberti, C.; Bordiga, S.; Lillerud, K. P. A New Zirconium Inorganic Building Brick Forming Metal Organic Frameworks with Exceptional Stability. *J. Am. Chem. Soc.* **2008**, *130* (42), 13850−13851.
(16) Li, H.; Eddaoudi, M.; O'Keeffe, M.; Yaghi, O. M. Design and Synthesis of an Exceptionally Stable and Highly Porous Metal-Organic Framework. *Nature* **1999**, *402* (6759), 276.
(17) Kim, M.; Cohen, S. M. Discovery, Development, and Functionalization of Zr(Iv)-Based Metal−Organic Frameworks. *CrystEngComm* **2012**, *14* (12), 4096−4104.
(18) Rowsell, J. L.; Yaghi, O. M. Effects of Functionalization, Catenation, and Variation of the Metal Oxide and Organic Linking Units on the Low-Pressure Hydrogen Adsorption Properties of Metal− Organic Frameworks. *J. Am. Chem. Soc.* **2006**, *128* (4), 1304−1315.
(19) Bai, Y.; Dou, Y.; Xie, L.-H.; Rutledge, W.; Li, J.-R.; Zhou, H.-C. Zr-Based Metal−Organic Frameworks: Design, Synthesis, Structure, and Applications. *Chem. Soc. Rev.* **2016**, *45* (8), 2327−2367.
(20) Schaate, A.; Roy, P.; Godt, A.; Lippke, J.; Waltz, F.; Wiebcke, M.; Behrens, P. Modulated Synthesis of Zr-based Metal−Organic Frameworks: From Nano to Single Crystals. *Chem. - Eur. J.* **2011**, *17* (24), 6643−6651.
(21) DeCoste, J. B.; Peterson, G. W.; Jasuja, H.; Glover, T. G.; Huang, Y.; Walton, K. S. Stability and Degradation Mechanisms of Metal−Organic Frameworks Containing the Zr6O4(OH)4 Secondary Building Unit. *J. Mater. Chem. A* **2013**, *1* (18), 5642.
(22) Kandiah, M.; Nilsen, M. H.; Usseglio, S.; Jakobsen, S.; Olsbye, U.; Tilset, M.; Larabi, C.; Quadrelli, E. A.; Bonino, F.; Lillerud, K. P. Synthesis and Stability of Tagged UiO-66 Zr-MOFs. *Chem. Mater.* **2010**, *22* (24), 6632−6640.
(23) Han, S. S.; Choi, S.-H.; van Duin, A. C. T. Molecular Dynamics Simulations of Stability of Metal−Organic Frameworks against H2O Using the ReaxFF Reactive Force Field. *Chem. Commun.* **2010**, *46* (31), 5713.
(24) Mohamed, S. A.; Chong, S.; Kim, J. Thermal Stability of Methyl-Functionalized MOF-5. *J. Phys. Chem. C* **2019**, *123* (49), 29686−29692.
(25) Huang, L.; Joshi, K. L.; van Duin, A. C. T.; Bandosz, T. J.; Gubbins, K. E. ReaxFF Molecular Dynamics Simulation of Thermal Stability of a Cu3(BTC)2 Metal−Organic Framework. *Phys. Chem. Chem. Phys.* **2012**, *14* (32), 11327.
(26) Lippi, R.; Howard, S. C.; Barron, H.; Easton, C. D.; Madsen, I. C.; Waddington, L. J.; Vogt, C.; Hill, M. R.; Sumby, C. J.; Doonan, C. J.; Kennedy, D. F. Highly Active Catalyst for CO 2 Methanation Derived from a Metal Organic Framework Template. *J. Mater. Chem. A* **2017**, *5* (25), 12990−12997.
(27) Alqarni, D. S.; Lee, C. W.; Knowles, G. P.; Vogt, C.; Marshall, M.; Gengenbach, T.; Chaffee, A. L. Ru-Zirconia Catalyst Derived from MIL140C for Carbon Dioxide Conversion to Methane. *Catal. Today* **2020**, DOI: 10.1016/j.cattod.2020.07.080, accepted for publication.
(28) Chaffee, A. CO2 Conversion to Hydrocarbons with MOF-Derived Materials as Catalysts. In *Abstracts of Papers of the American Chemical Society*; American Chemical Society: USA, 2019; Vol. *257*, Paper ENFL 47.
(29) Lippi, R.; D'Angelo, A. M.; Li, C.; Howard, S. C.; Madsen, I. C.; Wilson, K.; Lee, A. F.; Sumby, C. J.; Doonan, C. J.; Patel, J.; Kennedy, D. F. Unveiling the Structural Transitions during Activation of a CO2 Methanation Catalyst Ru0/ZrO2 Synthesised from a MOF Precursor. *Catal. Today* **2020**, DOI: 10.1016/j.cattod.2020.04.043, accepted for publication.
(30) Salavati-Niasari, M.; Mohandes, F.; Davar, F.; Mazaheri, M.; Monemzadeh, M.; Yavarinia, N. Preparation of NiO Nanoparticles from Metal-Organic Frameworks via a Solid-State Decomposition Route. *Inorg. Chim. Acta* **2009**, *362* (10), 3691−3697.
(31) Liu, X. Y.; Pai, S. J.; Han, S. S. ReaxFF Molecular Dynamics Simulations of Water Stability of Interpenetrated Metal−Organic Frameworks. *J. Phys. Chem. C* **2017**, *121* (13), 7312−7318.
(32) Ríos Gómez, M. L.; Lampronti, G. I.; Yang, Y.; Mauro, J. C.; Bennett, T. D. Relating Structural Disorder and Melting in Complex Mixed Ligand Zeolitic Imidazolate Framework Glasses. *Dalton Trans.* **2020**, *49* (3), 850−857.
(33) Yang, Y.; Shin, Y. K.; Li, S.; Bennett, T. D.; van Duin, A. C. T.; Mauro, J. C. Enabling Computational Design of ZIFs Using ReaxFF. *J. Phys. Chem. B* **2018**, *122* (41), 9616−9624.
(34) Yang, Y.; Wilkinson, C. J.; Lee, K.-H.; Doss, K.; Bennett, T. D.; Shin, Y. K.; van Duin, A. C. T.; Mauro, J. C. Prediction of the Glass Transition Temperatures of Zeolitic Imidazolate Glasses through Topological Constraint Theory. *J. Phys. Chem. Lett.* **2018**, *9* (24), 6985−6990.
(35) van Duin, A. C. T.; Merinov, B. V.; Jang, S. S.; Goddard, W. A. ReaxFF Reactive Force Field for Solid Oxide Fuel Cell Systems with Application to Oxygen Ion Transport in Yttria-Stabilized Zirconia. *J. Phys. Chem. A* **2008**, *112* (14), 3133−3140.
(36) Rahaman, O.; van Duin, A. C. T.; Goddard, W. A.; Doren, D. J. Development of a ReaxFF Reactive Force Field for Glycine and Application to Solvent Effect and Tautomerization. *J. Phys. Chem. B* **2011**, *115* (2), 249−261.
(37) Frisch, M. J.; Trucks, G. W.; Schlegel, H. B.; Scuseria, G. E.; Robb, M. A.; Cheeseman, J. R.; Scalmani, G.; Barone, V.; Petersson, G. A.; Nakatsuji, H.; et al. *Gaussian 09*, rev E.01; Gaussian, Inc.: Wallingford, CT, 2015.
(38) Zhao, Y.; Truhlar, D. G. The M06 Suite of Density Functionals for Main Group Thermochemistry, Thermochemical Kinetics, Noncovalent Interactions, Excited States, and Transition Elements: Two New Functionals and Systematic Testing of Four M06-Class

https://dx.doi.org/10.1021/acs.jpclett.0c02930
J. Phys. Chem. Lett. 2021, 12, 177−184

Functionals and 12 Other Functionals. *Theor. Chem. Acc.* **2008**, *120* (1−3), 215−241.
(39) Petersson, G. A.; Bennett, A.; Tensfeldt, T. G.; Al-Laham, M. A.; Shirley, W. A.; Mantzaris, J. A Complete Basis Set Model Chemistry. I. The Total Energies of Closed-Shell Atoms and Hydrides of the First-Row Elements. *J. Chem. Phys.* **1988**, *89* (4), 2193−2218.
(40) Hay, P. J.; Wadt, W. R. Ab Initio Effective Core Potentials for Molecular Calculations. Potentials for the Transition Metal Atoms Sc to Hg. *J. Chem. Phys.* **1985**, *82* (1), 270−283.
(41) Vanduyfhuys, L.; Verstraelen, T.; Vandichel, M.; Waroquier, M.; Van Speybroeck, V. Ab Initio Parametrized Force Field for the Flexible Metal−Organic Framework MIL-53(Al). *J. Chem. Theory Comput.* **2012**, *8* (9), 3217−3231.
(42) te Velde, G.; Bickelhaupt, F. M.; Baerends, E. J.; Fonseca Guerra, C.; van Gisbergen, S. J. A.; Snijders, J. G.; Ziegler, T. Chemistry with ADF. *J. Comput. Chem.* **2001**, *22* (9), 931−967.
(43) Guillerm, V.; Ragon, F.; Dan-Hardi, M.; Devic, T.; Vishnuvarthan, M.; Campo, B.; Vimont, A.; Clet, G.; Yang, Q.; Maurin, G.; et al. A Series of Isoreticular, Highly Stable, Porous Zirconium Oxide Based Metal−Organic Frameworks. *Angew. Chem., Int. Ed.* **2012**, *51* (37), 9267−9271.
(44) Berendsen, H. J. C.; Postma, J. P. M.; van Gunsteren, W. F.; DiNola, A.; Haak, J. R. Molecular Dynamics with Coupling to an External Bath. *J. Chem. Phys.* **1984**, *81* (8), 3684−3690.
(45) Liang, W.; Babarao, R.; Church, T. L.; D'Alessandro, D. M. Tuning the Cavities of Zirconium-Based MIL-140 Frameworks to Modulate CO_2 Adsorption. *Chem. Commun.* **2015**, *51* (56), 11286−11289.
(46) Boyd, P. G.; Moosavi, S. M.; Witman, M.; Smit, B. Smit Force-Field Prediction of Materials Properties in Metal-Organic Frameworks. *J. Phys. Chem. Lett.* **2017**, *8* (2), 357−363.
(47) Moosavi, S. M.; Boyd, P. G.; Sarkisov, L.; Smit, B. Improving the Mechanical Stability of Metal−Organic Frameworks Using Chemical Caryatids. *ACS Cent. Sci.* **2018**, *4* (7), 832−839.

https://dx.doi.org/10.1021/acs.jpclett.0c02930
J. Phys. Chem. Lett. 2021, 12, 177−184

Supplementary Information

Atomistic Mechanisms of Thermal Transformation in a Zr-Metal Organic Framework, MIL-140C

Swarit Dwivedi[1], Malgorzata Kowalik[2], Nilton Rosenbach[3], Dalal S. Alqarni[5], Yun Kyung Shin[2], Yongjian Yang[4], John C. Mauro[4], Akshat Tanksale[1], Alan L. Chaffee[5]and Adri C.T. van Duin[2*]*

1) Department of Chemical Engineering, Monash University, Clayton 3800, Victoria, Australia

2) Department of Mechanical Engineering, The Pennsylvania State University, University Park, Pennsylvania 16802, United States

3) Centro Universitário Estadual da Zona Oeste. Avenida Manuel Caldeira de Alvarenga, 1203, 23070-200, Campo Grande, Rio de Janeiro, Brazil

4) Department of Materials Science and Engineering, The Pennsylvania State University, University Park, Pennsylvania 16802, United States

5) School of Chemistry, Monash University, Clayton 3800, Victoria, Australia

** Corresponding authors, Email: alan.chaffee@monash.edu, acv13@psu.edu*

1. Development of ReaxFF parameters for Zr-MOF chemistry

Finite cluster models comprising the $Zr_6O_4(OH)_4$ node with degrees of coordination ranging from 8 to 12 formate/benzene-1,4-dicarboxylates (BDC), as depicted in the Figure S1(a), were optimised. ReaxFF and DFT energies for detachment of organic ligand from the metal cluster are tabulated in table given in Fig. S1(b).

(a)

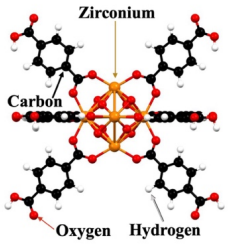

(b)

Reaction	$L = HCOO^-$		$L = HOOC-\varphi-COO^-$	
	DFT	ReaxFF	DFT	ReaxFF
$Zr_6O_4(OH)_4L_{12} \rightarrow Zr_6O_5(OH)_4L_{11} + HL$	51.4	45.6	41.9	46.5
$Zr_6O_4(OH)_3L_{11} \rightarrow Zr_6O_6(OH)_4L_{10} + HL$	49.8	51.9	35.1	33.4
$Zr_6O_4(OH)_2L_{10} \rightarrow Zr_6O_7(OH)_4L_9 + HL$	56.0	60.6	55.8	51.9
$Zr_6O_4(OH)_1L_9 \rightarrow Zr_6O_8L_8 + HL$	49.0	58.0	47.8	41.4

Figure S1. The final model structure and reaction energies comparison. (a) Zr_6O_8 cluster coordinated to 8 benzene-1,4-dicarboxylate linkers. (b) The energies for the removal of successive formate/benzene-1,4-dicarboxylates linkers (values in kcal/mol).

2. Accuracy and consistency of the simulations

Cell Parameters

The cell parameters after equilibration are compared to previously reported MIL-140C structures and the data is reported in Table S1. As the structure equilibrates and the density levels of at 1.09 gm/cm^3, the cell lengths a, b, and c increase sightly relative to previously reported cell lengths. However, the characteristic cell angle (β) remains similar which indicates which the shape of the cell does not changes. Also, the simulation for 1 ns at NPT ensemble were performed to validate the stability of structure (Fig. S2).

Table S1: Comparison of cell parameters of MIL-140C reported in this study with previously published works.

Method	a (Å)	b (Å)	c (Å)	α	β	γ
Exp[1]	31.03	15.51	7.82	90	93.26	90
DFT[2]	31.52	15.63	7.97	90	87.06	90
DFT[3]	31.30	15.64	7.57	90	84.51	90
This work (ReaxFF)	33.08	16.16	7.90	90	85.02	90

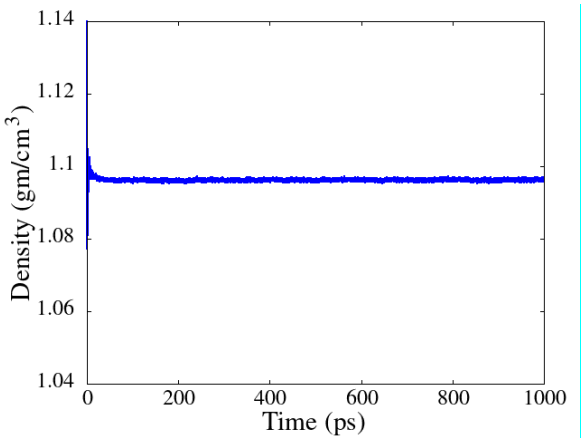

Figure S2. Density profile for a 1 ns long NPT simulation for atmospheric pressure and temperature 300 K.

Thermal Expansion Coefficient

The volumetric thermal expansion coefficient of MIL-140C is calculated by the volume change during the heating from 300 K to 500 K. Figure S3 shows the change in volume on increasing the temperature. The volume (V) decreases linearly with increasing temperature (T) and fitting $f(x) = m \times x + c$ results in a slope $\left(\frac{dV}{dT}\right)$ of -5.5666×10^{-3} Å^3. The volumetric expansion coefficient (α_V) is defined as,

$$\alpha = \frac{1}{V_0}\left(\frac{dV}{dT}\right)$$

Where V_0 is the volume of the MIL-140C at 300 K. The volumetric thermal expansion coefficient is -20.66×10^{-6} K^{-1}.

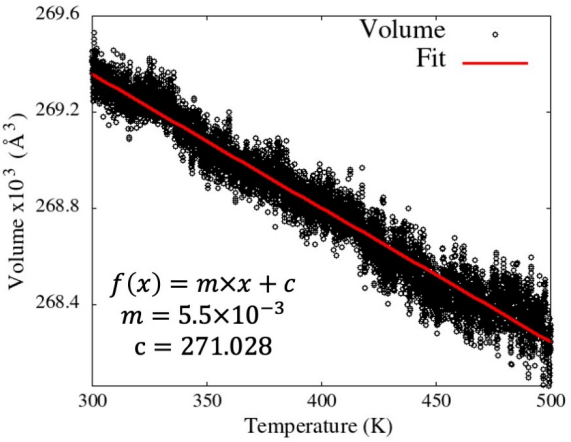

Figure S3. Shows the volume change on heating MIL-140C structure.

Statistical Consistency

The decomposition behaviour of MIL-140C has been evaluated based on equilibrated structures obtained after (a) 100 ps of equilibration and (b) 110 ps of equilibration. This is in addition to the decomposition behaviour reported in the main manuscript corresponding to a structure equilibrated at 300 K for 150 ps. These equilibrated structures all show similar behaviour and the temperatures at the onset of key events such as detachment of vertical and cross-linkers remains the same (Fig. S4). Moreover, the densities (Fig. S5(a)) as well as the potential energies (Fig. S5(b)) for both systems are comparable.

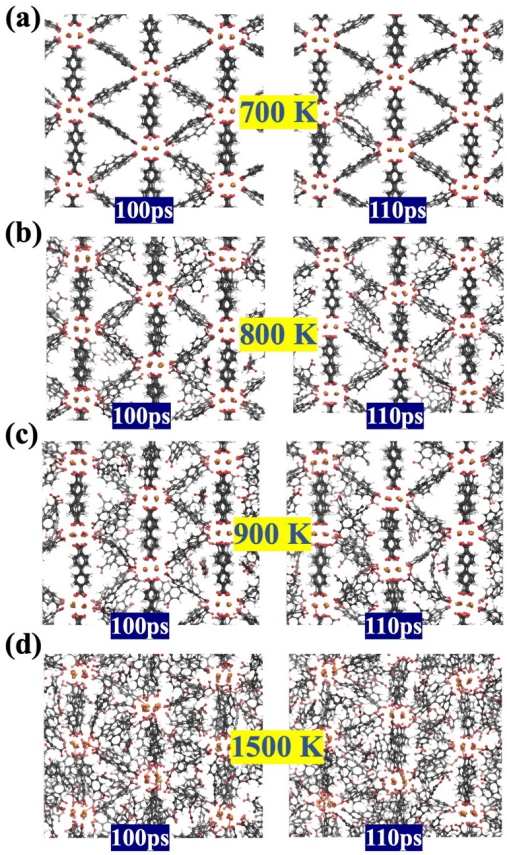

Figure S4. Shows the comparison of decomposition from different stating configurations, i.e. MIL-140C structure equilibrated at 300 K for 100ps and 110 ps. (a) shows the nearly all linkers connected to the metal cluster, (b) detachment of the crosslinkers, (c) contraction in the structure where crosslinkers occupy the pores, and (d) the detachment of vertical linkers.

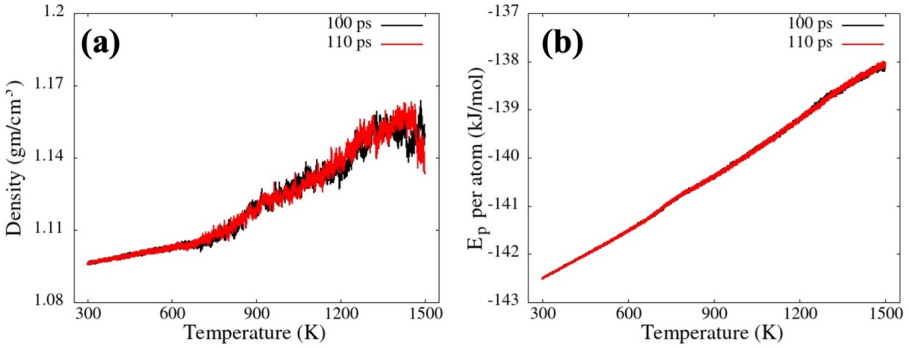

Figure S5. (a) The density variation and (b) the potential energy per atom on decomposing the MIL-140C after 100 ps equilibration and 110 ps equilibration at 300 K.

References:

(1) Guillerm, V., F. Ragon, M. Dan-Hardi, T. Devic, M. Vishnuvarthan, B. Campo, A. Vimont, G. Clet, Q. Yang, and G. Maurin A Series of Isoreticular, Highly Stable, Porous Zirconium Oxide Based Metal–Organic Frameworks. *Angewandte Chemie International Edition* **2012**, *51* (37), 9267–9271.

(2) Bennett, T. D., T. K. Todorova, E. F. Baxter, D. G. Reid, C. Gervais, B. Bueken, B. Van de Voorde, D. De Vos, D. A. Keen, and C. Mellot-Draznieks Connecting Defects and Amorphization in UiO-66 and MIL-140 Metal–Organic Frameworks: A Combined Experimental and Computational Study. *Phys. Chem. Chem. Phys.* **2016**, *18* (3), 2192–2201.

(3) Liang, W., R. Babarao, T. L. Church, and D. M. D'Alessandro Tuning the Cavities of Zirconium-Based MIL-140 Frameworks to Modulate CO_2 Adsorption. *Chem. Commun.* **2015**, *51* (56), 11286–11289.

```
Reactive MD-force field: C/H/O/N/S/Zr for Zr based MOFs
 39       ! Number of general parameters
   50.0000 !Overcoordination parameter
    9.5469 !Overcoordination parameter
   26.5405 !Valency angle conjugation parameter
    3.0000 !Triple bond stabilisation parameter
    6.5000 !Triple bond stabilisation parameter
    0.0000 !C2-correction
    1.0588 !Undercoordination parameter
    9.0000 !Triple bond stabilisation parameter
   12.1176 !Undercoordination parameter
   13.3056 !Undercoordination parameter
    0.0000 !Triple bond stabilization energy
    0.0000 !Lower Taper-radius
   10.0000 !Upper Taper-radius
    2.8793 !Not used
   33.8667 !Valency undercoordination
    6.0891 !Valency angle/lone pair parameter
    1.0563 !Valency angle
    2.0384 !Valency angle parameter
    6.1431 !Not used
    6.9290 !Double bond/angle parameter
    0.3989 !Double bond/angle parameter: overcoord
    3.9954 !Double bond/angle parameter: overcoord
   -2.4837 !Not used
    5.7796 !Torsion/BO parameter
   10.0000 !Torsion overcoordination
    1.9487 !Torsion overcoordination
   -1.2327 !Conjugation 0 (not used)
    2.1645 !Conjugation
    1.5591 !vdWaals shielding
    0.0100 !Cutoff for bond order (*100)
    2.1365 !Valency angle conjugation parameter
    2.0000 !Overcoordination parameter
    3.0000 !Overcoordination parameter
    1.8512 !Valency/lone pair parameter
    0.5000 !Not used
   20.0000 !Not used
    5.0000 !Molecular energy (not used)
    0.0000 !Molecular energy (not used)
    2.6962 !Valency angle conjugation parameter
  7    ! Nr of atoms;cov.r;valency;a.m.;Rvdw;Evdw;gammaEEM;cov.r2;#el;
           alfa;gammavdw;valency;Eunder;Eover;chiEEM;etaEEM;n.u.;
           cov.r3;Elp;Heat inc.;13BO1;13BO2;13BO3;XXX;n.u.;
           ov/un;vval1;XXX;vval2,vval3;n.u.;n.u.;n.u.
 C    1.3644   4.0000  12.0000   1.9803   0.1720   0.8712   1.2395   4.0000
      9.4734   2.1241   4.0000  31.8793  79.5548   5.7254   6.9235   0.0000
      1.2636   0.0000  -0.0537   5.7133  33.5629  11.9957   0.8563   0.0000
     -2.8983   4.7820   1.0564   4.0000   2.9663   0.0000   0.0000   0.0000
 H    0.6853   1.0000   1.0080   1.3588   0.0622   0.7625  -0.1000   1.0000
      9.3992   5.0518   1.0000   0.0000 121.1250   3.8520   9.3303   1.0000
     -0.1000   0.0000  -0.1609   3.9714   3.2094   0.9031   1.0698   0.0000
    -15.7683   3.3504   1.0338   1.0000   2.8793   0.0000   0.0000   0.0000
 O    1.2891   2.0000  15.9990   1.9741   0.0880   0.8659   1.0323   6.0000
     10.2186   7.7719   4.0000  30.8697 116.0768   8.5000   6.9585   2.0000
      0.9456   4.1347  -1.3533  20.7724   3.5512   0.5074   0.9745   0.0000
     -3.6141   2.7025   1.0493   4.0000   2.9225   0.0000   0.0000   0.0000
 N    1.2333   3.0000  14.0000   1.9324   0.1376   0.8596   1.1748   5.0000
     10.0667   7.8431   4.0000  32.2482 100.0000   6.8418   6.3404   2.0000
      1.0433  13.7673  -1.1806   2.1961   3.0696   2.7683   0.9745   0.0000
     -4.3875   2.6192   1.0183   4.0000   2.8793   0.0000   0.0000   0.0000
 S    1.9405   2.0000  32.0600   2.0677   0.2099   1.0336   1.5479   6.0000
      9.9575   4.9055   4.0000  52.9998 112.1416   6.5000   8.2545   2.0000
      1.4601   9.7177  71.1843   5.7487  23.2859  12.7147   0.9745   0.0000
    -11.0000   2.7466   1.0338   6.2998   2.8793   0.0000   0.0000   0.0000
 Zr   2.6383   4.0000  91.2240   2.2842   0.2481   0.5792  -1.0000   4.0000
     11.6632  48.5301   4.0000  -5.0000   0.0000  -1.5489   6.1282   0.0000
```

```
    -1.0000   0.0000 143.1770  48.2657   0.2144   0.0000   0.8563   0.0000
    -4.3695   3.3675   1.0338   8.0000   2.2632   0.0000   0.0000   0.0000
X   -0.1000   2.0000   1.0080   2.0000   0.0000   1.0000  -0.1000   6.0000
    10.0000   2.5000   4.0000   0.0000   0.0000   8.5000   1.5000   0.0000
    -0.1000   0.0000  -2.3700   8.7410  13.3640   0.6690   0.9745   0.0000
   -11.0000   2.7466   1.0338   6.2998   2.8793   0.0000   0.0000   0.0000
22      ! Nr of bonds;Edis1;LPpen;n.u.;pbe1;pbo5;13corr;pbo6;
                      pbe2;pbo3;pbo4;n.u.;pbo1;pbo2;ovcorr
 1  1 139.8093 110.6913  77.2102   0.2737  -0.7584   1.0000  38.4226   0.3288
        0.1235  -0.2010   8.6973   1.0000  -0.1042   6.1688   1.0000   0.0000
 1  2 159.8520   0.0000   0.0000  -0.4646   0.0000   1.0000   6.0000   0.6170
       12.3878   1.0000   0.0000   1.0000  -0.0098   8.5954   0.0000   0.0000
 1  3 161.6647  58.4169 126.5609   0.2952  -0.1638   1.0000  12.1551   0.4055
        0.3211  -0.2388   7.5568   1.0000  -0.1729   4.9857   0.0000   0.0000
 1  4 134.4562 139.7869  80.3761   0.0334  -0.1113   1.0000  27.0713   0.2076
        0.1315  -0.3049   7.0000   1.0000  -0.1355   5.2219   1.0000   0.0000
 1  5 128.9942  74.5848  55.2528   0.1035  -0.5211   1.0000  18.9617   0.6000
        0.2949  -0.2398   8.1175   1.0000  -0.1029   5.6731   1.0000   0.0000
 1  6   0.0000   0.0000   0.0000   0.2000  -0.1418   1.0000  13.1260   0.5000
        0.5000  -0.2000  20.0000   1.0000  -0.1000   9.0000   0.0000   0.0000
 2  2 170.0433   0.0000   0.0000  -0.3573   0.0000   1.0000   6.0000   0.7489
        9.6471   1.0000   0.0000   1.0000  -0.0169   5.8818   0.0000   0.0000
 2  3 198.1847   0.0000   0.0000  -0.4899   0.0000   1.0000   6.0000   0.3987
        2.4577   1.0000   0.0000   1.0000  -0.0549   5.6546   0.0000   0.0000
 2  4 231.8173   0.0000   0.0000  -0.3364   0.0000   1.0000   6.0000   0.4402
        8.8910   1.0000   0.0000   1.0000  -0.0327   6.5754   0.0000   0.0000
 2  5 151.5159   0.0000   0.0000  -0.4721   0.0000   1.0000   6.0000   0.6000
        9.4366   1.0000   0.0000   1.0000  -0.0290   7.0050   1.0000   0.0000
 2  6  38.8626   0.0000   0.0000  -0.1577   0.0000   1.0000   6.0000   0.5000
       17.8821   1.0000   0.0000   1.0000  -0.2095   6.3931   0.0000   0.0000
 2  7 192.2699   0.0000   0.0000  -0.4064  -0.2000   0.0000  16.0000   0.3162
        1.0201  -0.2000  15.0000   1.0000  -0.1078   5.2373   0.0000   0.0000
 3  3  87.8137 171.0665  40.0000   0.9810  -0.2106   1.0000  29.4721   1.0000
        0.8827  -0.1679   7.7980   1.0000  -0.1290   7.0000   1.0000   0.0000
 3  4 130.8596 169.4551  40.0000   0.3837  -0.1639   1.0000  35.0000   0.2000
        1.0000  -0.3579   7.0004   1.0000  -0.1193   6.8773   1.0000   0.0000
 3  5   0.0000   0.0000   0.0000   0.5563  -0.4038   1.0000  49.5611   0.6000
        0.4259  -0.4577  12.7569   1.0000  -0.1100   7.1145   1.0000   0.0000
 3  6 112.4500   0.0000   0.0000   0.3505  -0.3000   1.0000  36.0000   0.4053
        0.1765  -0.2000  15.0000   1.0000  -0.1300  10.6008   1.0000   0.0000
 3  7   0.0000   0.0000   0.0000   0.5000  -0.2000   0.0000  16.0000   0.5000
        1.0001  -0.2000  15.0000   1.0000  -0.1000  10.0000   0.0000   0.0000
 4  4 157.9384  82.5526 152.5336   0.4010  -0.1034   1.0000  12.4261   0.5828
        0.1578  -0.1509  11.9186   1.0000  -0.0861   5.4271   1.0000   0.0000
 4  5   0.0000   0.0000   0.0000   0.4438  -0.2034   1.0000  40.3399   0.6000
        0.3296  -0.3153   9.1227   1.0000  -0.1805   5.6864   1.0000   0.0000
 5  5  96.1871  93.7006  68.6860   0.0955  -0.4781   1.0000  17.8574   0.6000
        0.2723  -0.2373   9.7875   1.0000  -0.0950   6.4757   1.0000   0.0000
 6  6  74.5027   0.0000   0.0000  -0.2541  -0.2000   0.0000  16.0000   0.3564
        0.5882  -0.2000  15.0000   1.0000  -0.1315   6.4024   0.0000   0.0000
 7  7 109.2500   0.0000   0.0000   0.1803  -0.2000   0.0000  16.0000   0.3356
        0.9228  -0.2000  15.0000   1.0000  -0.1178   5.6715   0.0000   0.0000
14      ! Nr of off-diagonal terms;Ediss;Ro;gamma;rsigma;rpi;rpi2
 1  2   0.0431   1.7204  10.3632   1.0386  -1.0000  -1.0000
 1  3   0.1142   1.9602   9.4709   1.3065   1.1260   1.0865
 1  4   0.1445   1.8771  10.0000   1.7000   1.1885   1.1363
 1  5   0.1408   1.8161   9.9393   1.7986   1.3021   1.4031
 1  6   0.3000   1.6982  12.1919   1.2315   1.1212   0.9072
 2  3   0.0468   1.9998  10.2265   0.9368  -1.0000  -1.0000
 2  4   0.1059   1.8290   9.7818   0.9598  -1.0000  -1.0000
 2  5   0.0895   1.6239  10.0104   1.4640  -1.0000  -1.0000
 2  6   0.1000   1.7610  10.4809   0.1000  -1.0000  -1.0000
 2  7   0.1000   1.7500  10.5000   1.2000  -1.0000  -1.0000
 3  4   0.1058   2.0043  10.1244   1.7000   1.1096   1.0206
 3  5   0.1022   1.9887  10.0605   1.5799   1.4000  -1.0000
 3  6   0.1473   1.7130  12.0284   1.9555  -1.0000  -1.0000
 4  5   0.1505   1.9000  10.5104   1.8000   1.4000  -1.0000
```

```
67      ! Nr of angles;at1;at2;at3;Thetao;ka;kb;pconj;pv2;kpenal;pv3
 1   1   1   75.8304   33.9168    0.8043    0.0000    0.1780   10.5736    1.0400
 1   1   2   69.6421    9.2578    3.6521    0.0000    0.0058    0.0000    1.0400
 1   1   3   78.2305   16.3043    3.3209    0.0000    1.1127    0.0000    1.1880
 1   1   4   66.1305   41.9072    1.4346    0.0000    1.1127    0.0000    1.1880
 1   1   5   74.4180   33.4273    1.7018    0.1463    0.5000    0.0000    1.6178
 1   2   1    0.0000    3.4110    7.7350    0.0000    0.0000    0.0000    1.0400
 1   2   2    0.0000    0.0000    6.0000    0.0000    0.0000    0.0000    1.0400
 1   2   3    0.0000    0.0019    6.0000    0.0000    0.0000    0.0000    1.0400
 1   2   4    0.0000    0.0019    6.0000    0.0000    0.0000    0.0000    1.0400
 1   2   4    0.0000    0.0019    6.3000    0.0000    0.0000    0.0000    1.0400
 1   2   5    0.0000    0.0019    6.0000    0.0000    0.0000    0.0000    1.0400
 1   2   6    0.0000    0.0019    6.0000    0.0000    0.0000    0.0000    1.0400
 1   3   1   72.6402   38.4252    1.3200    0.0000    0.6142    0.0000    1.0783
 1   3   2   77.4332   39.5610    1.3429    0.0000    0.1218    0.0000    1.0500
 1   3   3   88.5142   45.0000    0.7808    0.0000    0.6142    0.0000    1.0783
 1   3   4   82.4890   43.2625    1.1759    0.0000    0.6142    0.0000    1.0783
 1   3   5   73.0990   33.8942    1.2098    0.0000    0.8161    0.0000    1.1776
 1   3   6   52.8005   19.2773    2.1458    0.0000    3.0000    0.0000    1.9934
 1   4   1   66.0330   22.0295    1.4442    0.0000    1.6777    0.0000    1.0500
 1   4   2   69.1106   25.5067    1.1003    0.0000    0.0222    0.0000    1.0369
 1   4   3  103.3204   33.0381    0.5787    0.0000    1.6777    0.0000    1.0500
 1   4   4  104.1335    8.6043    1.6495    0.0000    1.6777    0.0000    1.0500
 1   5   1   79.7037   28.2036    1.7073    0.1463    0.5000    0.0000    1.6453
 1   5   2   85.9449   38.3109    1.2492    0.0000    0.5000    0.0000    1.1000
 1   5   3   70.0000   35.0000    3.4223    0.0000    1.3550    0.0000    1.2002
 1   5   4   70.0000   35.0000    3.4223    0.0000    1.3550    0.0000    1.2002
 1   5   5   85.6645   40.0000    2.9274    0.1463    0.5000    0.0000    1.3830
 2   1   2   75.4958   14.5436    2.7438    0.0000    0.0127    0.0000    1.0400
 2   1   3   66.0941   11.3875    3.9388    0.0000    0.0755    0.0000    1.0500
 2   1   4   74.2929   10.7059    6.3074    0.0000    0.0755    0.0000    1.0500
 2   1   5   63.3289   29.4225    2.1326    0.0000    0.5000    0.0000    3.0000
 2   2   2    0.0000   27.9213    5.8635    0.0000    0.0000    0.0000    1.0400
 2   2   3    0.0000    0.0019    6.0000    0.0000    0.0000    0.0000    1.0400
 2   2   4    0.0000    0.0019    6.0000    0.0000    0.0000    0.0000    1.0400
 2   2   5    0.0000    0.0019    6.0000    0.0000    0.0000    0.0000    1.0400
 2   3   2   78.9033   33.3823    1.7364    0.0000    0.1218    0.0000    1.0500
 2   3   3   85.7907   10.5506    6.2301    0.0000    0.1218    0.0000    1.0500
 2   3   4   75.6201   45.0000    2.5874    0.0000    0.1218    0.0000    1.0500
 2   3   5   76.9521   20.0000    2.0903    0.0000    1.0000    0.0000    1.0400
 2   3   6   42.5058   10.0776    5.0000    0.0000    0.9289    0.0000    1.1912
 2   4   2   70.8687   12.0168    5.0132    0.0000    0.0222    0.0000    1.1243
 2   4   3   81.3686   40.0712    2.2396    0.0000    0.0222    0.0000    1.0369
 2   4   4   83.0104   43.4766    1.5328    0.0000    0.0222    0.0000    1.0500
 2   5   2   83.8555    5.1317    0.4377    0.0000    0.5000    0.0000    3.0000
 2   5   5   97.0064   32.1121    2.0242    0.0000    0.5000    0.0000    2.8568
 3   1   3   80.2229   45.0000    2.6995    0.0000    1.1127    0.0000    1.1880
 3   1   4   73.9544   45.0000    1.5778    0.0000    1.1127    0.0000    1.1880
 3   2   3    0.0000    5.0000    3.0000    0.0000    0.0000    0.0000    1.0400
 3   2   4    0.0000    0.0019    6.0000    0.0000    0.0000    0.0000    1.0400
 3   2   7    0.0000   15.0000    2.8900    0.0000    0.0000    0.0000    2.8774
 3   3   3   80.7324   35.1410    1.4999    0.0000    0.6142    0.0000    1.0783
 3   3   4   84.3637   25.1714    2.5361    0.0000    0.6142    0.0000    1.0783
 3   3   5   83.9753   31.0715    3.5590    0.0000    0.8161    0.0000    1.1776
 3   3   6   80.0000   10.0000    1.2500    0.0000    0.5554    0.0000    1.2000
 3   4   3   74.1978   42.1786    1.7845  -18.0069    1.6777    0.0000    1.0500
 3   4   4   74.8600   43.7354    1.1572   -0.9193    1.6777    0.0000    1.0500
 3   5   3   77.0699   39.4349    2.1313  -30.0000    0.9567    0.0000    1.1483
 3   5   4   70.0000   35.0000    3.4223    0.0000    1.3550    0.0000    1.2002
 3   6   3   55.8643   20.0000    0.3771    0.0000    0.1000    0.0000    1.4634
 3   6   3    1.1889   21.5079    5.6036    0.0000    0.0050    0.0000    2.3172
 4   1   4   64.1581   45.0000    0.6370    0.0000    1.1127    0.0000    1.1880
 4   2   4    0.0000    0.0019    6.0000    0.0000    0.0000    0.0000    1.0400
 4   2   7    0.0000   15.0000    2.8900    0.0000    0.0000    0.0000    2.8774
 4   3   4   89.7071   45.0000    1.2301    0.0000    0.6142    0.0000    1.0783
 4   4   4   75.0538   14.8267    5.2794    0.0000    1.6777    0.0000    1.0500
 5   4   5   62.0000   33.4273    1.7018    0.1463    0.5000    0.0000    1.0500
```

```
 6  3  6   5.9871   8.9966   0.2147   0.0000   2.7977   0.0000   3.0000
46      ! Nr of torsions;at1;at2;at3;at4;V1;V2;V3;V2(BO);vconj;n.u.;n.u.
 0  1  1  0   0.0000   0.6675   0.0000  -8.2352   0.0000   0.0000   0.0000
 0  1  2  0   0.0000   0.0000   0.0000   0.0000   0.0000   0.0000   0.0000
 0  1  3  0   3.9830  13.0320   0.4739  -1.9813  -2.0000   0.0000   0.0000
 0  1  4  0  -2.4242 128.1636   0.3739  -6.6098  -2.0000   0.0000   0.0000
 0  1  5  0   4.0885  78.7058   0.1174  -2.1639   0.0000   0.0000   0.0000
 0  2  2  0   0.0000   0.0000   0.0000   0.0000   0.0000   0.0000   0.0000
 0  2  3  0   0.0000   0.1000   0.0200  -2.5415   0.0000   0.0000   0.0000
 0  2  4  0   0.0000   0.1000   0.0200  -2.5415   0.0000   0.0000   0.0000
 0  2  5  0   0.0000   0.0000   0.0000   0.0000   0.0000   0.0000   0.0000
 0  3  3  0   0.0318  23.1045   1.2614 -12.3670   0.0000   0.0000   0.0000
 0  3  4  0   1.4816  55.6641   0.0004  -7.0465  -2.0000   0.0000   0.0000
 0  3  6  0   0.5784  18.0046  -0.3517  -7.5515  -1.0000   0.0000   0.0000
 0  4  4  0  -0.3244  27.7086   0.0039  -2.8272  -2.0000   0.0000   0.0000
 0  5  5  0  -0.0170 -56.0786   0.6132  -2.2092   0.0000   0.0000   0.0000
 1  1  1  1   0.0000  38.9174   0.3649  -8.2931  -2.0127   0.0000   0.0000
 1  1  1  2   0.0000  49.1001   0.2713  -8.5284  -1.5309   0.0000   0.0000
 1  1  1  3   1.2799  20.7787  -0.5249  -2.5000  -1.0000   0.0000   0.0000
 1  1  3  1   0.4816  19.6316  -0.0057  -2.5000  -1.0000   0.0000   0.0000
 1  1  3  2   1.2044  80.0000  -0.3139  -6.1481  -1.0000   0.0000   0.0000
 1  1  3  3  -0.0002  20.1851   0.1601  -9.0000  -2.0000   0.0000   0.0000
 1  1  3  3  -0.3566  10.0000   0.0816  -2.6110  -1.9631   0.0000   0.0000
 1  1  3  6   0.9999  75.2298   0.7066  -7.7179  -1.0102   0.0000   0.0000
 1  3  3  1   0.0002  80.0000  -1.5000  -4.4848  -2.0000   0.0000   0.0000
 1  3  3  1   1.1637 -17.3637   0.5459  -3.6005  -2.6938   0.0000   0.0000
 1  3  3  2  -2.1289  12.8382   1.0000  -5.6657  -2.9759   0.0000   0.0000
 1  3  3  3   2.5000 -25.0000   1.0000  -2.5000  -1.0000   0.0000   0.0000
 1  3  6  3  -0.2500   5.0000  -1.0000  -7.0978  -1.6888   0.0000   0.0000
 2  1  1  2   0.0000  34.0265   0.3804  -6.3917  -0.9965   0.0000   0.0000
 2  1  1  3   1.9159  19.8113   0.7914  -4.6995  -1.0000   0.0000   0.0000
 2  1  3  1  -2.5000  31.0191   0.6165  -2.7733  -2.9807   0.0000   0.0000
 2  1  3  2  -2.4875  70.8145   0.7582  -4.2274  -3.0000   0.0000   0.0000
 2  1  3  3  -1.4383  80.0000   1.0000  -3.6877  -2.8000   0.0000   0.0000
 2  1  3  6   0.9150  68.2937   0.8184  -2.7250  -3.0000   0.0000   0.0000
 2  1  4  2   0.0000  10.0000   0.3000  -6.0000  -1.0000   0.0000   0.0000
 2  3  3  2   2.5000 -22.9397   0.6991  -3.3961  -1.0000   0.0000   0.0000
 2  3  3  3  -2.5000  -2.5103  -1.0000  -2.5000  -1.0000   0.0000   0.0000
 2  3  6  3  -0.2500   5.0000  -1.0000  -6.9506  -1.8124   0.0000   0.0000
 3  1  1  3  -1.4477  16.6853   0.6461  -4.9622  -1.0000   0.0000   0.0000
 3  1  3  1  -1.1390  78.0747  -0.0964  -4.5172  -3.0000   0.0000   0.0000
 3  1  3  2  -2.5000  70.3345  -1.0000  -5.5315  -3.0000   0.0000   0.0000
 3  1  3  3  -0.1583  20.0000   1.5000  -9.0000  -2.0000   0.0000   0.0000
 3  1  3  3  -2.0234  80.0000   0.1684  -3.1568  -2.6174   0.0000   0.0000
 3  1  3  6  -0.2500  71.5675  -1.0000  -2.8166  -1.9054   0.0000   0.0000
 3  3  3  3  -2.5000 -25.0000   1.0000  -2.5000  -1.0000   0.0000   0.0000
 3  6  3  6   0.3319   5.6608   0.3356  -2.8511  -1.0718   0.0000   0.0000
 4  1  4  4  -5.5181   8.9706   0.0004  -6.1782  -2.0000   0.0000   0.0000
 9      ! Nr of hydrogen bonds;at1;at2;at3;Rhb;Dehb;vhb1;vhb2
 3  2  3   1.4000  -1.7731   1.4695   3.5257
 3  2  4   1.6337 -11.7496   1.4695   3.5257
 3  2  5   1.5000  -2.0000   1.4500  19.5000
 4  2  3   1.3999  -9.6921   1.4695   3.5257
 4  2  4   1.7514  -7.5768   1.4695   3.5257
 4  2  5   1.5000  -2.0000   1.4500  19.5000
 5  2  3   1.5000  -2.0000   1.4500  19.5000
 5  2  4   1.5000  -2.0000   1.4500  19.5000
 5  2  5   1.5000  -2.0000   1.4500  19.5000
```

Chapter 6

6 Understanding the effect of framework topology, linker chemistry, and chemical environment on the thermally decomposed MOFs

Swarit Dwivedi[1], Malgorzata Kowalik[2], Jeremy Mullins[3], Alessandria Sarmiento[3], Vignesh Pakkiam[3], Adri van Duin[2], Akshat Tanksale[1], Alan L. Chaffee[3]

1) Department of Chemical Engineering, Monash University, Clayton 3800, Victoria, Australia
2) Department of Mechanical Engineering, The Pennsylvania State University, University Park, PA, USA
3) School of Chemistry, Monash University, Clayton 3800, Victoria, Australia

Author contributions
In the case of chapter 6, my contribution to the work involved the following:

Thesis Chapter	Publication Title	Status	Nature and % of student contribution
6	Understanding the effect of framework topology, linker chemistry, and chemical environment on the thermally decomposed MOFs	In preparation	60%. Conception, designing experiments, collection and analysis of data, and writing first draft

Co-author names	Nature of contribution	Monash student?
Malgorzata Kowalik	5% discussion and suggestions, writing, Postdoc (Collaborator, Pennsylvania State University)	No
Vignesh Pakkiam	8% data analysis, simulation, writing, Bachelor Student (School of Chemistry)	Yes
Jeremy Mullins	8% data analysis, simulation, writing, Bachelor Student (School of Chemistry)	Yes
Alessandria Sarmiento	8% data analysis, simulation, writing, Bachelor Student (School of Chemistry)	Yes
Adri CT van Duin	3% suggestions, Professor (Collaborator, Pennsylvania State University)	No
Akshat Tanksale	3% suggestions, Supervisor	No
Alan L Chaffee	5% suggestions, Supervisor	No

6.1 Abstract

Metal Organic Frameworks (MOFs) are being rapidly explored for their application in the domain of catalysis. However, a wide variety of MOFs are unstable at high temperatures and pressures and in polar solvents, limiting their application. Thermal decomposition of MOF results in a carbonaceous material with a fine dispersion of metal or metal oxide clusters with excellent activity and potential for replacing traditional catalysts for industrial applications. However, the atomistic mechanisms of thermal decomposition and the control parameters for desired morphology is not well understood. We present a computational study of thermal transformations in Zr-based MOFs (MIL and UiO series). Using reactive molecular dynamics simulations (ReaxFF), we report the gas molecules that evolve during the decomposition and are responsible for the mass loss. The decomposed linkers form a fragmented network in which the cluster gets embedded while the metal clusters agglomerate. This linker network significantly hinders metal particle sintering. A partially modified MIL-140C (m-MIL-140C), the 2,2'-bipyridine-5,5'-dicarboxylate linker replaces 10% of the biphenyl dicarboxylate linkers, shows a more connected network of remnant linker material with smaller cluster size. The Zr-O coordination in the ZrO_x clusters (decomposed structure) is similar to the tetragonal phase of ZrO_2. Understanding the formation of these materials at a molecular length scale will help improve these advanced materials for specific applications.

Keywords: MOF-derived nanomaterials, Thermal decomposition, Zr-MOFs, UiO-66

6.2 Introduction

Rapidly rising anthropogenic carbon dioxide (CO_2) emissions have become a leading global environmental concern over the last two decades[1]. Increased atmospheric CO_2 concentrations have been attributed to our increasing dependence on fossil fuels that account for 86% of human-caused greenhouse gas emissions[2]. Even at the current target to limit the atmospheric heating above the pre-industrial era to less than 2ºC[3], CO_2 emissions are projected to rise due to economic and industrial progress, particularly in developing nations[4]. Thus, the developing strategies to minimise CO_2 emissions, such as renewable energy (solar and wind), are of significant scientific and technological importance. Moreover, possible ways to design and manufacture the materials capable of capturing CO_2 for sequestration or conversion to value added chemicals are intensively investigated as an effective strategy in combating anthropogenic CO_2 emissions[5]. Numerous catalytic systems have been studied and reported for

CO_2 conversion to value-added chemicals (methane, methanol, formaldehyde, formic acid, DME, OME, various Olefins, etc.). However, the energy cost and the catalyst deactivation limit their application as industrial catalysts.

MOFs are porous materials that consist of metal clusters coordinated to organic linkers and characterised by their intrinsically high surface area, porosity, and active site dispersion[6,7]. These MOFs properties, such as porosity or high surface area, are very important for various possible applications and can be further tuned via modular synthesis [5,8,9]. A potential application of MOFs as heterogeneous catalysts at mild temperature and in the presence of the solvent systems was recently considered[7,10–12]. However, there are concerns over MOFs' performance in gas-phase catalysis, as high temperatures and pressure can cause its decomposition[12,13]. This hydrolytically unstable nature of some MOFs limits their application in aqueous-phase catalysis[14,15]. Recently, attempts to work around these constraints have led researchers to utilise MOF's tuneability to design MOFs with improved binding strength. Zr-MOFs are an example of this[16–18]. However, these MOFs still decompose (or thermally transform) at the elevated temperatures typically used in gas phase heterogeneous catalysis. Furthermore, the framework with defects tends to collapse even at lower temperatures.

Thermally decomposed Zr-MOFs, with a noble metal incorporated into the pores, are reported for their ability in converting CO_2 into methane[19–21]. A fundamental understanding of the structural changes during thermal decomposition of MOFs and properties of thermally decomposed MOFs is yet to be established[13,22,23]. Thermal treatment of some Zr-MOFs under inert or oxidising atmospheres causes material transformations leading to the formation of Zr oxide nanoparticles embedded within carbonaceous ribbons derived from the linker[21]. While the decomposition mechanism remains uncertain, the metal (Ru) encapsulated thermally decomposed Zr-MOFs have been reported to have superior catalytic activity for CO_2 methanation relative to conventional noble metal catalysts[20,21]. Similar studies for thermally transformed MOFs other than Zr-MOFs also showed excellent activity and stability for different catalytic reaction system[23–26]. Hence, there is a growing effort to understand MOF-derived materials' exceptional catalytic capabilities and the mechanisms of thermal transformation of these materials [20,21,27–29].

In our recent work[27], the atomistic mechanisms leading to the MIL-140C collapse due to heating are discussed. We reported the morphology of the decomposed MOF, which was in good agreement with previously published experiments[21]. However, to the best of our knowledge, no study yet reports how the linkers and/or metal oxide cluster modification and

the decomposition environment might affect MOFs' thermal transformation. Our previous study was performed only on one supercell size of MIL-140C and one thermal regime. Here we present data for various system sizes to rule out a possible final size effect that might affect the metal cluster size evaluation, as well as various thermal regimes, to gain a statistically consistent size of the metal cluster in the decomposed MOF, different supercell sizes as well as temperature regimes should be compared.

In this study, using reactive molecular dynamics (ReaxFF) simulations, we elucidate the thermal decomposition behaviour of two MOF series with distinct metal cluster topologies (Fig. 6.1) – MIL-140C (ZrO_7 cluster), UiO-66 (Zr_6O_8 cluster), and UiO-67 (Zr_6O_8 cluster). The organic linker in MIL-140C and UiO-67 is biphenyl dicarboxylate (BPDC), whereas UiO-66 is benzene dicarboxylate (BDC). We also simulated MIL-140C under H_2 and CO_2 environments to understand the effect of thermal decomposition in a chemically active environment. We also simulate a modified MIL-140C, where a certain percentage of BPDC linkers are replaced with bipyridine dicarboxylate linker (BPyDC) to understand the effect of nitrogen-containing linkers. In numerous studies, nitrogen was reported as a promoter of carbonization. Therefore, the presence of nitrogen in the linker may influence the carbonaceous phase of the MOF-derived material. A better understanding of how linkers/metal oxide clusters modifications or the changes in the decomposition environment affects MOFs degradation is crucial in designing the derived materials for the catalytic application.

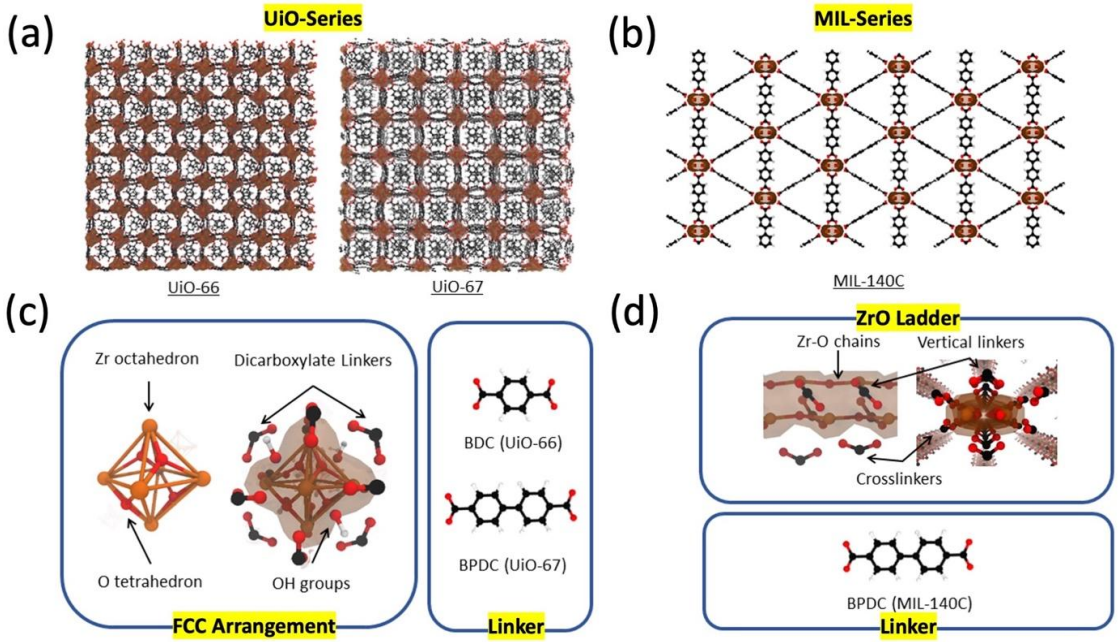

Figure 6.1: The molecular structures of MIL/UiO series and Zr-MOF. (a) The UiO series: UiO-66 and UiO-67, and (b) the MIL-140C structure. (c) The molecular structure for a metal oxide cluster and linkers in UiO-66 and UiO-67. (d) The ZrO cluster and the organic linker in MIL-140C.

6.3 Simulation Methodology

6.3.1 Molecular dynamics parameters

The ReaxFF[30] forcefield parameter set developed for Zr/C/H/O/N chemistry in Zr-MOFs is used for the molecular dynamics simulations performed using ADF modelling suite[31]. For all simulations, we use the Berendsen thermostat with a damping constant of 100 fs, and in the case of the *NPT* ensemble, the Berendsen barostat with a damping constant of 1500 fs is applied[32]. The periodic boundary conditions are applied for all three directions. Since the experimental timescale (~ hours) is not feasible computationally, we heat the system to temperatures much greater than experimental temperatures. We ensure that the decomposition reactions are not taking a free radical route at high temperatures.

First, the geometry was optimised to a tolerance of 1 kJ/mol. Then, the temperature was gradually increased using an *NPT* simulation to 300 K with a rate of 10 K/ps. After 100 ps of *NPT* simulations for all systems, the constant densities, comparable with the experimentally reported ones, were obtained. These equilibrated systems are heated up to 1500 K at the rate of 2 K/ps. After the collapse of the framework, linkers start losing mass in the form of small gaseous molecules. The decomposition is simulated in an NVT simulation for $T > 1500$K to avoid excessive expansion of the simulation box. We ran several simulations, both *NPT* and *NVT*, at higher temperatures to determine the simulation (temperature and ensemble) regime to best represent the experimental conditions. Figure 6.2 shows the simulation regimes and a comparison between different regimes is provided in the supplementary information (Appendix B). For the simulations presented the results and discussion, above 1500 K, the *NPT* simulation was performed. The structure was head till 2500 K and kept for 200 ps. After this short period of the simulations at the elevated temperature, the samples are cooled down to 300 K, and the decomposed structure is allowed to equilibrate at the constant temperature for another 100 ps.

6.3.2 Temperature regime

We heated the system in two different ways, and from 1500 K, the systems were heated in constant pressure (*NPT*) or volume (*NVT*) to both 2000 K and 2500 K, in 500 K intervals at the same heating rate. Above 2000 K, the timestep was altered to 0.1 fs to successfully capture the dynamics. Another constant temperature simulation was performed at 2000 K and 2500 K for 100 ps, followed by the system being cooled to 300 K at the rate of 4 K/ps. However, for the *NVT* simulations, once the system cooled to 1500 K, the subsequent cooling simulations are conducted under *NPT*. Once the system has cooled to 300 K for both *NVT* and *NPT* pathways

and 2000 and 2500 K regimes, the system was once again at 300 K for 100 ps at *NPT*, with a further simulation conducted on the system for 100 ps at a constant *T*, at *NVT*. In the *NPT* simulations, the resulting observations do not resemble the experimental data as the system undergoes excessive volume expansion under at artificially high temperatures used in this work. As such, the MOF was unable to stay stable above 1500 K, whereas at higher temperatures, an *NVT* ensemble is used to avoid artificial gasification, thus results of this investigation will be presented from the *NVT* route.

The heating simulations up to 2000 K were conducted with a 0.25 fs timestep, however above 2000 K, a 0.1 fs timestep was chosen due to higher thermal energy above 2000 K, as a 0.25 fs timestep was not suitable to capture the dynamics of the decomposition. Some simulations under 2000 K, most notably under *NVT* conditions, were unable to capture the dynamics therefore, the timestep of those reactions were altered from 0.25 fs to 0.1 fs. In this study, we explore a temperature regime that results in experimentally comparable morphology. After that, we compare the thermal transformations of different Zr-MOFs under same temperature regime. Although the simulations in this study do not use the exact experimental conditions, the comparison is expected to reveal the effect of MOF's features on the morphology of the decomposed structure.

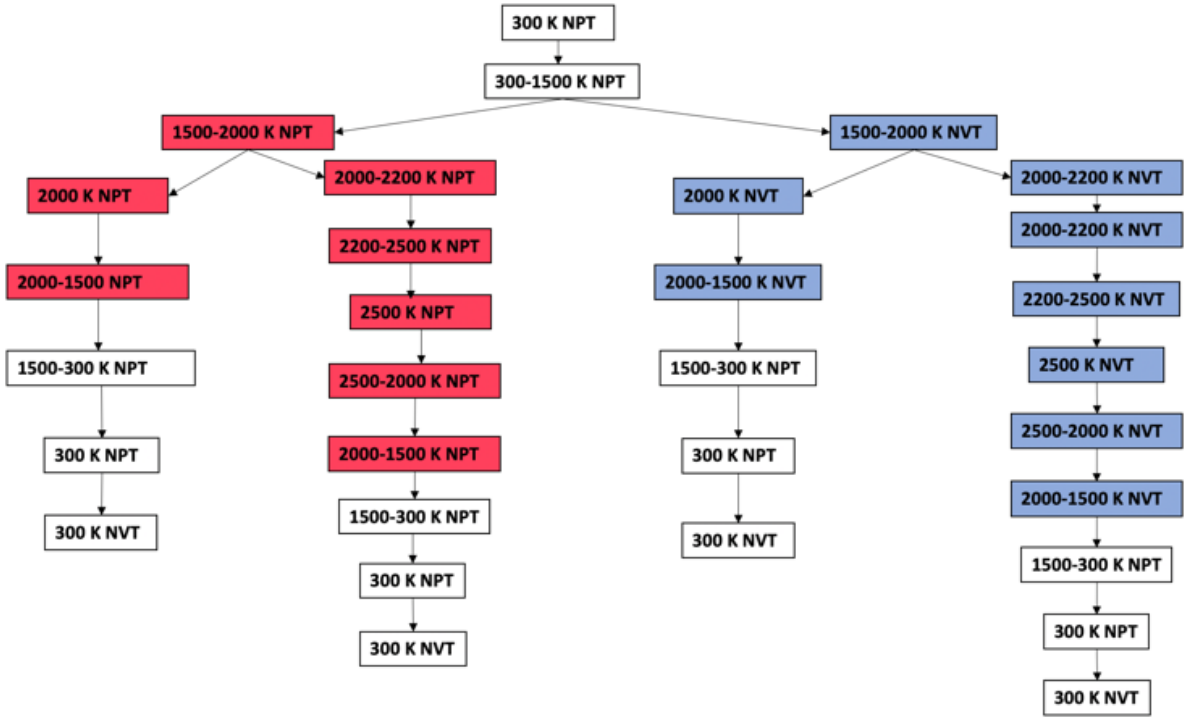

Figure 6.2: Temperature regime and simulation time. The simulation red boxes indicate the timestep of 0.01 fs and the blue box 0.25 fs.

6.3.3 Size of the supercell

We compared three supercell sizes of the DFT optimised unit cell of MIL-140C[33]. The supercells differ in repetitions parallel to the Zr-O ladder (z-axis) and are denoted as 3-3-4, 3-3-8, and 3-3-12 based on the repetition of unit cell in x-y-z directions. We compared the density, potential energy (*Ep*) per atom, and the size of metal nanoclusters formed after thermal decomposition to find the supercell size required for consistent results. The collapse of the framework and the chemical reactions in the organic phase were observed to be similar for all three supercells. For 3-3-12 supercell resulted with a consistent size distribution of metal oxide nanoparticles with three particles with 200 atoms. However, for 3-3-8 and 3-3-4 supercells, a consistent particle size is not observed due to insufficient number of Zr atoms in simulation cell.

6.3.4 Decomposition environment

We decomposed MIL-140C and m-MIL-140C in hydrogen and CO_2 to understand the effect of a chemically active reaction environment. The CO_2 or H_2 gas molecules are inserted randomly within the pores of the MIL-140C and m-MIL-140C. The number of molecules required of CO_2, previous reports of MIL-140C CO_2 adsorption capacity of 1.58 mmol/cm^3 was used[34]. Total 125 molecules for H_2 and 125 molecules of CO_2 were randomly distributed in 3-3-4 supercell of MIL-140C. For these simulations, the samples with the 3-3-4 supercell size are used. As the m-MIL-140C were not reported for the absorption co-efficient, we inserted 58 molecules of H_2 or CO_2 in the 3-3-4 supercell of m-MIL-140C. Therefore, a total of four simulation systems were performed: MIL-140C and m-MIL-140C in H_2 and CO_2 atmospheres.

6.4 Results and Discussion

6.4.1 Effect of organic linker (size)

To identify an effect of the length of the organic linker on the resulting decomposition mechanism and zirconia cluster aggregation, UiO-66 and UiO-67 are compared. Since UiO-67's linker (BDPC) has an extra phenyl group in comparison to the UiO-66's linker (BDC), the only difference of UiO-67 compared to UiO-66 is its lower packing efficiency (bigger pore size), where the Zr-O metal cluster configurations are identical. Therefore, any possible

difference in the final structure of the thermally decomposed MOFs will be a result of the difference in the pore sizes and the amount of organic phase per metal cluster.

At 300 K, both UiO-66 and UiO-67 are thermally stable, and the density plateaus indicate this (first 100 ps) in Fig. 6.2(a) and 6.2(c). As the temperature increase from 300 K to 1500 K (with of rate of 2 K/ps), the MOFs structures are stable up to temperature ~ 600 K, and thereafter the detachment of the organic linkers from the Zr-O cluster is observed. This detachment of linkers is followed by their decomposition, resulting in the production of gaseous molecules. From 300 K to 500 K, a linear rise in density with increasing temperature is observed in both cases, demonstrating negative thermal expansion behaviour characteristic of the UiO series[27,28]. The density increases by about ~ 0.11 g/cm^3 for UiO-66 and UiO-67 and about 0.36 g/cm^3 for UiO-67 during the temperature increase from 500 K to 1300 K. The greater increase in the density for UiO-67 is attributed to the intrinsically larger pore volume than UiO-66. In addition, for the temperature range of 580 K - 660 K linkers, we observe the onset of linker detachment (Fig. 6.2(b) and Fig. 6.2(d)) and the uniformity involved in the stacking of benzene rings within the pore sites is gradually lost. For both MOF structures, a decrease in density for temperature higher than 1300 K is observed, indicating the expansion of the system due to the production of the gas molecules and structural rearrangements after the framework collapse. Further heating (>1500 K) is simulated under the *NVT* ensemble, and the density remained constant.

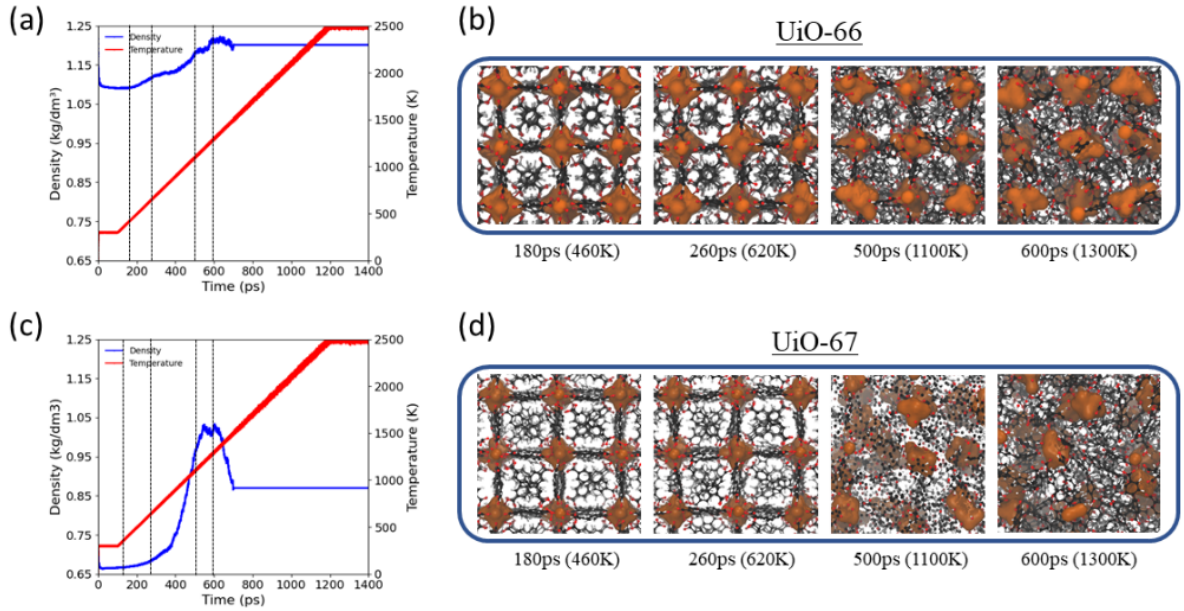

Figure 6.3: Density changes and the simulations snapshots for the first 1400 ps of thermal decomposition simulations for UiO series. The density variation as a finction of time for the heating

simulaiotns for (a) UiO-66 and (b) UiO-67. The snapshots from the molecular trajectories for (c) UiO-66 and (d) UiO-67.

Upon detachment of cross and vertical linkers, aggregation of the Zr-O clusters results in a zirconia amalgamation into nanoparticles. Figures 6.4 show the changing morphology during thermal decomposition. The equilibrated structures of the UiO-66 and UiO-67 are presented in Fig. 6.4(a, e) and the metal clusters agglomeration at higher temperature in Fig. 6.4 (b, f). The decomposed structures of both MOF systems are presented in Fig. 6.4(c, g). Finally, in Figure 6.4(d, h) only the Zr clusters are visualized, using one colour to represent each cluster. The dispersion of the evolved metal clusters is more visible for the UiO-67 system, where four particles are embedded in the organic phase instead of one large particle in the case of the UiO-66. The radius of gyration for the nanoparticle formed in UiO-66 (25.34 Å) is approximately twice the largest nanoparticle formed in UiO-67 (12.96 Å). The smaller ZrO clusters in the decomposed UiO-67 MOF show that the longer BPDC linkers can result in fewer zirconia nodes aggregating, meaning that the organic phase can prevent the cluster agglomeration.

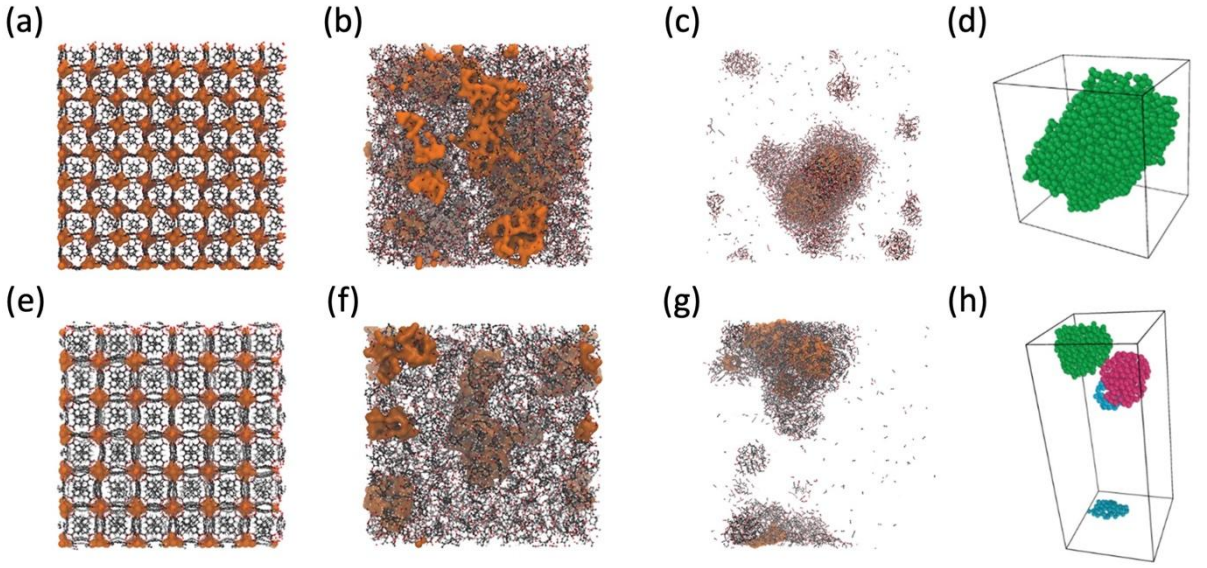

Figure 6.4: Thermal decomposition of UiO series. (a) & (e) are the equilibrated UiO-66 and UiO-67 structures at 300 K, (b) & (d) are broken MOFs at 2500 K, (c) & (g) are the final decomposed MOFs at 300 K. (d) & (h) The final metal oxide nanoparticles present in the decomposed MOFs. Each cluster is represented using one colours and the organic material is not shown. The Zr atoms in (a) – (c) and (e) – (g) are represented as an iso-surface for better visualisation.

Both UiO-66 and UiO-67 for the temperature range from 900K to 1200K (400ps to 550ps) produced O_2 from the carboxylate groups, before being consumed to form CO, CO_2, and H_2O after 700 ps. This thermal degradation behaviour can be associated with the simulation conditions, the first portion of which was performed at *NPT* conditions (until 1500 K or 700 ps). Thereafter the simulations progressed under *NVT* conditions, where the constant volume caused the molecules to be confined and react within the carbonaceous material. CO was the prominent gaseous product in both MOFs, a substantial increase after 1700 K (900 ps)[35]. However, significant H_2O production was observed in UiO-67, at fifteen times the abundance of H_2O produced in UiO-66 (Fig. 6.5(a)). This excess H_2O production for UiO-67 was via dehydroxylation (addition of hydrogen to hydroxide), also reported in previous studies with UiO-67[35,36], which could be due to the decreased density and larger pore volume compared to UiO-66. Moreover, a higher amount of CO_2 is produced upon dissociation from the carboxylate linkers for UiO-67. Therefore, the excess H_2O and CO_2 produced upon thermal decomposition of the organic linkers could be correlated with the density of the system, as only the organic linkers distinguish the structural make-up of both systems.

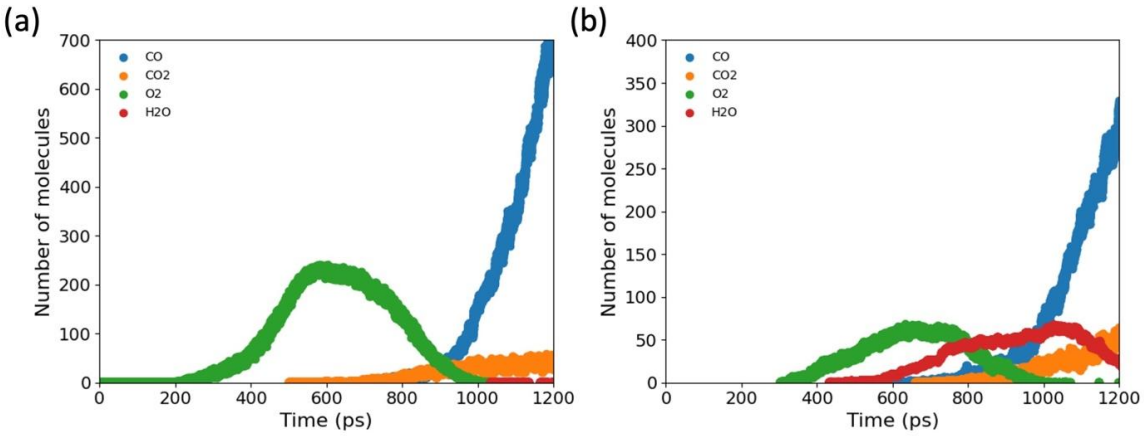

Figure 6.5: The small gaseous molecules evolved during the thermal decomposition of (a) UiO-66, and (b) UiO-67.

6.4.2 Effect of metal oxide cluster (coordination)

To assess the effect of the initial metal cluster geometry on the final aggregated clusters, the thermal degradation for MIL-140C and UiO67 is compared. Both MOFs have distinct Zr-O cluster geometries but common BPDC organic linkers. MIL-140C's clusters involve pairs of Zr-O chains with coordinating crosslinkers and vertical linkers, compared to UiO-67's Zr

octahedron encapsulating an oxygen tetrahedron (Fig. 6.1). Therefore, it was expected that the aggregation process of the Zr clusters during thermal decomposition would not be identical. Both MOFs ultimately collapsed into a carbonaceous material comprised of spherical zirconia particles of a similar radius of gyration of the largest nanoparticles (MIL-140C = 11.22 Å and UiO-67 = 12.96 Å). However, MIL-140C results in better dispersion of smaller particles. Moreover, the dynamics of cluster agglomeration are different. In UiO-67, once the linkers detach, the clusters become free to move, and small Zr_6O_8 clusters (~ 3.61 Å in diameter) arranged in FCC lattice were only hindered by the organic linkers in between. However, MIL-140C's structure involves pairs of Zr-O chains, which first need to break apart to form spherical zirconia particles. Manoeuvring through the carbonaceous material as fractured chains is easier for forming zirconia to agglomerate. Otherwise, the translation of long ZrO chains is resisted by the linkers in between. Figure 6.6 shows the initial breaking of the Zr-O chains at 1900K before completely breaking by 2300K. Around temperature 2500K, the Zr-O chains can wrap around each other to form spherical particles, as aggregation is now possible with the reduced zirconia cluster sizes. During the 200 ps simulation at 2500 K, the broken pairs of Zr-O chains continue to wrap around existing zirconia particles, ultimately forming bigger Zr clusters. Thus, the greater number of Zr clusters formed in MIL-140C results from the extra step of breaking Zr-O chain involved during thermal decomposition.

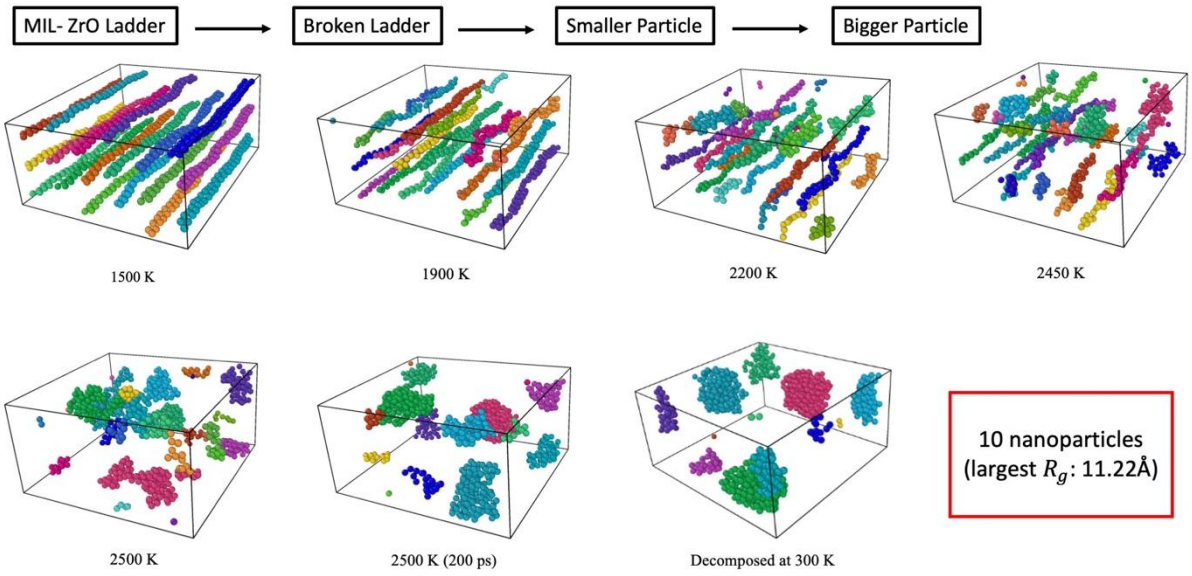

Figure 6.6: Gradual aggregation of zirconia clusters to form separate agglomerations. The agglomerations form due to sintering at higher temperatures and is achieved by initial breaking of the pairs of zirconia chains, and then subsequently forming spherical nanoparticles via aggregation with neighbouring zirconia nodes, to form a greater amalgamation of zirconia.

6.4.3 Effect of modified linker and chemical environment

Figure 6.7(a and c) indicates the change in density (blue) of MIL-140C (a) and m-MIL-140C (c) in a hydrogen atmosphere and the thermal history (red) over time. The density slightly increases linearly for the first 300 ps as the temperature rises. This can be attributed to a negative thermal expansion (NTE). The subsequent larger increase in density is due to the collapse of the framework after the detachment of the organic linkers from the ZrO metal clusters, as seen in Fig. 6.7(b). At 700 K and 1100 K, the crosslinkers begin to detach, whereas the vertical linkers remain stable due to π-stacking. The detached crosslinkers remain in the pore space and reconfigure themselves, triggering contraction of the system and the subsequent small increase in density reported for the experimental data[17]. On increasing the temperature from 1300 K to 1500 K, the density decreases from ~1.30 g/cm^3 to 1.02 g/cm^3. At 1500 K, the vertical linkers begin to detach from the ZrO nodes (Fig. 6.7(b)) and consequently causes the density of the system to rapidly decline and the structure to significantly expand in size as a combined result of gasification and a positive thermal expansion co-efficient.

The increase in density after the detachment of the linkers is higher for m-MIL-140C (Fig. 6.7(c)) than MIL-140C (Fig. 6.7(a). A possible reason for this could be the stronger intermolecular attraction between bipyridine dicarboxylic acid, as evident from its higher density (1.5 g/cm^3) than biphenyl dicarboxylic acid (1.3 g/cm^3). However, the density of m-MIL-140C rises even after the structure is cooled from 1500 K to 300 K under *NPT* simulation. The is because nitrogen promotes connectivity within the organic phase and stabilises the system.

Figure 6.7(e and f) shows the density changes for the MIL-140C and m-MIL140C in CO_2. During the decomposition phase, no significant difference between the density profile of CO_2 and H_2 environments for both MIL-140C and m-MIL-140C was observed. However, oxidising atmosphere such as CO_2 leads to the removal of carbon and the formation of metal oxide nanoparticles, whereas H_2 acts by breaking down the MOF framework[20]. While the CO_2 atmospheres have been previously reported for the thermal decomposition of Zr-MOFs, reports of thermal decomposition in H_2 are limited. Lippi et al.[20] observed the collapse of Ru^0/ZrO_2 in the H_2 environment into an amorphous mixture of products containing carbon, ruthenium, and zirconium phases, which is similar to the ZrO_x particles in the carbonaceous phases observed in this work.

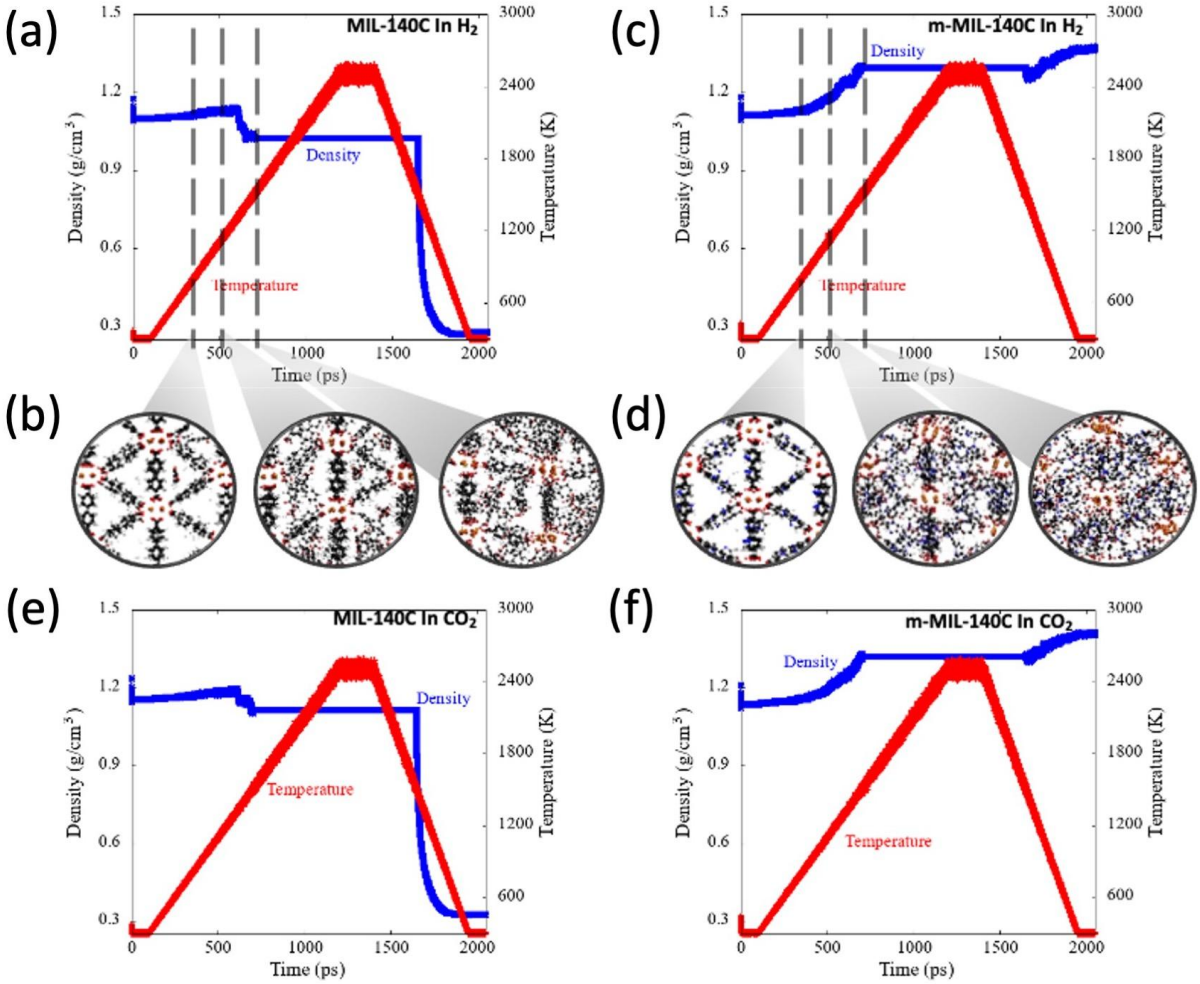

Figure 6.7: The density changes for the thermal decomposition simulations for MIL-series. (a) The density and temperature of the MIL-140C system in H_2 versus time. (b) Progression of structural change of MIL-140C in H_2 versus temperature: 700 K, 1100 K and 1500 K, from left to right. (c) the density and temperature of the m-MIL-140C system in H_2 versus time. (d) progression of structural changes of m-MIL-140C in H_2 versus temperature: 700 K, 1100 K and 1500 K, from left to right. (e) the density and temperature of the MIL-140C system in CO_2 versus time. (f) the density and temperature of the MIL-140C system in CO_2 versus time.

Figure 6.8(a and b) shows how the potential energy (E_p) per atom of the system varies with time over the same temperature regime. As shown in Figure 6.7, the MIL-140C and m-MIL-140C have their unique trend of how the potential energy per atoms changes as a function of the temperature. Nonetheless, the presence of active environments results in comparable changes in E_p per atom for both systems. An initial linear increase in E_p for MIL-series is a consequence of an increasing temperature. At a temperature around 1700K (700 ps), the E_p increases at a significantly slower rate even though the heating rate remains the same, 2 K/ps. This decrease in E_p change rate results from the decomposition of the organic linkers and

subsequent carbon monoxide (CO) production. At T = 2300K (1000 ps), we can observe an increase in the E_p change rate, which again the heating rate and is as a result of clustering of the decomposed structure, causing increase in pressure to maintain a constant volume.

After 1400 ps, the E_p decreases due to the cooling of the systems. A visible deviation in the E_p temperature profiles for m-MIL-140C compared to MIL-140 is a consequence of the linker modification. This gradual decrease in E_p at the temperature range 600K-2400K is likely due to the onset of carbonisation of the organic phase promoted by nitrogen. The m-MIL-140C with 100% of BPyDC linkers was reported for high hydrophilicity, and numerous strong interactions were observed in TGA analysis[37]. However, the MIL-140C with BPDC linkers was reported to be hydrophobic compared to minimal interactions in the same study. In our simulations, there is no water in the system. Therefore, it is highly likely that the nitrogen interacts with the carboxylic acid and CO_2 present in the system. Interaction of nitrogen is also observed in Figure 6.8(f), where CO_2 in m-MIL-140C essentially depletes within 250 ps and attaches to the linkers of the framework. At 1000 ps, similar to MIL-140C, the E_p of the m-MIL-140C fluctuates during the clustering of metal oxide, and decreases as the system is cooled.

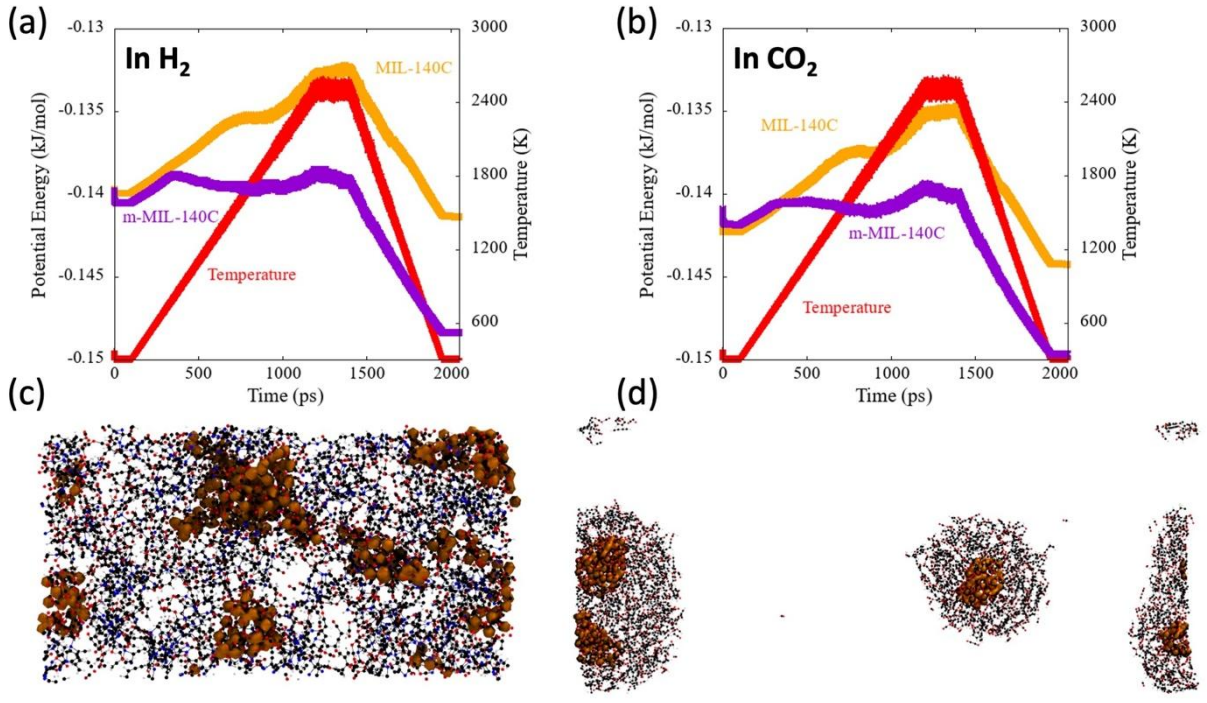

Figure 6.8: The density changes for the thermal decomposition simulations for MIL-series in H_2 and CO_2 environment. The potential energy per atom (E_p) as a function of temperature (time) for MIL-140C and m-MIL-140C under (a) H_2 and (b) CO_2 environments. The snapshots of the decomposed MOF at 300 K under H_2 environment for (c) m-MIL-140C and (d) MIL-140C.

Figure 6.9 illustrates the Zr-clusters that form due to the thermal decomposition of MIL-140C and m-MIL-140C in H_2 and CO_2 environments. As MIL-140C had weaker interaction and connectivity in the organic phase, the evolved Zr-clusters are larger, whereas in m-MIL-140C, several smaller clusters are observed. As tabulated in Figure 6.9(b), for the decomposed MIL-140C system, we see only 2-4 clusters compared to 9 clusters present in the decomposed m-MIL-140C system, with an average cluster of 95.7 Zr atoms in the MIL-140C and 31.9 Zr atoms in m-MIL-140C.

Figure 6.9(b) summarises the cluster size and radius of gyration of the clusters evolved for each decomposed system. As we mentioned previously, the thermally decomposed MIL-140C has a smaller number of clusters than decomposed m-MIL-140C, and the size of cluster is larger in the decomposed MIL-140C. The radius of gyration gives an indication of the size of the particle, where the larger clusters were typically between 2-3.5 nm in diameter. This diameter is twice what we reported in our earlier study[27], where the MIL-140C was heated to lower temperature, 2000 K, and the shorter simulation time at this temperature was considered, only 50 ps. Alqarni et al.[21] also reported the increase in cluster size (2-3 nm to 5 nm) on increasing the maximum temperature (500 °C to 850 °C). While our computational study does not directly correlate to the temperatures of this experimental study, we observe the same trend of an increase in cluster size. In Fig. 6.9(b) the ZrO clusters decomposed in H_2 and CO_2 environment for the MIL-series are presented. For MIL-140C and m-MIL-140C, the CO_2 environment results in a larger cluster size and gyration radius than H_2 environment. As we can see in Fig. 6.7, the final densities for MIL-140C and m-MIL-140C exposed to the CO_2 environment (Fig. 6.7(e-f) for temperature around 1200K) are slightly higher than the densities for these two systems exposed to the H_2 (Fig. 6.7(a-b) for a temperature around 1200K). This increased cluster size is likely due to the CO_2 atmosphere being an oxidant also previously reported to remove the carbon framework and promote Zr-O crystallisation[20], whereas H_2 is only capable of breaking down the MOF framework.

(a)

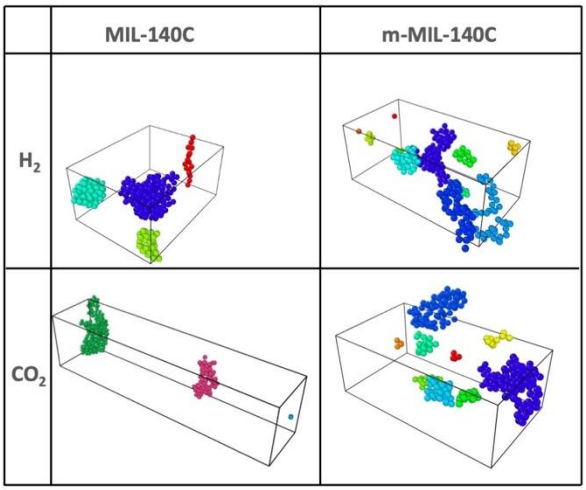

(b)

	Cluster	Cluster Size (No. of Zr atoms)	Radius of Gyration (Å)
MIL-140C in Hydrogen	1	176	10.7
	2	64	7.36
	3	32	6.01
	4	16	9.43
MIL-140C in Carbon Dioxide	1	206	15.6
	2	80	10.2
m-MIL-140C in Hydrogen	1	112	12.0
	2	50	8.92
	3	40	11.4
	4	32	5.55
	5	19	5.13
	6	13	4.65
	7	7	3.27
	8	7	3.05
	9	6	2.64
m-MIL-140C in Carbon Dioxide	1	115	15.9
	2	77	11.0
	3	32	6.66
	4	17	4.62
	5	16	4.89
	6	14	4.89
	7	9	4.49
	8	4	2.09
	9	4	2.03

Figure 6.9: (a) Zr atom of the metal oxide cluster in the decomposed MIL-140C and m-MIL-140C under H_2 and CO_2 environment. (b) Shows the number of Zr atoms and the radius of gyration of each ZrO_x cluster in the decomposed MOF.

To assess an oxidation state of Zr, the radial pair distribution function, $g(r)$, for Zr-O atom pairs is calculated. In Fig. 6.10, the $g(r)$ for Zr-O and Zr-Zr atom pairs are plotted for the initial structure of MIL-140C in H_2 and compared with the final thermally decomposed structures of the 2000 K and 2500 K simulations. We interpret the oxidation state of the ZrO_x clusters by understanding the local environment of Zr from the $g(r)$ and the coordination number for the characteristic peaks of the $g(r)$. Therefore, comparing the $g(r)$ allows us to identify the changes in the oxidation state of the ZrO_x decomposed structures. As seen in Fig. 6.10(b), the decomposed structure's first peak, which corresponds to the Zr-O bond of the ZrO ladder, remains similar to the initial structure after decomposition at 2000 K. However, after the decomposition at 2500 K, this peak reduces significantly. From the position of this peak, we can say that the bond length of the Zr-O was 1.98 Å. The second peak at 2.48 Å corresponding decreases in the decomposed structures. The coordination number of O around Zr till the first two peaks in the decomposed structures (both 2000 K and 2500 K routes) was five whereas the initial structure for the same two peaks showed seven O atoms coordinated around Zr. The coordination of oxygen reduces because of the detachment of linkers and the formation of ZrO_x clusters. There are significant differences between the heating routes in terms of Zr-Zr coordination (Fig. 6.10(a)). The 2000 K model was relatively similar to the initial structure and it shared the first two peaks, albeit smaller in height. This similarity caused both the initial and

2000 K decomposed structure to be a 4-coordinate Zr-Zr nanocluster, where the first peak (3.33 Å) corresponds to the Zr coordination to Zr of the same ladder, whereas second peak (3.98 Å) corresponds to the Zr-Zr interactions of the ZrO-ladder parallel to the specified Zr. However, the 2000 K route did not share the two small peaks at around 6 Å and 8 Å, but rather a very broad peak. This implies that a long-range order is not fully developed after the decomposition. The Zr-Zr peak after decomposition at 2500 K does not show the characteristic second peak that is present in monoclinic and tetragonal ZrO_2 structures, which implies (a) the ZrO ladders of MIL-140C has been broken completely and (b) the next neighbouring (Zr-Zr) order has not been attained in the decomposed ZrO_x nanocluster. Like, the 2000 K system, the 2500 K model shares that broad peak around 6 Å, however it is higher in $g(r)$. The radial pair distribution function of the other three systems (MIL-140C in CO_2, m-MIL-140C in H_2 & CO_2) was nearly identical to MIL-140C in H_2 for both Zr-O and Zr-Zr interactions.

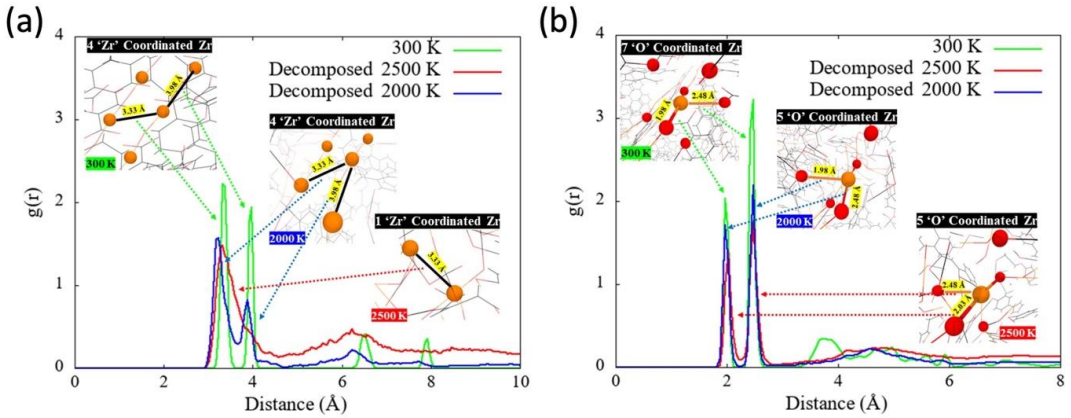

Figure 6.10: (a) Shows the radial pair distribution function of MIL-140C in H_2 where (a) & (b) indicates the g(r) of Zr-Zr and Zr-O, respectively, after decomposition at 2000 K (blue) and 2500 K (red).

6.5 Conclusion

To simulate thermal decomposition of UiO- and MIL-series, we use ReaxFF molecular dynamics simulation. First, we tested how the length of the organic linkers affects the MOFs' degradation. The effect of the organic linkers on thermal decomposition by comparing the simulation results for UiO-66 and UiO-67. For both MOFs, we observed the linkers detach around 540 K - 640 K, and in UiO-67 the detachment occurs at relatively lower temperatures. The decomposed UiO-66 structure was characterised by larger zirconia clusters, while the decomposed UiO-67 has smaller, finely dispersed nanoparticles. To test the impact of initial cluster geometry on zirconia aggregation, we compare MIL-140C and UiO-67. A finer dispersion of zirconia nanoparticles was observed for the MIL-140C system. This better

dispersion of the zirconia clusters for the MIL-140 system is a consequence of breaking the Zr-O chains to then forming spherical particles. In the case of UiO-67 system a 'more instant aggregation' of the zirconia clusters was observed via forming the particles upon detachment of the linkers. Interestingly, UiO-67 was the only MOF to demonstrate water production after the thermal decomposition of linkers, which can be attributed to the low packing efficiency of the MOF. Finally, the impact of nitrogen on degradation behaviour was observed, by substituting BPyDC linkers into MIL-140C. The key gaseous molecule produced due to the thermal degradation of the considered systems was CO, with CO_2, acetylene, and hydrogen being minor in comparison. The change in the oxidation state of the metal clusters due the thermal degradation for all MOFs changes from ZrO_7 to ZrO_5. These evolved ZrO_5 metal nanoclusters were embedded in the disrupted organic linkers. The CO_2 environment was determined to promote the larger clusters formation than the H_2 environment, which is a consequence of the oxidising nature of CO_2 environment. The linker modification for m-MIL-140C, by substituting 10% of the BPDC linkers with BPyDC, resulted in more dispersed smaller clusters in the decomposed structure compared to the decomposed MIL-140C. The m-MIL-140C systems were also identified for the formation of a better-connected carbonaceous phase. We recommend subjecting m-MIL-140C to higher degradation temperatures for a longer period explore possibilities of carbonization and graphitisation. Similarly, future work could be done to investigate the behaviours of UiO-67 regarding the unusually large production of water during decomposition. Since we know that the dispersion of the metal clusters in the organic material for the decomposed system affects the catalytic properties of this system, the presented simulations might help in the desired design of the decomposed MOFs.

ASSOCIATED CONTENT

Supporting Information

Supporting information consisting a detailed description of computational methodology, cluster size distribution data, and other supporting results is provided in Appendix B.

AUTHOR INFORMATION

Corresponding Author

* Email: Alan.Chaffee@monash.edu

* Email: Akshat.Tanksale@monash.edu

Author Contributions

The manuscript was written through contributions of all authors. All authors have given approval to the final version of the manuscript.

Funding Sources

Australian Research Council, Discovery Project, DP170104017.

ACKNOWLEDGMENT

This research was funded by the Australian Government through the Australian Research Council's Discovery Projects funding scheme (project DP170104017). The authors gratefully acknowledge a generous allocation of computer resources through the Monash eResearch Centre at the Monash Advanced Research Computing Hybrid (MonARCH) HPC/HTC Cluster.

References:

(1) Dong, K.; Jiang, H.; Sun, R.; Dong, X. Driving Forces and Mitigation Potential of Global CO_2 Emissions from 1980 through 2030: Evidence from Countries with Different Income Levels. *Science of The Total Environment* **2019**, *649*, 335–343. https://doi.org/10.1016/j.scitotenv.2018.08.326.

(2) Metz, B.; Davidson, O. De Coninck H., Loos M., L. Meyer. *Carbon dioxide capture and storage, IPCC Special* **2005**.

(3) Iyer, G. C.; Edmonds, J. A.; Fawcett, A. A.; Hultman, N. E.; Alsalam, J.; Asrar, G. R.; Calvin, K. V.; Clarke, L. E.; Creason, J.; Jeong, M.; Kyle, P.; McFarland, J.; Mundra, A.; Patel, P.; Shi, W.; McJeon, H. C. The Contribution of Paris to Limit Global Warming to 2 °C. *Environ. Res. Lett.* **2015**, *10* (12), 125002. https://doi.org/10.1088/1748-9326/10/12/125002.

(4) Core Writing Team eds. Contribution of Working Groups I, II and III to the Fourth Assessment Report of the Intergovernmental Panel on Climate Change. *IPCC 2007 : Climate Change 2007 : Synthesis Report* **2007**, *104*.

(5) D'Alessandro, D. M.; Smit, B.; Long, J. R. Carbon Dioxide Capture: Prospects for New Materials. *Angewandte Chemie International Edition* **2010**, *49* (35), 6058–6082. https://doi.org/10.1002/anie.201000431.

(6) Furukawa, H.; Cordova, K. E.; O'Keeffe, M.; Yaghi, O. M. The Chemistry and Applications of Metal-Organic Frameworks. *Science* **2013**, *341* (6149), 1230444–1230444. https://doi.org/10.1126/science.1230444.

(7) Lee, J.; Farha, O. K.; Roberts, J.; Scheidt, K. A.; Nguyen, S. T.; Hupp, J. T. Metal–Organic Framework Materials as Catalysts. *Chemical Society Reviews* **2009**, *38* (5), 1450–1459.

(8) Bae, Y.-S.; Snurr, R. Q. Development and Evaluation of Porous Materials for Carbon Dioxide Separation and Capture. *Angew. Chem. Int. Ed.* **2011**, *50* (49), 11586–11596. https://doi.org/10.1002/anie.201101891.

(9) Sumida, K.; Rogow, D. L.; Mason, J. A.; McDonald, T. M.; Bloch, E. D.; Herm, Z. R.; Bae, T.-H.; Long, J. R. Carbon Dioxide Capture in Metal–Organic Frameworks. *Chem. Rev.* **2012**, *112* (2), 724–781. https://doi.org/10.1021/cr2003272.

(10) Doonan, C. J.; Sumby, C. J. Metal–Organic Framework Catalysis. *CrystEngComm* **2017**, *19* (29), 4044–4048.

(11) Gascon, J.; Corma, A.; Kapteijn, F.; Llabres i Xamena, F. X. Metal Organic Framework Catalysis: Quo Vadis? *Acs Catalysis* **2013**, *4* (2), 361–378.

(12) Howarth, A. J.; Liu, Y.; Li, P.; Li, Z.; Wang, T. C.; Hupp, J. T.; Farha, O. K. Chemical, Thermal and Mechanical Stabilities of Metal–Organic Frameworks. *Nature Reviews Materials* **2016**, *1* (3), 15018.

(13) Healy, C.; Patil, K. M.; Wilson, B. H.; Hermanspahn, L.; Harvey-Reid, N. C.; Howard, B. I.; Kleinjan, C.; Kolien, J.; Payet, F.; Telfer, S. G.; Kruger, P. E.; Bennett, T. D. The Thermal Stability of Metal-Organic Frameworks. *Coordination Chemistry Reviews* **2020**, *419*, 213388. https://doi.org/10.1016/j.ccr.2020.213388.

(14) Burtch, N. C.; Jasuja, H.; Walton, K. S. Water Stability and Adsorption in Metal–Organic Frameworks. *Chemical reviews* **2014**, *114* (20), 10575–10612.

(15) Han, S. S.; Choi, S.-H.; van Duin, A. C. T. Molecular Dynamics Simulations of Stability of Metal–Organic Frameworks against H2O Using the ReaxFF Reactive Force Field. *Chem. Commun.* **2010**, *46* (31), 5713. https://doi.org/10.1039/c0cc01132k.

(16) Cavka, J. H.; Jakobsen, S.; Olsbye, U.; Guillou, N.; Lamberti, C.; Bordiga, S.; Lillerud, K. P. A New Zirconium Inorganic Building Brick Forming Metal Organic Frameworks with Exceptional Stability. *Journal of the American Chemical Society* **2008**, *130* (42), 13850–13851.

(17) Bai, Y.; Dou, Y.; Xie, L.-H.; Rutledge, W.; Li, J.-R.; Zhou, H.-C. Zr-Based Metal–Organic Frameworks: Design, Synthesis, Structure, and Applications. *Chemical Society Reviews* **2016**, *45* (8), 2327–2367.

(18) Kim, M.; Cohen, S. M. Discovery, Development, and Functionalization of Zr(Iv)-Based Metal–Organic Frameworks. *CrystEngComm* **2012**, *14* (12), 4096–4104. https://doi.org/10.1039/C2CE06491J.

(19) Lippi, R.; Howard, S. C.; Barron, H.; Easton, C. D.; Madsen, I. C.; Waddington, L. J.; Vogt, C.; Hill, M. R.; Sumby, C. J.; Doonan, C. J. Highly Active Catalyst for CO 2 Methanation Derived from a Metal Organic Framework Template. *Journal of Materials Chemistry A* **2017**, *5* (25), 12990–12997.

(20) Lippi, R.; D'Angelo, A. M.; Li, C.; Howard, S. C.; Madsen, I. C.; Wilson, K.; Lee, A. F.; Sumby, C. J.; Doonan, C. J.; Patel, J.; Kennedy, D. F. Unveiling the Structural Transitions during Activation of a CO_2 Methanation Catalyst Ru0/ZrO2 Synthesised from a MOF Precursor. *Catalysis Today* **2020**, S0920586120302376. https://doi.org/10.1016/j.cattod.2020.04.043.

(21) Alqarni, D. S.; Lee, C. W.; Knowles, G. P.; Vogt, C.; Marshall, M.; Gengenbach, T.; Chaffee, A. L. Ru-Zirconia Catalyst Derived from MIL140C for Carbon Dioxide Conversion to Methane. *Catalysis Today* **2020**, S0920586120305563. https://doi.org/10.1016/j.cattod.2020.07.080.

(22) Salavati-Niasari, M.; Mohandes, F.; Davar, F.; Mazaheri, M.; Monemzadeh, M.; Yavarinia, N. Preparation of NiO Nanoparticles from Metal-Organic Frameworks via a Solid-State Decomposition Route. *Inorganica chimica acta* **2009**, *362* (10), 3691–3697.

(23) Ji, S.; Chen, Y.; Fu, Q.; Chen, Y.; Dong, J.; Chen, W.; Li, Z.; Wang, Y.; Gu, L.; He, W.; Chen, C.; Peng, Q.; Huang, Y.; Duan, X.; Wang, D.; Draxl, C.; Li, Y. Confined Pyrolysis within Metal–Organic Frameworks To Form Uniform Ru $_3$ Clusters for Efficient Oxidation of Alcohols. *J. Am. Chem. Soc.* **2017**, *139* (29), 9795–9798. https://doi.org/10.1021/jacs.7b05018.

(24) Shen, K.; Chen, X.; Chen, J.; Li, Y. Development of MOF-Derived Carbon-Based Nanomaterials for Efficient Catalysis. *ACS Catal.* **2016**, *6* (9), 5887–5903. https://doi.org/10.1021/acscatal.6b01222.

(25) Zhong, W.; Liu, H.; Bai, C.; Liao, S.; Li, Y. Base-Free Oxidation of Alcohols to Esters at Room Temperature and Atmospheric Conditions Using Nanoscale Co-Based Catalysts. *ACS Catal.* **2015**, *5* (3), 1850–1856. https://doi.org/10.1021/cs502101c.

(26) Bai, C.; Yao, X.; Li, Y. Easy Access to Amides through Aldehydic C–H Bond Functionalization Catalyzed by Heterogeneous Co-Based Catalysts. *ACS Catal.* **2015**, *5* (2), 884–891. https://doi.org/10.1021/cs501822r.

(27) Dwivedi, S.; Kowalik, M.; Rosenbach, N.; Alqarni, D. S.; Shin, Y. K.; Yang, Y.; Mauro, J. C.; Tanksale, A.; Chaffee, A. L.; van Duin, A. C. T. Atomistic Mechanisms of Thermal Transformation in a Zr-Metal Organic Framework, MIL-140C. *J. Phys. Chem. Lett.* **2021**, *12* (1), 177–184. https://doi.org/10.1021/acs.jpclett.0c02930.

(28) Goodenough, I.; Devulapalli, V. S. D.; Xu, W.; Boyanich, M. C.; Luo, T.-Y.; De Souza, M.; Richard, M.; Rosi, N. L.; Borguet, E. Interplay between Intrinsic Thermal Stability and Expansion Properties of Functionalized UiO-67 Metal–Organic Frameworks. *Chem. Mater.* **2021**, *33* (3), 910–920. https://doi.org/10.1021/acs.chemmater.0c03889.

(29) Mohamed, S. A.; Chong, S.; Kim, J. Thermal Stability of Methyl-Functionalized MOF-5. *J. Phys. Chem. C* **2019**, *123* (49), 29686–29692. https://doi.org/10.1021/acs.jpcc.9b08060.

(30) Senftle, T. P.; Hong, S.; Islam, M. M.; Kylasa, S. B.; Zheng, Y.; Shin, Y. K.; Junkermeier, C.; Engel-Herbert, R.; Janik, M. J.; Aktulga, H. M.; Verstraelen, T.; Grama, A.; van Duin, A. C. T. The ReaxFF Reactive Force-Field: Development, Applications and Future Directions. *npj Comput Mater* **2016**, *2* (1), 15011. https://doi.org/10.1038/npjcompumats.2015.11.

(31) te Velde, G.; Bickelhaupt, F. M.; Baerends, E. J.; Fonseca Guerra, C.; van Gisbergen, S. J. A.; Snijders, J. G.; Ziegler, T. Chemistry with ADF. *J. Comput. Chem.* **2001**, *22* (9), 931–967. https://doi.org/10.1002/jcc.1056.

(32) Berendsen, H. J. C.; Postma, J. P. M.; van Gunsteren, W. F.; DiNola, A.; Haak, J. R. Molecular Dynamics with Coupling to an External Bath. *The Journal of Chemical Physics* **1984**, *81* (8), 3684–3690. https://doi.org/10.1063/1.448118.

(33) Ryder, M. R.; Civalleri, B.; Tan, J.-C. Isoreticular Zirconium-Based Metal–Organic Frameworks: Discovering Mechanical Trends and Elastic Anomalies Controlling Chemical Structure Stability. *Phys. Chem. Chem. Phys.* **2016**, *18* (13), 9079–9087. https://doi.org/10.1039/C6CP00864J.

(34) Liang, W.; Babarao, R.; Church, T. L.; D'Alessandro, D. M. Tuning the Cavities of Zirconium-Based MIL-140 Frameworks to Modulate CO_2 Adsorption. *Chem. Commun.* **2015**, *51* (56), 11286–11289. https://doi.org/10.1039/C5CC02539G.

(35) Kaur, G.; Øien-Ødegaard, S.; Lazzarini, A.; Chavan, S. M.; Bordiga, S.; Lillerud, K. P.; Olsbye, U. Controlling the Synthesis of Metal–Organic Framework UiO-67 by Tuning Its Kinetic Driving Force. *Crystal Growth & Design* **2019**, *19* (8), 4246–4251. https://doi.org/10.1021/acs.cgd.9b00916.

(36) Hester, P.; Xu, S.; Liang, W.; Al-Janabi, N.; Vakili, R.; Hill, P.; Muryn, C. A.; Chen, X.; Martin, P. A.; Fan, X. On Thermal Stability and Catalytic Reactivity of Zr-Based Metal–Organic Framework (UiO-67) Encapsulated Pt Catalysts. *Journal of Catalysis* **2016**, *340*, 85–94. https://doi.org/10.1016/j.jcat.2016.05.003.

(37) Trannoy, V.; Guillou, N.; Livage, C.; Roch-Marchal, C.; Haouas, M.; Léaustic, A.; Allain, C.; Clavier, G.; Yu, P.; Devic, T. Fluorescent Zr(IV) Metal–Organic Frameworks Based on an Excited-State Intramolecular Proton Transfer-Type Ligand. *Inorg. Chem.* **2019**, *58* (10), 6918–6926. https://doi.org/10.1021/acs.inorgchem.9b00388.

Chapter - 7

7 Development of a ReaxFF reactive force field for CO_2 hydrogenation on ruthenium

Swarit Dwivedi[1], Ojus Mohan[2], Malgorzata Kowalik[3], Alan L. Chaffee[4], Samir H. Mushrif[2], Adri van Duin[3], Akshat Tanksale[1]

1) Department of Chemical Engineering, Monash University, Clayton 3800, Victoria, Australia
2) Department of Chemical and Materials Engineering, University of Alberta, 9211-116 Street Northwest, Edmonton, Alberta T6G 1H9, Canada
3) Department of Mechanical Engineering, The Pennsylvania State University, University Park, PA, USA
4) School of Chemistry, Monash University, Clayton 3800, Victoria, Australia

Author contributions

In the case of chapter 7, my contribution to the work involved the following:

Thesis Chapter	Publication Title	Status	Nature and % of student contribution
7	Development of a ReaxFF reactive force field for CO_2 hydrogenation on ruthenium	In preparation	80%. Conception, designing experiments, collection and analysis of data, and writing first draft

Co-author names	Nature of contribution	Monash student?
Ojus Mohan	3% discussion and suggestions, Postdoc (Collaborator, University of Alberta)	No
Malgorzata Kowalik	2% discussion and suggestions, Postdoc (Collaborator, Pennsylvania State University)	No
Alan L Chaffee	2% discussion and suggestions, Supervisor	No
Samir H. Mushrif	3% discussion and suggestions, Supervisor	No
Adri CT van Duin	5% discussion and suggestions, Professor (Collaborator, Pennsylvania State University)	No
Akshat Tanksale	5% discussion and suggestions, Supervisor	No

7.1 Abstract

Quantum mechanics-based methods are inefficient for simulating a large number of atoms (>100 atoms) or for longer time spans (>100 ps). Here, we show a reactive molecular dynamics force field parameter to study bigger system sizes with the aim of understanding the structure-activity relationship of catalyst and the synergy of the catalyst-support. The Ru/C/H/O forcefield parameters are trained for the binding energy of reaction intermediates relevant to CO_2 methanation and Fischer-Tropsch synthesis. A good agreement between the binding energy of ReaxFF and various DFT optimised structures has been obtained. We simulate Ru hcp 001 surface interaction with water and observe a hexagonal hydrogen-bonded network of water on the surface. We explore the CO fission on ruthenium nanoparticles of varying size and shape. We also explore the widely debated mechanism of adlayer dynamics for C-C coupling on ruthenium nanoparticles. The ReaxFF force field parameter presented in this work is capable of simulating Pt/Ru/Ni/C/H/O/N.

Keywords: CO_2 hydrogenation, ReaxFF, Ruthenium, CO activation

7.2 Introduction

CO_2 methanation and Fischer Tropsch synthesis (FTS) are widely studied catalytic reaction systems[1]. Numerous reports explore the size and shape of the catalyst, reactant concentration, temperature, pressure, and chemical composition of the catalyst. Nonetheless, there are no widely accepted mechanism of CO_2 hydrogenation on Ruthenium (Ru) nanoparticles that covers the horizon from CO_2 methanation to various products formed via FTS. Furthermore, due to the lack of understanding about the rate-limiting step[2–5], the possibilities of overcoming the energy barriers are still being explored. Ru, Cobalt, and Iron are the most active metals for FTS with high turnover frequencies (TOF)[6]. The turnover frequency is greatly affected by the particle size, support, and promoters. For Ru, fcc-111 and hcp-001 facets have been reported for FTS, but the activity is optimum at ~ 10 nm particle size[7,8].

The most stable surface of ruthenium is hcp-001, which is also more active than fcc-111 for C-O dissociation. On Ru hcp 001 facet, CO_2 methanation is expected to be initiated by CO_2 dissociation to CO and O followed by C-O bond fission, the rate limiting step[1,5,9]. On a flat Ru (hcp-001) surface, it is reported that CO activation is favoured after CO hydrogenation to either COH*, HCO*, or H2CO*[2]. However, on a Ru hcp-001 nanoparticle, C-O bond fission has a lower barrier on the stepped edge site[10]. Therefore, on a Ru nanoparticle, the kinetics of CO_2 hydrogenation is controlled by the availability of a stepped edge site for CO activation.

In FTS synthesis, although CO activation is the rate-limiting step, it also initiates C-C coupling[3]. Amid ongoing contradictions about the C-C coupling mechanism, the widely accepted studies suggest that C-C coupling is facilitated by on the edge sites on Ru nanoparticles by two neighbouring CO molecules[5,8]. One CO is hydrogenated to COH*, followed by COH* dissociation to OH* and C*-CO* intermediate, also termed adlayer dynamics since dense layers of CO* on edge sites promote the C-C coupling[3]. However, the effect of particle size on the dynamics adlayer remains unclear. A key reason is the inability of QM-based simulation methods to study system size of the order ~ 8 nm.

In the presence of a liquid media, Ru is active for CO and CO_2 hydrogenation into various value-added C1 platform chemicals such formaldehyde, formic acid, DME, and OME[11–13]. The polar liquid phase, such as water and alcohols, has the ability to stabilise the polar reaction intermediates and effect selectivity of the reaction. Moreover, the yield of the product can be tuned by designing a secondary reaction scheme within the liquid media and micro-phase solvation. The role of liquid media in the reaction system could be complex and affect different aspects (e.g., surface coverage, stability of intermediates and transition state, acidity, overall free energy, and entropic barriers) simultaneously[14,15]. Computationally, researchers have manily studied specific individual aspects of liquid-phase heterogeneous catalytic reactions even after rigorous and expensive simulations.

Reactive molecular dynamic is an effective strategy of simulating chemical reactions with a large number of atoms (>10,000). The reactive forcefields are generally trained on a target QM simulation data set. Once trained and tested for the physical and chemical properties of relevant molecules, the forcefield is expected to simulate the target chemistry at larger scales (> 10 nm). The ReaxFF forcefield parameters[16,17] for Ru/C/H/O atoms are provided with the standalone version of the ReaxFF code and are also included in the LAMMPS software package[18]. Kim et al.[19] developed Ru/N/H parameters to study the effect of Ru nanoparticle size and shape on ammonia synthesis. No literature reports the Ru/C/H/O parameters to simulate the CO_2 hydrogenation. We aim to train Ru/C/H/O ReaxFF parameters (a bond-order based reactive force field) to simulate CO/CO_2 hydrogenation on the Ru hcp-001 surface. After training the ReaxFF parameters, we aim to study the CO_2 hydrogenation reaction energy coordinates, Ru-water interface, and CO activation on Ru nanoparticles.

7.3 Simulation Methodology

ReaxFF is a reactive molecular dynamics force-field, the force-field parameters are empirical, and the overall energy of the system is defined as the sum of several bonded and non-bonded energy contributions (Eq. 1). The non-bonded energies are defined as the coulombic and van der Walls energies like a classical force-field. The bonded interactions are defined as a function of bond-order (BO_{ij}), which is calculated as a function of inter-atomic distances (r_{ij}, Eq. 2). The energy contributions due to sigma (σ) bond, single (π) and double pi ($\pi\pi$) bonds are separately taken into account based on the interatomic distance. A detailed description of ReaxFF can be found elsewhere[16,17]. The force field was parameterized using a successive one-parameter search technique. The aim of optimisation was to minimise the error function defined in Eq. 3 where $X_{i,QM}$ is the energy calculated by QM, $X_{i,ReaxFF}$ is the energy calculated by ReaxFF, and σ_i is the weight assigned to the i^{th} training set.

$$E_{system} = E_{bond} + E_{lp} + E_{over} + E_{under} + E_{val} + E_{pen} + E_{coa} + E_{C2} + E_{tors} + E_{conj} + E_{H-bond} + E_{vdWaals} + E_{coulomb} \quad \text{(Eq. 1)}$$

$$BO_{ij} = BO_{ij}^{\sigma} + BO_{ij}^{\pi} + BO_{ij}^{\pi\pi}$$
$$= \exp\left[p_{bo1}\left(\frac{r_{ij}}{r_0^{\sigma}}\right)^{p_{bo2}}\right] \quad \text{(Eq. 2)}$$
$$+ \exp\left[p_{bo3}\left(\frac{r_{ij}}{r_0^{\pi}}\right)^{p_{bo4}}\right] + \exp\left[p_{bo5}\left(\frac{r_{ij}}{r_0^{\pi\pi}}\right)^{p_{bo6}}\right]$$
$$Error = \Sigma_{i=1}^{N}\left(\frac{X_{i,QM} - X_{i,ReaxFF}}{\sigma_i}\right)^2 \quad \text{(Eq. 3)}$$

The ReaxFF force-field parameters Ru/C/H/O ReaxFF parameter set was first developed by Adri van Duin and co-workers[17]. The parent parameters were trained for consists of equation or states, heats of formation of bulk phases, surface energies of Ruthenium hcp and fcc facets. Ojus et al.[2] have recently reported an extensive set of DFT and micro-kinetic modelling data of CO_2 hydrogenation on Ni (fcc-111) and Ru (hcp-001) surface. We use the DFT optimised structures and the electronic binding energy data of key reaction intermediates on Ru hcp-001 surface reported by Ojus et al.[2] to train the ReaxFF parameters. Ojus et al.[2] used the rPBE-vdW exchange-correlation functional and the binding energy was calculated for one adsorbed reaction intermediate on a 4-layer p (4×4) unit cell. For computational methodology including the thermodynamic corrections used in the DFT study, refer to the work by Ojus et al.[2]

The equations used for binding energy calculation are mentioned in Table 7.1. For the reaction intermediates stable in the gas-phase (CO, CO_2, CH_2O, CH_3OH, HCOOH, and CH_4), the binding energies are calculated by subtracting the energy of slab (*slab*) and the energy of gas-phase molecule (*molecule(g)*) from the adsorbed molecule (*molecule**). However, for the intermediates that are not stable in the gas-phase, we calculated the binding energy by taking gas-phase reference energy of $(CH_{4(g)} - 2 * H_{2(g)})$ for C, $\frac{1}{2}H_{2(g)}$ for H, and $\frac{1}{2}O_{2(g)}$ for O atom. Figure 7.1 shows a parity plot for the training DFT energies and the trained ReaxFF energies. ReaxFF reproduces the DFT binding energies excluding water. A stronger affinity of water to the metal is common is ReaxFF. However, the deviation (-63.36 kcal/mol by DFT and 85.06 kcal/mol by ReaxFF) is considered acceptable in this work.

Table 7.1: Shows the comparison of binding energy data of DFT (rPBE-vdW exchange-correlation) optimised reaction intermediates by Ojus et al.[2] and of trained ReaxFF Ru/C/H/O force-field in this work.

Equation	**DFT (kcal/mol)**	**ReaxFF (kcal/mol)**
CO^*- slab – $CO_{(g)}$	-40.29	-39.69
CO_2^*- slab - $CO_{2(g)}$	-10.75	-10.32
CH_2O^*- slab - $CH_{2(g)}$	-23.52	-21.15
CH_3OH^*- slab - $CH_3OH_{(g)}$	-12.52	-11.59
CH_4^*- slab - $CH_{4(g)}$	-4.57	-4.99
$HCOOH^*$- slab - $HCOOH_{(g)}$	-14.51	-21.04
C^* - slab - $CH_{4(g)} + 2\times H_{2(g)}$	23.63	23.28
CH^* - slab - $CH_{4(g)} + 1.5\times H_{2(g)}$	10.99	12.24
CH_2^* -slab - $CH_{4(g)} + H_{2(g)}$	15.65	15.84
CH_3^* -slab - $CH_{4(g)} + 0.5\times H_{2(g)}$	7.97	15.84
CHO^* - slab - $CH_{4(g)} + 1.5\times H_{2(g)} - 0.5\times O_{2(g)}$	-25.93	-22.11
CH_3O^* - slab - $CH_{4(g)} + 0.5\times H_{2(g)} - 0.5\times O_{2(g)}$	-44.20	-41.57
CH_2OH^* - slab - $CH_{4(g)} + 0.5\times H_{2(g)} - 0.5\times O_{2(g)}$	-26.71	-31.23
COH^* - slab - $CH_{4(g)} + 1.5\times H_{2(g)} - 0.5\times O_{2(g)}$	-31.20	-33.18
$HCOO^*$ - slab - $CH_{4(g)} + 1.5\times H_{2(g)} - O_{2(g)}$	-93.08	-89.03
O^* - slab - $0.5\times O_{2(g)}$	-70.38	-68.49
H^* - slab - $0.5\times H_{2(g)}$	-10.10	-13.70
$CHOH^*$ - slab - $CH_{4(g)} + H_2 - 0.5\times O_{2(g)}$	-21.04	-22.70
H_2O^* - slab - $\times H_{2(g)} - 0.5\times O_{2(g)}$	-63.36	-85.06

We first compare the FCC and HCP structures of Ru using the trained forcefield parameters. The energy per atom of optimised FCC structure (10-10-10 supercell) is -6.15 eV. However, for an HCP structure (10-10-10 supercell), the energy per atom for the optimised structure is -6.68 eV. We tested the trained force-field to optimise a Ru hcp simulation cell (16000 atoms, 20×20×20 supercell) to an energy tolerance of 1 kcal/mol. Table 7.2 shows the comparison

between the cell parameters and the density of Ru hcp cell in the Materials Project database[23], the experiments[24], and this work. An acceptable deviation of ~ 1.9% in density and an acceptable maximum difference of ~ 2.8% in cell length is observed whereas the cell angles are consistent as $\alpha = 90°$, $\beta = 90°$, and $\gamma = 120°$.

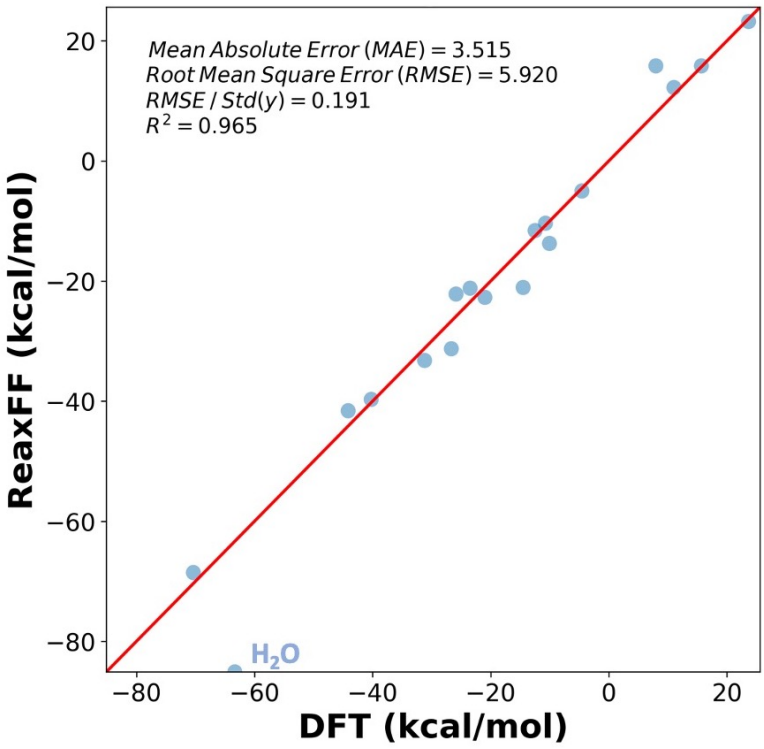

Figure 7.1 Shows the comparison between the energy of DFT optimised structure as calculated by DFT (Ojus et. al) and ReaxFF (this work)

Table 7.2: Ru HCP cell parameters comparison between ReaxFF, DFT, and experiments

Method	**Density (g/cm^3)**	***α***	***β***	***γ***	***a* (Å)**	***b* (Å)**	***c* (Å)**
Materials Project[23] (PAW Ru_pv)	12.03	90º	90º	120º	2.73	2.73	4.31
ReaxFF (this work)	12.12	90º	90º	120º	2.70	2.70	4.40
Experiment[24] (300 K)	12.36	90º	90º	120º	2.70	2.70	4.28

7.4 Results and Discussion

7.4.1 ReaxFF optimised reaction intermediates and reaction coordinates

The binding energies in Table 7.1 are for the minimum energy configuration of the reaction intermediates as predicted by DFT. However, the energy landscape under the ReaxFF forcefield may differ and lead to a different minimum energy configuration. To ensure that the minimum energy configuration under ReaxFF forcefield is similar to DFT, we optimised the geometry predicted by DFT to a tolerance of 1 kcal/mol by the conjugate gradient method. After this, we compare the energies predicted by DFT and ReaxFF for reaction intermediate involved reaction pathways for CO_2 hydrogenation to methane.

Figure 7.2 shows the comparison between the energies of optimised DFT structures and the energies of optimised ReaxFF structures of key reaction intermediates for CO_2 hydrogenation to methane, formaldehyde, methanol, and formic acid. Figure 7.2 (a) compares the C and H rich species, whereas Fig. 7(b) shows the O rich species. The O-rich species have comparatively higher negative binding energies due to Ru's affinity for electrons. One of the anomalies is the relatively higher positive binding energies for C, CH, and CH_2 when ReaxFF predicts relatively smaller binding energy for other reaction intermediates. If this appear to be an issue during the application, we recommend re-training the forcefield with additional Ru-C-H data.

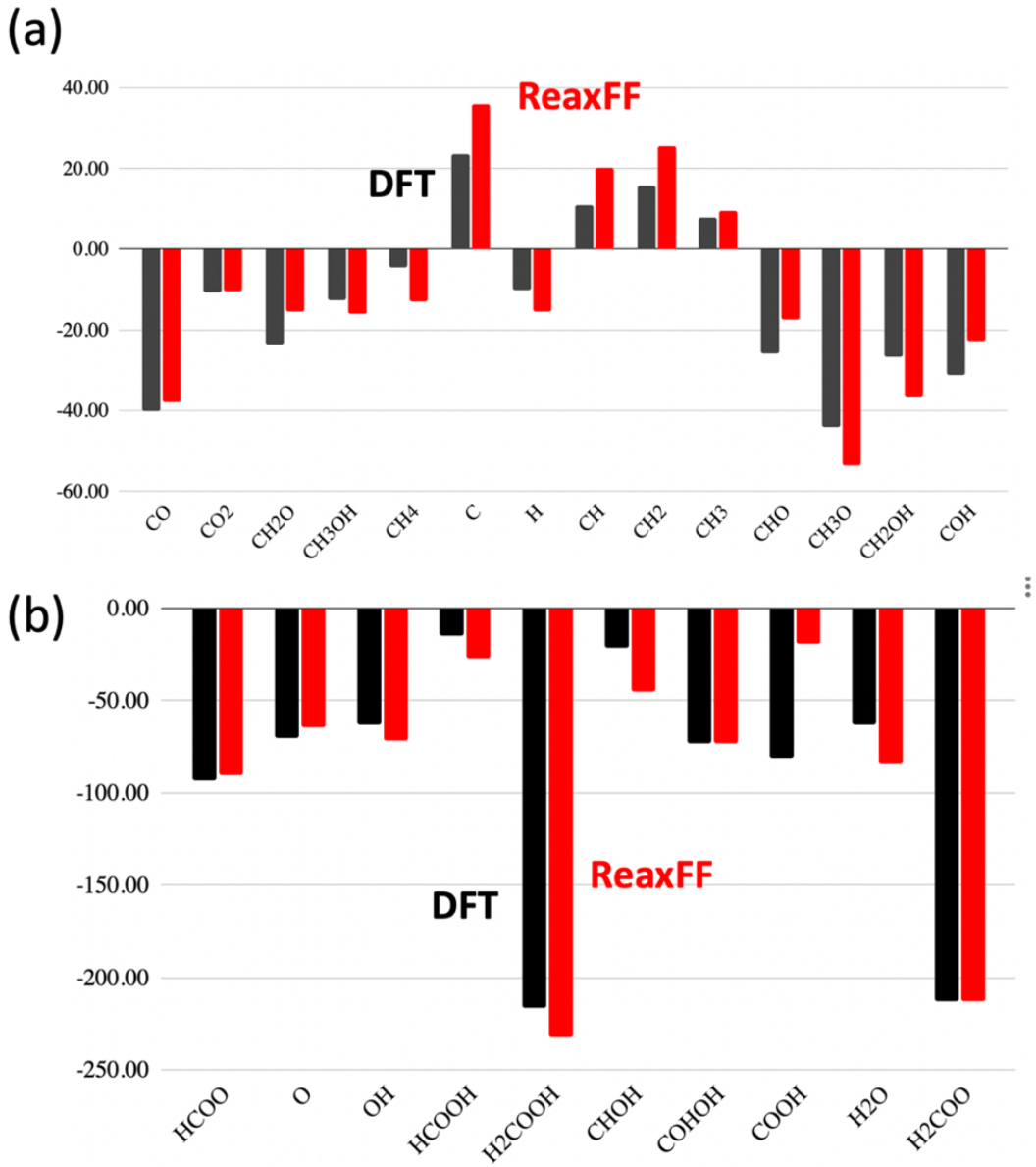

Figure 7.2: (a) and (b) show the energy (kcal/mol) of minimum energy configuration by DFT (black) and ReaxFF (red).

Figure 7.3 shows the optimised structures by DFT and ReaxFF for key intermediates of CO_2 hydrogenation into methane. The optimised geometries of ReaxFF and DFT are similar in orientation and the type of adsorption site. We observe some minor differences, such as Ru-C-O angle in COH* and Ru-C-Ru angle in CH_3*. For future optimisation, these angle parameters can be corrected by feeding more binding energy data at different sites of the hcp-001 surface for these reaction intermediates.

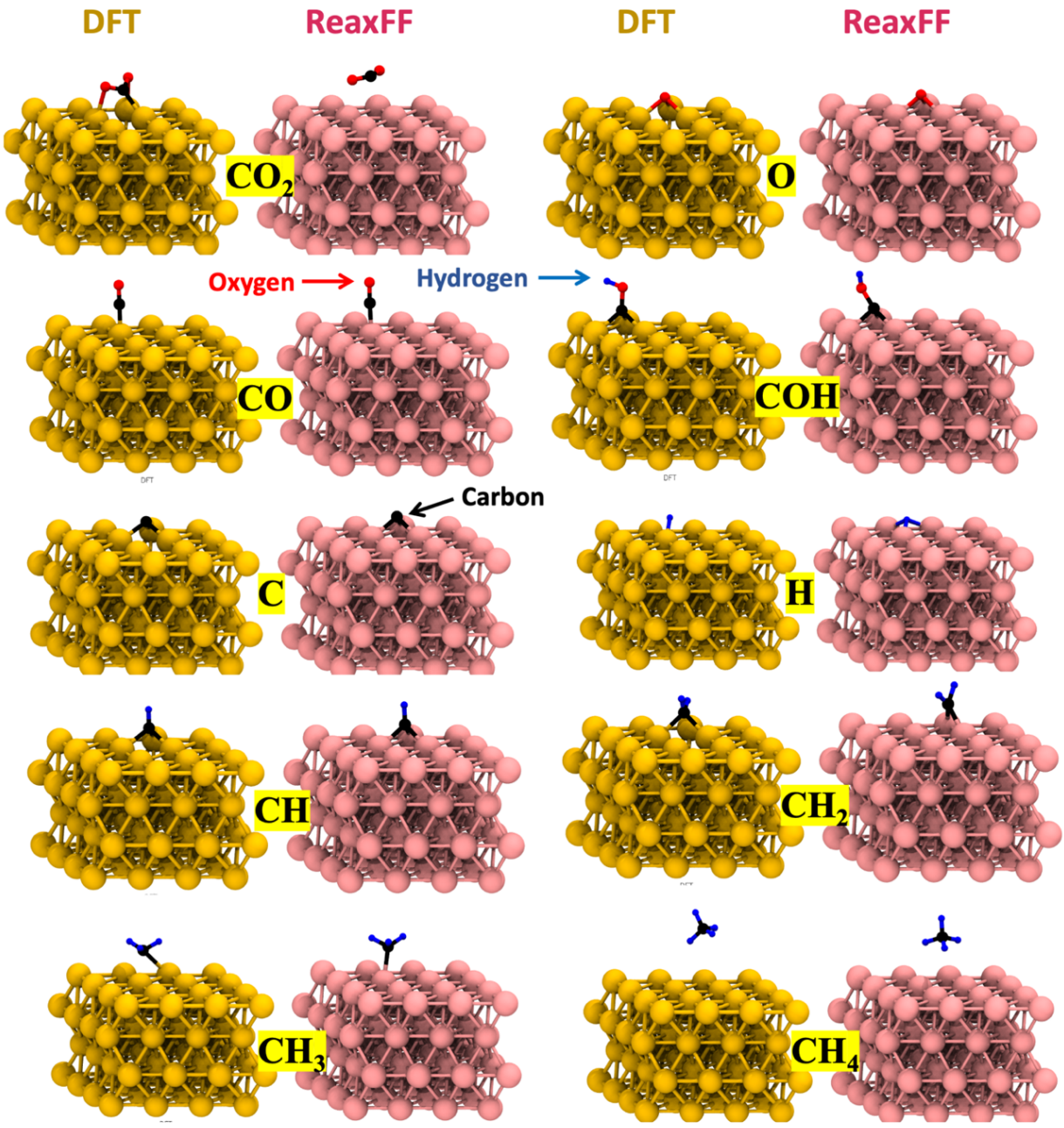

Figure 7.3 shows the comparison of between ReaxFF and DFT energies of most feasible reaction pathway for CO_2 hydrogenation to methane.

Figure 7.4 (a) Shows the CO_2 dissociation pathway on a Ru hcp-001. The reaction pathway is similar to the DFT pathway, but a minor difference is observed during OH* hydrogenation to form water. This step in ReaxFF is exothermic, whereas in the DFT it is endothermic. As the difference in energy is not large despite the opposite signs and the step is not crucial for

understanding CO_2 hydrogenation, we may ignore this small discrepancy. Figure 7.4(b) shows the reaction pathway for CO hydrogenation. The reaction pathway for ReaxFF is similar to the DFT pathway. However, it has one considerable deviation. Although of the same nature, the endothermic step of CO* hydrogenation to COH* has more energy requirement for ReaxFF. Therefore, based on the application and simulation conditions, retraining of force-field parameters may be required.

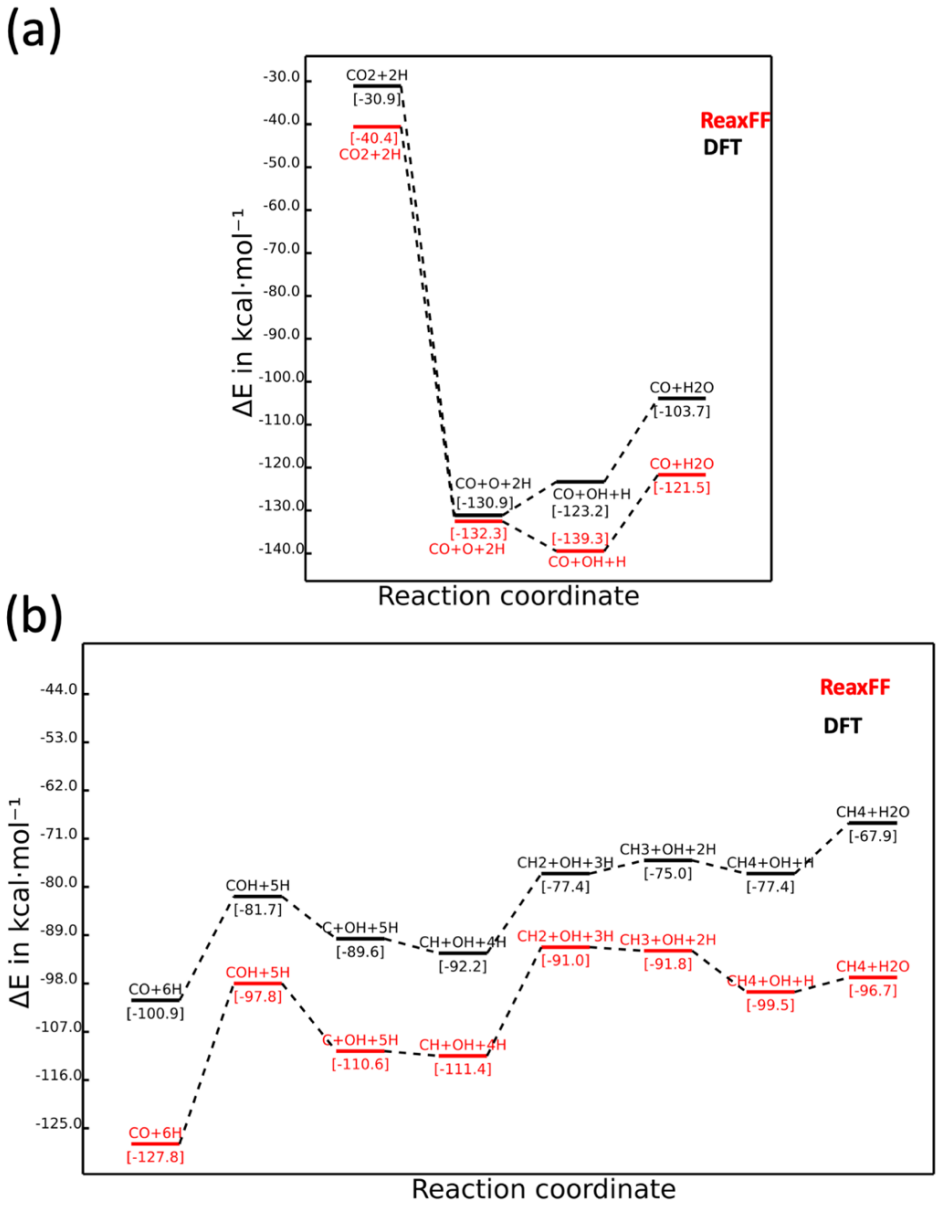

Figure 7.4: Comparison between DFT[2] and ReaxFF energies of reaction intermediates of CO_2 hydrogenation to methane. (a) Shows CO_2 activation by dissociation whereas (b) shows CO hydrogenation to methane.

7.4.2 Ruthenium-water interface

Over the years, various force-fields parameters have been reported for predicting the interactions in the aqueous phase. Even some of the most successful water potentials are unable to accurately reproduce of the wide spectrum of physical and chemical properties of water. Not all ReaxFF forcefields are developed to simulate the complex hydrogen-bonding interactions in the presence of water, and the ones that do are termed to be in the aqueous branch of ReaxFF force-fields[17]. The Ru/C/H/O force-field parameters developed in this work is part of the aqueous branch and we train water adsorptions and dissociated QM data in the training data set (Table 7.1). We simulate a box of 1000 water molecules on a Ru hcp 001 surface (800 Ru atoms, 10-10-4 supercell). Figure 7.5(a) shows the final structure after 1 ns of NPT simulation at 300 K. Water molecules form a hydrogen-bonded hexagonal network on the surface. The hexagonal network is similar to the previously reported bilayer hexagonal network of water on Ru hcp-001 surface (Fig. 7.5(b))[20,21].

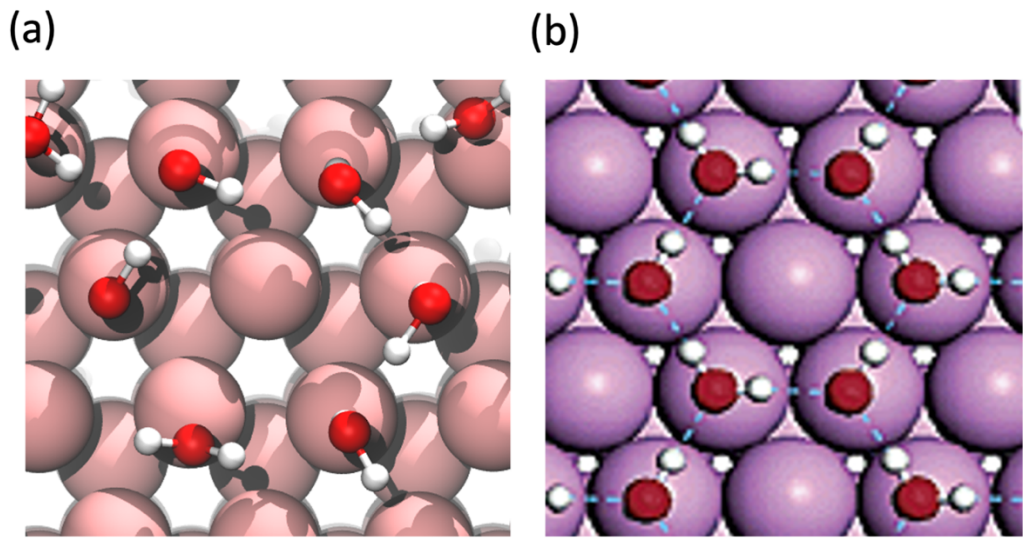

Figure 7.5: Shows the interaction of water at Ru hcp-001 surface for (a) ReaxFF and (b) previously reported ab initio MD simulation[21].

The adsorbed water on the hcp surface of transition metals may undergo partial dissociation, especially at higher temperatures. The heterolytic dissociation of the H-OH bond of water

depends upon the ability of the metal surface to stabilise the reactive OH^- on the surface by transfer of one electron and formation of OH*. Kizhakevariam et. al[22] reported that the energy of proton transfer is positive if the work function for metal is more than 4.88 eV. However, Ru has a work-function of 25.7 eV, therefore, water may dissociate at higher temperatures aided by the hydrogen-bonded bilayer with a presence of an H+ and OH- on the surface is unlikely.

7.4.3 Effect of nanoparticle size for C-O activation

The size of the nanoparticle is an important parameter for the activity of CO hydrogenation reactions. Approximately 10 nm size nanoparticles are reported for optimum activity. However, there is no direct computational study that simulates these large nanoparticles and the size effect on CO hydrogenation. We compare 4 Ru octahedral nanoparticles with hcp 001 surface to compare the effect of particle size on the adlayer dynamics and FTS. These nanoparticles were optimised and reported in an earlier QM simulation study. One Ru nanoparticle, 300 CO, and 1200 H_2 molecules were randomly packed in a simulation box. The system was subject to 80 bar pressure and under 1000 K temperature for 1 ns to observe the CO adsorption and activation of the nanoparticle. A higher temperature accelerates the reaction kinetics, which is a common practice in reactive molecular dynamics simulations.

Figure 7.6 shows the surface of Ru nanoparticles after 1 ns. The smallest particles are most active for C-O bond fission and the activity decreases with the increase of particle size since the stepped edge site of the nanoparticle is the active site, and the fraction of stepped edge surface area reduces with increasing particle size. Although CO and CO_2 methanation reactions are limited by the activation of C-O bond dissociation, the stepped edge sites of smaller particles (Fig. 7.6(a), 7.6(b), and 7.6(c)) are coked, and blocked. However, for larger nanoparticles, although the C-O activation is slower, coking the not observed (Fig. 7.6(d) & 7.6(e)).

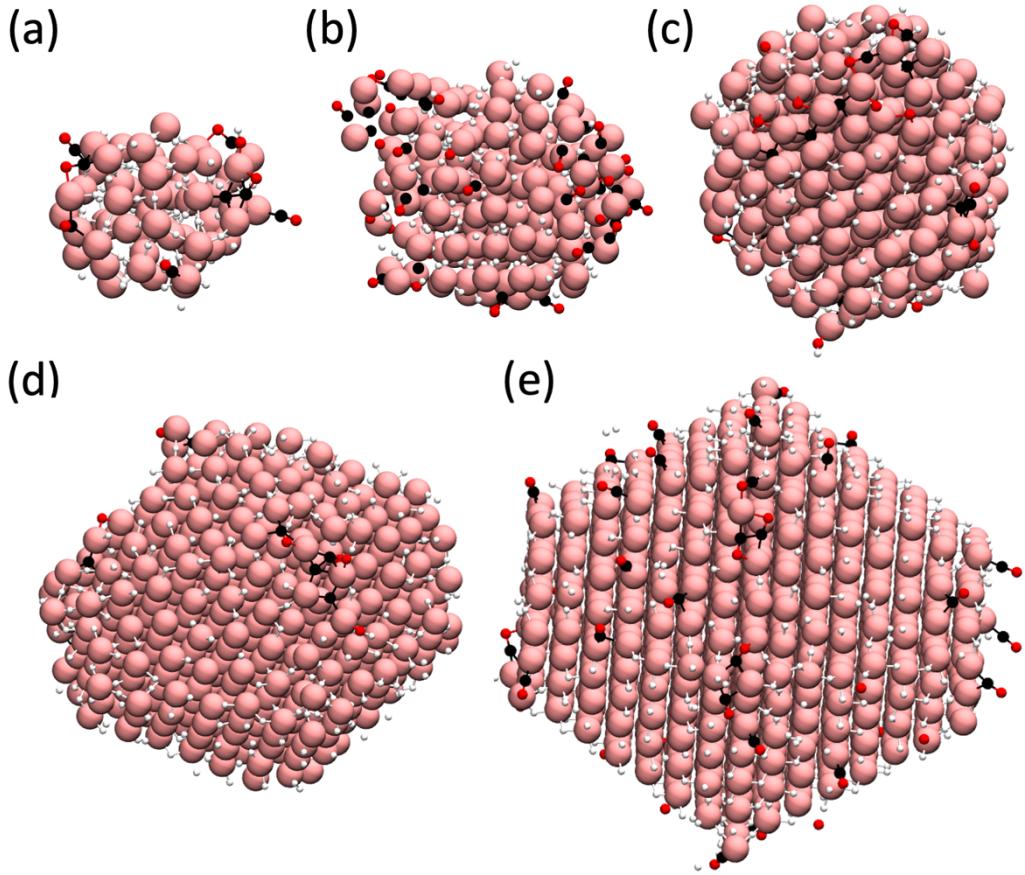

Figure 7.6: The surface of Ru hcp-001 nanoparticles of varying size after 1 ns of reaction under CO and H_2 at 1000 K at 80 bar pressure. (a) 63 Ru atoms (~ 1.2 nm), (b) 167 Ru atoms (~ 1.7 nm), (c) 347 Ru atoms (~ 2.1 nm), (d) 625 Ru atoms (~ 2.8 nm), and (e) 1021 Ru atoms (~ 3.5 nm)

7.5 Conclusion

We trained Ru/C/H/O force-field parameters to reproduce the binding energy data of key reaction intermediates in CO_2 hydrogenation to methane on a Ru hcp-001 surface. The force-field parameters successfully reproduced the binding energies. However, the binding energies of C, CH, CH2 under the developed ReaxFF description are higher than the DFT values. The reaction pathway for CO_2 dissociation to CO is reproduced. The water formation by hydrogenation of OH is endothermic in ReaxFF, whereas exothermic in DFT. However, the difference is small, so it is not critical for the understanding of CO_2 hydrogenation mechanisms.

The CO hydrogenation to methane reaction pathway is overall consistent with DFT results. However, the C* hydrogenation to CH* is endothermic in ReaxFF which is exothermic in DFT data. Therefore, the forcefield may require additional training on Ru-C-H parameters. The forcefield is capable of simulating the aqueous phase interactions and water molecules at the Ru hcp-001 surface form a hydrogen-bonded hexagonal network similar to earlier reports. We also simulated CO activation on Ru nanoparticles of varying size and observed the C deposition deactivating stepped edge sites in small size particles. The Ru/C/H/O forcefield presented here can be merged with other aqueous branch force-field to simulate metal-support synergy and similar target applications.

ASSOCIATED CONTENT

Supporting Information

Supporting information consisting Ru/C/H/O force-field parameters provided in Appendix C.

7.6 References

(1) Jahangiri, H.; Bennett, J.; Mahjoubi, P.; Wilson, K.; Gu, S. A Review of Advanced Catalyst Development for Fischer–Tropsch Synthesis of Hydrocarbons from Biomass Derived Syn-Gas. *Catal. Sci. Technol.* **2014**, *4* (8), 2210–2229. https://doi.org/10.1039/C4CY00327F.

(2) Mohan, O.; Shambhawi, S.; Xu, R.; Lapkin, A. A.; Mushrif, S. H. Investigating CO_2 Methanation on Ni and Ru: DFT Assisted Microkinetic Analysis. *ChemCatChem* **2021**, cctc.202100073. https://doi.org/10.1002/cctc.202100073.

(3) Foppa, L.; Iannuzzi, M.; Copéret, C.; Comas-Vives, A. Adlayer Dynamics Drives CO Activation in Ru-Catalyzed Fischer–Tropsch Synthesis. *ACS Catal.* **2018**, *8* (8), 6983–6992. https://doi.org/10.1021/acscatal.8b01232.

(4) Yang, J.; Ma, W.; Chen, D.; Holmen, A.; Davis, B. H. Fischer–Tropsch Synthesis: A Review of the Effect of CO Conversion on Methane Selectivity. *Applied Catalysis A: General* **2014**, *470*, 250–260. https://doi.org/10.1016/j.apcata.2013.10.061.

(5) Loveless, B. T.; Buda, C.; Neurock, M.; Iglesia, E. CO Chemisorption and Dissociation at High Coverages during CO Hydrogenation on Ru Catalysts. *J. Am. Chem. Soc.* **2013**, *135* (16), 6107–6121. https://doi.org/10.1021/ja311848e.

(6) Gual, A.; Godard, C.; Castillón, S.; Curulla-Ferré, D.; Claver, C. Colloidal Ru, Co and Fe-Nanoparticles. Synthesis and Application as Nanocatalysts in the Fischer–Tropsch Process. *Catalysis Today* **2012**, *183* (1), 154–171. https://doi.org/10.1016/j.cattod.2011.11.025.

(7) Kang, J.; Deng, W.; Zhang, Q.; Wang, Y. Ru Particle Size Effect in Ru/CNT-Catalyzed Fischer-Tropsch Synthesis. *Journal of Energy Chemistry* **2013**, *22* (2), 321–328. https://doi.org/10.1016/S2095-4956(13)60039-X.

(8) Li, W.-Z.; Liu, J.-X.; Gu, J.; Zhou, W.; Yao, S.-Y.; Si, R.; Guo, Y.; Su, H.-Y.; Yan, C.-H.; Li, W.-X.; Zhang, Y.-W.; Ma, D. Chemical Insights into the Design and Development of Face-Centered Cubic Ruthenium Catalysts for Fischer–Tropsch Synthesis. *J. Am. Chem. Soc.* **2017**, *139* (6), 2267–2276. https://doi.org/10.1021/jacs.6b10375.

(9) Mutschler, R.; Moioli, E.; Züttel, A. Modelling the CO_2 Hydrogenation Reaction over Co, Ni and Ru/Al2O3. *Journal of Catalysis* **2019**, *375*, 193–201. https://doi.org/10.1016/j.jcat.2019.05.023.

(10) Ciobica, I. M.; van Santen, R. A. Carbon Monoxide Dissociation on Planar and Stepped Ru(0001) Surfaces. *J. Phys. Chem. B* **2003**, *107* (16), 3808–3812. https://doi.org/10.1021/jp030010x.

(11) Ahmad, W.; Chan, F. L.; Chaffee, A. L.; Wang, H.; Hoadley, A.; Tanksale, A. Dimethoxymethane Production via Catalytic Hydrogenation of Carbon Monoxide in Methanol Media. *ACS Sustainable Chem. Eng.* **2020**, *8* (4), 2081–2092. https://doi.org/10.1021/acssuschemeng.9b06913.

(12) Álvarez, A.; Bansode, A.; Urakawa, A.; Bavykina, A. V.; Wezendonk, T. A.; Makkee, M.; Gascon, J.; Kapteijn, F. Challenges in the Greener Production of Formates/Formic Acid, Methanol, and DME by Heterogeneously Catalyzed CO_2 Hydrogenation Processes. *Chem. Rev.* **2017**, *117* (14), 9804–9838. https://doi.org/10.1021/acs.chemrev.6b00816.

(13) Bahmanpour, A. M.; Hoadley, A.; Mushrif, S. H.; Tanksale, A. Hydrogenation of Carbon Monoxide into Formaldehyde in Liquid Media. *ACS Sustainable Chem. Eng.* **2016**, *4* (7), 3970–3977. https://doi.org/10.1021/acssuschemeng.6b00837.

(14) Varghese, J. J.; Mushrif, S. H. Origins of Complex Solvent Effects on Chemical Reactivity and Computational Tools to Investigate Them: A Review. *React. Chem. Eng.* **2019**, *4* (2), 165–206. https://doi.org/10.1039/C8RE00226F.

(15) van Santen, R. A.; Neurock, M. *Molecular Heterogeneous Catalysis*; Wiley-VCH Verlag GmbH & Co. KGaA: Weinheim, Germany, 2006. https://doi.org/10.1002/9783527610846.

(16) van Duin, A. C. T.; Dasgupta, S.; Lorant, F.; Goddard, W. A. ReaxFF: A Reactive Force Field for Hydrocarbons. *J. Phys. Chem. A* **2001**, *105* (41), 9396–9409. https://doi.org/10.1021/jp004368u.

(17) Senftle, T. P.; Hong, S.; Islam, M. M.; Kylasa, S. B.; Zheng, Y.; Shin, Y. K.; Junkermeier, C.; Engel-Herbert, R.; Janik, M. J.; Aktulga, H. M.; Verstraelen, T.; Grama, A.; van Duin, A. C. T. The ReaxFF Reactive Force-Field: Development, Applications and Future Directions. *npj Comput Mater* **2016**, *2* (1), 15011. https://doi.org/10.1038/npjcompumats.2015.11.

(18) Plimpton, S. Fast Parallel Algorithms for Short-Range Molecular Dynamics. *Journal of Computational Physics* **1995**, *117* (1), 1–19. https://doi.org/10.1006/jcph.1995.1039.

(19) Kim, S.-Y.; Lee, H. W.; Pai, S. J.; Han, S. S. Activity, Selectivity, and Durability of Ruthenium Nanoparticle Catalysts for Ammonia Synthesis by Reactive Molecular Dynamics Simulation: The Size Effect. *ACS Appl. Mater. Interfaces* **2018**, *10* (31), 26188–26194. https://doi.org/10.1021/acsami.8b05070.

(20) Desai, S. K.; Neurock, M. First-Principles Study of the Role of Solvent in the Dissociation of Water over a Pt-Ru Alloy. *Phys. Rev. B* **2003**, *68* (7), 075420. https://doi.org/10.1103/PhysRevB.68.075420.

(21) Michaelides, A.; Alavi, A.; King, D. A. Different Surface Chemistries of Water on Ru{0001}: From Monomer Adsorption to Partially Dissociated Bilayers. *J. Am. Chem. Soc.* **2003**, *125* (9), 2746–2755. https://doi.org/10.1021/ja028855u.

(22) Kizhakevariam, N.; Stuve, E. M. Coadsorption of Water and Hydrogen on Pt(100): Formation of Adsorbed Hydronium Ions. *Surface Science* **1992**, *275* (3), 223–236. https://doi.org/10.1016/0039-6028(92)90796-9.

(23) Jain, A.; Ong, S. P.; Hautier, G.; Chen, W.; Richards, W. D.; Dacek, S.; Cholia, S.; Gunter, D.; Skinner, D.; Ceder, G.; Persson, K. A. Commentary: The Materials Project: A Materials Genome Approach to Accelerating Materials Innovation. *APL Materials* **2013**, *1* (1), 011002. https://doi.org/10.1063/1.4812323.

(24) Arblaster, J. W. Crystallographic properties of ruthenium. *Platinum Metals Review* **2013**, *57*(2), 127-136. http://dx.doi.org/10.1595/147106713X665030

Chapter 8

8 Conclusions and future recommendations

8.1 Conclusions

We discuss micro-phase solvation and MOF-derived advanced materials in relation to the catalytic systems recently reported to provide better yield, kinetics, and selectivity of CO/CO_2 hydrogenation to value-added products. Moreover, we also develop a reactive molecular dynamics force-field (ReaxFF) to simulate CO_2 hydrogenation chemistry at a large scale (> 10000 atoms). We summarise our key finding hereby,

8.1.1 Micro-phase solvation

We study formaldehyde-methanol-water mixtures using classical molecular dynamics simulations and Small-Angle Neutron Scattering (SANS) measurements. We report the presence of molecular clusters at low methanol and high methanol concentrations. We first demonstrate a rigorous methodology for observing hydrophobic clusters of small molecules in a ternary liquid mixture by small-angle neutron scattering measurements. Formaldehyde (< 4 wt. %) in low methanol concentration methanol-water mixtures (x_m < 0.3), solvated as methoxymethanol, forms hydrophobic clusters with methanol. However, water in these mixtures forms a strong 3-D network. At high methanol concentrations, methanol exists in hydrogen-bonded linear chains and methoxymethanol hydrogen-bonded to methanol chains and is solvated in a pocket of ring/chain of methanol molecules. Water mostly exists in free form in these mixtures. At near equimolar compositions, the hydrophobic and hydrophilic clustering by methanol is disrupted. Fragments of hydrogen-bonded water molecules are present at the hydrophilic sites of methoxymethanol. This study, for the first time, establishes the micro-phase behaviour of formaldehyde-methanol-water mixtures. Moreover, it extends the previous hypothesis of micro-phase clustering in the liquid media affecting the yield of formaldehyde across all concentrations of methanol-water mixtures.

8.1.2 MOF-derived advanced materials

To simulate the thermal decomposition of Zr-MOFs at a large scale (>10000 atoms), we report Zr/C/H/O ReaxFF force-field parameters. An atomistic mechanism of thermal decomposition of Zr-MOF to a carbonaceous material with embedded metal oxide nanoparticles. We study the thermal decomposition of MIL-140C, m-MIL-140C (with modified linkers), UiO-66, and UiO-67 under vacuum, H_2, and CO_2 atmospheres. UiO-66 results in a larger nanoparticle size in comparison to MIL-140C and UiO-67. The cluster aggregation mechanism is different for MIL and UiO series. However, its effect on the final morphology is minor, considering MOFs are subject to sufficient heat. We identify that more organic material per metal atom and consequently larger pore size of the parent MOF results in smaller nanoparticles with better dispersion MOF-derived nanomaterial. Small gaseous molecules like CO, CO_2, and H_2 evolved from the function group the inker. However, in the UiO series, a considerable amount of water is produced from the OH ligand in the metal cluster. The decomposed MOFs have small nanoparticles in disrupted organic linkers. The metal oxide particles are stable in the organic phase, which provides these catalysts their expectational stability.

8.1.3 Ru/C/H/O ReaxFF force-field parameters

We report Ru/C/H/O ReaxFF parameters to simulate CO_2 hydrogenation chemistry on Ru. The trained force-field is developed in the aqueous branch of ReaxFF, and it successfully reproduces the physical properties of Ru metal and Ru-water interactions. The reaction pathway for CO_2 hydrogenation calculated by the trained force-field is similar to earlier QM reports with some minor differences. We simulate CO activation on Ru nanoparticles of different sizes. The stepped edge site is active for CO bond dissociation. For small nanoparticles (< 2.5 nm), coking deactivated the surface of the particle, whereas bigger nanoparticles remain fairly active after 1 ns at 1000 K.

8.2 Future recommendations

After understanding the dynamics of the liquid phase, we report that the solvation of at low co-solvent concentration in water may lead to the formation of hydrophobic molecular clusters that provide an additional stability to the product. We recommend researchers explore micro-phase solvation as a strategy to increase product yield in liquid phase heterogeneous catalytic reactions. For further understanding such ternary mixtures at a molecular length scale, we recommend free energy calculation to identify the entropic barriers of the hydrophobic and

hydrophilic clusters. Furthermore, the interaction of the liquid phase clusters with metal nanoparticles may provide direct evidence of the role these molecular clusters play during the liquid phase heterogeneous catalysis.

The MOF-derived nanomaterials have gained popularity within the last decade. Although a wide variety of well categorised MOFs have been reported, there is no mapping between the properties of MOFs and their thermally decomposed derivatives. We recommend researchers explore the thermal decomposition of MOFs, computationally and experimentally, to map the size and oxidation state of nanoclusters and the chemistry of decomposed linkers to the parent MOF. We also recommend the use of machine learning tools as more thermal decomposition data become available.

The encapsulated materials such as metal nanoparticles in carbonaceous materials may lead to a different decomposition behaviour of MOF. Moreover, the collapse of the framework may be controlled selectively by encapsulation. Graphene flakes and nitrogen constraining organic polymers are known to promote graphitisation. We recommend the decomposition of MOF in the presence of these materials either in the pores or after capping MOF nanoparticles with such materials.

We recommend combining the Ru/C/H/O parameters with Zr/C/H/O or Al/Si/C/H/O force-field parameters to understand the metal-support synergy observed during catalysis. We also recommend exploring these force-field parameters for liquid-phase catalytic reaction systems.

We recommend researchers use the SANS methodology presented in this thesis to explore ternary mixtures similar to formaldehyde-methanol-water. Specifically, studying other acetaldehyde-alcohol-water mixtures would fundamentally understand the hydrophobic tail's effect on the molecular cluster.

Appendix A1

Front page of published articles.

Journal of Molecular Liquids 301 (2020) 112444

Contents lists available at ScienceDirect

Journal of Molecular Liquids

journal homepage: www.elsevier.com/locate/molliq

Solvation behaviour and micro-phase structure of formaldehyde-methanol-water mixtures

Swarit Dwivedi[a], Samir H. Mushrif[b], Alan L. Chaffee[c], Akshat Tanksale[a,*]

[a]Department of Chemical Engineering, Monash University, Clayton 3800, Victoria, Australia
[b]Department of Chemical and Materials Engineering, University of Alberta, 9211-116 St., Edmonton, Alberta T6G 1H9, Canada
[c]School of Chemistry, Monash University, Clayton 3800, Victoria, Australia

ARTICLE INFO

Article history:
Received 16 September 2019
Received in revised form 9 December 2019
Accepted 1 January 2020
Available online 8 January 2020

Keywords:
Solvation dynamics
Formaldehyde
Formalin solution

ABSTRACT

Solvation of formaldehyde as methanediol and/or methoxymethanol in methanol-water mixtures of varying concentration was studied using classical molecular dynamics simulations. Varying strength of hydrophobic and hydrophilic interactions affect the arrangement of solvent within the solvation shell. Ether oxygen of methoxymethanol was observed to be hydrophobic in nature with hydrophilic interactions weaker than bulk due to the steric hindrance by the methyl group. At equimolar methanol-water compositions, water is more likely to occupy the hydrophilic sites. The total number of hydrogen bonds formed between solute and solvent decreased non-linearly, which was attributed to formaldehyde forming a distribution of different metastable complexes and micro-phase ordering. This non-linearity may influence the energetics of these solutions. The lifetime of hydrogen bonding was studied to build an understanding of the strength of hydrophilic interactions. The arrangement of methanol and water around solvated formaldehyde was visualised using spatial distribution function.

1. Introduction

Formaldehyde is a valuable chemical used as a raw material for the production of several commodities ranging from commercial to household products [1]. Formaldehyde consumption rate exceeds 30 million tonnes per year with a predicted annual growth of 4% [1]. It is used for the preparation of formaldehyde based resins (with urea, phenol, melamine, etc.), nano-porous organics gels, adhesives, plastics, foam, polyurethane paints, disinfectant, and in biomedical fixation. Commercially available formaldehyde solution, better known as formalin, is an aqueous solution of formaldehyde (37 wt%), where some methanol (10–15 wt%) is added to prevent precipitation of high molecular weight oligomers. This solution is then diluted or concentrated according to the requirements of the application. Formaldehyde in methanol-water mixtures has been a subject of study for almost a century across various disciplines of science and technology. However, the complex physical and chemical behaviour of this ternary mixture is still not very well understood. The complexities arise due to the oligomerisation of hydrated (methanediol) and alkoxylated (methoxymethanol) forms of formaldehyde. In the presence of water and methanol, formaldehyde rapidly converts into methanediol Eq. (1) and methoxymethanol Eq. (2), respectively. Methanediol and methoxymethanol are metastable and they undergo dehydration and de-alkoxylation when being isolated, respectively [2-5].

$$\underset{\text{Formaldehyde}}{HCHO} + \underset{\text{Water}}{H_2O} \rightleftharpoons \underset{\text{Methanediol}}{CH_2(OH)_2} \quad (1)$$

$$\underset{\text{Formaldehyde}}{HCHO} + \underset{\text{Methanol}}{CH_3OH} \rightleftharpoons \underset{\text{Methoxymethanol}}{HOCH_2OCH_3} \quad (2)$$

The hydration of formaldehyde and the formation of its oligomers has been studied in much more detail [6-10] in comparison to the alkoxylation of formaldehyde and their oligomerisation [11,12]. Over the years researchers have tried to determine the equilibrium constants of these reactions using NMR spectroscopy [6,5,12,13] and other experimental techniques, such as chemically enhanced absorption rate of solvation of formaldehyde gas coupled with high resolution densimetry [13] and vapour–liquid equilibrium modelling [14]. Even after many attempts, an accurate quantitative estimation of the chemical composition of the liquid phase of formaldehyde–methanol–water mixtures across broad temperature and concentration range is not yet established. This is mainly because of the number of different reactions involved (hydration, alkoxylation and

* Corresponding author.
E-mail address: Akshat.Tanksale@monash.edu (A. Tanksale).

https://doi.org/10.1016/j.molliq.2020.112444
0167-7322/

THE JOURNAL OF PHYSICAL CHEMISTRY LETTERS
A JOURNAL OF THE AMERICAN CHEMICAL SOCIETY

pubs.acs.org/JPCL Letter

Molecular Clustering in Formaldehyde–Methanol–Water Mixtures Revealed by High-Intensity, High-q Small-Angle Neutron Scattering

Swarit Dwivedi, Jitendra Mata, Samir H. Mushrif, Alan L. Chaffee, and Akshat Tanksale*

Cite This: J. Phys. Chem. Lett. 2021, 12, 480–486 Read Online

ACCESS | Metrics & More | Article Recommendations | Supporting Information

ABSTRACT: Methanol–Water (mw) mixtures, with or without a solute, display a nonideal thermodynamic behavior, typically attributed to the structure of the microphase. However, experimental observation of the microphase structures at the molecular length scale has been a challenge. We report the presence of molecular clusters in mw and formaldehyde–methanol–water (fmw) mixtures using small-angle neutron scattering (SANS) experiments and molecular dynamics (MD) simulations. Hydrophobic clusters of methanol in mw and formaldehyde–methanol in fmw mixtures were observed at low methanol compositions ($x_m \leq 0.3$). A three-dimensional hydrogen-bonded network of water with the solute is observed at $x_m = 0.5$. Linear chains of methanol surrounding the formaldehyde and water molecules were observed at high methanol compositions ($x_m \geq 0.7$). The calculated size of the molecular clusters ($r \approx 0.5$ nm, spherical) from the SANS data and their volume fraction closely matched the MD simulation results.

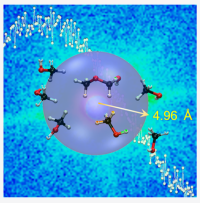

The composition of methanol–water (mw) mixtures affect the mixture's thermodynamic properties, including the enthalpy of mixing, free energy of solvation, and the excess molar volume, which do not vary linearly. This anomalous thermodynamic behavior is attributed to the dynamic structures at a molecular length scale, referred to as the "microphase".[1−4] The formation of microphase structures is due to trade-offs between the enthalpic gains and the entropic penalties, which eventually stabilize the system. In the midst of ongoing contradicting views,[5−8] the common understanding is that methanol forms hydrophobic clusters at low methanol compositions,[2,9] a bipercolating mixture near equimolar compositions,[9] and linear chains of methanol at high methanol compositions, in which the water molecule is either caged or exists in a free form within the mixture.[5,10] To understand the structure of the microphase, researchers explored experimental techniques such as neutron diffraction,[9−12] X-ray techniques,[5,13−15] and Raman spectroscopy.[16] Ab initio[5,17] and classical molecular dynamics simulations[2,10,18] were also used to simulate the microphase structure and complement the experimental observations. However, a quantitative analysis of the presence of microphase structures as a function of solvent composition is yet to be established.

Recently, we showed that syngas and CO_2 can be hydrogenated into formaldehyde in methanol–water mixtures and that the concentration of methanol has a significant impact on the product yield.[19] It is known that, when a small organic compound[20] is solvated in mw mixtures, the chemical and the physical behaviors of the solute are distinct at different mixture compositions. For example, the equilibrium of heterogeneous catalysis reactions[19] are greatly affected by the mw mixture composition. The solvation structure plays a central role in explaining most of these phenomena.

Formaldehyde hydrates in the presence of water and exists in its metastable form, methanediol (md).[21,22] At higher formaldehyde concentrations (>3 wt %), dimers and trimers of formaldehyde start forming, and as formaldehyde concentrations increase further, a precipitate of paraformaldehyde (pFa) is obtained.[22,23] Addition of methanol prevents the oligomerization of formaldehyde, and such formaldehyde–methanol–water (fmw) mixtures are commonly known as formalin solutions. In the presence of methanol, formaldehyde mostly remains in its metastable monomeric form, methoxymethanol (mm).[24] The ability of the metastable monomers (md and mm) to react or adsorb/desorb on to the catalytic surface is likely to be affected by their solvation environment. For example, Mugnai et al.[25] reported a cagelike solvation structure around formaldehyde in water, which hindered the translation and rotation of the formaldehyde and thus affected its hydration.[25−27] Moreover, mm is solvated by a ring/chain structure of 8–10 methanol molecules, which is reported to be the reason for the high catalytic yield of formaldehyde in the presence of methanol.[19] However, the stability and the solvation environment of mm in the mw mixtures remains poorly understood.[24,28] Our recent molecular dynamics (MD) work predicted the presence of methanol around the hydrophobic sites of mm and methanol at low methanol concentrations.[29] To the best of our knowledge, no

Received: November 26, 2020
Accepted: December 16, 2020
Published: December 29, 2020

https://dx.doi.org/10.1021/acs.jpclett.0c03515
J. Phys. Chem. Lett. 2021, 12, 480–486

THE JOURNAL OF PHYSICAL CHEMISTRY Letters

pubs.acs.org/JPCL Letter

Atomistic Mechanisms of Thermal Transformation in a Zr-Metal Organic Framework, MIL-140C

Swarit Dwivedi, Malgorzata Kowalik, Nilton Rosenbach, Dalal S. Alqarni, Yun Kyung Shin, Yongjian Yang, John C. Mauro, Akshat Tanksale, Alan L. Chaffee,* and Adri C.T. van Duin*

Cite This: J. Phys. Chem. Lett. 2021, 12, 177−184 Read Online

ACCESS | Metrics & More | Article Recommendations | Supporting Information

ABSTRACT: To understand the mechanisms responsible for thermal decomposition of a Zr-MOF (MIL-140C), we perform atomistic-scale molecular dynamics (MD) simulations and discuss the simulation data in comparison with the TEM images obtained for the decomposed Zr-MOF. First, we introduce the ReaxFF parameters suitable for the Zr/C/H/O chemistry and then apply them to investigate the thermal stability and morphological changes in the MIL-140C during heating. Based on the performed simulations we propose an atomic mechanism for the collapse of the MIL-140C and the molecular pathways for carbon monoxide formation, the main product of the MIL-140C thermal degradation. We also determine that the oxidation state of the ZrO_x clusters, evolved due to the thermal degradation, approximates the tetragonal phase of ZrO_2. Both simulations and experiments show a distribution of very small ZrO_x clusters embedded in the disrupted organic sheet that could contribute to the unusual high catalytic activity of the decomposed MIL-140C.

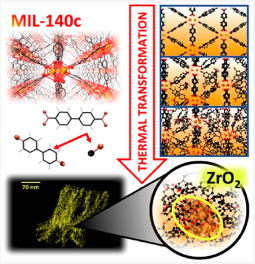

Metal organic frameworks (MOFs) consist of an ordered array of metal clusters connected via organic molecules defined as the linkers. There is an extraordinary variety of novel structures, both known and conceivable.[1] Researchers have explored MOFs as potential heterogeneous catalysts due to their high porosity, active site dispersion, and large surface area.[2−7] There are many examples of their successful use as a catalyst in solvent systems at relatively mild temperatures,[8−11] whereas there are not quite as many examples for gas-phase catalytic reactions, since high temperatures and pressures can lead to decomposition of the MOF structures.[3,5,12] For many MOFs, poor stability in water also limits their application for aqueous phase catalytic reactions.[13,14] Over the years, researchers have tried to overcome these limitations by choosing a combination of metal cluster and linkers that provide improved binding strength[15,16] and by functionalizing the organic linkers for improved hydrophobicity, adsorption capacity, framework flexibility,[17,18] etc.

Zr-MOFs, where the metal cluster is a zirconium oxide-based coordinated complex, are inherently more stable at elevated temperatures (e.g., 700−800 K) and in water.[12,17,19,20] Nevertheless, when subjected to temperatures higher than 800 K, Zr-MOFs start losing mass due to the decomposition of the organic linkers and result in the evolution of organic gaseous molecules[21,22] and the characteristics of the residual solid change. The chemistry associated with the thermal decomposition of these MOFs is still not well studied.[12,23−25] Yet, in select circumstances, decomposed MOF structures, incorporating active metal atoms, have demonstrated exceptional activity for gas-phase catalytic reactions.[26,27] MIL-140C is a Zr-MOF with ZrO_7 metal oxide-based clusters with BPDC (biphenyl dicarboxylic acid) linkers. MIL-140C is a good candidate for separating biomolecules from aqueous solutions of amino acids and is also being explored as a potential heterogeneous catalyst.[14,19] Recently, a thermally decomposed MIL-140C with Ru and a small proportion of modified linkers was reported as a stable catalyst for CO_2 conversion into methane.[27] It was suggested that after the decomposition, the metal clusters are finely dispersed within the disrupted or even carbonized organic linkers, which is responsible for the exceptional catalytic properties of the thermally decomposed MOFs.[28,29] Understanding thermal decomposition of MIL-140C is crucial for the development of a controlled pyrolysis route to candidate catalytic materials at temperatures and pressures appropriate to gas-phase reactions.[30]

Here, we combine ReaxFF molecular dynamics and experiments to understand the thermal decomposition of MIL-140C. The ReaxFF force field has been successfully applied to the understanding of the thermal stability,[24,25] the water stability,[23,31] and the glass-forming ability[32−34] of a number of different MOFs. First, a ReaxFF parameter set suitable for the Zr/C/H/O chemistry simulations is introduced. Then, the proposed ReaxFF force field is used to

Received: September 24, 2020
Accepted: November 30, 2020
Published: December 15, 2020

Appendix 2

Supplementary information

Understanding the effect of framework topology, linker chemistry, and chemical environment on the thermally decomposed MOFs

Swarit Dwivedi[1], Malgorzata Kowalik[2], Vignesh Pakkiam[3], Jeremy Mullins[3], Alessandria Sarmiento[3], Adri van Duin[2], Akshat Tanksale[1], Alan L. Chaffee[3]

1)Department of Chemical Engineering, Monash University, Clayton 3800, Victoria, Australia

2) Department of Mechanical Engineering, The Pennsylvania State University, University Park, PA, USA

3) School of Chemistry, Monash University, Clayton 3800, Victoria, Australia

B.1. NVT vs NPT

For temperatures over 1500 K, the density drops exponentially due to extremely high simulation temperature. As mentioned earlier, these high temperatures are required to accelerate the chemical reaction. However, the expansion of the simulation box leads to the separation of the different segments of the broken structure further apart, which is not the case experimentally. The structure at 2000 K by NPT route (Figure B.1(a)) has the segments of the MIL-140C structure drifted apart, whereas the structure at 2000 K by NVT route (Figure B.1(b)) remains connected during decomposition. Therefore, the NVT simulations is more likely to produce data that is similar to that of experimental reality. This is due to the atoms still being able to interact with one another, whereas in NPT simulations where pressure is constant, there is no restriction on volume and hence atoms may stray from one another. Therefore, although generally the NPT simulations are more reliable in simulating constant pressure experimental conditions, we are using NVT at higher temperatures because of the disconnect between experiment and simulation, and hence to avoid excessive expansion of the simulation box.

NVT simulations are more realistic as the space that atoms and molecules can be in the system is limited to only a certain amount. Therefore, atoms are not able to move further into a space that would not be allowed in an experimental setting. As shown in Figure B.1, decomposition in NPT leads to the molecules and atoms occupying more space. On the other hand, the NVT image in this figure demonstrates that since the volume is fixed, the particles do not go far from one another.

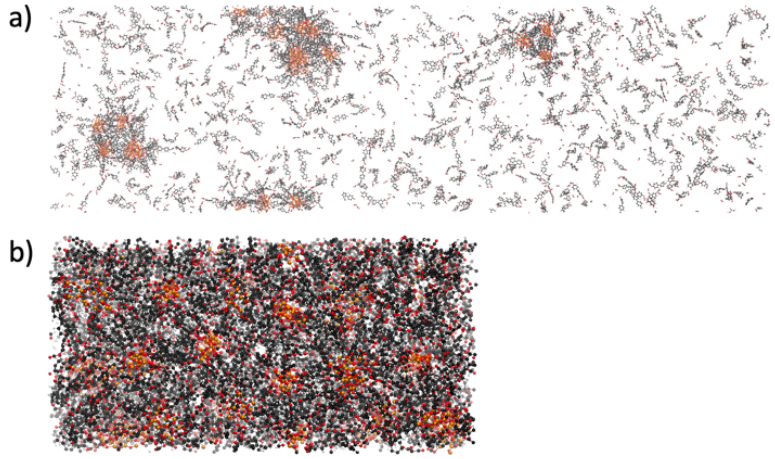

Figure B.1. (a) MIL-140C 3-3-12 after 200 ps @ 2000 K – NPT simulation regime. (b) MIL-140C 3-3-12 after 200 ps @ 2000 K – NVT simulation regime. Figures are not scalable to one another.

B.2 Optimising the supercell size in the z-direction

We considered three supercell size from the DFT optimised unit cell of MIL-140C. Three supercells vary in the z-direction (3-3-4, 3-3-8, and 3-3-12). We compared the density (Fig. B.2 & B.3) and the potential energy (E_p, Fig. B.4 & B.5) per atom during the thermal decomposition. As seen in Figure B.2, the densities of all three overlap, demonstrating that bond breaking activity was the same in all systems. Here, density starts of as a plateau, then increases by 0.06 g/cm^3 when heating from 600 to approximately 1500 K. At around 1500 K, density decreases and falls very low at 2000 K. The increase in density is also observed in the NVT simulations, but after slightly decreasing, density stays at a plateau from 1500K, as seen in Figure 6. At temperatures higher than 1500 K, the density remains constant, which is obvious as this is a *NVT* simulation, and the density cannot increase. The constant final density of 3-3-12 is different from the other two sizes in the *NVT* simulations.

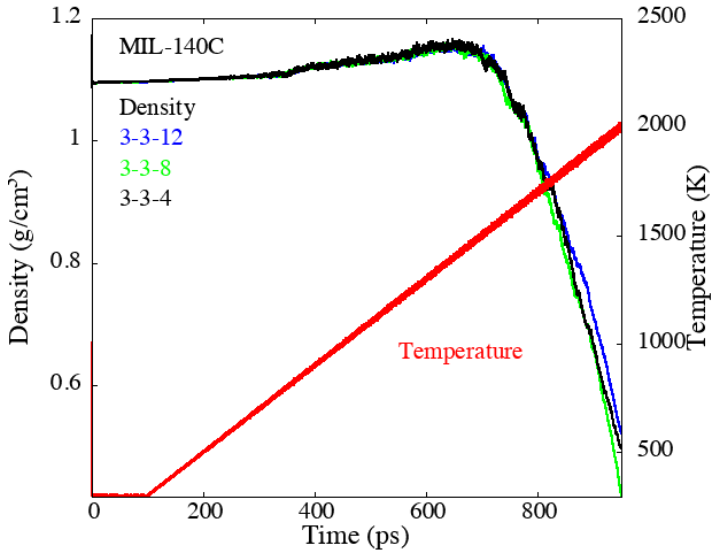

Figure B.2: Densities of different sizes of MIL-140C throughout thermal decomposition from 300-2000 K, under NPT (constant pressure).

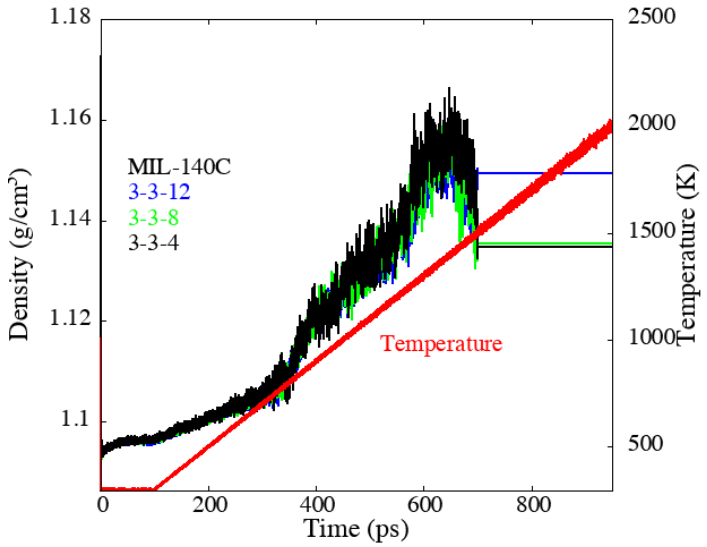

Figure B.3: Densities of different sizes of MIL-140C throughout thermal decomposition from 300-2000 K, under NVT (constant volume).

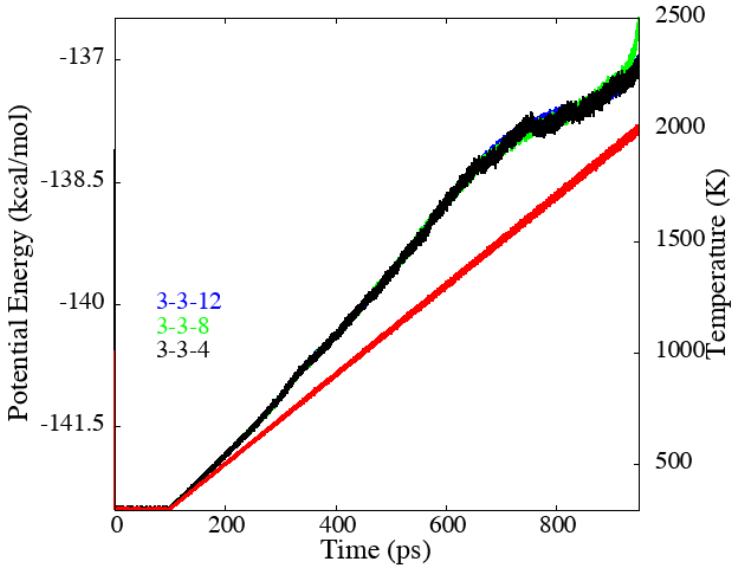

Figure B.4. Potential energy of the different sizes of MIL-140C throughout NPT simulation from 300-2000 K decomposition.

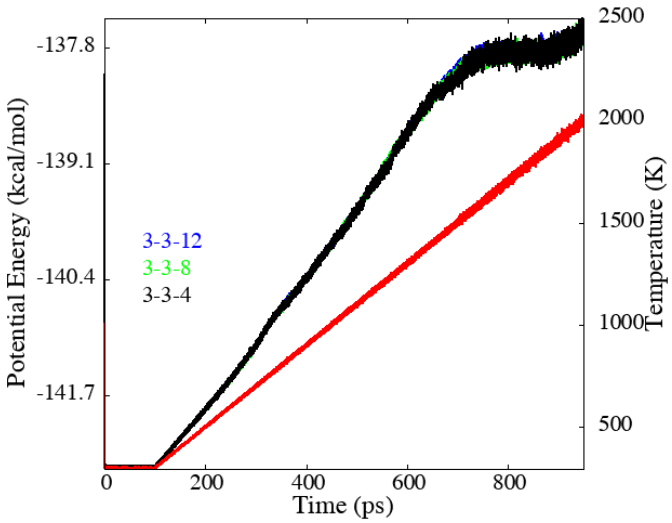

Figure B.5. Potential energy of the different sizes of MIL-140C throughout NVT simulation from 300-2000 K decomposition.

B.3 Decomposition at higher temperatures

Two temperatures were tested for decomposition – 2000 K and 2500 K. It has been observed that decomposition is does not complete at 2000 K, as the Zr-O ladder within MIL-140C was not being decomposed and Zr clusters were not forming as much (Figure 18a). Therefore, simulation regimes that reached 2500 K were completed, where larger Zr clusters were being formed (Figure 18b).

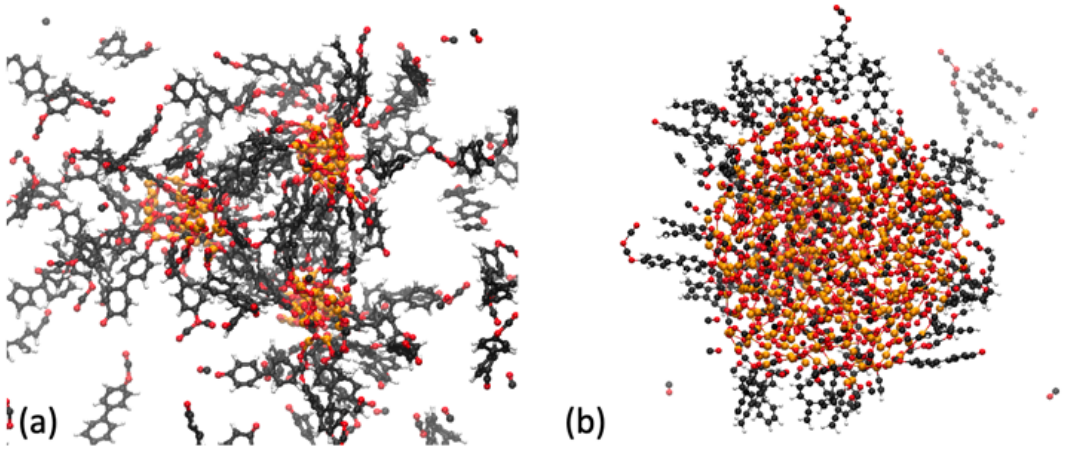

Figure B.6: (a) Three Zr clusters formed in MIL-140C 3-3-12, after being decomposed at 2000 K. (b) One relatively large Zr cluster formed in MIL-140C 3-3-12, after being decomposed at 2500 K.

Appendix C

Supplementary Information

Reactive MD-force field: Water/Pt/Ni/nafion/Ru

39 ! Number of general parameters
50.0000 !Overcoordination parameter
9.5469 !Overcoordination parameter
26.5405 !Valency angle conjugation parameter
1.7224 !Triple bond stabilisation parameter
6.8702 !Triple bond stabilisation parameter
60.4850 !C2-correction
1.0588 !Undercoordination parameter
4.6000 !Triple bond stabilisation parameter
12.1176 !Undercoordination parameter
13.3056 !Undercoordination parameter
-51.3259 !Triple bond stabilization energy
0.0000 !Lower Taper-radius
10.0000 !Upper Taper-radius
2.8793 !Not used
33.8667 !Valency undercoordination
6.0891 !Valency angle/lone pair parameter
1.0563 !Valency angle
2.0384 !Valency angle parameter
6.1431 !Not used
6.9290 !Double bond/angle parameter
0.3989 !Double bond/angle parameter: overcoord
3.9954 !Double bond/angle parameter: overcoord
-2.4837 !Not used
5.7796 !Torsion/BO parameter
10.0000 !Torsion overcoordination
1.9487 !Torsion overcoordination
-1.2327 !Conjugation 0 (not used)
2.1645 !Conjugation
1.5591 !vdWaals shielding
0.1000 !Cutoff for bond order (*100)
2.1365 !Valency angle conjugation parameter
0.6991 !Overcoordination parameter
50.0000 !Overcoordination parameter
1.8512 !Valency/lone pair parameter
0.5000 !Not used

```
 20.0000 !Not used
  5.0000 !Molecular energy (not used)
  0.0000 !Molecular energy (not used)
  2.6962 !Valency angle conjugation parameter
11    ! Nr of atoms; cov.r; valency;a.m;Rvdw;Evdw;gammaEEM;cov.r2;#
        alfa;gammavdW;valency;Eunder;Eover;chiEEM;etaEEM;n.u.
        cov r3;Elp;Heat inc.;n.u.;n.u.;n.u.;n.u.
        ov/un;val1;n.u.;val3,vval4
C   1.3817   4.0000  12.0000   1.8903   0.1838   0.9000   1.1341   4.0000
    9.7559   2.1346   4.0000  34.9350  79.5548   5.9666   7.0000   0.0000
    1.2114   0.0000 202.5551   8.9539  34.9289  13.5366   0.8563   0.0000
   -2.8983   2.5000   1.0564   4.0000   2.9663   0.0000   0.0000   0.0000
H   0.8930   1.0000   1.0080   1.3550   0.0930   0.8203  -0.1000   1.0000
    8.2230  33.2894   1.0000   0.0000 121.1250   3.7248   9.6093   1.0000
   -0.1000   0.0000  61.6606   3.0408   2.4197   0.0003   1.0698   0.0000
  -19.4571   4.2733   1.0338   1.0000   2.8793   0.0000   0.0000   0.0000
O   1.2450   2.0000  15.9990   2.3890   0.1000   1.0898   1.0548   6.0000
    9.7300  13.8449   4.0000  37.5000 116.0768   8.5000   8.3122   2.0000
    0.9049   0.4056  59.0626   3.5027   0.7640   0.0021   0.9745   0.0000
   -3.5500   2.9000   1.0493   4.0000   2.9225   0.0000   0.0000   0.0000
N   1.2333   3.0000  14.0000   1.9324   0.1376   0.8596   1.1748   5.0000
   10.0667   7.8431   4.0000  32.2482 100.0000   6.8418   6.3404   2.0000
    1.0433  13.7673 119.9837   2.1961   3.0696   2.7683   0.9745   0.0000
   -4.3875   2.6192   1.0183   4.0000   2.8793   0.0000   0.0000   0.0000
S   1.9405   2.0000  32.0600   2.0677   0.2099   1.0336   1.5479   6.0000
    9.9575   4.9055   4.0000  52.9998 112.1416   5.6210   8.2545   2.0000
    1.4601   9.7177  71.1843   5.7487  23.2859  12.7147   0.9745   0.0000
  -11.0000   2.7466   1.0338   6.2998   2.8793   0.0000   0.0000   0.0000
F   1.2100   1.0000  18.9984   1.8601   0.1200   0.3000  -0.1000   7.0000
   11.5000   7.5000   4.0000   9.2533   0.2000   9.0000  15.0000   0.0000
   -1.0000  35.0000   1.5000   6.9821   4.1799   1.0561   0.0000   0.0000
   -7.3000   2.6656   1.0493   4.0000   2.9225   0.0000   0.0000   0.0000
Pt  1.9820   2.0000 195.0800   2.0423   0.3309   0.6000  -1.0000   2.0000
   12.3677   6.0083   2.0000   0.0000   0.0000   4.6363   6.1590   0.0000
   -1.0000   0.0000 133.1770  27.2704   1.8727   0.1586   0.8563   0.0000
  -13.0000   1.7287   1.0338   5.0000   2.5791   0.0000   0.0000   0.0000
Cl  1.8478   1.0000  35.4500   2.0064   0.2210   0.7524  -1.0000   7.0000
   11.5472   8.1426   1.0000   0.0000   0.0000   7.9820   7.9758   0.0000
   -1.0000   0.0000 143.1770   6.2293   5.2294   0.1542   0.8563   0.0000
   -7.4990   3.1823   1.0338   1.0000   2.5791   0.0000   0.0000   0.0000
Ni  1.8201   2.0000  58.6900   1.9449   0.1880   0.8218   0.1000   2.0000
   12.1594   3.8387   2.0000   0.0000   0.0000   4.8038   7.3852   0.0000
   -1.0000   0.0000 104.1070  50.6786   0.6762   0.0981   0.8563   0.0000
   -3.7733   3.6035   1.0338   8.0000   2.5791   0.0000   0.0000   0.0000
```

Ru 2.3595 4.0000 101.0700 2.0555 0.3164 0.8777 0.1000 8.0000
12.4373 4.7377 4.0000 0.0000 0.0000 4.4613 5.5506 0.0000
0.1000 0.0000 92.5070 66.6047 14.4716 0.1542 0.8563 0.0000
-7.3451 3.0222 1.0338 8.0000 2.5791 0.0000 0.0000 0.0000
X -0.1000 2.0000 1.0080 2.0000 0.0000 1.0000 -0.1000 6.0000
10.0000 2.5000 4.0000 0.0000 0.0000 8.5000 1.5000 0.0000
-0.1000 0.0000 -2.3700 8.7410 13.3640 0.6690 0.9745 0.0000
-11.0000 2.7466 1.0338 2.0000 2.8793 0.0000 0.0000 0.0000
45 ! Nr of bonds; Edis1;LPpen;n.u.;pbe1;pbo5;13corr;pbo6
pbe2;pbo3;pbo4;n.u.;pbo1;pbo2;ovcorr
1 1 158.2004 99.1897 78.0000 -0.7738 -0.4550 1.0000 37.6117 0.4147
0.4590 -0.1000 9.1628 1.0000 -0.0777 6.7268 1.0000 0.0000
1 2 169.4760 0.0000 0.0000 -0.6083 0.0000 1.0000 6.0000 0.7652
5.2290 1.0000 0.0000 1.0000 -0.0500 6.9136 0.0000 0.0000
2 2 153.3934 0.0000 0.0000 -0.4600 0.0000 1.0000 6.0000 0.7300
6.2500 1.0000 0.0000 1.0000 -0.0790 6.0552 0.0000 0.0000
1 3 165.7010 107.8426 73.9004 -0.8452 -0.3081 1.0000 11.1499 1.0971
0.7754 -0.3270 6.8632 1.0000 -0.1018 5.3643 0.0000 0.0000
3 3 142.2858 145.0000 50.8293 0.2506 -0.1000 1.0000 29.7503 0.6051
0.3451 -0.1055 9.0000 1.0000 -0.1225 5.5000 1.0000 0.0000
1 4 134.1215 140.2179 79.9745 0.0163 -0.1428 1.0000 27.0617 0.2000
0.1387 -0.3681 7.1611 1.0000 -0.1000 5.0825 1.0000 0.0000
3 4 130.8596 169.4551 40.0000 0.3837 -0.1639 1.0000 35.0000 0.2000
1.0000 -0.3579 7.0004 1.0000 -0.1193 6.8773 1.0000 0.0000
4 4 157.9384 82.5526 152.5336 0.4010 -0.1034 1.0000 12.4261 0.5828
0.1578 -0.1509 11.9186 1.0000 -0.0861 5.4271 1.0000 0.0000
2 3 160.0000 0.0000 0.0000 -0.5725 0.0000 1.0000 6.0000 0.5626
1.1150 1.0000 0.0000 0.0000 -0.0920 4.2790 0.0000 0.0000
2 4 231.8173 0.0000 0.0000 -0.3364 0.0000 1.0000 6.0000 0.4402
8.8910 1.0000 0.0000 1.0000 -0.0327 6.5754 0.0000 0.0000
1 5 128.7959 56.4134 39.0716 0.0688 -0.4463 1.0000 31.1766 0.4530
0.1955 -0.3587 6.2148 1.0000 -0.0770 6.6386 1.0000 0.0000
2 5 136.1049 0.0000 0.0000 -0.4669 0.0000 1.0000 6.0000 0.3803
10.5730 1.0000 0.0000 1.0000 -0.1000 7.0000 1.0000 0.0000
3 5 165.3308 220.0000 40.0000 0.7131 -0.2406 1.0000 22.1005 0.2000
0.8027 -0.2748 8.3393 1.0000 -0.1043 5.6108 1.0000 0.0000
4 5 130.0000 180.0000 0.0000 0.5000 -0.2000 1.0000 40.0000 0.3000
0.4000 -0.2500 9.0000 1.0000 -0.1000 6.0000 1.0000 0.0000
5 5 96.1871 93.7006 68.6860 0.0955 -0.4781 1.0000 17.8574 0.6000
0.2723 -0.2373 9.7875 1.0000 -0.0950 6.4757 1.0000 0.0000
1 6 237.8781 0.0000 0.0000 -0.7438 -0.5000 1.0000 35.0000 1.0460
3.6661 -0.2500 15.0000 1.0000 -0.0800 5.4719 1.0000 0.0000
2 6 0.0000 0.0000 0.0000 -0.4643 0.0000 1.0000 6.0000 0.6151
12.3710 1.0000 0.0000 1.0000 -0.1008 8.5980 0.0000 0.0000

3 6 0.0000 0.0000 0.0000 0.2500 -0.5000 1.0000 45.0000 0.6000
0.4000 -0.2500 15.0000 1.0000 -0.1000 10.0000 1.0000 0.0000
4 6 0.0000 0.0000 0.0000 -0.4643 0.0000 1.0000 6.0000 0.6151
12.3710 1.0000 0.0000 1.0000 -0.0098 8.5980 0.0000 0.0000
5 6 0.0000 0.0000 0.0000 0.2500 -0.5000 1.0000 45.0000 0.6000
0.4000 -0.2500 15.0000 1.0000 -0.1000 10.0000 1.0000 0.0000
6 6 250.0765 0.0000 0.0000 0.2298 -0.3500 1.0000 25.0000 0.8427
0.1167 -0.2500 15.0000 1.0000 -0.1506 7.3516 1.0000 0.0000
6 7 -0.0100 0.0000 0.0000 0.9248 -0.3500 1.0000 35.0000 0.1231
0.3064 -0.2500 25.0000 1.0000 -0.1903 8.4146 1.0000 0.0000
1 7 167.9451 0.0000 0.0000 -0.1620 -0.2000 1.0000 16.0000 0.3702
1.7129 -0.2000 15.0000 1.0000 -0.1971 7.4949 1.0000 0.0000
2 7 161.1691 0.0000 0.0000 -0.2641 0.0000 1.0000 6.0000 0.1273
8.0163 1.0000 0.0000 1.0000 -0.1717 9.3297 0.0000 0.0000
3 7 179.8510 0.0000 0.0000 -0.6047 -0.2000 1.0000 16.0000 0.0388
0.5748 -0.2000 15.0000 1.0000 -0.1458 5.0000 1.0000 0.0000
4 7 183.3242 0.0000 0.0000 0.5441 -0.2000 1.0000 16.0000 0.6888
-0.0634 -0.2000 15.0000 1.0000 -0.1558 5.0000 1.0000 0.0000
5 7 0.0000 0.0000 0.0000 0.2500 -0.5000 1.0000 45.0000 0.6000
0.4000 -0.2500 15.0000 1.0000 -0.1000 10.0000 1.0000 0.0000
7 7 122.1369 0.0000 0.0000 -0.3578 -0.2000 0.0000 16.0000 0.2877
0.9897 -0.2000 15.0000 1.0000 -0.0853 5.4801 0.0000 0.0000
1 8 50.6675 0.0000 0.0000 0.0004 -0.2000 0.0000 16.0000 0.3115
1.0000 -0.2000 15.0000 1.0000 -0.1062 5.1596 0.0000 0.0000
2 8 50.6675 0.0000 0.0000 0.0004 -0.2000 0.0000 16.0000 0.3115
1.0000 -0.2000 15.0000 1.0000 -0.1062 5.1596 0.0000 0.0000
3 8 50.6675 0.0000 0.0000 0.0004 -0.2000 0.0000 16.0000 0.3115
1.0000 -0.2000 15.0000 1.0000 -0.1062 5.1596 0.0000 0.0000
4 8 50.6675 0.0000 0.0000 0.0004 -0.2000 0.0000 16.0000 0.3115
1.0000 -0.2000 15.0000 1.0000 -0.1062 5.1596 0.0000 0.0000
7 8 140.6675 0.0000 0.0000 0.0004 -0.2000 0.0000 16.0000 0.3115
1.0000 -0.2000 15.0000 1.0000 -0.1062 5.1596 0.0000 0.0000
8 8 125.6675 0.0000 0.0000 0.0004 -0.2000 0.0000 16.0000 0.3115
1.0000 -0.2000 15.0000 1.0000 -0.1062 7.0000 0.0000 0.0000
1 9 75.7495 12.7904 0.0000 0.4276 -0.2000 1.0000 16.0000 0.1333
0.5004 -0.1246 12.4887 1.0000 -0.1113 5.1759 1.0000 0.0000
2 9 109.4050 0.0000 0.0000 0.3531 0.0000 1.0000 6.0000 0.1075
0.0230 1.0000 0.0000 1.0000 -0.0756 5.8346 0.0000 0.0000
3 9 118.6999 0.0000 0.0000 -0.1042 -0.2000 1.0000 16.0000 0.1724
0.8280 -0.2500 15.0000 1.0000 -0.1013 5.6326 1.0000 0.0000
9 9 91.2220 0.0000 0.0000 -0.2538 -0.2000 0.0000 16.0000 0.2688
1.4651 -0.2000 15.0000 1.0000 -0.1435 4.3908 0.0000 0.0000
7 9 68.1705 0.0000 0.0000 0.9869 -0.2000 0.0000 16.0000 0.0100
0.2118 -0.2000 15.0000 1.0000 -0.2148 4.0000 0.0000 0.0000

1 10 154.4715 19.5378 0.0000 -0.7948 -0.2000 1.0000 16.0000 0.2377
0.3543 -0.3479 9.1411 1.0000 -0.1385 5.0985 1.0000 0.0000
2 10 91.4950 0.0000 0.0000 -0.0491 0.0000 1.0000 6.0000 0.1119
0.2447 1.0000 0.0000 1.0000 -0.0885 5.0480 0.0000 0.0000
3 10 148.4765 97.0930 63.8410 0.0879 -0.2572 1.0000 24.7279 0.0803
0.9776 -0.2644 12.3194 1.0000 -0.1717 6.4806 1.0000 0.0000
4 10 0.0000 0.0000 0.0000 0.1073 -0.5000 1.0000 25.0000 0.5000
1.0000 -0.5000 15.0000 1.0000 -0.2000 10.0000 1.0000 0.0000
7 10 108.2468 0.0000 0.0000 -0.1484 -0.2000 0.0000 16.0000 0.2733
3.2947 -0.2000 15.0000 1.0000 -0.0927 5.6435 0.0000 0.0000
10 10 73.1425 0.0000 0.0000 -0.0100 -0.2000 0.0000 16.0000 0.1000
0.1000 -0.2000 15.0000 1.0000 -0.1744 8.2223 0.0000 0.0000
25 ! Nr of off-diagonal terms; Ediss;Ro;gamma;rsigma;rpi;rpi2
1 2 0.1239 1.4004 9.8467 1.1210 -1.0000 -1.0000
2 3 0.0283 1.2885 10.9190 0.9215 -1.0000 -1.0000
2 4 0.1059 1.8290 9.7818 0.9598 -1.0000 -1.0000
1 3 0.1156 1.8520 9.8317 1.2854 1.1352 1.0706
1 4 0.1447 1.8766 9.7990 1.3436 1.1885 1.1363
3 4 0.1048 2.0003 10.1220 1.3173 1.1096 1.0206
1 5 0.1408 1.8161 9.9393 1.7986 1.3021 1.4031
2 5 0.0895 1.6239 10.0104 1.4640 -1.0000 -1.0000
3 5 0.2250 1.7911 10.2423 1.4546 1.4011 -1.0000
4 5 0.1505 1.9000 10.5104 1.8000 1.4000 -1.0000
1 6 0.1071 1.6243 11.0402 1.3176 -1.0000 -1.0000
2 6 0.0431 1.7204 10.3632 0.5386 -1.0000 -1.0000
1 7 0.1180 1.7341 12.4934 1.8280 -1.0000 -1.0000
2 7 0.1644 1.3669 12.0930 1.5859 -1.0000 -1.0000
3 7 0.1128 1.9155 10.1129 1.5035 -1.0000 -1.0000
4 7 0.1000 2.0294 12.2593 1.5743 -1.0000 -1.0000
7 8 0.1847 2.1006 11.0261 1.7524 -1.0000 -1.0000
1 9 0.1806 1.6000 10.1488 1.6502 1.3988 -1.0000
2 9 0.0578 1.4623 11.5257 1.2242 -1.0000 -1.0000
3 9 0.0504 1.7959 11.7893 1.4423 -1.0000 -1.0000
7 9 0.1919 2.1352 12.2879 1.8319 -1.0000 -1.0000
1 10 0.1957 1.5041 13.6357 1.8525 1.4000 -1.0000
2 10 0.0456 1.5612 11.7206 1.4507 -1.0000 -1.0000
3 10 0.1282 1.8008 11.7025 1.6471 1.4974 1.2433
7 10 0.4018 2.0209 12.3922 2.1021 -1.0000 -1.0000
132 ! Nr of angles;at1;at2;at3;Thetao,o;ka;kb;pv1;pv2
1 1 1 59.0573 30.7029 0.7606 0.0000 0.7180 6.2933 1.1244
1 1 2 65.7758 14.5234 6.2481 0.0000 0.5665 0.0000 1.6255
2 1 2 70.2607 25.2202 3.7312 0.0000 0.0050 0.0000 2.7500
1 2 2 0.0000 0.0000 6.0000 0.0000 0.0000 0.0000 1.0400
1 2 1 0.0000 3.4110 7.7350 0.0000 0.0000 0.0000 1.0400

2 2 2 0.0000 27.9213 5.8635 0.0000 0.0000 0.0000 1.0400
1 1 3 49.6811 7.1713 4.3889 0.0000 0.7171 10.2661 1.0463
3 1 3 77.7473 40.1718 2.9802 -25.3063 1.6170 -46.1315 2.2503
1 1 4 66.1305 12.4661 7.0000 0.0000 3.0000 50.0000 1.1880
3 1 4 73.9544 12.4661 7.0000 0.0000 3.0000 0.0000 1.1880
4 1 4 64.1581 12.4661 7.0000 0.0000 3.0000 0.0000 1.1880
2 1 3 58.5010 15.8793 4.6279 0.0000 1.2351 0.0000 1.1381
2 1 4 74.2929 31.0883 2.6184 0.0000 0.0755 0.0000 1.0500
1 2 4 0.0000 0.0019 6.3000 0.0000 0.0000 0.0000 1.0400
1 3 1 73.5312 44.7275 0.7354 0.0000 3.0000 0.0000 1.0684
1 3 3 79.4761 36.3701 1.8943 0.0000 0.7351 67.6777 3.0000
1 3 4 82.4890 31.4554 0.9953 0.0000 1.6310 0.0000 1.0783
3 3 3 80.7324 30.4554 0.9953 0.0000 1.6310 50.0000 1.0783
3 3 4 84.3637 31.4554 0.9953 0.0000 1.6310 0.0000 1.0783
4 3 4 89.7071 31.4554 0.9953 0.0000 1.6310 0.0000 1.1519
1 3 2 60.0000 25.0000 0.4201 0.0000 0.1000 0.0000 2.1900
2 3 3 75.6935 50.0000 2.0000 0.0000 1.0000 0.0000 1.1680
2 3 4 75.6201 18.7919 0.9833 0.0000 0.1218 0.0000 1.0500
2 3 2 85.8000 9.8453 2.2720 0.0000 2.8635 0.0000 1.5800
1 4 1 66.0330 22.0295 1.4442 0.0000 1.6777 0.0000 1.0500
1 4 3 103.3204 33.0381 0.5787 0.0000 1.6777 0.0000 1.0500
1 4 4 104.1335 8.6043 1.6495 0.0000 1.6777 0.0000 1.0500
3 4 3 74.1978 42.1786 1.7845 -18.0069 1.6777 0.0000 1.0500
3 4 4 74.8600 43.7354 1.1572 -0.9193 1.6777 0.0000 1.0500
4 4 4 75.0538 14.8267 5.2794 0.0000 1.6777 0.0000 1.0500
1 4 2 69.1106 25.5067 1.1003 0.0000 0.0222 0.0000 1.0369
2 4 3 81.3686 40.0712 2.2396 0.0000 0.0222 0.0000 1.0369
2 4 4 83.0104 43.4766 1.5328 0.0000 0.0222 0.0000 1.0500
2 4 2 70.8687 12.0168 5.0132 0.0000 0.0222 0.0000 1.1243
1 2 3 0.0000 25.0000 3.0000 0.0000 1.0000 0.0000 1.0400
1 2 4 0.0000 0.0019 6.0000 0.0000 0.0000 0.0000 1.0400
1 2 5 0.0000 0.0019 6.0000 0.0000 0.0000 0.0000 1.0400
3 2 3 0.0000 15.0000 2.8900 0.0000 0.0000 0.0000 2.8774
3 2 4 0.0000 0.0019 6.0000 0.0000 0.0000 0.0000 1.0400
4 2 4 0.0000 0.0019 6.0000 0.0000 0.0000 0.0000 1.0400
2 2 3 0.0000 8.5744 3.0000 0.0000 0.0000 0.0000 1.0421
2 2 4 0.0000 0.0019 6.0000 0.0000 0.0000 0.0000 1.0400
1 1 5 74.4180 33.4273 1.7018 0.1463 0.5000 0.0000 1.6178
1 5 1 79.7037 28.2036 1.7073 0.1463 0.5000 0.0000 1.6453
2 1 5 63.3289 29.4225 2.1326 0.0000 0.5000 0.0000 3.0000
1 5 2 85.9449 38.3109 1.2492 0.0000 0.5000 0.0000 1.1000
1 5 5 85.6645 40.0000 2.9274 0.1463 0.5000 0.0000 1.3830
2 5 2 83.8555 5.1317 0.4377 0.0000 0.5000 0.0000 3.0000
2 5 5 97.0064 32.1121 2.0242 0.0000 0.5000 0.0000 2.8568

3	5	3	81.0971	22.5308	7.4511	-2.3089	2.8609	0.0000	2.0914
1	5	3	70.0000	35.0000	3.4223	0.0000	1.3550	0.0000	1.2002
1	3	5	58.9977	36.2016	1.7948	0.0000	0.4304	0.0000	3.0000
3	3	5	83.9753	31.0715	3.5590	0.0000	0.8161	0.0000	1.1776
2	3	5	90.0000	17.5000	3.5000	0.0000	1.9770	0.0000	3.0000
1	1	6	74.0446	35.8484	6.6125	0.0000	0.9453	0.0000	3.0000
6	1	6	77.8443	49.0744	5.9913	0.0000	0.7835	0.0000	2.3020
1	6	1	0.0000	19.9962	3.2299	0.0000	2.1012	0.0000	1.1537
1	6	6	0.0000	25.0000	1.0000	0.0000	1.0000	0.0000	1.0400
6	1	2	69.6421	10.0000	2.0000	0.0000	1.0000	0.0000	1.0400
3	1	6	70.0000	35.0000	2.0000	0.0000	1.0000	0.0000	1.2500
5	1	6	70.0000	35.0000	3.4223	0.0000	1.3550	0.0000	1.2002
1	1	7	48.5613	31.6283	3.3259	0.0000	0.1000	0.0000	1.9693
7	1	7	80.8069	1.4012	3.5365	0.0000	0.1092	0.0000	1.0500
1	7	7	17.1757	10.0139	3.8895	0.0000	0.3173	0.0000	2.8844
1	7	1	37.5291	7.4679	1.6697	0.0000	1.0031	0.0000	2.2937
2	1	7	65.9447	15.1337	2.8716	0.0000	2.0061	0.0000	1.3774
1	7	2	74.9052	4.6753	0.6941	0.5000	1.3645	0.0000	2.5028
1	2	7	0.0000	1.2168	2.1384	0.0000	0.3244	0.0000	1.0500
2	7	2	95.0000	60.0000	1.4541	0.0000	4.0000	0.0000	1.2813
2	2	7	0.0000	1.0000	1.0243	0.0000	1.0001	0.0000	4.0000
3	2	7	0.0000	50.0000	4.0000	0.0000	1.0000	0.0000	1.2500
7	2	7	0.0000	26.7290	6.8612	0.0000	4.0000	0.0000	1.5552
2	7	7	89.4351	14.8824	3.8943	0.0000	2.2377	0.0000	2.4840
7	3	7	100.6048	32.2362	8.0087	0.0000	0.4198	0.0000	2.1758
3	7	7	100.3871	42.0526	2.2625	0.0000	-0.0110	0.0000	1.9253
3	3	7	90.0186	48.0852	0.9241	0.0000	1.5394	0.0000	1.3490
3	7	3	22.1744	28.4797	0.7861	0.0000	0.3044	0.0000	1.1850
1	7	3	47.7252	50.0000	4.2693	0.0000	1.4676	0.0000	1.1000
1	3	7	101.1629	33.2272	6.2808	0.0000	2.4718	0.0000	1.1000
3	1	7	99.4051	23.7689	0.6911	0.0000	3.4481	0.0000	1.2075
2	3	7	74.1000	8.5500	3.9501	0.0000	1.0500	0.0000	1.4519
2	7	3	14.3493	50.0000	4.1953	0.5000	2.3152	0.0000	1.1000
5	1	7	70.0000	35.0000	3.4223	0.0000	1.3550	0.0000	1.2002
2	7	7	180.0000	-50.0000	10.0000	0.0000	3.8624	0.0000	1.1000
7	2	8	0.0000	35.0000	3.0000	0.0000	0.0000	0.0000	1.0400
5	3	7	70.0000	10.0000	1.0000	0.0000	0.1000	0.0000	2.8838
1	9	1	75.6483	43.0233	0.6577	0.0000	1.4507	0.0000	1.8072
1	1	9	90.0000	30.6206	0.2855	0.0000	0.0100	0.0000	1.0400
9	1	9	87.1014	21.3282	7.0000	0.0000	0.0100	0.0000	2.2535
1	9	9	48.4493	0.9823	0.0798	0.0000	0.2181	0.0000	2.9000
3	9	3	49.6374	27.4219	1.6709	0.0000	0.0369	0.0000	2.5673
3	3	9	90.0000	31.1442	5.0000	0.0000	0.5686	0.0000	2.0931
9	3	9	42.4507	5.2354	0.5469	0.0000	1.5478	0.0000	1.0400

3 9 9 39.2561 2.4303 3.7193 0.0000 0.8924 0.0000 1.9950
2 9 2 106.3969 30.0000 0.9614 0.0000 1.9664 0.0000 2.2693
2 2 9 0.0000 23.6564 4.1965 0.0000 0.3810 0.0000 1.2323
9 2 9 0.0000 60.0000 4.7836 0.0000 0.0500 0.0000 1.6605
2 9 9 84.9500 7.3152 2.0189 0.0000 0.5938 0.0000 2.4292
2 9 9 180.0000 -50.0000 17.4604 0.0000 0.8112 0.0000 1.0400
1 9 2 62.2304 12.4120 3.4647 0.5000 1.4224 0.0000 1.8517
1 2 9 0.0000 0.2044 1.7494 0.0000 1.2268 0.0000 3.1652
2 1 9 40.5703 22.5348 1.5796 0.5000 0.0100 0.0000 1.1131
2 3 9 29.3808 16.2484 2.5832 0.5000 0.0100 0.0000 1.9017
1 9 3 70.0000 25.0000 1.0000 0.0000 1.0000 0.0000 1.2500
1 3 9 70.0000 25.0000 1.0000 0.0000 1.0000 0.0000 1.2500
3 1 9 70.0000 25.0000 1.0000 0.0000 1.0000 0.0000 1.2500
3 2 9 0.0000 7.1233 1.9895 0.5000 0.3233 0.0000 1.1000
10 3 10 89.0000 30.9123 1.2444 0.0000 1.8346 0.0000 2.4374
3 10 10 53.9732 23.9266 0.5584 0.0000 0.1000 0.0000 1.2468
3 3 10 87.9754 39.9500 1.6753 0.0000 1.4085 0.0000 1.1000
3 10 3 90.0000 15.8070 4.3055 -1.3391 0.0500 0.0000 1.2613
3 10 7 29.1970 14.8073 0.4103 0.0000 0.4114 0.0000 1.1397
3 7 10 52.7349 29.5543 3.9193 0.0000 0.3802 0.0000 1.8419
7 3 10 53.5915 28.4087 4.1195 0.0000 2.0000 0.0000 1.1000
1 1 10 70.2978 22.9682 4.5447 0.0000 0.0100 0.0000 2.0473
10 1 10 55.1674 26.9402 4.8152 0.0000 -0.0055 0.0000 1.3644
1 10 10 19.2134 7.3188 0.8554 0.0000 2.7222 0.0000 1.9226
1 10 1 44.6392 5.9626 1.9326 0.0000 2.4239 0.0000 1.5752
2 1 10 19.5673 25.3814 1.8682 0.0000 1.7527 0.0000 1.9545
1 10 2 25.3765 7.5721 1.5104 0.5000 2.7929 0.0000 2.8621
1 2 10 0.0000 5.7992 0.1000 0.0000 2.7446 0.0000 2.9673
2 10 2 85.5103 19.8100 1.0777 0.0000 0.9403 0.0000 2.4668
2 10 10 90.0000 6.9481 7.5000 0.0000 0.2223 0.0000 3.0215
10 2 10 0.0000 21.1639 5.3405 0.0000 0.0100 0.0000 1.6919
10 10 7 0.0000 3.4273 1.6387 0.0000 0.3575 0.0000 1.8131
1 10 3 86.0792 3.1964 0.3358 0.0000 1.4963 0.0000 1.5093
1 3 10 74.0333 44.1932 0.7625 0.0000 2.3684 0.0000 1.3963
3 1 10 8.7515 32.4970 4.7138 0.0000 1.3873 0.0000 2.0396
2 3 10 100.0000 2.9862 7.5000 0.0000 2.9087 0.0000 1.0400
3 2 10 0.0000 22.5000 3.5000 0.0000 2.3179 0.0000 1.0487
2 10 3 83.8460 18.9559 3.5000 0.0000 0.2131 0.0000 1.2337
2 2 10 0.0000 1.0000 1.0000 0.0000 0.0100 0.0000 2.0000
52 ! Nr of torsions;at1;at2;at3;at4;;V1;V2;V3;V2(BO);vconj;n.u;n
1 1 1 1 -0.2500 34.7453 0.0288 -6.3507 -1.6000 0.0000 0.0000
1 1 1 2 -0.2500 29.2131 0.2945 -4.9581 -2.1802 0.0000 0.0000
2 1 1 2 -0.2500 31.2081 0.4539 -4.8923 -2.2677 0.0000 0.0000
1 1 1 3 -0.3495 22.2142 -0.2959 -2.5000 -1.9066 0.0000 0.0000

2 1 1 3 0.0646 24.3195 0.6259 -3.9603 -1.0000 0.0000 0.0000
3 1 1 3 -0.5456 5.5756 0.8433 -5.1924 -1.0180 0.0000 0.0000
1 1 3 1 1.7555 27.9267 0.0072 -2.6533 -1.0000 0.0000 0.0000
1 1 3 2 -1.4358 36.7830 -1.0000 -8.1821 -1.0000 0.0000 0.0000
2 1 3 1 -1.3959 34.5053 0.7200 -2.5714 -2.1641 0.0000 0.0000
2 1 3 2 2.0000 69.9830 1.0000 -3.6538 -2.9929 0.0000 0.0000
1 1 3 3 0.6852 11.2819 -0.4784 -2.5000 -2.1085 0.0000 0.0000
2 1 3 3 0.1933 80.0000 1.0000 -4.0590 -3.0000 0.0000 0.0000
3 1 3 1 -1.9889 76.4820 -0.1796 -3.8301 -3.0000 0.0000 0.0000
3 1 3 2 0.2160 72.7707 -0.7087 -4.2100 -3.0000 0.0000 0.0000
3 1 3 3 -2.5000 71.0772 0.2542 -3.1631 -3.0000 0.0000 0.0000
1 3 3 1 2.5000 -0.6002 1.0000 -3.4297 -2.8858 0.0000 0.0000
1 3 3 2 -2.5000 -3.3822 0.7004 -5.4467 -2.9586 0.0000 0.0000
2 3 3 2 2.5000 -4.0000 0.9000 -2.5000 -1.0000 0.0000 0.0000
1 3 3 3 1.2329 -4.0000 1.0000 -2.5000 -1.7479 0.0000 0.0000
2 3 3 3 0.8302 -4.0000 -0.7763 -2.5000 -1.0000 0.0000 0.0000
3 3 3 3 -2.5000 -4.0000 1.0000 -2.5000 -1.0000 0.0000 0.0000
0 1 2 0 0.0000 0.0000 0.0000 0.0000 0.0000 0.0000 0.0000
0 2 2 0 0.0000 0.0000 0.0000 0.0000 0.0000 0.0000 0.0000
0 2 3 0 0.0000 0.1000 0.0200 -2.5415 0.0000 0.0000 0.0000
0 1 1 0 0.0000 50.0000 0.3000 -4.0000 -2.0000 0.0000 0.0000
0 3 3 0 0.5511 25.4150 1.1330 -5.1903 -1.0000 0.0000 0.0000
0 1 4 0 -2.4242 128.1636 0.3739 -6.6098 -2.0000 0.0000 0.0000
0 2 4 0 0.0000 0.1000 0.0200 -2.5415 0.0000 0.0000 0.0000
0 3 4 0 1.4816 55.6641 0.0004 -7.0465 -2.7203 0.0000 0.0000
0 4 4 0 -0.3244 27.7086 0.0039 -2.8272 -2.0000 0.0000 0.0000
4 1 4 4 -5.5181 8.9706 0.0004 -6.1782 -2.0000 0.0000 0.0000
0 1 5 0 3.3423 30.3435 0.0365 -2.7171 0.0000 0.0000 0.0000
0 5 5 0 -0.0555 -5.0000 0.1515 -2.2056 0.0000 0.0000 0.0000
0 2 5 0 0.0000 0.0000 0.0000 0.0000 0.0000 0.0000 0.0000
1 1 1 6 0.5000 0.1000 0.4683 -11.5274 -1.7255 0.0000 0.0000
2 1 1 6 0.0000 49.3871 0.2000 -10.5765 -1.7255 0.0000 0.0000
6 1 1 6 -0.5000 95.4727 -0.2080 -4.8579 -1.7255 0.0000 0.0000
0 1 6 0 4.0000 45.8264 0.9000 -4.0000 0.0000 0.0000 0.0000
0 6 6 0 4.0000 45.8264 0.9000 -4.0000 0.0000 0.0000 0.0000
2 3 7 7 0.0000 0.0100 0.0100 -5.2275 0.0000 0.0000 0.0000
2 3 3 7 2.5000 2.1635 2.0000 -3.5654 -1.0000 0.0000 0.0000
7 3 3 7 1.7276 50.0000 0.0100 -2.5000 -1.0000 0.0000 0.0000
2 3 1 7 0.8042 9.9858 1.7500 -4.6466 -1.0000 0.0000 0.0000
1 1 1 7 2.1746 45.0000 0.6721 -2.5000 0.0000 0.0000 0.0000
7 1 1 7 -0.3957 50.0000 0.0100 -2.5173 0.0000 0.0000 0.0000
2 1 1 7 2.5000 0.0100 0.0100 -2.7611 0.0000 0.0000 0.0000
2 3 5 3 2.5000 2.5000 0.2237 -10.0000 -1.0000 0.0000 0.0000
0 3 5 0 -2.5000 50.0000 -0.5000 -10.0000 -1.0000 0.0000 0.0000

1 1 1 9 0.1109 33.5901 -0.7768 -4.2047 0.0000 0.0000 0.0000

9 1 1 9 0.0509 16.5248 -1.9621 -3.0000 0.0000 0.0000 0.0000

2 1 1 9 1.2085 -2.0000 1.3837 -4.0804 0.0000 0.0000 0.0000

9 3 3 9 0.0509 30.0000 0.5000 -4.0000 0.0000 0.0000 0.0000

9 ! Nr of hydrogen bonds;at1;at2;at3;Rhb;Dehb;vhb1

3 2 3 2.1200 -3.5800 1.4500 19.5000

3 2 4 1.6658 -3.8907 3.0582 19.1627

4 2 3 1.8738 -3.5421 3.0582 19.1627

4 2 4 1.8075 -4.1846 3.0582 19.1627

3 2 5 1.5000 -2.0000 3.0582 19.1627

4 2 5 1.5000 -2.0000 3.0582 19.1627

5 2 3 1.5000 -2.0000 3.0582 19.1627

5 2 4 1.5000 -2.0000 3.0582 19.1627

5 2 5 1.5000 -2.0000 3.0582 19.1627